Ph.D. Program in Civil, Chemical and Environmental Engineering
Curriculum in Fluid Dynamics and Environmental Engineering

Department of Civil, Chemical and Environmental Engineering
Polytechnic School, University of Genoa, Italy.

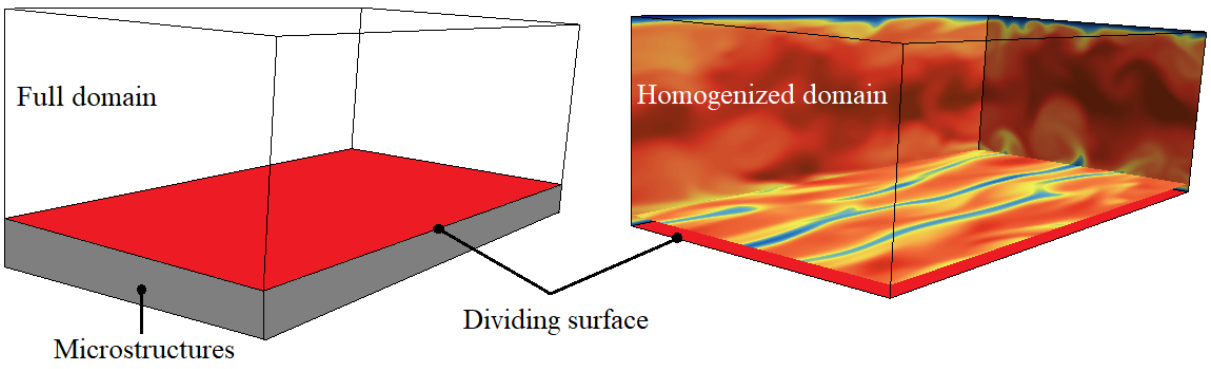

Application of Homogenization Theory to the Flow Over and Through Micro-Structured, Porous and Elastic Surfaces

Sahrish Batool Naqvi

Application of Homogenization Theory to the Flow Over and Through Micro-Structured, Porous and Elastic Surfaces by

Sahrish Batool Naqvi

Dissertation discussed in partial fulfillment of

the requirements for the Degree of

DOCTOR OF PHILOSOPHY

Civil, Chemical and Environmental Engineering

Curriculum in Fluid Dynamics and Environmental Engineering,

Department of Civil, Chemical and Environmental Engineering, University of Genoa, Italy

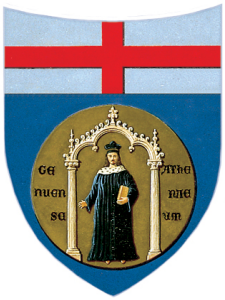

Month, YEAR

Adviser(s):
Prof. Alessandro Bottaro - Department of Civil, Chemical and Environmental Engineering, University of Genoa, Italy

External Reviewers:
Prof. Ricardo García-Mayoral - Department of Engineering, University of Cambridge
Prof. Francisco José Valdés Parada - Ingeniería de procesos e Hidráulica, Universidad Autonóma Metropolitana

Examination Committee:
Prof. Jan Pralits - Department of Civil Chemical and environmental Engineering, University of Genoa, Italy
Prof. Simone Camarri - Department of Civil and industrial Engineering, University of Pisa, Italy
Prof. Franco Auteri - Department of Science and Aerospace Technology, University of Milan, Italy

Ph.D. program in Civil, Chemical and Environmental Engineering
Curriculum in Fluid Dynamics and Environmental Engineering
Cycle XXXX

Acknowledgements

Firstly, I would like to express my sincere gratitude to my advisor Prof. Alessandro Bottaro for the continuous support of my Ph.D study and related research, for his patience, motivation, and immense knowledge. His guidance helped me in all the time of research and writing of this thesis. Secondly, I would like to acknowledge:

- Open access funding provided by Universita‘ degli Studi di Genova within the CRUI-CARE Agreement.
- The financial support of the Italian Ministry of University and Research, program PRIN 2017, Project 2017X7Z8S3 LUBRI-SMOOTH, is gratefully acknowledged.

I would like to dedicate this thesis to my loving parents, supervisor, husband, all teachers, friends and colleagues.

Declaration

I hereby declare that except where specific reference is made to the work of others, the contents of this dissertation are original and have not been submitted in whole or in part for consideration for any other degree or qualification in this, or any other university. This dissertation is my own work and contains nothing which is the outcome of work done in collaboration with others, except as specified in the text and Acknowledgements.

Sahrish Batool Naqvi

September 00, 0000

ABSTRACT

This research is aimed to develop a homogenized model for practical applications of the fluid flow over and through the microstructured surfaces, which prescribed reliable estimates of the linear response of overall structures. The up-scaling method based on asymptotic theories is used to treat the fluid flow problems where various spatial scales (microscopic and macroscopic) are present. The goal of this work is to provide an inexpensive high-order homogenized framework for the flows over complex textures such as elastic and rigid rough surfaces, isotropic and orthotropic porous media, with periodic internal distributions, independent of the material properties and the constituent's geometrical arrangement in a reliable way. The framework includes effective conditions corrected up to the high-order as a replacement of the micro-textured surfaces, producing sizeable effects on the overlaying flow as compared to the classical Navier's conditions. These effective conditions contain parameters that are non-empirical and stems from the numerical solution of auxiliary Stokes-like problems. These conditions developed for different applications are tested on the classical problems such as Hiemenz stagnation point flow over a rough plate, Hiemenz stagnation point flow over isotropic and orthotropic porous bed, backward-facing step with porous step region, and flow over the permeable channel, to test the accuracy and working capability of the framework for different flow situations. For simulation purposes, commercial software COMSOL Multiphysics (2019) academic version 5.4, open-source solver FreeFEM Hecht (2012), and commercial software Star-CCM+ by Siemens (2021) are used. The outcomes of the model simulations are compared with exact simulations of our own and with literature. The overall results suggested that the homogenized model is computationally inexpensive compared to the feature-resolving simulations and can provide a quick design of drag-altering micro-textured surfaces. Moreover, the present model is flexible for further amendments to tackle complex engineered and industrial fluid flow problems.

List of Figures

List of Tables

INDEX

INTRODUCTION

1.1. Objectives

The main objectives of this thesis are:

- High-order accurate approach to model the regularly microstructured walls without the need to numerically resolve fine-scale near-wall details to limit the computational cost.
- To check the effect of microstructure engineered surfaces (rough, porous, and elastic) through the use of high order effective conditions on the overlaying fluid flow in various situations often used in practical applications.
- To provide the base of complex modeling of quasi-periodic and irregular rough walls and anisotropic porous media which will not present fundamental nor numerical difficulties in the future.
- To provide an optimal design of drag-altering micro-textured surfaces using an inexpensive model.

1.2. Applications

In practical engineering applications, many biological systems (see some example in figure 1.1) contain surfaces exhibiting microstructure features and properties. Identification of these special features such as surface corrugation, porosity, elasticity. are the goals of biomimetics (Bhushan (2009); Jung and Bhushan (2009); Bixler and Bhushan (2012))) together with understanding how these features are generated and providing base information for their mimicking in engineering devices (Bottaro (2019)). For example, low drag surfaces can be seen in biological structures such as shark skin. The shark's skin is coated in tiny tooth-like denticles with longitudinal grooves that prevent vortices formation on a smooth surface, Bechert and Reif (1985). The lotus plant leaves are an example of superhydrophobic, self-cleaning, and low drag surfaces, Bottaro (2019). Therefore, creation of a micro-scale drag-reducing surface becomes the key to breakthroughs in drag-reduction technology. Fabrication methods used in the drag reduction are; (i) direct micro-imprinting method, (ii) bio-replicated rolling method, (iii) 3D printing, (iv) precision machining, and (v) coating technology. The special properties of the superhydrophobic surface are associated with wax ducts that create particular surface topography. A butterfly wing demonstrates a mixture of effects from shark skin and lotus leaves (Bixler and Bhushan (2012)). The exterior porous surface of the exoskeleton is an example of porous structures.

Micro-textured surfaces are ubiquitous, even though they do not always have a biological basis. Due to the applicability in a broad range of industrial, engineering, and environmental applications, flow phenomena over and through textured surfaces attracted considerable interest for decades. Examples of engineering applications that include porous media and fluid flow include oil extraction from ground wells, water bed basin control, and pollutant filtration through aquifers. Besides, engineering applications that use porous media include: (i) transpiration cooling in which a porous material is used to increases the material's heat exchange potential, (ii) filtration techniques to separate rigid particles from fluids, (iii) wall transpiration for flow control, (iv) heat transfer delay in industrial applications. They have also been utilized as transport methods for medical and biological applications, including transport in human tissues, bio-convection in biological media, blood flow in micro-vessels, and flow through polymer brushes and chains (Fu-quan et al. (2007); Khanafer et al. (2008); Kuznetsov (2008); Li et al. (2015)).

1.3. Motivation

The above examples show the potential benefits of using correctly chosen surface structures, assuming a complete understanding of how these structures influence the overlaying fluid flow. The several potential applications in various industries that require fluid flows over and through these micro-textured, regular or irregular, impermeable or permeable surfaces are the reasons and motivations for the present research work.

1.4. Related Literature Review and State of the Art

Since the current literature is extensive, the following review will be limited to a few examples from a wide range of application fields, emphasizing fluid dynamic issues.

1.4.1. Flow over Rough Surfaces

Fluid flow over a rough surface texture is one of the most fundamental and vibrant problems in fluid dynamics, but few studies (details of which are given below) have addressed (from theoretical point of view) their effect on the flow. The lack of closure is most likely due to the wide range of potential responses, which depend on roughness topography information and flow conditions. The several studies are focused on determining the effects of surface roughness. Before 1990, much of the literature concerned itself with the universal scaling of flows over rough walls; more recent studies have illustrated the discrepancies between various roughness forms/types. Furthermore, different types of geometrical shapes that are artificially constructed from simple roughness elements and arranged in regular, staggered or random patterns (Figure 1.2) are common in recent studies (Naqvi and Bottaro (2021); Valdés-Parada and Lasseux (2021)). Such surfaces typically possess

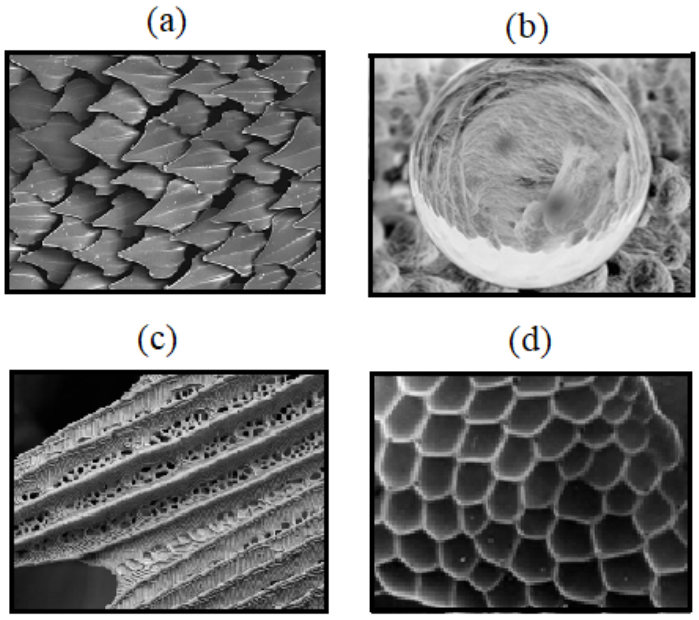

Figure 1.1: (a): Microscopic image of shark skin (source:www.biomimicrybe.org); (b) Microscopic image of a leaf of lotus plant (source: www.company7.com); (c): Microscopic image of a moth wing (source: www.reddit.com); (d): Chitin cuticles, the exterior porous surface of an insect's exoskeleton, image courtesy by Toby Burgess (source: www. blogspot.com)

small characteristic length scales and can quickly evaluate their surface properties such as roughness heights and spacing. They are also simple to construct for experimentation or computational simulations. Most textbooks on turbulence include some description of the effect induced by rough-textured surfaces, and the one by Schlichting (1937) and Bird (2002) are still valuable references. For example; Bird (2002) stated that wall roughness is assumed to be only relevant in turbulent flow conditions and equations that are used are usually heuristic.

1.4.2. Effect of Surface Roughness on Laminar Flow

In the classical perspective, roughness does not impact the laminar flow in a channel flow. The study of Choi et al. (1991) presented the viscous drag changes associated with the presence of longitudinal grooves (with a triangular shape) in a fully developed laminar channel flow. They concluded that the results are independent of the Reynolds number. The Reynolds number independence implies that there will be no drag reduction in fully developed laminar channel flow with grooved walls. However, significant deviations from standard theory in micro-channels are predicted, and in recent years such flows have attracted considerable interest. In contrast with typical laminar-sized macro-flux for dynamically comparable conditions, those latter tests indicate an improvement in the Darcy friction factor. This finding reveals that laminar drag is caused by surface roughness. The experimental study of flows of micro-machined channels is carried out by

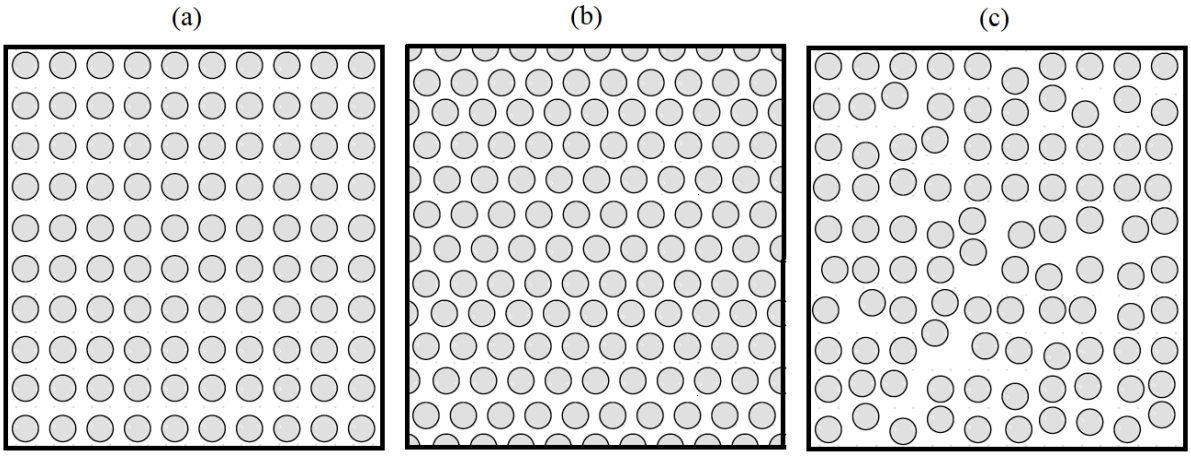

Figure 1.2: Top views of (a) uniform, (b) staggered, and (c) non-uniform distributions of roughness element over a wall.

Papautsky et al. (1999).

1.4.3. Effect of Surface Roughness on Laminar-Turbulence Transition

The effect of roughness on the onset of transition from laminar to turbulent flow has been extensively investigated. Reynolds (1883) was the first to study the effects of distributed surface roughness on the laminar-turbulent transition and concluded that the hydraulically rough wall could promote transition. In contrast, a hydraulically smooth wall had no impact on transition. Saric et al. (1998) demonstrated that roughness could stabilize the flow and thus delay the transition process. Later on, Jiménez (2004) and Floryan (2007) stated that surface texture affects the form of turbulence, and it may plays a significant role in the laminar-turbulent transition. Some type of roughness may be able to either promote or delay the transition from the laminar to the turbulent state (Batchelor and Batchelor (2000); Aleyev (1977)).

When considering roughness-sensitive designs, researchers use different criteria to determine the size of the critical roughness. The most common standard is the roughness Reynolds number $Re_h = U_h h\nu$ where h is the roughness height, U_h the undisturbed velocity at the height of h and ν the kinematic viscosity. It has widely accepted that roughness does not play a role when $Re_h < 25$ (Morkovin (1990)). This criterion cannot, however, account for the shape and distribution of roughness. Another way to render roughness-sensitive prototypes is to use experimental evidence (Schlichting and Gersten (1979)). This evidence is typically defined as the set of correlations between roughness height, flow conditions, and the critical Reynolds number.

The effect of roughness in transitional flows depends on the degree of disturbance in the flow. Both theoretical research and experimental findings suggest that two-dimensional scattered roughness destabilizes traveling wave disturbances that play a critical role in

the transition process (Asai and Floryan (2006); Floryan (2005)). Floryan (2002) analyzed three dimensional Couette flow, and Floryan (2003) and Floryan and Floryan (2009) investigated Poiseuille flows in a converging-diverging channel; they have shown that surface corrugations produce streamwise vortices. The same roughness is reported by Szumbarski and Floryan (2006) to stimulate optimal disturbances in streamwise eddies and increase their transient development. The distributed roughness is mechanism providing a wide variety of stability responses that have yet to be studied (Szumbarski and Floryan (2006)). Experimental observations confirmed the theoretical projections for sinusoidal surface corrugations by Asai and Floryan (2006).

1.4.4. Effect of Surface Roughness on Turbulence Drag

In recent decades, the development of complex surfaces to reduce turbulent drag has been an area of scientific interest. The pioneering experiments of Hagen (1854) and Darcy (1857) have reported that roughness often increases the resistance. Measurements of total drag in terms of friction factor by Nikuradse (1933) and Moody and Princeton (1944) also demonstrated that roughness has little impact on laminar drag, or at the very least, the effect is too small to be measured using the techniques available. However, the suggested correlations indicate that surface roughness has a significant impact on turbulent flow. Jiménez (2004) discussed experimental evidence on turbulent flows over rough walls and measures two important aspects: one is roughness Reynolds number which measures the effect of the roughness on the buffer layer, and second is the ratio of the boundary layer thickness to the roughness height, which determines whether a logarithmic layer survives since most commonly used rough surfaces such as riblets and other drag-reducing cases belong to logarithmic regime.

The need for a suitable method for reducing viscous drag in wall-bounded flows has piqued interest in several fields, including shipping, piping and petroleum, medical equipment, micro-fluidics, and nano-fluidics systems, to name a few (Goldstein (2006)). Lee et al. (1996). The existing methods can divided into three categories: (i) delaying boundary layer separation by suction or injection of fluid, or through promoting the laminar-turbulent transition; (ii) changing the fluid viscosity; (iii) through proper wall geometry design (Luchini (2013)). The first two methods have well-understood fundamentals and are used extensively in a wide range of applications. The third method has limited use due to the lack of understanding of a correlation between surface topography and surface drag. Information on the types of drag and how they are affected by roughness shape could lead to the identification of surface topographies that reduce drag.

The traditional belief that surface roughness increases flow resistance contradicted by Walsh (1983) in turbulent flow regimes. It shown that there exists a particular class of surface topography that is capable of reducing drag to below what is found for a smooth wall. Based on these predictions, researchers have started to focus on the performance of corrugated surfaces such as those used in complex (biological and engineered) systems. For example, the analysis of shark skins, which represent biologically formed surfaces,

Figure 1.3: (a): Triangular grooves; (b): Saw-tooth grooves; (c): Rectangular grooves; (d): Sinusoidal grooves.

attracted much attention, and many simple physical models are suggested to replicate their function (Bechert et al. (1997b); Bechert and Reif (1985); Bechert et al. (1986); Bechert et al. (1997a)). Sharks have drawn the most interest as deep-sea predators due to their powerful bursts and long cruise ranges, which have evolved through a long period of natural selection.

A variety of adaptations have been honed and thoroughly investigated to minimize energy consumption. As a result, sharks skin develops streamlined structures to minimize pressure drag caused by a difference in pressure across the body. Sharks' gills are thought to be their primary respiratory organ, and they have been found to minimize drag caused by lift. Sharkskin can also minimize skin friction drag caused by boundary layer formation. The excellent drag reduction capacity of shark skin has been extensively studied among the many ways to reduce drag (Walsh (1983); Bechert et al. (1997b); Goldstein et al. (1995); Zhang et al. (2011)).

1.4.5. Effect of Biological vs. Engineered Surfaces on Drag

Shark skin denticles that stick out of the skin are tooth-like with enameled and dentine outer layers, inner pulp cavity with nerves and blood vessels, and a unique structure consisting of the outer crown, neck, and extended base imbedded into the dermis, as opposed to prototypical riblets (Ankhelyi et al. (2018), Pu et al. (2016), Han et al. (2008)). Sharks' denticles, which protect their skin, have distinct functional morphotypes. These denticles have been modeled as riblets. At an early stage, the hydrodynamic effects of riblets at different scales were thoroughly investigated. Moreover, engineered riblets are much more effective at reducing drag than natural shark skins, and this is due to the shark's versatile denticles, which can adapt to the flow passively.

To control flow separation, bristled shark denticles can be used as vortex generators. The mechanism of flow separation controlled by a vortex generator is different from that controlled by a traditional vortex generator. Domel et al. (2018a), and Tian et al. (2021) explore the design of shark denticle bioinspired structures for aerodynamics. Shark denticles are used as vortex generators in numerical simulations to control the flow separation while energizing the boundary layer. The scale, shape, and orientation of the denticles all

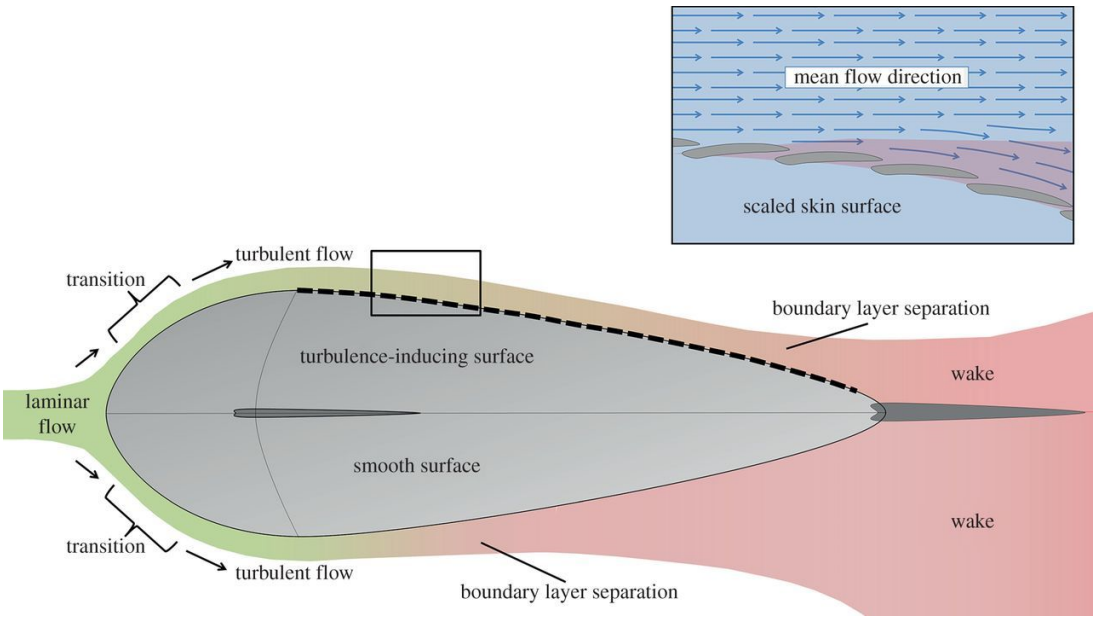

Figure 1.4: The effect of roughness on flow regime and wake formation is demonstrated by creating and separating boundary layers over a fish-like form. By comparing the non-smooth surface to the smooth surface, it is discovered that roughness controls the boundary layer separation, reducing the wake area and hence the pressure drag, Fletcher et al. (2014).

influence the boundary layer's ability to minimize drag. Vortex generators have provided the passive mechanism for regulating flow separation (Lang et al. (2011)).

Denticles, according to research, act similarly to special vortex generators in energizing the boundary layer and controlling flow separation. Streamwise vortices are formed downstream when the fluid reaches vortex generators, and high momentum turbulent energy is mixed in the boundary layer, thereby reducing the capacity exchange and shear stress to the boundary layer, locking vortices generated in the viscous sublayer inside the groove to achieve drag reduction. These characteristics of shark skin have been shown in many studies to reduce drag through passive flow control mechanisms, Lang et al. (2008). Research has shown that these particular features of shark skin can reduce drag through passive flow control mechanisms (Fletcher et al. (2014), , see figure 1.4). Moreover, flow separation can be controlled by the bristling capability of flexible denticles, thereby reducing the pressure drag in the opposite direction of the body movement (Lang et al. (2014)).

1.4.6. Riblets: Viscous Drag Reduction Technique

Regular grooves with triangular or rectangular cross-sections, known as riblets, are often used used in hydrodynamic and aerodynamic tests to demonstrate the drag-reduction mechanisms. Riblets are aligned in the same direction as the flow and are assumed to

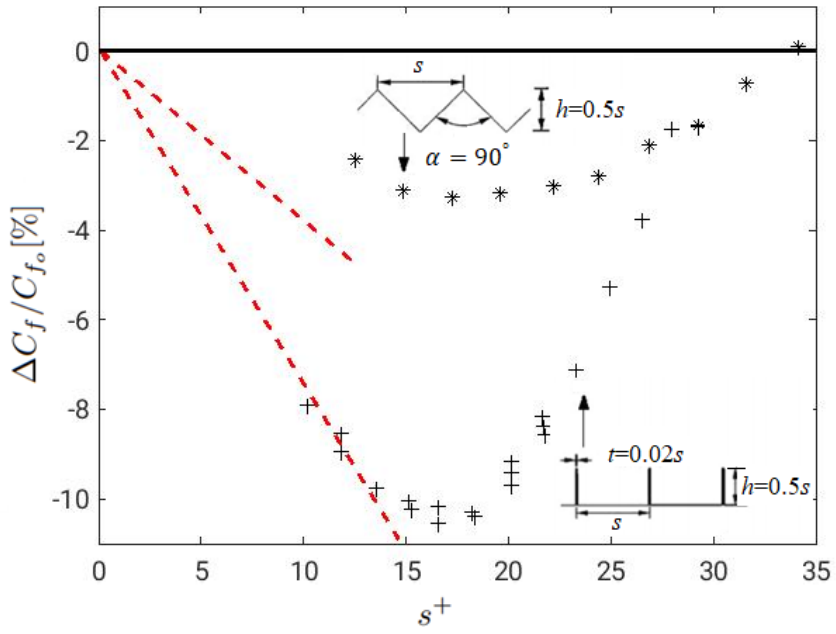

Figure 1.5: Experimental drag reduction data (symbols) for triangular and blade riblets. The straight dashed lines correspond to the linear regime for the two wall corrugations, Bechert et al. (1997b).

promoting anisotropic flow and effectively controlling the naturally occurring turbulent vortex, lowering shear stress to the boundary layer, and locking vortices created in the viscous sublayer inside the groove to reduce drag (Walsh and Lindemann (1984)), thus, improve the over all swimming performance of the shark in a turbulent flow. A maximum drag reduction of the order of $7\% - 10\%$ was achieved by using such grooves (Walsh and Lindemann (1984), Walsh (1990), Bruse et al. (1993); Bechert et al. (1997b)). The viscous regime of vanishing grooves (riblets) spacing is well understood (Bechert and Bartenwerfer (1989), Luchini et al. (1991), Luchini (1992)) and confirmed by experiments (Walsh and Lindemann (1984); Walsh (1990); Bruse et al. (1993); Bechert et al. (1997b)). Choi et al. (1991), Chu and Karniadakis (1993), Goldstein et al. (1995), and Goldstein and Tuan (1998) performed direct numerical simulations of laminar and turbulent flow over ribbed-mounted surfaces and showed that in the laminar regime there is no drag reduction (while a contrary argument on the laminar drag reduction and increase by grooves was passed by Luchini (1995)), while in the transitional and turbulent regimes, drag reduction up to $4\% - 10\%$ exists for the ribbed-mounted wall in comparison with the smooth wall of the channel. The effectiveness of the grooved surface as a drag-reducing tool depends on its geometrical shape. Bechert et al. (1997b) carried out detailed theoretical measurements of grooves with adjustable geometry and performed parametric optimization to determine the best possible drag reduction (see Figure 1.5). Bechert et al. (1997b) performed experiments in the open channel with oil as the working fluid and showed that the surface replicating shark skins had a drag decrease of about 5%. Itoh

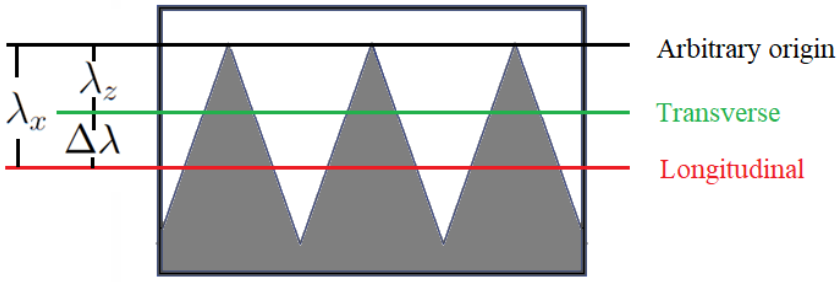

Figure 1.6: Interrelations between the protrusion heights and the positions of the virtual plane walls seen by longitudinal and transverse flow, adapted from Luchini et al. (1991).

et al. (2006) have been measuring turbulent channel flow over seal fur and have achieved a total 12% drag reduction when working with a glycerol water mixture. For larger grooves, the minimum drag is related to the viscous regime's breakdown, but this process relevance has been recognized only recently by García-Mayoral and Jiménez (2011).

Since these authors found that skin friction drag was not increased with respect to the flat-wall case, under the same working conditions, the importance of the flow viscous response was highlighted. Subsequent research focussed on the viscous near-wall flow, to extract salient features of microstructured surfaces. Today, the mechanism by which riblets operate is believed to be related to the creation of an offset between the virtual origin of the longitudinal mean flow and that of the transverse turbulent eddies. Provided that the riblets are embedded in the viscous sublayer, their effect can be modeled by the Stokes equation to yield two distinct protrusion heights, or Navier's slip lengths, longitudinal, λ_x, and transverse, λ_z, which are the distances from the rim of the riblets to the position where, respectively, streamwise and cross-stream flows originate. Once the two protrusion heights are defined, we arrive at the overall picture given in figure 1.6. (Note that the riblet tips themselves do not hold any particular significance in relation to the flow, and must be considered for all purposes an arbitrary origin of the y-axis which has been set there just for geometrical convenience.)

The above concepts have been basically introduced by Bechert and Bartenwerfer (1989) and Luchini (2013), and tested experimentally by Bechert et al. (1997b), among others. The results show that riblets remain in the linear (Stokes) regime as long as their dimensionless spanwise periodicity, s^+, measured in viscous wall units, remains below a value close to 10 (cf. figure 1.5). The optimal riblet spacing is about 15 for a variety of riblet shapes, and skin friction drag can be reduced by at most 10% in the case of thin, blade-like riblets (Bechert et al. (1997b)). Above $s^+ \approx 15$ drag starts increasing again and, for $s^+ \gtrsim 30$, the skin friction coefficient exceeds the value of the corresponding smooth wall because of the appearance of a Kelvin–Helmholtz-like instability of the mean flow which increases the spanwise coherence of the turbulent structures, therefore disintegrating the longitudinal streaks, via the creation of spanwise rollers (García-Mayoral and Jiménez

(2011)). For drag to decrease, for any kind of wall indentation fully immersed in the viscous sublayer, the origin of the secondary flow must be farther away from the base of the indentation than the origin of the mean streamwise motion or, in other words, $\Delta\lambda = \lambda_x - \lambda_z$ must be positive. When this occurs, crossflow is impeded (more than the longitudinal flow) and high velocity bursts from the surface are mitigated, resulting in smaller drag. The amount by which drag reduction is achieved is given to leading order in $\Delta\lambda$ by:

$$\frac{\Delta C_f}{C_{f_0}} = -\frac{\Delta\lambda^+}{(2C_{f_0})^{-1/2} + (2\kappa)^{-1}} \tag{1.1}$$

as first shown by Luchini (1996). In Eq. 1.1, C_f is the skin friction coefficient, C_{f_0} its value for the case of a smooth surface under the same outer flow conditions, and $\kappa = 4.48$ is von Kármán's constant (Luchini (2018). Despite the fact that the equatio above holds only in the initial part of the drag curve, the agreement of this theoretical estimate with experiments is satisfactory and strongly endorses the idea of maximizing $\Delta\lambda$ when drag reduction is sought for. Figure 1.5 demonstrates the advantage of using blade riblets (of thickness t equal to $0.02s$ in the case of the figure) as compared, for example, to triangular riblets with a top opening angle of 90°. It is also interesting to observe that the theoretical results embodied by Eq. 1.1 (and shown with dashed lines in the figure) are in excellent agreement with the experimental data for blade riblets almost until the point of maximal drag reduction (close to $s^+ = 15$), whereas for the triangular wall corrugations the range of validity of the theoretical result is smaller and extends to $s^+ \approx 5$.

A theory of Luchini (2013) has been further extended by Ibrahim et al. (2021) where the virtual origin perceived by the streamwise velocity is proposed to set by the streamwise slip length and they set this independently for the mean flow and the fluctuations, verifying that the one affecting U^+ is the origin for the mean flow. They found that the virtual origin perceived by the streamwise velocity fluctuations, which are a proxy for the near-wall streaks, appears to be essentially inactive in setting the origin for turbulence, and hence has a negligible effect on the drag, at least in the regime where the origin perceived by the streaks is deeper than the origin perceived by the turbulence, where, in the opposite regime, the region occupied by the streaks eventually becomes too confined, and the near-wall turbulence no longer remains smooth-wall-like. This analysis is valid for surfaces of small texture size, which do not alter the canonical nature of the turbulence, and we show that this result can also be predicted by introducing a virtual origin for turbulence into an a priori, eddy-viscosity model for the Reynolds shear stress. The exploratory results that suggest that the effect on the flow of opposition control, an active flow-control technique, can be interpreted in terms of virtual origins is also one of their core finding.

1.4.7. Deformable Riblets and Drag Reduction

Another aspect of the near-wall indentations which deserves attention is the possibility for the solid material at the fluid–solid interface to deform under the action of the fluid.

Research on elastic and viscoelastic interfaces has enjoyed waves of renewed attention in the past fifty years, coinciding with the growing or diminishing interest of funding agencies. The initial stimulus to the idea of using compliant surfaces for drag reduction came from Kramer (1957), Kramer (1961), who ascribed the extraordinary swimming ability of dolphins to the pliability of their skin. Kramer's argument was that shear layer fluctuations were damped near the dolphin's compliant dermis, thus leading to extended regions of laminar flow on the body. This, is turn, was assumed to be the cause of drag reduction. Much research ensued, particularly on the onset of transition to turbulence for the flow over compliant walls, culminating with the modeling efforts of Peter W. Carpenter and collaborators (Carpenter and Garrad (1985), Carpenter and Garrad (1986), Dixon et al. (1994), Carpenter et al. (2000)). On the experimental side, Gad-El-Hak et al. (1984) performed several experiments in a water channel with a flat plate coated with a compliant material, under laminar, transitional and turbulent conditions, highlighting the presence of hydroelastic instabilities capable to lead to early transition and rise in drag. Turbulent drag increase was typically associated to the appearance of a large-amplitude deformation of the compliant surface, resulting from a static-divergence instability. Conversely, when the surface deformation of the wall was maintained significantly within the viscous sublayer (for the wall to remain hydrodynamically smooth), some success in reducing skin friction drag by the use of compliant viscoelastic panels was reported (Lee et al. (1993), Choi et al. (1997)). Drag reduction was accompanied by reduction of the turbulent intensity across the boundary layer.

The idea of combining the presence of regular micro-grooves with the fact of rendering them elastic stems from the realization that frictional drag in turbulent flows decreases when the spanwise motion of the streaks is hampered (Choi (1989), Lee and Choi (2008)). This effect is possibly achieved by combining the properties of a compliant material with the design of appropriate micro-indentations. It is thus aimed for compliance to impair the lateral movement of the streaks, reducing violent ejections and bursts, with a positive effect on skin friction resistance. A further consideration applies: the optimal geometrical characteristics of riblets depend on the outer flow conditions, and what is optimal for one condition (say, level flight of an aircraft at cruise speed) may not be optimal any more under different conditions. Suitably designed microstructures capable to deform elastically and adapt to the outer flow conditions might provide an answer to this practical shortcoming. Recently, a patent has been submitted describing the manufacturing of elastomeric riblets (Rawlings and Burg, 2016), with the claim that their optimized structural design provides the capability for riblets to be "thinner, lower weight and more aerodynamically efficient".

1.4.8. Role of Pressure Gradient in Rough Surface Drag Reduction

In the drag reduction induced by the surface groove, the pressure gradient also plays a significant part. Walsh (1983) found the effectiveness of groove surfaces under this situation by measuring and analyzing the effects of an adverse pressure gradient. To account for the

roughness properties, they used the concept of equivalent roughness. Nieuwstadt et al. (1993) studied the turbulent boundary layer on a grooved surface to explore skin friction reduction and found that the drag reduction exists for all pressure gradients. Still, for higher pressure gradients, it is slightly higher. Debisschop and Nieuwstadt (1996) performed experiments in a wind tunnel on longitudinal grooves with adverse pressure gradients and found improvement in the drag reduction from 7% to 13%.

Gamrat et al. (2008) used different methods to predict the effect of roughness on laminar flow in micro-channels and found that the Poiseuille numbers Po (the product of a friction factor and the Reynolds number) increase with an increase in the relative roughness and are independent of the number Reynolds in the laminar flow regime ($Re < 2000$). Mohammadi and Floryan (2013b) evaluated pressure losses for laminar flows to achieve a laminar drag reduction using a properly-shaped groove surface. The drag minimizing longitudinal grooves and using optimization strategies to classify types of those grooves are investigated by Mohammadi and Floryan (2013a) to optimize potential pressure loss reductions. Mohammadi and Floryan (2012) studied mechanisms responsible for drag formation using a sinusoidal-shaped transversely grooved channel. The first mechanism relied on the wall shear stress, the second on the interaction between the mean pressure gradient and the surface geometry. The third is on the interaction of the periodic part of the pressure field with the surface topology. The laminar flow produces more frictional drag than turbulence flow, and it supports laminar flow in many applications.

1.4.9. Modelling of the Flow Over the Rough Surface: The Slip Boundary Condition

The above discussion indicates that the applications of structured surfaces are broad enough. These surfaces have complex geometries/shapes, and their modeling is one of the biggest challenges in flow analysis. Since surface shape can lead to several instabilities, it is recommended to model the flow over the rough corrugated wall with high accuracy to allow bifurcation points to be captured reliably.

The need to develop accurate models of the flow (specifically turbulent) near patterned walls is notably felt, as it occurs in multiple technical applications, for example; Bons (2002) used scaled models of rough surfaces based on scans of damaged turbine surfaces in the wind tunnel experiment. A systematic study showed the impact of irregular roughness on turbulent channel flow using roughened steel plates by Van Rij et al. (2002). It is understood that skin friction drag typically increases compared to a smooth-walled case under the same conditions, except for cleverly engineered wall patterns. Examples of the latter include riblets (in the form of grooves) (Walsh and Lindemann (1984) (as mentioned above), Bechert and Bartenwerfer (1989), Luchini et al. (1991), Garcia-Mayoral and Jiménez (2011)) and other nature-inspired wall indentations (Bechert and Reif (1985), Sirovich and Karlsson (1997), Bechert et al. (2000), Domel et al. (2018b)). Provided the roughness is embedded within the viscous sublayer, the effective rough-wall conditions

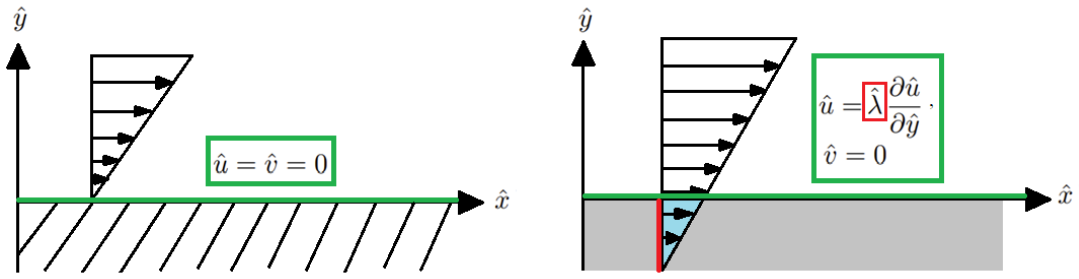

Figure 1.7: Sketch of the solid plane wall with no-slip condition (left) and complex homogenized surface with slip velocity (right) in two-dimensional configurations.

develop herein will permit to carry out, at a fraction of the time, parametric searches of regular surface patterns apt, for example, at minimizing skin friction.

The classic approach to determining flow fields bounded by irregular rough surface requires considerable manual labor since geometry has to be modeled by the use of numerically generated grid points (Gamrat et al. (2008), Herwig et al. (2008)). These approaches suffer from low-order spatial accuracy associated with their discretization schemes and are usually based on finite-difference, finite-element, or finite-volume methods. Using finer grids can improve their accuracy but with a substantial increase in computational costs. Also, the use of these methods is impractical for systematic investigation of different features of the roughness geometry.

Another approach/method for treating boundary irregularities relies on the up-scaling method for example; homogenization (briefly described in the subsequent section). In this method, the effective slip boundary conditions are derived/modeled and enforced to apply at a fictitious wall above the roughness crest. These effective boundary conditions fully characterize the flow at the natural micro-textured surface (on a scale larger than the pattern characteristic length) and can be used to solve complex hydrodynamic problems without tedious calculations.

The definition of boundary conditions at a solid, impermeable wall upon contact with a viscous, incompressible liquid had preoccupied researchers even before Navier (1823) derived the equations that now carry his name. Navier (1823) claimed in his seminal paper that the viscous force exerted on a wall by the fluid is balanced by the flow resistance, resisted by the wall, the latter being proportional to the *slip velocity*. If the wall-normal direction is denoted by $\hat{y}$ and the wall-tangent velocity by $\hat{u}$, the slip velocity reads (for example see Figure 1.7 for further detail) in dimensional form:

$$\hat{u} = \hat{\lambda}\frac{\partial \hat{u}}{\partial \hat{y}}, \tag{1.2}$$

where $\hat{\lambda}$ is the dimensional Navier constant, an effective penetration depth (also called slip length), equal to the distance into the wall where the linearly extrapolated velocity

component vanishes.

Navier's condition has been discussed and questioned for a hundred years before Taylor (1923) resolved the issue with a series of experiments on the flow between concentric, rotating cylinders near the onset of the first hydrodynamic instability. Taylor's theoretical treatment, which resulted in excellent agreement with the experiments, was based on the assumption that the fluid could not slip while in contact with the solid surface. The no-slip condition gained (almost) universal acceptance from that moment. Dussan V. (1976) investigated the sensitivity of the overall flow field to the form of the slip boundary condition and found that the characteristic of the slip boundary condition which affects the overall flow field over a rough wall is the magnitude of the slip length. Hocking (1976) examined a simple type of corrugated surface such as grooves (of finite and infinite depth), and calculated the effective slip coefficient. In the study, it is suggested that, when a fluid displaces another on a rough surface, the displaced fluid remains in the hollows on the surface, thus providing a partly fluid boundary for the displacing fluid and leading to a slip coefficient for the flow. The asymptotic structure of the solution for a random surface with finite slope is discussed by Jansons (1988) and stated that very small amounts of roughness can well approximate a no-slip boundary condition macroscopically. The surface roughness is modelled by compact protrusions on an underlying smooth surface by Sarkar and Prosperetti (1996) and overlaying stokes flow is analyzed for a sparse distribution of arbitrarily shaped protrusions and explicit numerical results are given for hemispheres. They found that, in an ensemble-average sense, the effect of the roughness can be approximately represented by a partial slip boundary condition on the component of the velocity tangent to smooth surface,

Miksis and Davis (1994) studied the effect of surface roughness and coatings on fluid flow over a solid surface and able to derived asymptotically an effective slip boundary condition to replace the no-slip condition over the surface but in the certain limit of small-amplitude roughness and thin lubricating films. It is also observed that When the film is absent, the result is a Navier slip condition in which the slip coefficient equals the average amplitude of the roughness and limiting cases in which the film dynamics can be decoupled from the outer flow has also been identified. The configurations for which the slip condition remained in use included the triple-line flow (to illustrate the leading edge motion of a liquid drop sliding down the incline), the flow of rarified gases (in micro-fluidic devices), the flow over micro-corrugated surfaces, eventually impregnated with a lubricant, see Bottaro (2019). Most of these exceptional cases share the peculiarity that either the continuum description of the flow breaks down or becomes too difficult/expensive to resolve, e.g., by a computational technique. It becomes better to provide a conjugate, micro-macroscopic view. These are the cases in which a homogenization strategy proves very effective.

Achdou et al. (1998) are credited for the most important early publication detailing the application of a two-scale expansion to infer effective conditions at a rough wall. These authors focused on the two-dimensional, incompressible case and derived conditions to second order. For a later comparison, the (nonlinear) conditions in Achdou et al. (1998)

read:.

$$\hat{u} = \hat{\lambda}\frac{\partial \hat{u}}{\partial \hat{y}} - \left[\hat{\xi}\frac{\partial \hat{p}}{\partial \hat{x}} + \hat{\chi}\hat{u}^2\right], \tag{1.3}$$

$$\hat{v} = 0, \tag{1.4}$$

with $\hat{p}$ the pressure. The dimensional coefficients $\hat{\lambda}$, $\hat{\xi}$, and $\hat{\chi}$ arise from the solution of Stokes-like problems in a periodic unit cell built around a single roughness element. Achdou and colleagues obtained good results when comparing complete simulations for the macroscopic laminar flow configurations tested in their studies, leading them to claim that the first-order condition is already very accurate and conclude that it is not assured that it is worth using the second-order condition. We are going to argue below that condition (1.4) is not second-order accurate.

Subsequent developments of the rough wall's effective conditions did not follow the path established by Achdou and collaborators (Achdou et al. (1998)) and were mostly limited to investigating different aspects of the Navier condition. Jäger and Mikelić (2001), for instance, provided a rigorous justification of the Navier slip for the plane channel flow case and carried out asymptotic estimates of the tangential drag force and the effective flow rate of mass. Basson and Gérard-Varet (2008) used stochastic homogenization in order to extend the previous study to the case of a channel flow with roughness modeled by a spatially homogeneous random field. Kamrin et al. (2009) recovered a tensorial form of Navier slip for the flow over periodic surfaces as a second-order approximation using various scaling variables from those used here. They introduced the *mobility tensor* $\mathbf{\Lambda}$ (or Navier slip tensor) and provided a formula for $\mathbf{\Lambda}$ after decomposing the wall in the Fourier series, demonstrating its symmetry. The analysis was further extended by Luchini (2013) who considered two configurations. The surface considered was $Y = \epsilon H(X, Z)$ in the *shallow-roughness* limit, i.e. the roughness becomes smoother as $\varepsilon \to 0$. The second limit, called *small-roughness*, concerned a family of surfaces described by $Y = \epsilon H(X/\epsilon, Z/\epsilon)$, i.e., a pattern which, with varying ϵ, remains geometrically similar to itself. The influence of the roughness aspect ratio via *protrusion coefficient* and the interference between equal roughness elements placed in a periodic arrangement via *proximity coefficient* were accounted for by Luchini's first-order analysis.

The Navier slip condition of the first order is recovered in this case. Bolaños and Vernescu (2017), Zampogna et al. (2019b) and Lācis et al. (2020) performed more recent studies based on multiscale asymptotic approach. The latter study was the only one to push development to the second-order, but only for the wall-normal velocity component, resulting in a fictitious wall transpiration condition. In a turbulent channel flow bound by a rough wall, the condition has been tested, demonstrating the importance of accounting for wall-normal velocity fluctuations in a rough wall model. The present contribution starts from these premises.

In contrast to above, Introïni et al. (2011) and Guo et al. (2016)] examined aspects associated with heat transfer and concentration gradients across heterogeneous and rough

boundaries through an upscale analysis based on the theory of volume averaging. Prat et al. (2002) discussed averaged Reynolds equation for flows between rough surfaces in sliding motion and shown that the effective transport coefficients, traditionally termed "flow factors" in the lubrication literature, that appear in the average equations can be obtained from the solution to two closure problems.

1.4.10. Flow Over and Through the Porous Media

Flow over and through porous media has a wide range of applications in many areas of real-life problems and has been extensively investigated experimentally (Beavers and Joseph (1967); Gupte and Advani (1997); Agelinchaab et al. (2006); Arthur et al. (2009); Morad and Khalili (2009); Terzis et al. (2019); Holt and Smith (1989)), analytically (Richardson (1971a); Saffman (1971); Jones (1973); Chandesris and Jamet (2006); Jamet and Chandesris (2009); Lācis and Bagheri (2017); Lasseux et al. (2016)), and numerically Larson and Higdon (1986, 1987); Liu and Prosperetti (2011); Carraro et al. (2013); Kuwata and Suga (2016, 2017), most often with a focus on understanding the nature of interface[1] conditions.

1.4.11. Turbulence Transport Across a Permeable Interface

Experiments on the turbulence transport across a permeable interface that have already been conducted provide details on the accessible areas. Different experimental studies with various configurations, such as turbulent open-channel flows over porous media consisting of spheres, have confirmed the control of turbulence by using the permeable surface. Kuwata and Suga (2017) used particle image velocimetry (PIV) measurements to analyze spanwise turbulence structures over permeable walls. A channel's permeable bottom wall is made up of three different types of anisotropic porous media. The spanwise turbulent structures are investigated using their wall permeability tensor, designed to have a larger wall-normal diagonal dimension (wall-normal permeability) than the other components. However, high-resolution measurements within porous media are difficult to perform due to the difficulty of performing measurements within the narrow and tortuous space (Kuwata and Suga (2016)). Efstathiou and Luhar (2018) conducted a boundary layer experiment over high-porosity foams ($\theta = 0.97$), with a friction Reynolds number of $Re_\tau \approx 196$ upstream of the porous portion.According to mean statistics, the porous interface had a significant slip velocity (greater than 30% of mean velocity). While the mean velocity deficit grew in size with average pore size, the slip velocity remained relatively constant. Terzis et al. (2019) investigated the hydrodynamic interaction between a uniform porous medium and an adjacent free-flow channel at low Reynolds numbers. The

[1]The word "interface" is used interchangeably with the words "dividing line" and "dividing surface" to mean that line or surface which separates the free-fluid region, where the Navier-Stokes equation holds, from the region which can be described by macroscopic equations, such as Darcy's or Brinkman's models.

porous medium in their study is made up of uniformly spaced micro-structured rectangular pillars organized in a uniform pattern, allowing for direct flow measurement within the porous structure. Guo et al. (2020) investigated the velocity distribution above and within porous media with a high Reynolds number. They discovered that the thickness of the transition layer in the porous-medium region is unaffected by changes in Reynolds number as porosity increases.

1.4.12. Effect of Porous Media on Drag

In general, it is assumed that a flow over a porous wall experiences higher drag and turbulent intensities near the wall than the same flow over a flat impermeable surface. Kleinstreuer and Koo (2004) measured pressure losses in laminar flow numerically by considering grooves as a porous medium layers, which inspired investigators to search for methods to design surface topographies to reduce the flow resistance. Tilton and Cortelezzi (2006) and Tilton and Cortelezzi (2008) investigated the stability of channel flows over porous walls, and they showed that wall permeability has a destabilizing effect, which leads to lowering the critical Reynolds number. This result indicates the potential of porous materials in applications involving transition and turbulence (such as flow control, drag reduction, and enhancement, transition triggering and delaying, moreover, amplifying the mixing properties of turbulent flows).

Abderrahaman-Elena and García-Mayoral (2017) and Gómez-de Segura et al. (2018) have suggested anisotropic permeable substrates for turbulent drag reduction and found that the drag-reducing capacity of porous substrates is controlled by the mechanism developed for riblets (Luchini et al. (1991), Luchini (1996),) and for complex surfaces (Jiménez (1994)) in general. Complex surfaces, such as permeable substrates, can produce non-zero velocities at the substrate-channel interface. The experimental work carried out by Klausmann and Ruck (2017) found that due to their porous coating on their lee side, a circular cylinder can experience drag reduction. Measurements of the drag force showed that the lee's cylinder cover minimized the drag for various cylinder and pore layer configurations. They also noted that drag is minimized regardless of whether the porous coating is added on the top of, or integrated into the body's shape.

1.4.13. On the Effective Conditions at the Boundary between a Free Fluid and a Porous Medium

Flow over and through porous media have been treated in a variety of ways. At first, Darcy's law Darcy (1857) is used to determine the flow through porous media. This establishment of the flow through the porous media was the pure empirical-based approach. Using this law, the velocity at the interface between the porous medium and the free fluid region changes sharply (causes discontinuity). Later on Brinkman added an effective

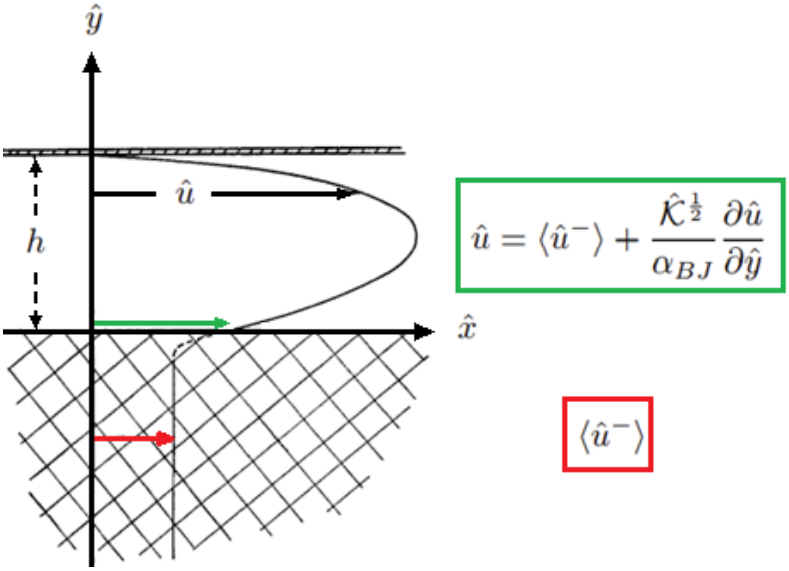

Figure 1.8: Velocity profile for a rectilinear flow in a horizontal channel formed by a permeable lower wall ($\hat{y} = 0$) and impermeable upper wall ($\hat{y} = h$), figure imported from Beavers and Joseph (1967).

viscosity term to the Darcy model to combine the Darcy flow and viscous Stokes flow. The Brinkman model makes it possible to retain continuity of the velocity profile at the interfaces of porous media that may have permeability in the range e $0 << \kappa << \infty$, where κ is permeability of the porous medium. The primary difficulty in the coupling of the Darcy or Brinkman equation with the Navier–Stokes equations is modelling the interface between the porous medium and the free fluid, which remains a somewhat unresolved problem.

To overcome the difficulties listed above, Beavers and Joseph (1967) have proposed an interface condition ((1.5)). They performed several experiments of laminar flow in a channel bounded by a porous layer. They found that the viscous shear from the free-fluid region penetrates the porous medium, ultimately altering the fluid's velocity distribution in an intermediate layer across the dividing surface (Figure 1.8). Such a layer has a thickness of the same order as the characteristic microscale of the porous matrix, typically the interpore distance. Reducing such a layer to a two-dimensional surface (which, for simplicity, can be taken to coincide with the dividing fluid-porous surface) permits expressing the interface boundary condition as a *slip velocity*, that is:

$$\hat{u} = \langle \hat{u}^- \rangle + \frac{\hat{\mathcal{K}}^{1/2}}{\alpha_{BJ}} \frac{\partial \hat{u}}{\partial \hat{y}}, \tag{1.5}$$

and analogously for $\hat{w}$. The velocity components $\hat{u}$ and $\hat{w}$ are parallel to the dividing surface, of normal coordinate $\hat{y}$ (cf. figure 1.8); α_{BJ} is an empirical, order one dimensionless constant introduced by Beavers and Joseph; $\hat{\mathcal{K}}$ is the permeability of the porous matrix (a scalar quantity for the an isotropic arrangement of pores and solid inclusions). The

term $\langle \hat{u}^- \rangle$ represents the Darcy velocity through the porous medium, the superscript $^-$ indicating that the variable is evaluated sufficiently below the dividing line/surface, with angle brackets denoting volume averaging (see later equation (2.121)). Darcy's law stipulates that the mean velocity in the porous medium, away from boundaries, is linearly dependent on the pore pressure gradient, that is:

$$\langle \hat{u}^- \rangle = -\frac{\hat{\mathcal{K}}}{\mu} \frac{\partial \hat{p}^-}{\partial \hat{x}}, \tag{1.6}$$

and similarly for the other two components, with μ the dynamic viscosity of the fluid and $\hat{p}^-$ the interstitial pressure.

Saffman (1971); Taylor (1971); Richardson (1971b) was the first to provide a theoretical justification for Beavers and Joseph's empirical condition; he considered the Stokes equations in a domain across the dividing surface and performed asymptotic matching at the two edges of the interface layer. A few other studies along similar lines were conducted after Saffman, leading to similar conclusions (Jäger and Mikelić (2001); Lācis and Bagheri (2017)). The result by Saffman takes the form:

$$\hat{u} = -\frac{B\,\hat{\mathcal{K}}}{\mu} \frac{\partial \hat{p}^-}{\partial \hat{x}} + \hat{\lambda} \frac{\partial \hat{u}}{\partial \hat{y}}, \tag{1.7}$$

with B an order one constant used to adapt the permeability of the porous medium to the geometric interface conditions, and $\hat{\lambda}$ (equal to $\hat{\mathcal{K}}^{1/2}/\alpha_{BJ}$ in Beavers and Joseph's notations) a slip coefficient. In the equation above, the dimensional quantity $\hat{\mathcal{K}}$, homogeneous to a surface area, is of order ϵ^2 and the quantity $\hat{\lambda}$, a length, is of order ϵ, and this reason prompted Saffman to discard the term containing the pore pressure gradient and to write the slip velocity at the porous/free-fluid interface in the form of simple *Navier slip* (for a thorough discussion of Navier slip, the reader is referred to Bottaro (2019)).

Conditions such as those proposed by Beavers and Joseph are necessary when the so-called *two-domain* approach is employed, i.e., when the free-fluid region is approached by solving the Stokes or Navier-Stokes equations, and the porous domain is treated by the use of the Darcy (or more elaborate) macroscopic model. Alternatives to the Beavers and Joseph condition have been proposed, e.g., in refs. Ochoa-Tapia et al. (2017), Ochoa-Tapia and Whitaker (1995), and Valdés-Parada et al. (2013).

Instead of the two-domain approach, one can also carry out the solution of the volume-averaged Navier-Stokes equations across the whole domain (Whitaker (1986)). This latter *one-domain* approach has been used successfully by several researchers to treat the interface region (Luminari et al. (2019); Angot et al. (1999); Carbou (2008); Bruneau et al. (2020)). Recntly, A novel one-domain approach for modeling flow in a fluid-porous system including inertia and slip effects has proposed (Valdés-Parada and Lasseux (2021)). In this novel approach an operational average description of one-phase flow in the classical Beavers and Joseph configuration including a porous medium topped by a fluid channel is discussed where it has the form of Darcy's law with a position-dependent permeability tensor.

1.5. The Homogenization Approach

Accurate fluid flow simulation over and through the natural surfaces is challenging if surface texture exhibits an irregular/rough/compliant/ porous nature. These media are characterized by periodic/quasi-periodic/non-periodic patterns that possess small-scale features (having dimensions smaller than the relevant flow scale). These features have a significant role in the motion of fluid, whose effects cannot be measured/treated entirely by direct numerical simulations due to the cost required for resolving very fine-grain coupling detail between fluid and wall/material. Such small details might include the effect of the surface texture, its porosity, compliance, and the interactions between the flow of the outer fluid and a different fluid trapped within near-wall micro-cavities. It is difficult to describe such microstructures geometrically, if not impractical. Thus, in practice, the small-scale structures are either idealized or simplified, so a rational analysis methodology can be developed to conduct characterization.
In the above connection, the *theory of homogenization* is employed as the fundamental basis for characterization of composite materials. All such materials, regardless of whether they have been artificially engineered or naturally formed, are composed of several phases or constituents on a particular spatial scale. Based on this fact, it can be claimed that the scale to which the material is referred is what decides whether material is treated as homogeneous or heterogeneous. Within the framework of continuum mechanics, by using numerical techniques based on physical and mathematical concepts developed within the scope of computational mechanics, it is now possible to analyze almost any homogeneous material subjected to some motion results sufficiently close to reality. When working with composite materials or structures made of two or more materials, each material that is part of the composite can be described by the physical and chemical properties governing its behavior, such as elastic, porous, or rigid materials. The majority of the homogenization techniques developed so far are only applicable for composites that have a periodic distribution over the entire structure domain so that one element representative of the composite volume (or unit cell) can be defined. However, in some cases, more than one kind of periodic domain distribution may form the structure or composite, making the existing homogenization techniques not suitable for evaluating this type of case in which more than one recurring configuration occurs.

Concluding from above, one can say that "*Homogenization*" is an approach that studies the macro behavior of a medium by its micro properties, see Babuska [1], where he presents a concept of replication of high-resolution "*heterogenous*" properties with an "*equivalent homogenous*" one. Mei and Vernescu (2010) presented homogenization theory as an analytical scheme that allows up-scaling the differential equations in multiscale inhomogeneous media literature.

Briefly, the theory attempts to replace the composite with an endowed microstructure by an equivalent material without microstructure. It can be achieved by a sequence of assumptions made in describing the microstructure and in developing the analysis methodology. Roughly speaking, homogenization is a mathematical method that offers

formulas for upscaling the differential equations and provides tools for producing rigorous mathematical convergence proofs (Hornung (1996)).

Many studies evoking different multiscale methods to upscale equations of heterogeneous medium (Battiato and Tartakovsky (2011); Boso and Battiato (2012); Battiato et al. (2019)). Nowadays, the effort to achieve predictive understanding across scales is indeed within reach even for highly heterogeneous systems like porous media, due to the development of improved theoretical frameworks and the ever-increasing computational power available.

1.5.1. Content of Homogenization

Attempts to derive or re-derive the macroscale equations have been applied to numerous fields of applications in recent decades. A vital tool of the homogenization theory is the multiscale singular perturbation method (Nayfeh (2008)). At this point, it is useful to make an imprecise distinction between regular perturbation and singular perturbation problems before going into further details. On one hand, a regular perturbation problem is one for which the perturbed problem for small, nonzero values of small parameter ϵ is qualitatively the same as the unperturbed problem for $\epsilon = 0$. One typically obtains a convergent expansion of the solution with respect to ϵ, consisting of the unperturbed solution and higher order corrections. On the other hand, a singular perturbation problem is one for which the perturbed problem is qualitatively different from the unperturbed problem. One typically obtains an asymptotic, but possibly divergent, expansion of the solution, which depends singularly on the parameter ϵ. Although singular perturbation problems may appear atypical, they are the most interesting problems to study because they allow one to understand qualitatively new phenomena.

The multiscale singular perturbation method proposed by Nayfeh (2008) is being used extensively in a variety of problems in applied analysis, such as in many different fields of physics, mathematics, engineering, mechanics. The method is also used for various properties of interest range from the thermal conductivity of a heterogeneous medium to the stiffness tensor of an elastic multi-layered material, from the permeability of a porous matrix to the magnetic conductivity of some electrically conducting media. However, there are many other fields where homogenization is relevant other than described above. For example, the majority of applications of the theory have so far dealt with problems in solid mechanics, and techniques to homogenize material properties, including approaches to statistically characterize the microstructure when local properties have a random distribution, are described in a large number of monographs and books (see, e.g., Torquato and Haslach Jr. (2002) and reference therein).

1.5.2. The Evolution of Homogenization Techniques

The evolution of the different multiscale homogenization techniques starts with the effective medium approximation of Eshelby (1957) and follows on until what we know nowadays as the *multiscale homogenization*. The asymptotic homogenization theory laid the foundation for studying composite materials in media with periodic structures using a multiscale approach. This theory has proven to be a powerful technique for analyzing structural arrangements in which two or more length scales naturally exist. These two scales are the microscopic scale of inter-second phase spacing and the macroscopic scale characterizing the structure's overall dimensions. Three main monographic books on the subject laid the mathematical basis for the method and emphasized its application in the solution of mechanical problems by Sánchez-Palencia (1980), Auriault et al. (2010), and Bensoussan et al. (2011). Bensoussan et al. (2011) developed an asymptotic expansion of the solution in terms of ϵ (a ratio between micro and macro-scales). If the structure period is small compared to the macro-region size in which the system is to be studied, the asymptotic analysis is used to expand the link between microscopic and macroscopic descriptions. The asymptotic problem is formulated in mathematical terms as a family of partial differential operators, depending on the small parameter ϵ. The partial differential operators may be time-independent or time-dependent, linear or nonlinear. These operators have coefficients that are periodic functions in all or some variables with periods proportional to ϵ. Since ϵ is assumed to be small compared to 1, we have a family of operators with rapidly oscillating coefficients. The two-scale process introduced in the partial differential equations of the problem produces $\mathbf{x}$ (microscopic space variable) and $\mathbf{X}$ (macroscopic space variable). Generally speaking, equations in x are 'solvable' if the microscopic structure is periodic, leading to a 'rigorous' deduction of the macroscopic equations (in $\mathbf{X}$) for the global behavior. 'Rigorous' is here understood in the sense of 'straight-forward if the two-scale scheme is postulated' and, in most problems, a mathematical proof of the convergence of solutions to the "homogenized solutions" must be done. The detailed procedure of two-scale expansion is illustrated in the subsequent chapters.

Multiscale homogenization has emerged as one of the most promising methods to compute composite structures' response. In the last years, various direct micro-macro methods, also known as global-local analysis, have been developed (Lene and Leguillon (1982); Devries et al. (1989); Guedes and Kikuchi (1990); Ghosh et al. (1995); Fish et al. (1997); Lācis and Bagheri (2017); Lācis et al. (2020); Sudhakar et al. (2019); Bottaro (2019), and references their in) as the evolving result of applying the asymptotic homogenization theory. These approaches estimate the relevant stress-strain relationship at a macroscopic point by performing calculations on a separate scale determined by a macroscopic point using different methods to compute the different scales' structural response. Suquet et al. (1983) laid down the basic principles of homogenization to find the constitutive equations for the averaged effective or macroscopic properties of heterogeneous material. The establishment of multiscale homogenization in this study can be summarized:

- **Representation Volume Element (RVE):** RVE statistically represents the whole

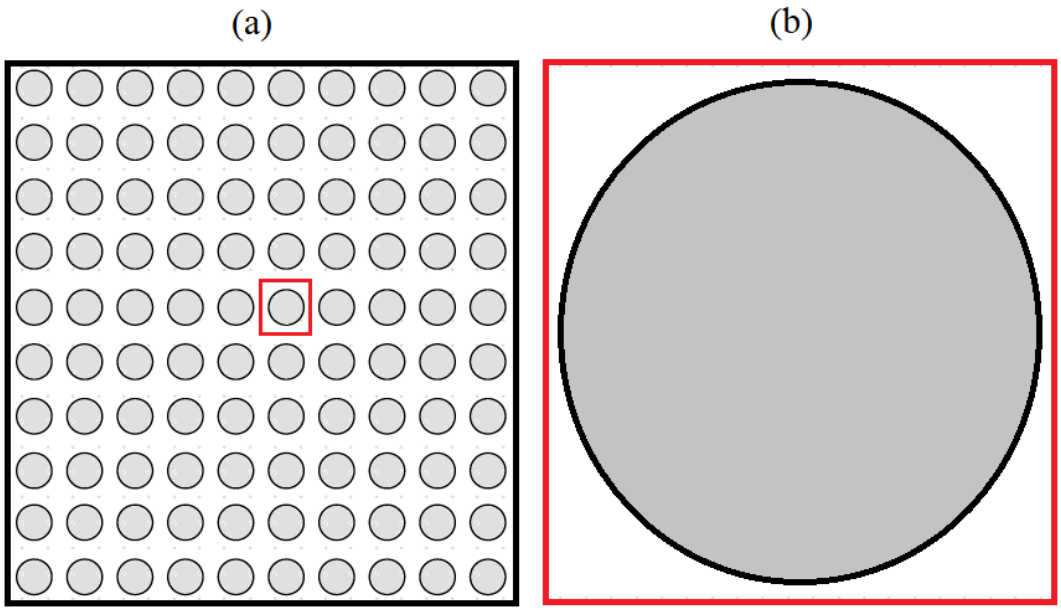

Figure 1.9: (a) Full macroscopic domain, (b) microscopic domain as a representative volume element.

microstructure under consideration. The size of the representative volume element (RVE) should be large enough to contain a sufficient number of micro-heterogeneities whose constitutive behavior is assumed to be known.

- **Derivation of Auxiliary Systems of Equations:** The auxiliary system needs to be derived and solved either numerically or analytically, to obtain effective macroscopic properties such as permeability, elasticity, slip velocity, and transpiration.

- **Effective Boundary Conditions:** Write the effective boundary conditions with the effective properties obtained by auxiliary problems. These effective conditions close the macroscopic problem. Therefore, the macroscopic problem is then solved together with the effective boundary conditions to analyze heterogeneous surfaces' effect on the fluid flow.

1.5.3. Representative Volume Element (RVE)

The multiscale homogenization is based on the use of an RVE, as mentioned in the section above. The RVE is a representative domain used to evaluate the corresponding effective properties of the homogenized macroscopic model. In an average context, the RVE term refers to a microstructural sub-region that represents the entire microstructure. The efficient moduli of composites are presumed to be independent of assumed homogeneous

tractions or displacements on the RVE boundary since they must have a sufficient number of inclusions.
According to the literature review by Starzewski (1998), the RVE is well-identified for two situations given below;

- When a periodic microstructure contains a unit inclusion (i.e., the volume portion is selected to include a single inclusion in a matrix phase), as displayed in figure 1.9.
- When a volume contains a significant number of micro-scale components with statistically homogeneous and ergodic properties (cf. Chapter 2 for the non-uniform arrangement of porous media.)

1.5.4. Features of Multiscale Homogenization

As reported by Kouznetsova et al. (2002), multi-scale computational homogenization techniques have many features that make composite material analysis very convenient. Below are some of the most notable features:

- The macroscopic constitutive behavior is obtained from the solution of the related microscopic auxiliary problem, so no explicit assumptions on the form of the macroscopic local constitutive equations are needed.
- The techniques can be implemented for any material behavior, including mechanically nonlinear and time-dependent behavior.
- Deformations and rotations to be incorporated at both the micro and macro levels.
- It is possible to introduce detailed microstructural information, including the microstructure's physical and geometrical evolution, into the macroscopic analysis.
- Consent to use almost every simulation approach to compute the numerical solution on a microscale.

1.6. Overview of the Present Work

The present study is devoted to describing an up-scaling method to derive the high-order effective conditions for micro-textured walls such that these structures can be replaced in a practical application by a smooth, fictitious surface over which the flow can slip and through which transpiration is possible, resulting in the same result as the actual surface texture. This method allows microscale effects to be captured, avoiding the prohibitively expensive numerical resolution of microscopic flow structures. The considered structures pattern is presumed to repeat itself periodically over a scale significantly shorter than a

characteristic dimension of the macroscopic flow (as in most previous studies); this makes the problem suitable for a multiple-scale description such as that employed by Mei and Vernescu (2009). As opposed to the literature discussed above, the effective conditions obtained here are correct to the higher than the first order in terms of a small parameter ϵ (the ratio of microscopic to macroscopic length scales). Laminar and turbulence flow configurations are considered for different problems such as: (i) Hiemenz stagnation point flow over rough and prous walls, (ii) flow over backward facing step with porous block, and (iii) pressure-driven flow in a periodic channel. Accuracy and functionality of the developed conditions are checked by comparison of the model solutions with our own fully resolved simulations and with the literature.

1.7. Outline of the Dissertation

In Chapter 2, effective boundary conditions capable of modeling a regularly microstructured wall, correct to third order in ϵ, are derived by homogenization technique for an incompressible fluid flow over a rough wall with periodic micro-indentations. The strategy opted here is similar to the one presented by Sudhakar et al. (2019). The coefficients involved in the effective conditions are non-empirical and computed numerically from the auxiliary problems. In the same chapter, the conditions for a porous-fluid interface (whose location must be set), are also derived. All the coefficients of these conditions are computed numerically (see numerical settings in "Appendix A.1."). and reported in tabular and graphical form for possible future use. In the end of Chapter 2, mathematical formulation of the of the flow over compliant riblets is developed to set the framework in order to optimize their geometrical and structural properties, for drag reduction purposes. In Chapter 3, applications of the effective conditions representing the effect of rough wall and interfacial conditions containing the porous medium (specific shapes and arrangements) effects on overlaying fluid are carried out to check their accuracy and to test their functionality for different flow situations. The results are compared against fully feature-resolving simulations and with literature to demonstrate the approach's accuracy even for situations beyond the formal domain of validity of the conditions. In chapter 4, main conclusions are summarized and suggestions are provided for future work.

MICROSCOPIC PROBLEMS

2.1. Summary

This chapter describes the mathematical modeling of two problems; (i) the fluid flow over a rough wall, and (ii) the flow over and through a porous medium where the following task are performed:

1. Effective boundary conditions, correct to third order in a small parameter ϵ, are derived by homogenization theory for the motion of an incompressible fluid over a rough wall with periodic micro-indentations. A multiple scale expansion of the variables allows recovering at leading order, the usual Navier slip condition. At next order the slip velocity includes a term arising from the streamwise pressure gradient; furthermore, a transpiration velocity $\mathcal{O}(\epsilon^2)$ appears at the fictitious wall where the effective boundary conditions are enforced. Additional terms appear at third order in both wall-tangent and wall-normal components of the velocity.

2. Interface conditions at the dividing surface (interface between a free-fluid and a porous region) are of utmost importance when a two-domain approach is used to treat the coupled problem. Using homogenization theory, intefacial conditions are derived here; they are akin to the classical Beavers-Joseph-Saffman conditions, the difference being that the coefficients which appear in the fluid-porous matching relations stem from the solution of microscopic, Stokes-like problems in a cell around the dividing surface with periodic conditions along the interface-parallel directions, and do not need to be fixed ad-hoc. The case of isotropic porous media is considered, and the effective coefficients are provided for both two- and three-dimensional grains, for varying porosity. Parametric variation as a function of variable porosity is also done in this section and compared with previous literature.

3. Generalized Navier slip boundary conditions for small-scale, deformable riblets, embedded within the viscous sublayer of a turbulent boundary layer, capable of adapting to the overlying motion are developed in this example. The contribution is dedicated to studying the interface problems, in both the fluid and the solid domains, for prototypical triangular and blade riblets made of a linearly elastic material. The outcome of the work is to obtain the macroscopic equations ruling the fluid-solid interactions, plus the effective coefficients (or convolution kernels, by virtue of the time-dependent nature of the fluid-solid coupling).

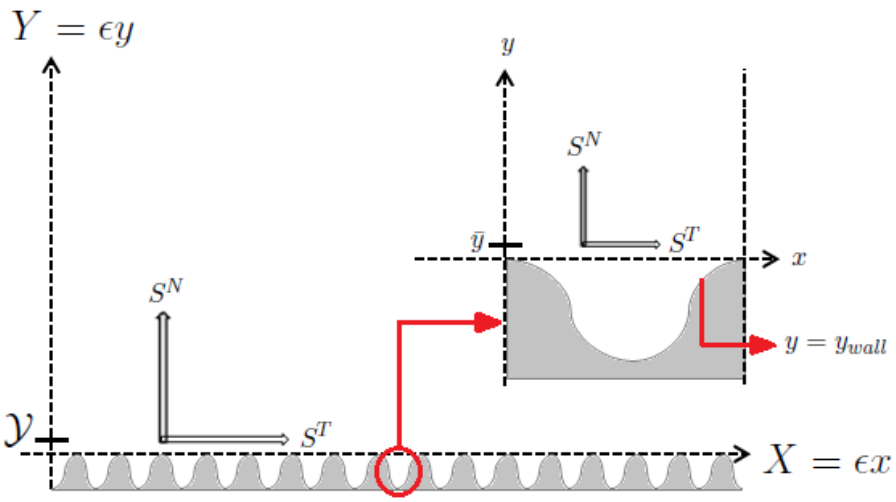

Figure 2.1: Sketch of a regularly microstructured surface with close-up of a unit cell.

2.2. Mathematical Formulation of Two-Dimensional Flow over a Rough Wall

A regularly microstructured two-dimensional surfaces are considered with Cartesian coordinates. The wall has a characteristic scale of microscopic length equal to l (say, pattern periodicity); the scale of macroscopic length is L (say, half-thickness of the channel, or flat plate length). In terms of the small parameter $\epsilon = l/L$, the presence of two characteristic dimensions makes the problem amenable to a two-scale expansion. The situation is schematized in 2.1. It is possible to set up two domains, one macroscopic, outer one (with variables denoted by capital letters) and one microscopic, one inner (small letters).

A matching in velocity and traction vectors between the two domains must be enforced and, anticipating the scalings of inner and outer velocities, we formally have

$$\lim_{Y \to 0} \mathbf{U} = \lim_{y \to \infty} \epsilon \, \mathbf{u}, \tag{2.1}$$

and similarly for traction. In actual numerical practice the outer, effective boundary conditions will be enforced at some vertical position (as an alternative to the expensive alternate of computing all details of the flow fields within the rough pattern) denoted $\mathcal{Y}$, with the corresponding inner velocity evaluated at $\bar{y} = \mathcal{Y}/\epsilon$, for the condition to read

$$\mathbf{U}|_{Y=\mathcal{Y}} = \epsilon \, \mathbf{u}|_{y=\bar{y}}. \tag{2.2}$$

The goal of this section is to formulate the effective boundary conditions for the outer flow, pushing the development beyond the leading order Navier slip term. Such conditions will depend on the inner flow regime and geometry of the roughness elements.

To set up the small-scale problem we need to normalize the equations properly. The flow in the inner domain is driven by a dimensional force, per unit surface area, which we will indicate for two dimensional case as $\hat{\mathbf{S}}$=($\hat{S}^T$, $\hat{S}^N$), applied in $\bar{y}$ (homogeneous and steady state). The superscripts T and N indicate, respectively, the tangential and the normal component of this force. Since the shear component of $\hat{\mathbf{S}}$ drives the flow in the roughness layer, the velocity scale there is $\mathcal{U} = \mathcal{O}(\hat{S}^T l/\mu)$, with μ the dynamic viscosity of the fluid. Using l as inner length scale, $l/\mathcal{U}$ as time scale, and $\mu\mathcal{U}/l$ (i.e. as pressure scale $\mathcal{U}l/\mu << 1$), the dimensionless equations in the inner region read:

$$\frac{\partial u_i}{\partial x_i} = 0, \quad \mathcal{R}\left(\frac{\partial u_i}{\partial t} + u_j\frac{\partial u_i}{\partial x_j}\right) = -\frac{\partial p}{\partial x_i} + \frac{\partial^2 u_i}{\partial x_j^2}. \tag{2.3}$$

The quantity $\mathcal{R}$ is the microscopic Reynolds number, defined by $\mathcal{R} = \rho\mathcal{U}l/\mu$, ρ being the fluid density, u_i representing the dimensionless velocity vector and x_i are the dimensionless directional coordinates.

The velocity scale in the outer domain is U_{out} (equal, for example, to the bulk velocity in a macroscopic channel), so that $S_{12} = \dfrac{\hat{S}^T L}{\mu U_{out}}$ and $S_{22} = \dfrac{\hat{S}^N L}{\mu U_{out}}$ are the dimensionless traction components in $Y = \mathcal{Y}$. By introducing also the outer time and pressure scales, L/U_{out} and ρU_{out}^2 (assume ρU_{out}^2), the dimensionless equations in the macroscopic domain become:

$$\frac{\partial U_i}{\partial X_i} = 0, \quad \left(\frac{\partial U_i}{\partial T} + U_j\frac{\partial U_i}{\partial X_j}\right) = -\frac{\partial P}{\partial X_i} + Re^{-1}\frac{\partial^2 U_i}{\partial X_j^2}. \tag{2.4}$$

with $U_i = (U, V)$, $X_i = (X, Y)$) and $Re = \rho U_{out} L/\mu$, Reynolds number of the outer flow. The ratio between inner and outer length scales yields $X_i = \epsilon x_i$ (where $x_i = (x, y)$) and this suggests expressing the variables in the near-wall region as power series expansions in terms of the small parameter ϵ, i.e.

$$\phi = \phi^{(0)} + \epsilon\phi^{(1)} + \epsilon^2\phi^{(2)}..., \tag{2.5}$$

with $\phi = u_i$, or p. Whereas the outer flow variables (U_i, P) depend only on the macroscopic independent variable X_i plus eventually time T, the inner flow variables, at all orders in ϵ, are assumed to depend on both X_i and x_i, plus time t.
Thus, in system 2.3 we need to pose:

$$\frac{\partial}{\partial x_i} = \frac{\partial}{\partial x_i} + \epsilon\frac{\partial}{\partial X_i}. \tag{2.6}$$

Which provide the equation at zero order in ϵ is:

$\mathcal{O}(\epsilon^0)$

$$\frac{\partial u_i^{(0)}}{\partial x_i} = 0, \quad -\frac{\partial p^{(0)}}{\partial x_i} + \frac{\partial^2 u_i^{(0)}}{\partial x_j^2} + F = 0 \tag{2.7}$$

where $F = \delta(y - \mathcal{Y})S_{i2} = 0$ is added by following the approach of Lācis et al. (2020) in order to have equation which should be valid above and below Y.

$\mathcal{U}$ is chosen as $\mathcal{U} = \epsilon U_{out}$ so that $\mathcal{R} = \epsilon^2 Re$. With the present choice, inner and outer time scales coincide, i.e. $t = T$. The (arbitrary) position $\bar{y} = \mathcal{Y}/\epsilon$ where the traction force impressed by the outer flow, modeled via a Dirac delta function, is assumed to apply can be taken on the outer edge of the wall micro-structure, i.e. $\mathcal{Y} = \bar{y} = 0$ (cf. 2.1). Any other position different from $\bar{y} = 0$ is equally acceptable[1]) and applying the effective boundary condition in the macroscopic problem at a position $\mathcal{Y} \neq 0$ leads to a solution endowed with the same formal accuracy as the choice $\mathcal{Y} = 0$. In two and three-dimensional configurations, the components of the dimensionless traction vector $\mathbf{S}$ are respectively defined as:

$$S_{12} = \frac{\partial U}{\partial Y} + \frac{\partial V}{\partial X}, \quad S_{22} = -ReP + 2\frac{\partial V}{\partial Y}. \tag{2.8}$$

The system of equations at first order in ϵ is:

$\mathcal{O}(\epsilon^1)$

$$\frac{\partial u_i^{(1)}}{\partial x_i} = -\frac{\partial u_i^{(0)}}{\partial X_i}, \quad -\frac{\partial p^{(1)}}{\partial x_i} + \frac{\partial^2 u_i^{(1)}}{\partial x_j^2} = \frac{\partial p^{(0)}}{\partial X_i} - 2\frac{\partial^2 u_i^{(0)}}{\partial X_j x_j}. \tag{2.9}$$

Microscopic domain must hold periodicity along x, therefore, both microscopic systems must be solved subject to periodic conditions along tangential and crossflow direction, with "no-slip" at $y = y_{wall}$, and vanishing "stress" at $y \to \infty$. For two-dimensional, the latter reads;

$$\begin{aligned} \frac{\partial u^{(0)}}{\partial y} + \frac{\partial v^{(0)}}{\partial x} &= -p^{(0)} + 2\frac{\partial v^{(0)}}{\partial y} = 0, \\ \frac{\partial u^{(1)}}{\partial y} + \frac{\partial v^{(1)}}{\partial x} &= -\frac{\partial u^{(0)}}{\partial Y} - \frac{\partial v^{(0)}}{\partial X}, \\ -p^{(1)} + 2\frac{\partial v^{(1)}}{\partial y} &= -2\frac{\partial v^{(0)}}{\partial Y}. \end{aligned} \tag{2.10}$$

Once the solutions of zero and first order systems are found, the macroscopic, effective conditions (see equations 2.1 and 2.2) for the outer flow at the fictitious wall in $Y = 0$ are:

$$U_i(X, 0, t) = \epsilon \left[\int_0^1 (u_i^{(0)} + \epsilon u_i^{(1)}) \Big|_{y=0} dx_i \right] + \mathcal{O}(\epsilon^3). \tag{2.11}$$

[1]This is true provided we remain in the vicinity of the roughness and do not incur in numerical instabilities in the solution of the macroscopic problem by some unwise choice of $\bar{y}$. A choice can be *unwise* if, for example, the Navier slip coefficient becomes negative i.e. the two virtual origins, for the longitudinal and the transverse motion, sit above the $\bar{y}$ with reverse flow in the region underneath the virtual origin. This causes numerical problems because of loss of ellipticity (Achdou et al. (1998)

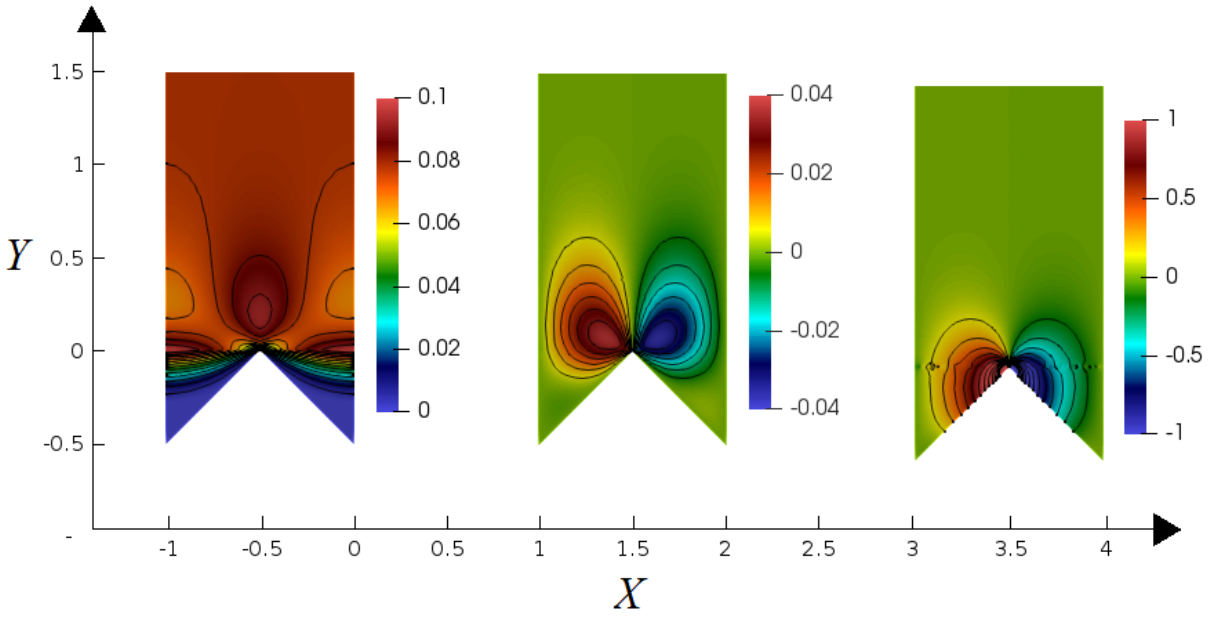

Figure 2.2: Isolines of $u^\dagger$ (left), $v^\dagger$ (center) and $p^\dagger$. The domain has been cut at $y = 1.5$ to focus on the behavior close to the roughness, even if in the actual computation $y_\infty = 5$. The small irregularity visible in the isolines of $p^\dagger$ is related to the presence of the delta function in $y = 0$.

The zero-order solution

System 2.7 is linear and this permits the search of a solution of leading order in the form:

$$\phi^{(0)} = \phi^\dagger(x, y)S_{12} + \phi^\ddagger(x, y)S_{22}, \tag{2.12}$$

for the generic dependent variable $\phi^{(0)}$. The ansatz yields two decoupled systems for the unknowns.

System 1: Forcing by S_{12}

$$\frac{\partial u_i^\dagger}{\partial x_i} = 0, \quad \frac{\partial p^\dagger}{\partial x_i} + \frac{\partial^2 u_i^\dagger}{\partial x_j^2} + \delta(y)\delta_{1i} = 0. \tag{2.13}$$

System 2: Forcing by S_{22}

$$\frac{\partial u_i^\ddagger}{\partial x_i} = 0, \quad \frac{\partial p^\ddagger}{\partial x_i} + \frac{\partial^2 u_i^\ddagger}{\partial x_j^2} + \delta(y)\delta_{2i} = 0. \tag{2.14}$$

These two systems are endowed with boundary conditions of "no-slip" and "zero stress" at $y = y_{wall}$ and $y \to \infty$, respectively.

Considering, for example, a triangular microscopic roughness element, the numerical approach is readily available for the solutions of the systems 2.13 and 2.14. An example of the *system 1* solution is shown in figure 2.2 in the form of isolines for each unknown of the

system 2.13. The flow is driven by a forcing of Dirac delta function (see appendix A.1.3.) in x-direction at $y = 0$. Therefore the physical interpretation of these solutions is the flow response to delta forcing (to match the inner and outer solutions) in the horizontal direction at $y = 0$. To obtain reliable results, the numerical domain extends from $y = -0.5$ (roughness troughs) to $y = 5$; for the solution to be independent of height y, the latter value, denoted y_∞ in the following, must be taken sufficiently far from the roughness crest at $y = 0$. We have verified for the geometry under consideration that the solution near the roughness does not change when y_∞ is taken farther away from 3. and it is constant farther away from the roughness crest. By averaging the streamwise velocity distribution along x in $y = 0$ it is found that $\lambda_x := \int_0^1 u^\dagger(x,0)\,\mathrm{d}x = 0.0780$, whereas the x-averaged values of $v^\dagger$ and $p^\dagger$ at $y = 0$ are equal to zero as also shown by symmetric contour plots of $v^\dagger$ and $p^\dagger$ around the vertical centre axis. It goes without saying that, had we chosen a value of $\bar{y}$ different from 0, we would have found a different result for λ_x.

System 2 has a simple solution i.e. $u^\ddagger = v^\ddagger = 0$, and $p^\ddagger_x = 0$ together with $p^\ddagger_y = \delta(y)$. From the definition of the Heaviside step function, $\mathrm{d}H/\mathrm{d}y := \delta(y)$, and the boundary condition $p^\ddagger = 0$ at $y \to \infty$, it is simple to find $p^\ddagger = H(y) - 1$, i.e. $p^\ddagger$ is identically equal to -1 when $y < 0$, and it vanishes for $y > 0$. Eventually, we have

$$\int_0^1 u_i^{(0)}(x,0,t)\,\mathrm{d}x = \lambda_x S_{i2}\delta_{i1}, \quad \int_0^1 p^{(0)}(x,0^-,t)\,\mathrm{d}x = ReP - 2\frac{\partial V}{\partial Y}. \tag{2.15a}$$

The first-order solution:
On account of 2.12, the linear system of equations 2.9 becomes

$$\frac{\partial u_i^{(1)}}{\partial x_i} = -u_j^\dagger \frac{\partial S_{12}}{\partial X_j}, \quad -\frac{\partial p^{(1)}}{\partial x_i} + \frac{\partial^2 u_i^{(1)}}{\partial x_j^2} = p^\dagger \frac{\partial S_{12}}{\partial X_i} + p^\ddagger \frac{\partial S_{22}}{\partial X_i} - 2\frac{\partial u_i^\dagger}{\partial x}\frac{\partial S_{12}}{\partial X} - 2\frac{\partial u_i^\dagger}{\partial y}\frac{\partial S_{12}}{\partial Y}, \tag{2.16}$$

subject to the condition at $y \to \infty$:

$$\frac{\partial u^{(1)}}{\partial y} + \frac{\partial v^{(1)}}{\partial x} = -u_j^\dagger \frac{\partial S_{12}}{\partial X_j}, \; -p^{(1)} + 2\frac{\partial v^{(1)}}{\partial y} = -2v^\dagger \frac{\partial S_{12}}{\partial Y}. \tag{2.17}$$

Thus, the solution has a generic form:

$$\phi^{(1)} = \hat{\phi}_1(x,y)\frac{\partial S_{12}}{\partial X} + \breve{\phi}_1(x,y)\frac{\partial S_{22}}{\partial X} + \hat{\phi}_2(x,y)\frac{\partial S_{12}}{\partial Y} + \breve{\phi}_2(x,y)\frac{\partial S_{22}}{\partial Y}. \tag{2.18}$$

Equipped with "no-slip" conditions at $y = y_{wall}$ and periodicity at x, four separate systems can be set up, see below:

System 3: Forcing by gradient of S_{12}

$$\begin{gathered}\frac{\partial \hat{u}_{ij}}{\partial x_i} = -u_j^\dagger, \quad -\frac{\partial \hat{p}_j}{\partial x_i} + \frac{\partial^2 \hat{u}_{ij}}{\partial x_k^2} = \delta_{ij}p^\dagger - 2\frac{\partial u_i^\dagger}{\partial x_j}, \\ \text{subject to} \quad -\hat{p}_j\delta_{i2} + \frac{\partial \hat{u}_{2j}}{\partial x_i} + \frac{\partial \hat{u}_{ij}}{\partial y} = -v^\dagger\delta_{ij} - u^\dagger\delta_{2j} \text{ at } y \to \infty.\end{gathered} \tag{2.19}$$

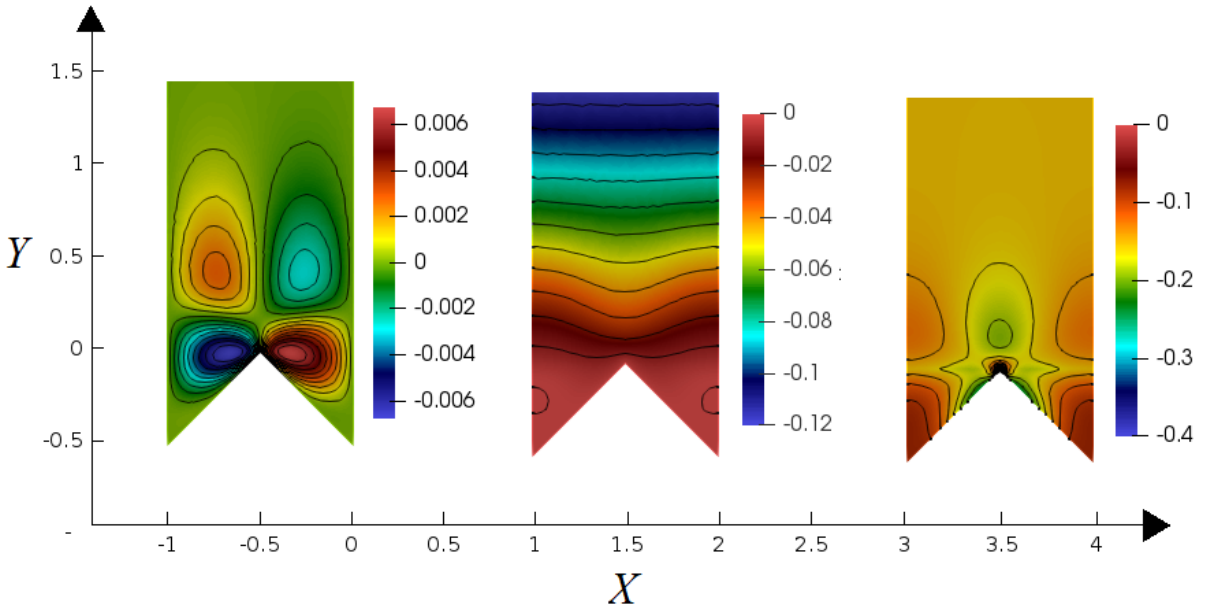

Figure 2.3: Isolines of $\hat{u}_1$ (left), $\hat{v}_1$ (center) and $\hat{p}_1$.

System 4: Forcing by gradient of S_{22}

$$\begin{aligned} &\frac{\partial \breve{u}_{ij}}{\partial x_i} = 0, \quad -\frac{\partial \breve{p}_j}{\partial x_i} + \frac{\partial^2 \breve{u}_{ij}}{\partial x_k^2} = \delta_{ij}(H(y) - 1), \\ &\text{subject to} \quad -\hat{p}\delta_{i2} + \frac{\partial \hat{u}_{2j}}{\partial x_i} + \frac{\partial \hat{u}_{ij}}{\partial y} = 0 \text{ at } y \to \infty. \end{aligned} \tag{2.20}$$

Systems 3 (for $i = 1,\, 2$; $j = 1,\, 2$) to 4 (i=1, 2; j=1) are determined by the same numerical method used so far; figures 2.3 to2.5 display the fields. The only results of interest are $m_{21} := \int_0^1 \hat{u}_{21}(x,0)\,\mathrm{d}x = -0.0058$, and $m_{12} := \int_0^1 \breve{u}_{11}(x,0)\,\mathrm{d}x = 0.0058$. Systems 4 (for $i = 1\,,2$; $j = 2$) admits the simple analytical solution $\breve{u}_{12} = \breve{u}_{22} = 0$ and $\breve{p}_2 = y\,H(-y)$. An approximation of the macroscopic slip and transpiration velocity components at $Y = 0$ is now available using the equations 2.11. To close this part, we observe that

- We could expand the solution easily to the next order, including inertial terms.
- In order to determine slip and transpiration conditions for the outer flow, the above method is not the only one that can be built to mimic the effect of a rough wall.

An alternative approach is described in the next subsection, following the lines initiated by Luchini et al. (1991) in the case of riblets. The concentrated volume force in equations 2.7 at $\bar{y}$ is absent in this second approach and as such, there is no need to approximate a delta or unit step distribution using an extremely dense mesh around $\bar{y}$. The results obtained in this subsection will be reproduced next with this alternative approach, and extended to the subsequent ϵ order.

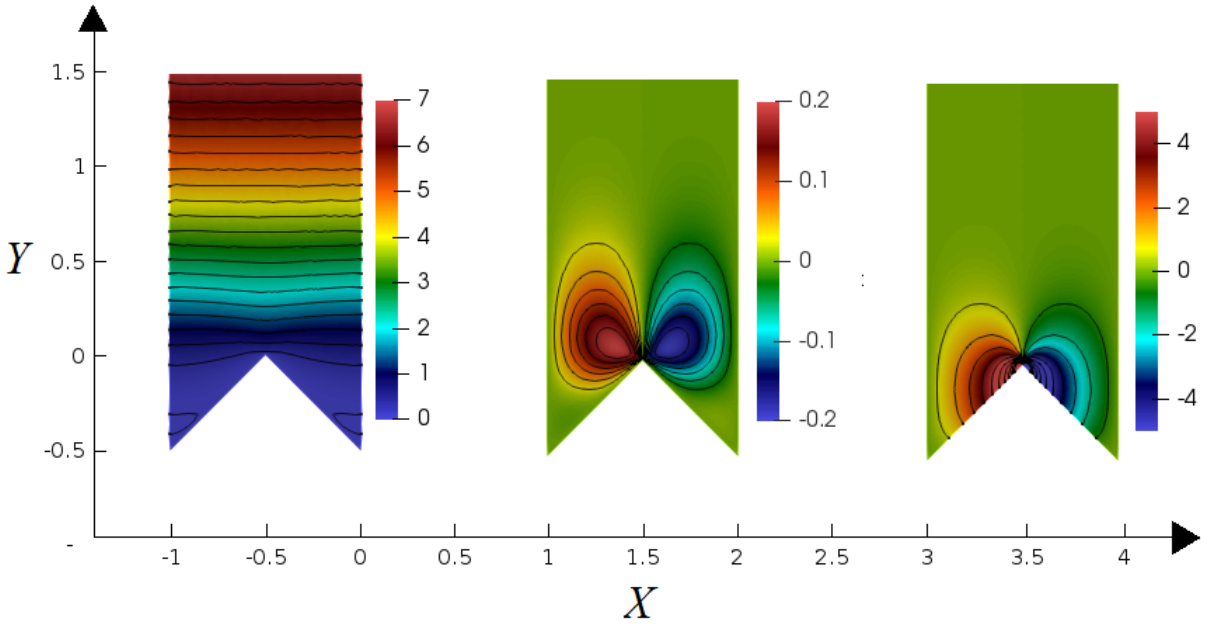

Figure 2.4: Isolines of $\breve{u}_1$ (left), $\breve{v}_1$ (center) and $\breve{p}_1$.

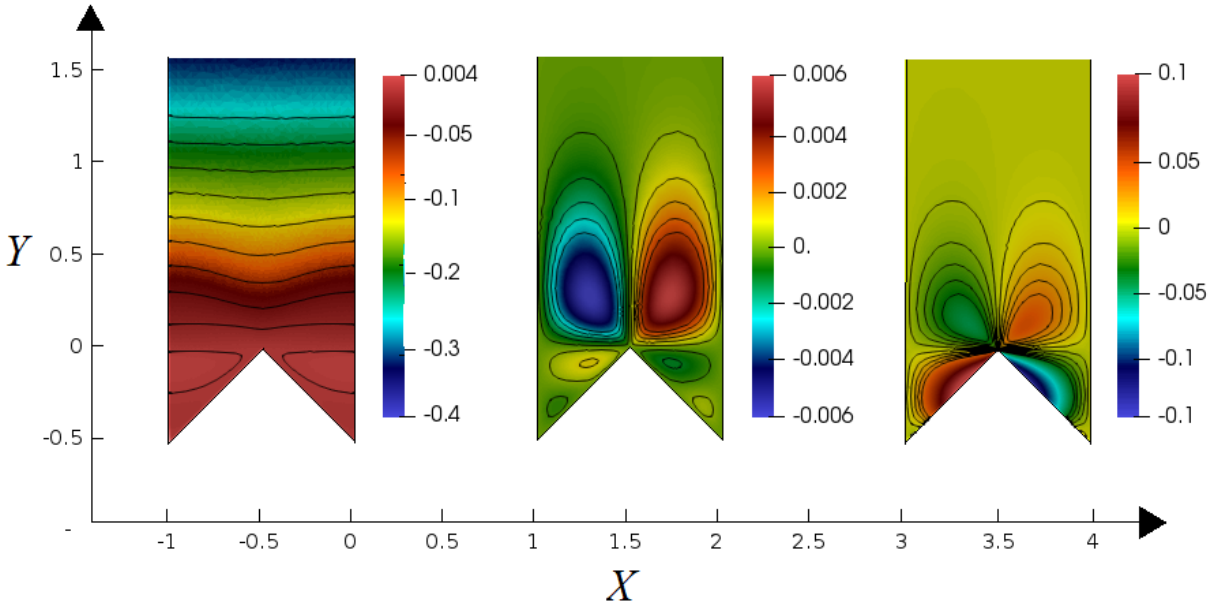

Figure 2.5: Isolines of $\hat{u}_2$ (left), $\hat{v}_2$ (center) and $\hat{p}_2$.

2.2.1. The Alternative Approach

Here, the same inner and outer scales used in the last section are employed here. The main difference in this approach and what was done in the previous section is that the equations do not have a source term now, and the flow is assumed to be driven by the $\mathbb{S}_{12}$ horizontal shear traction in $y \to \infty$ defined in Luchini et al. (1991) and Kamrin et al. (2009). Notice that the traction vector at y_∞ differs from (S_{12}, S_{22}), the latter denoting the force on $y = \bar{y}$ (with $\bar{y}$ in the previous section set to zero). The outer limit (boundary) at $y = y_\infty$ is taken far enough from the rough wall to ensure that the results have lost memory of the rough-wall shape at the outer edge of the microscopic domain, i.e. the solution there becomes x-independent. In the present approach, this value of y_∞ can then be taken to coincide with the position $\bar{y}$ where matching (2.2) is applied. At the outer edge of the domain the conditions are thus

$$\frac{\partial u}{\partial y} + \frac{\partial v}{\partial x} = \mathbb{S}_{12}, \quad -p + 2\frac{\partial v}{\partial y} = \mathbb{S}_{22}. \tag{2.21}$$

System (2.3) is the inner system of equations, equipped with no-slip conditions at $y = y_{wall}$ and periodicity at x. As before (see last section), we assume a series expansion in powers of ϵ for the dependent variables and plug in the inner flow equations, obtaining the homogeneous Stokes system for the leading order variables. The traction imposed by the outer flow at y_∞ is transferred to the order zero microscopic variables, i.e.

$$\frac{\partial u^{(0)}}{\partial y} + \frac{\partial v^{(0)}}{\partial x} = \mathbb{S}_{12}, \quad -p^{(0)} + 2\frac{\partial v^{(0)}}{\partial y} = \mathbb{S}_{22}. \tag{2.22}$$

At higher orders we have:

$$\frac{\partial u^{(i)}}{\partial y} + \frac{\partial v^{(i)}}{\partial x} = -\frac{\partial u^{(i-1)}}{\partial Y} - \frac{\partial v^{(i-1)}}{\partial X}, \quad -p^{(i)} + 2\frac{\partial v^{(i)}}{\partial y} = -2\frac{\partial v^{(i-1)}}{\partial Y} \quad i = 1, 2, ... \tag{2.23}$$

The zero-order solution

Using the result of the Bolaños and Vernescu (2017), the zero-order solution is:

$$u_i^{(0)} = u_i^\dagger(x, y)\mathbb{S}_{12}, \tag{2.24}$$

$$p^{(0)} = p^\dagger(x, y)\mathbb{S}_{12} - \mathbb{S}_{22}. \tag{2.25}$$

The † variables used here are different from those introduced in the previous section. For the sake of convenience, we maintain the same notation, and will do the same with the variables denoted by $\hat{\bullet}$ and $\breve{\bullet}$. The system in terms of † variables is the homogeneous Stokes system and the boundary conditions for y_∞ are given below:

$$\frac{\partial u^\dagger}{\partial y} + \frac{\partial v^\dagger}{\partial x} = 1, \quad -p^\dagger + 2\frac{\partial v^\dagger}{\partial y} = 0. \tag{2.26}$$

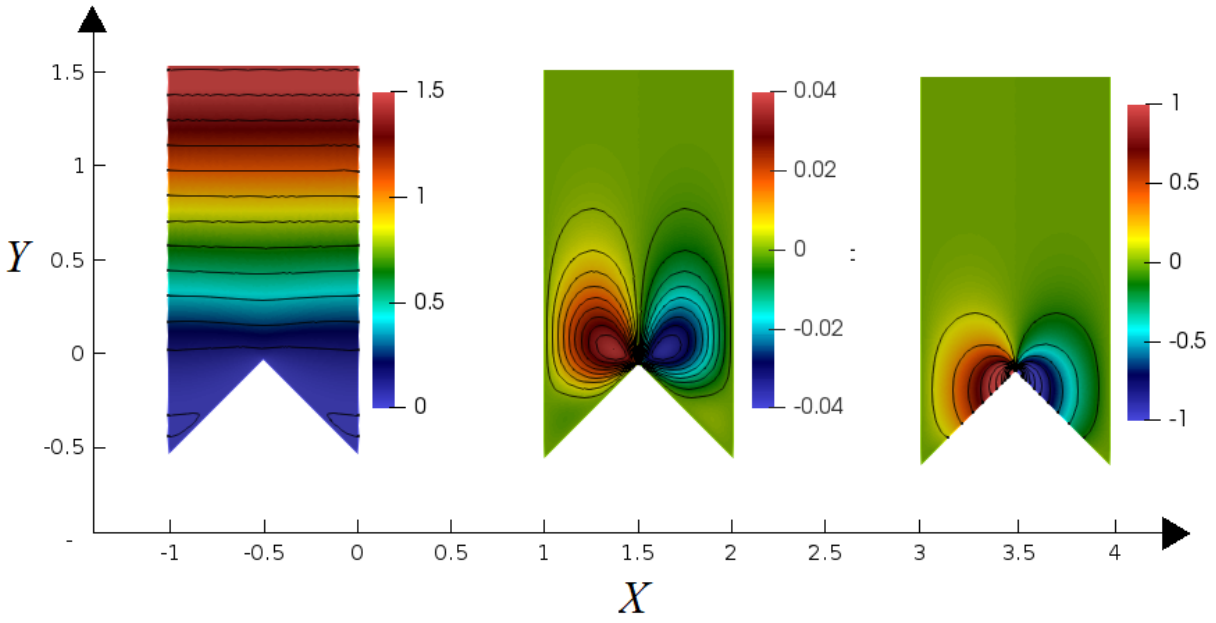

Figure 2.6: Isolines of $u^\dagger$ (left), $v^\dagger$ (center) and $p^\dagger$.

The solution for the triangular roughness geometry of this system (written in † variables) is given in figure 2.6. In particular, it is found that $y_\infty = 5$ is taken to be at the outer edge of the unit cell, where $\gamma^x := u^\dagger(x, 5) = 5.07778$ and $v^\dagger(x, 5) = p^\dagger(x, 5) = 0$. It should also be noted that the isolines of $v^\dagger$ and $p^\dagger$ are similar to those shown in figure 2.2 (central and right Frames). The isolines of $u^\dagger$ is different because of the different forcing in both cases but lead to the same solution of $\int_0^1 u^\dagger \mathrm{dx}$ at $y = 0$.

The first-order solution

The system at $\mathcal{O}(\epsilon)$ is

$$\frac{\partial u_i^{(1)}}{\partial x_i} = -u_j^\dagger \frac{\partial \mathbb{S}_{12}}{\partial X_j}, \quad -\frac{\partial p^{(1)}}{\partial x_i} + \frac{\partial^2 u_i}{\partial x_j^2} = p^\dagger \frac{\partial \mathbb{S}_{12}}{\partial X_i} - \frac{\partial \mathbb{S}_{22}}{\partial X_i} - 2\frac{\partial u_i^\dagger}{\partial x}\mathbb{S}_{12X} - 2\frac{\partial u_i^\dagger}{\partial y}\mathbb{S}_{12Y}, \tag{2.27}$$

and at y_∞ we have boundary conditions

$$\frac{\partial u^{(1)}}{\partial y} + \frac{\partial v^{(1)}}{\partial x} = -u^\dagger \frac{\partial \mathbb{S}_{12}}{\partial Y} - v^\dagger \frac{\partial \mathbb{S}_{12}}{\partial X}, \quad -p^{(1)} + 2\frac{\partial v^{(1)}}{\partial y} = -2v^\dagger \frac{\partial \mathbb{S}_{12}}{\partial Y}. \tag{2.28}$$

The general solution similar to the equation (2.18) reads as:

$$\phi^{(1)} = \hat{\phi}_1(x, y)\mathbb{S}_{12X} + \breve{\phi}_1(x, y)\mathbb{S}_{22X} + \hat{\phi}_2(x, y)\mathbb{S}_{12Y} + \breve{\phi}_2(x, y)\mathbb{S}_{22Y}, \tag{2.29}$$

and it is possible to set up four additional systems equipped with the same boundary conditions along the x and on the wall as the previous ones. These new systems read exactly as *systems 3* to *6*, with the exception that the $H(y)$ Heaviside function now

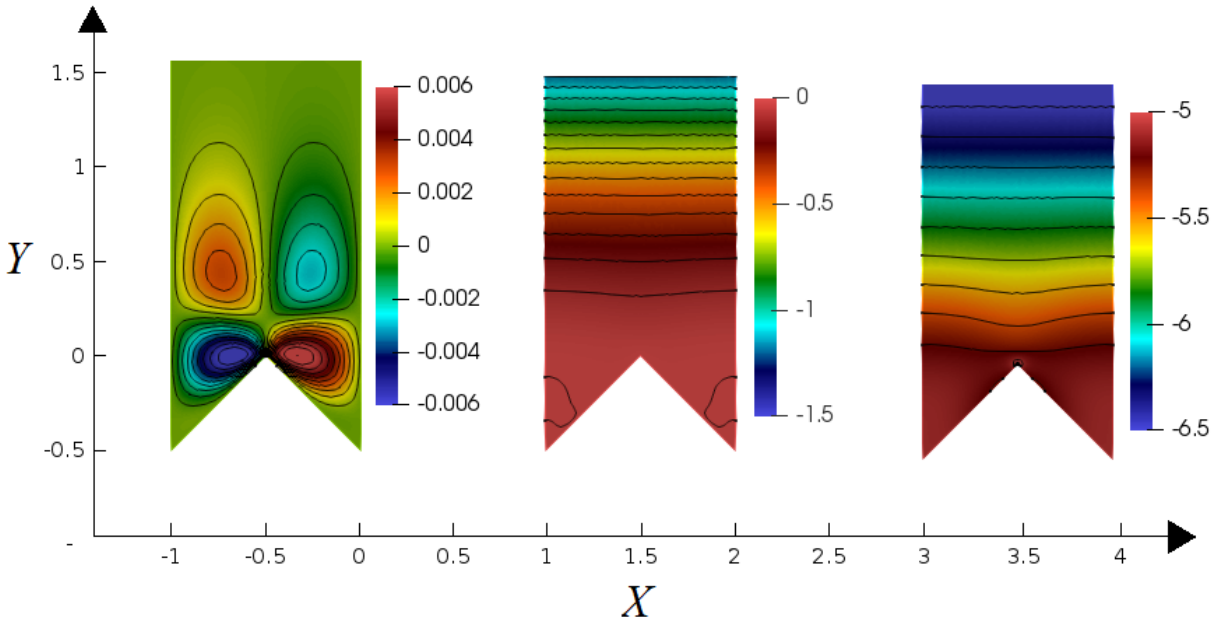

Figure 2.7: Isolines of $\hat{u}_1$ (left), $\hat{v}_1$ (center) and $\hat{p}_1$.

disappears from the right side of 2.20). The new *system 4*, for instance, becomes

$$\frac{\partial \breve{u}_{i\,1}}{\partial x_i}, \; -\frac{\partial \breve{p}_1}{\partial x_i} + \frac{\partial^2 \breve{u}_{i\,1}}{\partial x_j^2} = -\delta_{ij}. \tag{2.30}$$

$$\text{subject to} \quad -\breve{p}\delta_{i2} + \frac{\partial \breve{u}_{2j}}{\partial x_i} + \frac{\partial \breve{u}_{ij}}{\partial y} = 0 \text{ at } y \to \infty. \tag{2.31}$$

All the new systems are solved numerically as done previously, except for that relative to $(\breve{u}_{12}, \breve{u}_{22}, \breve{p}_2)$ which admits the simple analytical solution $\breve{u}_{12} = \breve{u}_{22} = 0$, and $\breve{p}_2 = y - y_\infty$. The solution of the system for $(\hat{u}_{11}, \hat{u}_{21}, \hat{p}_1)$ (equations 36) is displayed in figure 2.7 and, as expected, the field of $\hat{u}_1$ is the same as that reported in figure 2.2 (left frame.) We find that $\hat{u}_{11}(x, 5) = 0$ and $n_{21} := \hat{u}_{21}(x, 5) = -12.89469$.
The fields of $(\breve{u}_{11}, \breve{u}_{21}, \breve{p}_1)$ are identical, to graphical accuracy, to those shown in figure 2.4; the coefficients of interest at $\bar{y} = y_\infty = 5$ are $n_{12} := \breve{u}_{11}(x, 5) = 12.89469$ and $\breve{u}_{21}(x, 5) = \breve{p}_1(x, 5) = 0$. The numerical solution for $(\hat{u}_{12}, \hat{u}_{22}, \hat{p}_2)$ yields vanishing values of the fields at $y = y_\infty$. The field of $\hat{u}_{12}$ does not go to zero monotonically for increasing y, unlike $\hat{u}_{22}$ and $\hat{p}_2$. For y larger than about 1 we observe that $\hat{u}_{12}$ becomes uniform in x and follows closely the quadratic behavior $\hat{u}_{12} = (y + \gamma^x - y_\infty)(y_\infty - y)$ as also satisfied analytically.

The coefficients we have found so far are different from those obtained previously and this is due to the fact that the boundary conditions in the macroscopic problem at the fictitious wall are now not implemented at $\mathcal{Y} = \epsilon\bar{y} = 0$ (as we did in section 2), but at

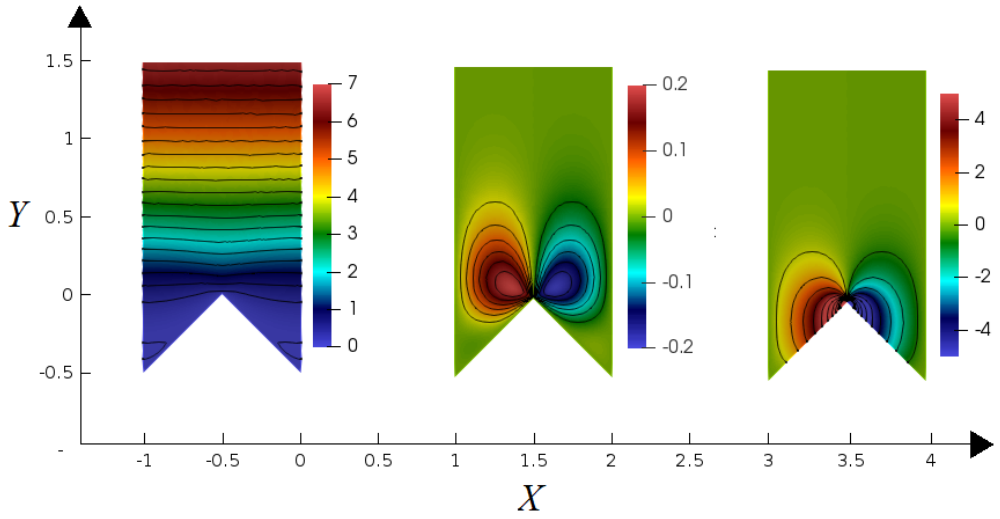

Figure 2.8: Isolines of $\check{u}_1$ (left), $\check{v}_1$ (center) and $\check{p}_1$.

Table 2.1: Variation of higher-order coefficients with the choice of y_∞.

$y_\infty = \bar{y}$	4	5	6	7	8	9
γ^x	4.07778	5.07778	6.07778	7.07778	8.07778	9.07778
$n_{12} = -n_{21}$	8.31693	12.89469	18.47249	25.05028	32.62806	41.20585

$\mathcal{Y} = \epsilon\bar{y} = \epsilon y_\infty$. Thus, Equation (5) reads

$$U(X, \epsilon y_\infty, t) \approx \epsilon\gamma^x \mathbb{S}_{12} + \epsilon^2 n_{12} \frac{\partial \mathbb{S}_{22}}{\partial X}, \tag{2.32}$$

$$V(X, \epsilon y_\infty, t) \approx \epsilon^2 n_{21} \frac{\partial \mathbb{S}_{12}}{\partial X}. \tag{2.33}$$

Nevertheless, it is easy to compare the results found here with those described in previous section. Table 1 shows how the coefficients vary as y_∞ is modified. All the data matches very well with either a straight line or a parabola (analytic solution), so the results can be easily extrapolated to any desired position of $\bar{y}$ where we choose to match internal and external solutions.
In particular, we have

$$n_{12} = -n_{21} = \frac{\bar{y}^2}{2} + \lambda_x \bar{y} + m_{12}, \tag{2.34}$$

$$\gamma^x = \frac{dn_{12}}{d\bar{y}} = \bar{y} + \lambda_x, \tag{2.35}$$

with $\lambda_x = 0.07778$ and $m_{12} = -m_{21} = 0.00581$. By setting $\bar{y} = 0$ in (2.34) and (2.35), we recover the coefficients given in last section, up to the error of $\mathcal{O}(10^{-4})$ which we relate to the approximations made in the distributions of Dirac and Heaviside modeling.

The results embodied by equations (2.34-2.35) allow us to state that it is necessary to solve (2.30-2.31) *twice* and test n_{12} for two separate values for two-dimensional roughness elements such as those considered here. For example, to recover the two coefficients λ_x and $m12$ for two different values of $\bar{y} = y_\infty$, see result in figure 3.9.

However, an even better result is available. We observe that in fact,

$$n_{12} = -n_{21} = \int_0^1 \int_{y_{wall}}^{y_\infty} u^\dagger \, \mathrm{d}y \, \mathrm{d}x; \tag{2.36}$$

this implies that the *single* resolution of the Stokes homogeneous system for the † variables equipped with (2.26) is sufficient to recover the *all* coefficients required to write second-order matching interface conditions, whether enforced at $\bar{y} = y_\infty$ (cf. equations 2.32-2.33) or $\bar{y} = 0$.
This is verified by several other calculations, reported in subsection A.1.5., for various roughness patterns. The advantage of the strategy described in this section is its simplicity, accuracy and precision; all the numerical results here and in subsection A.1.5. are assumed to be accurate up to the last decimal digit reported.

Eventually, at $Y = 0$ the effective conditions to second order read:

$$U(X, 0, t) = U_S \approx \epsilon \lambda_x S_{12} + \epsilon^2 m_{12} \frac{\partial S_{22}}{\partial X}, \tag{2.37}$$

$$V(X, 0, t) = V_T \approx \epsilon^2 m_{21} \frac{\partial S_{12}}{\partial X}. \tag{2.38}$$

Going to higher order in ϵ
A higher-order correction can be obtained, and is relatively simple to obtain, in order to assess the role of convective terms in effective conditions at a large scale. The $\mathcal{O}(\epsilon^2)$ microscopic equations are

$$\frac{\partial u_i^{(2)}}{\partial x_i} = F^{mass}, \quad -\frac{\partial p^{(2)}}{\partial x_i} + \frac{\partial^2 u_i^{(2)}}{\partial x_j^2} = F^{x_i - mom}, \tag{2.39}$$

subject to the usual "no-slip" and x-periodic boundary conditions, plus

$$\frac{\partial u^{(2)}}{\partial y} + \frac{\partial v^{(2)}}{\partial x} = -\frac{\partial u^{(1)}}{\partial Y} - \frac{\partial v^{(1)}}{\partial X}, \quad -p^{(2)} + 2\frac{\partial v^{(2)}}{\partial y} = -2\frac{\partial v^{(1)}}{\partial Y} \quad \text{at} \quad y_\infty. \tag{2.40}$$

The source terms present in the system of $\mathcal{O}(\epsilon^2)$ are

$$
\begin{aligned}
F^{mass} &= -\hat{u}_{11}\frac{\partial^2 \mathbb{S}_{12}}{\partial X^2} - \breve{u}_{11}\frac{\partial^2 \mathbb{S}_{22}}{\partial X^2} - \hat{u}_{12}\frac{\partial^2 \mathbb{S}_{12}}{\partial X \partial Y} - \hat{u}_{21}\frac{\partial^2 \mathbb{S}_{12}}{\partial X \partial Y} - \breve{u}_{21}\frac{\partial^2 \mathbb{S}_{22}}{\partial X \partial Y} - \hat{u}_{22}\frac{\partial^2 \mathbb{S}_{12}}{\partial Y^2}, \\
F^{x-mom} &= \left[\hat{p}_1 - 2\frac{\partial \hat{u}_{11}}{\partial x} - u^\dagger\right]\frac{\partial^2 \mathbb{S}_{12}}{\partial X^2} + \left[\breve{p}_1 - 2\frac{\partial \breve{u}_{11}}{\partial x}\right]\frac{\partial^2 \mathbb{S}_{22}}{\partial X^2} + \left[\hat{p}_2 - 2\frac{\partial \hat{u}_{12}}{\partial x} - 2\frac{\partial \hat{u}_{11}}{\partial y}\right]\frac{\partial^2 \mathbb{S}_{12}}{\partial X \partial Y} \\
&\quad + \left[\breve{p}_2 - 2\frac{\partial \breve{u}_{11}}{\partial y}\right]\frac{\partial^2 \mathbb{S}_{22}}{\partial X \partial Y} - \left[2\frac{\partial \hat{u}_{12}}{\partial y} + u^\dagger\right]\frac{\partial^2 \mathbb{S}_{12}}{\partial Y^2} + Re\left[u^\dagger\frac{\partial \mathbb{S}_{12}}{\partial t} + (u^\dagger\frac{\partial u^\dagger}{\partial x} + v^\dagger\frac{\partial u^\dagger}{\partial y})\left(\mathbb{S}_{12}\right)^2\right], \\
F^{y-mom} &= \left[-2\frac{\partial \hat{u}_{21}}{\partial x} - v^\dagger\right]\frac{\partial^2 \mathbb{S}_{12}}{\partial X^2} - 2\frac{\partial \breve{u}_{21}}{\partial x}\frac{\partial^2 \mathbb{S}_{22}}{\partial X^2} + \left[\hat{p}_1 - 2\frac{\partial \hat{u}_{22}}{\partial x} - 2\frac{\partial \hat{u}_{22}}{\partial y}\right]\frac{\partial^2 \mathbb{S}_{12}}{\partial X \partial Y} \\
&\quad + \left[\breve{p}_1 - 2\frac{\partial \breve{u}_{21}}{\partial y}\right]\frac{\partial^2 \mathbb{S}_{22}}{\partial X \partial Y} + \left[\hat{p}_2 - 2\frac{\partial \hat{u}_{22}}{\partial y} - v^\dagger\right]\frac{\partial^2 \mathbb{S}_{12}}{\partial Y^2} + \breve{p}_2\frac{\partial^2 \mathbb{S}_{22}}{\partial Y^2} \\
&\quad + Re\left[v^\dagger\frac{\mathbb{S}_{12}}{\partial t} + (u^\dagger\frac{\partial v^\dagger}{\partial y} + v^\dagger\frac{\partial v^\dagger}{\partial y})(\mathbb{S}_{12})^2\right],
\end{aligned}
\tag{2.41}
$$

in such a way that the unknown vector $\mathbf{g}^{(2)} = (u^{(2)}, v^{(2)}, p^{(2)})$ can be written as

$$
\begin{aligned}
\mathbf{g}^{(2)} = \mathbf{g}_1\frac{\partial^2 \mathbb{S}_{12}}{\partial X^2} + \mathbf{g}_2\frac{\partial^2 \mathbb{S}_{22}}{\partial X^2} + \mathbf{g}_3\frac{\partial^2 \mathbb{S}_{12}}{\partial X \partial Y} + \mathbf{g}_4\frac{\partial^2 \mathbb{S}_{22}}{\partial X \partial Y} \\
+\mathbf{g}_5\,\mathbb{S}_{12YY} + \mathbf{g}_6\frac{\partial^2 \mathbb{S}_{22}}{\partial Y^2} + \mathbf{g}_7\frac{\partial \mathbb{S}_{12}}{\partial t} + \mathbf{g}_8\left(\mathbb{S}_{12}\right)^2,
\end{aligned}
\tag{2.42}
$$

with g_k where $k = 1, ..., 8$, leads to eight new auxiliary problems (all equipped with the same boundary conditions along x at the wall) given below. As was previous case, we are interested in the constant values at y_∞, for $k = 1...8$, respectively.

System 5: Forcing by $\mathbb{S}_{12_{XX}}$

$$
\begin{aligned}
&\frac{\partial u_{i1}}{\partial x_i} = -\hat{u}_{11}, \quad -\frac{\partial p_1}{\partial x_i} + \frac{\partial^2 u_{i1}}{\partial x_j^2} = \delta_{i1}\hat{p}_1 - 2\frac{\partial \hat{u}_{i1}}{\partial x} - u_i^\dagger, \\
\text{subject to} \quad &\frac{\partial u_{11}}{\partial y} + \frac{\partial u_{21}}{\partial x} = -\hat{u}_{21} \;\text{ and }\; -p_1 + 2\frac{\partial u_{21}}{\partial y} = 0 \quad \text{at} \quad y_\infty.
\end{aligned}
\tag{2.43}
$$

System 6: Forcing by $\mathbb{S}_{22_{XX}}$

$$
\begin{aligned}
&\frac{\partial u_{i2}}{\partial x_i} = -\breve{u}_{11}, \quad -\frac{\partial p_2}{\partial x_i} + \frac{\partial^2 u_{i2}}{\partial x_j^2} = \delta_{i1}\breve{p}_1 - 2\frac{\partial \breve{u}_{i1}}{\partial x}, \\
\text{subject to} \quad &\frac{\partial u_{12}}{\partial y} + \frac{\partial u_{22}}{\partial x} = -\breve{u}_{12} \;\text{ and }\; -p_2 + 2\frac{\partial u_{22}}{\partial y} = 0 \quad \text{at} \quad y_\infty.
\end{aligned}
\tag{2.44}
$$

System 7: Forcing by $\mathbb{S}_{12_{XY}}$

$$
\begin{aligned}
&\frac{\partial u_{i3}}{\partial x_i} = -\hat{u}_{12} - \hat{u}_{21}, \quad -\frac{\partial p_3}{\partial x_i} + \frac{\partial^2 u_{i3}}{\partial x_j^2} = \delta_{i1}\hat{p} + \delta_{i2}\hat{p}_1 - 2\frac{\partial \hat{u}_{12}}{\partial x} - 2\frac{\partial \hat{u}_{11}}{\partial y}, \\
\text{subject to} \quad &\frac{\partial u_{13}}{\partial y} + \frac{\partial u_{23}}{\partial x} = -\hat{u}_{11} - \hat{u}_{22} \;\text{ and }\; -p_3 + 2\frac{\partial u_{23}}{\partial y} = -2\hat{u}_{21} \quad \text{at} \quad y_\infty.
\end{aligned}
\tag{2.45}
$$

System 8: Forcing by $\mathbb{S}_{22_{XY}}$

$$\begin{aligned} &\frac{\partial u_{i4}}{\partial x_i} = -\breve{u}_{21}, \quad -\frac{\partial p_4}{\partial x_i} + \frac{\partial^2 u_{i4}}{\partial x_j^2} = \delta_{i1}\breve{p} + \delta_{i2}\breve{p}_1 - 2\frac{\partial \breve{u}_{11}}{\partial y}, \\ \text{subject to} \quad &\frac{\partial u_{14}}{\partial y} + \frac{\partial u_{24}}{\partial x} = -\breve{u}_{11} \ \text{ and } \ -p_4 + 2\frac{\partial u_{24}}{\partial y} = -2\breve{u}_{21} \quad \text{at} \quad y_\infty. \end{aligned} \tag{2.46}$$

System 09: Forcing by $\mathbb{S}_{12_{YY}}$

$$\begin{aligned} &\frac{\partial u_{i5}}{\partial x_i} = -\hat{u}_{22}, \quad -\frac{\partial p_5}{\partial x_i} + \frac{\partial^2 u_{i5}}{\partial x_j^2} = \delta_{i2}\,\hat{p}_i - 2\frac{\partial \hat{u}_{i2}}{\partial y} - u_i^\dagger, \\ \text{subject to} \quad &\frac{\partial u_{15}}{\partial y} + \frac{\partial u_{25}}{\partial x} = -\hat{u}_{12} \ \text{ and } \ -p_5 + 2\frac{\partial u_{25}}{\partial y} = -2\hat{v}_2 \quad \text{at} \quad y_\infty. \end{aligned} \tag{2.47}$$

System 10: Forcing by $\mathbb{S}_{22_{YY}}$

$$\begin{aligned} &\frac{\partial u_{i6}}{\partial x_i} = 0, \quad -\frac{\partial p_6}{\partial x_i} + \frac{\partial^2 u_{i6}}{\partial x_j^2} = \delta_{i2}\,\breve{p}_i, \\ \text{subject to} \quad &\frac{\partial u_{16}}{\partial y} + \frac{\partial u_{26}}{\partial x} = 0 \ \text{ and } \ -p_6 + 2\frac{\partial u_{26}}{\partial y} = 0 \quad \text{at} \quad y_\infty. \end{aligned} \tag{2.48}$$

Given that $\breve{p}_2 = y - y_\infty$ it is simple to find $u_{16} = u_{26} = 0$ and $p_6 = -\dfrac{(y-y_\infty)^2}{2}$.

System 11: Forcing by $\mathbb{S}_{12_t}$

$$\begin{aligned} &\frac{\partial u_{i7}}{\partial x_i} = 0, \quad -\frac{\partial p_7}{\partial x_i} + \frac{\partial^2 u_{i7}}{\partial x_j^2} = Re(u_i^\dagger), \\ \text{subject to} \quad &\frac{\partial u_{17}}{\partial y} + \frac{\partial u_{27}}{\partial x} = 0 \ \text{ and } \ -p_7 + 2\frac{\partial u_{27}}{\partial y} = 0 \quad \text{at} \quad y_\infty. \end{aligned} \tag{2.49}$$

System 12: Forcing by $(\mathbb{S}_{12})^2$

$$\begin{aligned} &\frac{\partial u_{i8}}{\partial x_i} = 0, \quad -\frac{\partial p_8}{\partial x_i} + \frac{\partial^2 u_{i8}}{\partial x_j^2} = Re(u_j^\dagger \frac{\partial u_i^\dagger}{\partial x_j}), \\ \text{subject to} \quad &\frac{\partial u_{18}}{\partial y} + \frac{\partial u_{28}}{\partial x} = 0 \ \text{ and } \ -p_8 + 2\frac{\partial u_{28}}{\partial y} = 0 \quad \text{at} \quad y_\infty. \end{aligned} \tag{2.50}$$

The numerical solutions of the systems are computed above at $\mathcal{O}(\epsilon^2)$ and the non-trivial results of interest obtained using $y_\infty = 5$ are:

$$\begin{aligned} \rho^x &:= u_{11}(x,5) = 218.21, \\ p_{12} &:= \frac{1}{Re}u_{71}(x,5) = -43.64, \\ p_{21} &:= u_{22}(x,5) = -43.64. \end{aligned}$$

Table 2.2: Variation of higher-order coefficients with $\bar{y}$.

$\bar{y}$	4	5	6	7	8	9
ρ^x	113.01	218.21	374.18	590.94	878.47	1246.77
$p_{12} = p_{21}$	-22.60	-43.64	-74.84	-118.19	-175.69	-249.36

With the coefficients in hands, the microscopic second order terms evaluated in $y_\infty = \bar{y} = 5$ finally is

$$u^{(2)} = \rho^x \frac{\partial^2 \mathbb{S}_{12}}{\partial X^2} + Re\, p_{12} \frac{\partial \mathbb{S}_{12}}{\partial t}, \tag{2.51}$$

$$v^{(2)} = p_{21} \frac{\partial^2 \mathbb{S}_{22}}{\partial X^2}. \tag{2.52}$$

To infer trends for the effective conditions to be applied, for example at the roughness rim, it is possible to calculate the coefficients at different values of $\bar{y} = y_\infty$. Table 2.2 summarizes the results we have computed and we have verified that they fit cubic curves to very excellent accuracy.

$$\rho^x = \frac{5}{3}(\gamma^x)^3 = \frac{5}{3}(\bar{y} + \lambda_x)^3, \tag{2.53}$$

$$p_{12} = p_{21} = -\frac{(\gamma^x)^3}{3} = -\frac{1}{3}(\bar{y} + \lambda_x)^3; \tag{2.54}$$

The coefficients to be used in the macroscopic conditions for U and V for $Y = 0$ by setting $\bar{y} = 0$, are:

$$\theta^x = \frac{5}{3}(\lambda_x)^3 = 0.00078, \tag{2.55}$$

$$q_{12} = q_{21} = -\frac{(\lambda_x)^3}{3} = -0.00016. \tag{2.56}$$

Again it is important to stress that the choice $\bar{y} = 0$ is just one of many other possibilities. A different option is always possible for the fictitious wall for example, Lācis et al. (2020) typically set $\bar{y}$ slightly above the upper rim of the roughness elements.

2.2.2. The Effect of Two-Dimensional Wall Conditions

The matching interface conditions for two-dimensional micro-indentations are:

$$U(X, 0, t) = \epsilon \lambda_x S_{12} + \epsilon^2 m_{12} \frac{\partial S_{22}}{\partial X} + \epsilon^3 \left[\theta^x \frac{\partial^2 S_{12}}{\partial X^2} + Re\, q_{12} \frac{\partial S_{22}}{\partial t} \right] + \mathcal{O}(\epsilon^4), \tag{2.57}$$

$$V(X, 0, t) = \epsilon^2 m_{21} \frac{\partial S_{12}}{\partial X} + \epsilon^3 q_{21} \frac{\partial^2 S_{22}}{\partial X^2} + \mathcal{O}(\epsilon^4). \tag{2.58}$$

In other words, the X-velocity component at the fictitious $Y = 0$ wall is $\mathcal{O}(\epsilon)$ and the Y-velocity component is $\mathcal{O}(\epsilon^2)$. Note that $m_{12} = -m_{21} > 0$ and $q_{12} = q_{21} < 0$.

The shear stress at $Y = 0$ is observed as

$$S_{12} = \frac{\epsilon^{-1}}{\lambda_x} U(X, 0, t) + \mathcal{O}(\epsilon), \tag{2.59}$$

and using continuity, we can write the leading term of the transpiration velocity in $Y = 0$ as

$$V(X, 0, t) \approx -\epsilon \lambda_y \frac{\partial U}{\partial X}, \tag{2.60}$$

where

$$\lambda_y = m_{12}/\lambda_x, \tag{2.61}$$

a (positive) *transpiration length*, as Gómez-de Segura et al. (2018) postulated. It's $\lambda_y \approx .0.0747$ with the geometry considered here. By writing out the traction components, it is possible to write the effective rough-wall conditions (up to second order) as:

$$U(X, 0, t) \approx \underbrace{\epsilon \lambda_x \frac{\partial U}{\partial Y}} - \epsilon^2 m_{12} Re \, \frac{\partial P}{\partial X} + \epsilon^2 \left(2\, m_{12} + \lambda_x \lambda_y\right) \frac{\partial^2 V}{\partial X \partial Y}, \tag{2.62}$$

$$V(X, 0, t) \approx \underbrace{\epsilon \lambda_y \frac{\partial V}{\partial Y}}. \tag{2.63}$$

The underbraces terms in (2.62-2.63) refer to those previously used by Bottaro (2019) and Lācis et al. (2020) for the purpose of assessing the effect of wall transpiration in the case of turbulent flow in a regularly corrugated channel. However all of the terms $\mathcal{O}(\epsilon^2)$ in equation (2.62) should be included to be formally correct. Equation (2.63) states that in $Y = 0$, blowing and suction occur through the fictitious wall and that the location where the vertical velocity vanishes is a *penetration distance* equal to about $\epsilon\lambda_y$ below $Y = 0$. Also note that if the rough surface is impermeable, the V integral must vanish over the whole $Y = 0$ plane.

2.2.3. Three-Dimensional Wall Conditions: Flow over a Rough Wall

A regularly three-dimensional microstructured rough wall is considered in this section. The micro and macroscopic dimensional coordinates $x_i = (x_1, x_2, x_3) = (x, y, z)$ and $X_i = (X_1, X_2, X_3) = (X, Y, Z)$, y and Y being orthogonal to the mean surface plane. These independent variables have been scaled similarly to what was proposed in the two-dimensional case. A unit cell is defined in a box which extends from $y = y_{wall}(x, z)$ to $y \to \infty$; along the wall parallel directions, it is assumed that the representative roughness element (in this case cone and cylinder) is contained in a rectangular box, with periodic

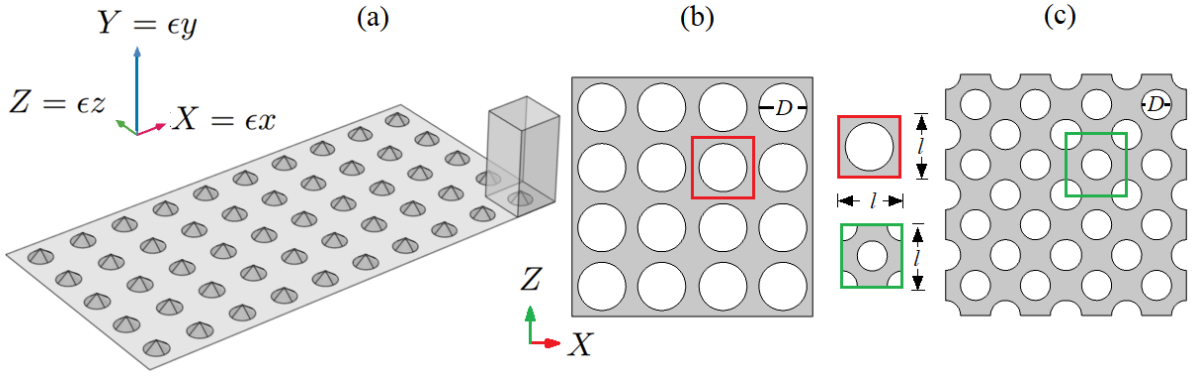

Figure 2.9: (a) Sketch of the conical microstructured surface with a unit cell (three-dimensional box on the right corner); (b) Two-dimensional view of the inline arrangement of cones; (c) Two-dimensional view of staggered arrangement of cones with the framework of the unit cells of each arrangement.

conditions which apply along x and z. All microscopic coordinates x_i have been normalized with microscopic length scale l and are thus dimensionless. The dependent variables are expanded in power series of the small parameter $\epsilon = l/L$, and following a similar pattern defined in a two-dimensional case.

The whole physical domain is divided into two regions; the inner and outer one, where the inner region goes from the wall to $y \to \infty$ whereas the outer region sits above, i.e., it goes from $Y = 0^+$ to $Y = Y_{max}$ with Y_{max} a function of the problem considered. In the inner and outer region, the dimensionless equations are the same as described previously. The component of outer forcing term S_i2 in this case are;

$$S_{12} = \frac{\partial U}{\partial Y} + \frac{\partial V}{\partial X}, \quad S_{22} = -Re\, P + 2\frac{\partial V}{\partial Y}, \quad S_{32} = \frac{\partial W}{\partial Y} + \frac{\partial V}{\partial Z}, \tag{2.64}$$

If we plug the series of ϵ in the inner flow equation, we obtain a homogeneous Stokes system for the leading order variables (just like in the two-dimensional settings of the so called alternative approach), subject to the boundary condition at y_∞:

$\mathrm{O}(\epsilon^0)$

$$\frac{\partial u^{(0)}}{\partial y} + \frac{\partial v^{(0)}}{\partial x} = S_{12}, \quad \frac{\partial w^{(0)}}{\partial y} + \frac{\partial v^{(0)}}{\partial z} = S_{32}, \quad -p^o + 2\frac{\partial v^{(0)}}{\partial y} = S_{22}, \tag{2.65}$$

assuming that the outer traction acts on the field at leading order. On account of linearity, as a consequence, the following assumptions for unknowns can be set:

$$u_i^{(0)} = u_i^{\dagger} S_{12} + u_i^{\ddagger} S_{32}, \quad p^{(0)} = p^{\dagger} S_{12} + p^{\ddagger} S_{32} - S_{22}. \tag{2.66}$$

After substituting this solution into the Stokes system of leading order and in associated boundary conditions, the following systems are obtained:

System 13: Forcing by S_{12}

$$\begin{aligned} &\frac{\partial u_i^\dagger}{\partial x_i} = 0, \quad -\frac{\partial p^\dagger}{\partial x_i} + \frac{\partial^2 u_i^\dagger}{\partial x_j^2} = 0, \\ \text{subject to} \quad &\frac{\partial u^\dagger}{\partial y} + \frac{\partial v^\dagger}{\partial x} = 1, \quad \frac{\partial w^\dagger}{\partial y} + \frac{\partial v^\dagger}{\partial z} = 0 \ \text{ and } \ -p^\dagger + 2\frac{\partial v^\dagger}{\partial y} = 0 \text{ at } y_\infty, \end{aligned} \tag{2.67}$$

together with $u_i^\dagger = 0$ at $y = y_{wall}$.

System 14: Forcing by S_{12}

$$\begin{aligned} &\frac{\partial u_i^\ddagger}{\partial x_i} = 0, \quad -\frac{\partial p^\ddagger}{\partial x_i} + \frac{\partial^2 u_i^\ddagger}{\partial x_j^2} = 0, \\ \text{subject to} \quad &\frac{\partial u^\ddagger}{\partial y} + \frac{\partial v^\ddagger}{\partial x} = 0, \quad \frac{\partial w^\ddagger}{\partial y} + \frac{\partial v^\ddagger}{\partial z} = 1 \ \text{ and } \ -p_2^\ddagger + 2\frac{\partial v_2^\ddagger}{\partial y} = 0 \text{ at } y_\infty, \end{aligned} \tag{2.68}$$

together with $u_i^\dagger = 0$ at $y = y_{wall}$. As far as normal stress force S_{22} is concerned, this has already been accounted for by expressing $p^{(0)}$ as given in (2.66).
The system of order one is:
$\mathcal{O}(\epsilon^1)$

$$\begin{aligned} &\frac{\partial u_i^{(1)}}{\partial x_i} = -\frac{\partial u_i^{(0)}}{\partial X_i}, \quad -\frac{\partial p^{\dagger(1)}}{\partial x_i} + \frac{\partial^2 u_i^{\dagger(1)}}{\partial x_j^2} = \frac{\partial p^{(0)}}{\partial X_i} - 2\frac{\partial^2 u_i^{(0)}}{\partial x_j \partial X_j}, \\ \text{subject to} \quad &-p^{(1)}\delta_{i2} + \frac{\partial v^{(1)}}{\partial x_i} + \frac{\partial u_i^{(1)}}{\partial y} = -\frac{\partial v^{(0)}}{\partial X_i} - \frac{\partial u_i^{(0)}}{\partial Y} \text{ at } y_\infty. \end{aligned} \tag{2.69}$$

By using a solution of order zero system, the system of order one becomes:

$$\begin{aligned} &\frac{\partial u_i^{(1)}}{\partial x_i} = -u_i^\dagger \frac{\partial S_{12}}{\partial X_i} - u_i^\ddagger \frac{\partial S_{32}}{\partial X_i}, \\ &-\frac{\partial p^{(1)}}{\partial x_i} + \frac{\partial^2 u_i^{(1)}}{\partial x_j^2} = p^\dagger \frac{\partial S_{12}}{\partial X_j}\delta_{ij} + p^\ddagger \frac{\partial S_{32}}{\partial X_j}\delta_{ij} - \frac{\partial S_{22}}{\partial X_j}\delta_{ij} - 2\frac{\partial u_i^\dagger}{\partial x_j}\frac{\partial S_{12}}{\partial X_j} - 2\frac{\partial u_i^\ddagger}{\partial x_j}\frac{\partial S_{32}}{\partial X_j}, \\ \text{subject to} \quad &-p^{(1)}\delta_{i2} + \frac{\partial v^{(1)}}{\partial x_i} + \frac{\partial u_i^{(1)}}{\partial y} = -v^\dagger \frac{\partial S_{12}}{\partial X_i} - v^\ddagger \frac{\partial S_{12}}{\partial X_i} - u_i^\dagger \frac{\partial S_{12}}{\partial Y} - u_i \frac{\partial S_{32}}{\partial Y} \text{ at } y_\infty, \end{aligned} \tag{2.70}$$

together with periodicity in x and z and no-slip at the wall.
The linear system (2.70) admits a solution in the form:

$$u_i^{(1)} = \hat{u}_{ij}\frac{\partial S_{12}}{\partial X_j} + \tilde{u}_{ij}\frac{\partial S_{32}}{\partial X_j} + \breve{u}_{ij}\frac{\partial S_{22}}{\partial X_j}, \quad p^{(1)} = \hat{p}_j\frac{\partial S_{12}}{\partial X_j} + \tilde{p}_j\frac{\partial S_{32}}{\partial X_j} + \breve{p}_j\frac{\partial S_{22}}{\partial X_j} \tag{2.71}$$

Three sets of problems arise if we substitute the above solution in the system of order one.

System 15: Forcing by gradient of S_{12}

$$\begin{aligned} &\frac{\partial \hat{u}_{ij}}{\partial x_i} = -u_j^{\dagger}, -\frac{\partial \hat{p}_j}{\partial x_i} + \frac{\partial^2 \hat{u}_{ij}}{\partial x_k^2} = p^{\dagger}\delta_{ij} - 2\frac{\partial u_j^{\dagger}}{\partial x_j}, \\ \text{subject to} \quad &- \hat{p}_j\delta_{i2} + \frac{\partial \hat{u}_{2j}}{\partial x_i} + \frac{\partial \hat{u}_{ij}}{\partial y} = -v^{\dagger}\delta_{ij} - u_j^{\dagger}\delta_{i2} \quad \text{at} \quad y_{\infty}. \end{aligned} \tag{2.72}$$

System 16: Forcing by gradient of S_{32}

$$\begin{aligned} &\frac{\partial \tilde{u}_{ij}}{\partial x_i} = -u_j^{\ddagger}, -\frac{\partial \tilde{p}_j}{\partial x_i} + \frac{\partial^2 \tilde{u}_{ij}}{\partial x_k^2} = p^{\ddagger}\delta_{ij} - 2\frac{\partial u_j^{\ddagger}}{\partial x_j}, \\ \text{subject to} \quad &- \tilde{p}_j\delta_{i2} + \frac{\partial \tilde{u}_{2j}}{\partial x_i} + \frac{\partial \tilde{u}_{ij}}{\partial y} = -v^{\ddagger}\delta_{ij} - u_j^{\ddagger}\delta_{i2} \quad \text{at} \quad y_{\infty}. \end{aligned} \tag{2.73}$$

System 17: Forcing by gradient of S_{22}

$$\begin{aligned} &\frac{\partial \breve{u}_{ij}}{\partial x_i} = 0, -\frac{\partial \breve{p}_j}{\partial x_i} + \frac{\partial^2 \breve{u}_{ij}}{\partial x_k^2} = -\delta_{ij}, \\ \text{subject to} \quad &- \breve{p}_j\delta_{i2} + \frac{\partial \breve{u}_{2j}}{\partial x_i} + \frac{\partial \breve{u}_{ij}}{\partial y} = 0 \quad \text{at} \quad y_{\infty}. \end{aligned} \tag{2.74}$$

The other boundary conditions for $\hat{\bullet}$, $\tilde{\bullet}$ and $\breve{\bullet}$ variables stem simply from no-slip at y_{wall} and periodicity along spatial direction. After solving microscopic, Stokes-like problems, the solution can easily be assembled to yield an effective condition for the macroscopic problem at $Y = \epsilon y_{\infty}$ (like in the case of a two-dimensional problem). This condition can be easily transferred into a plane positioned at $Y = 0$ (tangent to the rim of roughness). This condition will turn out to be an extended Navier slip condition, including at higher-order a blowing/suction term.

The case considered here is conical roughness (it is clear that cones are isotropic embedded in the $(x, z)-$plane) where the cone's rim is at $y = 0$. The reason of this conical shape type roughness is; it is simple isotropic shape to test the functionality and the accuracy of our high-order effective boundary conditions developed for three-dimensional rough walls. All equations at order zero and one have been solved numerically by the use of COMSOL Multiphysics (ww.comsol.com). The solutions of the system of variables $\bullet^{\dagger}$, $\hat{\bullet}$, $\tilde{\bullet}$ and $\breve{\bullet}$ in tabular form are given in table 2.4. Where the parameters of interest $n_{21} = \int_0^1 \int_0^1 \hat{u}_{12}\, dzdx$, $n_{12} = \int_0^1 \int_0^1 \breve{u}_{11}\, dzdx$ and $u^{\dagger}(= \lambda_x + y_{\infty})$ are listed as function of y_{∞} and H/D. All other coefficients which are not reported in the table simply vanish or behave symmetric about vertical mid plane located at (x, y) (or (z, y))-plane.

Table 2.3 shows the variation of parameters against y_{∞} and for each H/D. All the data matches well with either a straight line or a parabola (like in the previous two-dimensional case), so the results can easily be extrapolated to any desired location of $\bar{y}$ where we want to compare internal and external solutions.

2.2.4. Fixing the Boundary Conditions at the Fictitious Wall

The dimensionless effective boundary conditions for the outer flow to be enforced on the plane of the roughness element's crest, which is assumed to be $Y = 0$ are:

$$U(X,0,t) = \epsilon\lambda_x S_{12} + \epsilon^2 m_{12} S_{22_X} + \mathcal{O}(\epsilon^3), \tag{2.75}$$

$$V(X,0,t) = \epsilon^2 m_{21} S_{12_X} + m_{23} S_{32_Z} + \mathcal{O}(\epsilon^3), \tag{2.76}$$

$$W(X,0,t) = \epsilon\lambda^z S_{32} + \epsilon^2 m_{32} S_{22_Z} + \mathcal{O}(\epsilon^3). \tag{2.77}$$

For the isotropic roughness indentations, the conditions further simplify by replacing $\lambda_x = \lambda^z = \lambda$ and $m_{21} = m_{12} = m_{23} = m_{32}$. It should be noted that, since the transpiration velocity V is of order two in the small parameter ϵ, equations (2.75)-(2.77) can be re-written to the same formal order of accuracy, as follows:

$$U(X,0,t) = \epsilon\lambda \frac{\partial U}{\partial Y} + \epsilon^2 m_{12} Re \frac{\partial P}{\partial X} + \mathcal{O}(\epsilon^3), \tag{2.78}$$

$$V(X,0,t) = \epsilon^2 m_{12} \frac{\partial^2 V}{\partial Y^2} + \mathcal{O}(\epsilon^3), \tag{2.79}$$

$$W(X,0,t) = \epsilon\lambda \frac{\partial W}{\partial Y} + \epsilon^2 m_{12} Re \frac{\partial P}{\partial Z} + \mathcal{O}(\epsilon^3). \tag{2.80}$$

From these it is easy to see that at the virtual wall it is;

$$\frac{\partial U}{\partial X} + \frac{\partial W}{\partial Z} = -\frac{\partial V}{\partial Y} = \epsilon\lambda \left[\frac{\partial^2 U}{\partial X \partial Y} + \frac{\partial^2 W}{\partial Z \partial Y} \right] + \mathcal{O}(\epsilon^2), \tag{2.81}$$

and thus

$$-\frac{\partial V}{\partial Y} = -\epsilon\lambda \frac{\partial^2 V}{\partial Y^2} + \mathcal{O}(\epsilon^2). \tag{2.82}$$

After further simplifying it, we have

$$\frac{\partial^2 V}{\partial Y^2} = \frac{1}{\epsilon\lambda} \frac{\partial V}{\partial Y} + \mathcal{O}(\epsilon), \tag{2.83}$$

and inserting into the condition for V on $Y = 0$ we end up with

$$V = \epsilon^2 \frac{m_{12}}{\epsilon\lambda} \frac{\partial V}{\partial Y} + \mathcal{O}(\epsilon^3). \tag{2.84}$$

Note that the above replacement is valid only for isotropic roughness. Finally the three dimensional boundary conditions at the fictitious wall in $Y = 0$ read:

$$U = \epsilon\lambda \frac{\partial U}{\partial Y} + \epsilon^2 m_{12} Re \frac{\partial P}{\partial X} + \mathcal{O}(\epsilon^3), \tag{2.85}$$

Table 2.3: Variation of coefficients with respect to the height of cone

	inline		
H/D	0.1	0.2	0.4
λ	0.05058	0.09694	0.17370
m_{12}	0.00115	0.00426	0.01400

	staggered		
H/D	0.1	0.2	0.4
λ	0.03878	0.07359	0.12857
m_{12}	0.00056	0.00184	0.00675

$$V = \epsilon\lambda_y \frac{\partial V}{\partial Y} + \mathcal{O}(\epsilon^3), \tag{2.86}$$

$$W = \epsilon\lambda \frac{\partial W}{\partial Y} + \epsilon^2 m_{12} Re \frac{\partial P}{\partial Z} + \mathcal{O}(\epsilon^3), \tag{2.87}$$

with λ_y the penetration distance of the vertical velocity, defined as $\lambda_y = \dfrac{m_{12}}{\lambda}$: it is the distance below the virtual wall where the vertical velocity, extrapolated to negative values of Y , goes to zero. It is convenient to express the boundary conditions along Y in this form since, numerically, the evaluation of the second derivative $\dfrac{\partial^2 V}{\partial Y^2}$ in $Y = 0$ can lead to numerical stability errors. The coefficient m_{12} can be obtained in a same way as done in two dimensional case and are given below.

Table 2.4: Microscopic variables evaluated at y_∞ for different heights of cone H/D (where D is the diameter of the cone).

	In-line			
H/D	y_∞	$u^\dagger = w^\ddagger$	$-\hat{u}_{21} = \breve{u}_{11} = -\tilde{u}_{23} = \breve{u}_{33}$	$\hat{u}_{12} = \tilde{u}_{32}$
0.1	2	2.05058	2.10186	4.20469
0.1	3	3.05058	4.65207	9.30574
0.1	4	4.05058	8.20205	16.40689
0.2	2	2.09694	2.19807	4.39659
0.2	3	3.09694	4.79443	9.59012
0.2	4	4.09694	8.39093	16.78376
0.4	2	2.17370	2.36403	4.72372
0.4	3	3.17372	5.03585	10.07083
0.4	4	4.17369	8.70918	17.41604
	Staggered			
0.1	2	2.03879	2.07840	4.15634
0.1	3	3.03877	4.61713	9.23379
0.1	4	4.03882	8.15610	16.31124
0.2	2	2.07361	2.15023	4.29820
0.2	3	3.07356	4.72368	9.44536
0.2	4	4.07355	8.29722	16.59212
0.4	2	2.12890	2.26768	4.52829
0.4	3	3.12891	4.89659	9.23377
0.4	4	4.12880	8.52505	17.04304

2.3. Mathematical Formulation of the Interface Conditions: Flow over Porous Media

In the case of isotropic solid grains, the study to be pursued relies on the separation of scales; this means that the inter-grain distance must be much smaller than the characteristic length scale of the macroscopic flow in the free-fluid region. Thus, the entire domain is divided into three portions: the outer (free-fluid part denoted by the $^+$ superscript), the intermediate (thin interfacial region), and the third part as porous region ($^-$ superscript, where Darcy's equation governs fluid motion). The asymptotic analysis is described in the subsequent section, and the conditions which hold at a porous-fluid interface, whose position must be set, are derived thoroughly. All the coefficients of these conditions are computed and reported in tabular form for possible future use.

A regularly microstructured porous medium is taken to bound a free-fluid region; for reasons of clarity we limit the present analysis to two-dimensional Cartesian coordinates. The porous medium has a characteristic microscopic length scale equal to l (say, the periodicity of the pattern); the macroscopic length scale is L (for example, the channel

half-thickness). With reference to figure 2.10, the dividing surface where outer flow conditions will be enforced is arbitrarily positioned in $\hat{y} = 0$, with hat variables denoting dimensional quantities. Other choices are possible for the position, close to $\hat{y} = 0$, where interface conditions can be enforced, but the results are very weakly dependent on the choice made (for a discussion on this issue, see Lācis and Bagheri (2017); Lācis et al. (2020)). The presence of two characteristic scales renders the problem amenable to a multiple scale expansion, in terms of the small parameter $\epsilon = l/L$, along the lines of Mei and Vernescu Mei and Vernescu (2009).

2.3.1. Scalings and Equations in the Three Regions

Three regions can be identified, and will be normalized successively, starting from the outer one (+, or free-fluid region) up to the inner one (−, or porous region).
In the free-fluid, we use $L, L/\mathcal{U}, \mathcal{U}$, and $\rho\mathcal{U}^2$ to scale, respectively, length, time, velocity and pressure. The velocity $\mathcal{U}$ is a characteristic speed, for example, the free stream velocity in a boundary layer, and ρ is the fluid density. The dimensionless system in the + region is simply

$$\frac{\partial U_i^+}{\partial X_i} = 0, \quad \frac{\partial U_i^+}{\partial t} + U_j^+ \frac{\partial U_i^+}{\partial X_j} = -\frac{\partial P^+}{\partial X_i} + \frac{1}{Re}\frac{\partial^2 U_i^+}{\partial X_j^2}. \tag{2.88}$$

We define $X_1 = X = \hat{x}/L$, $X_2 = Y = \hat{y}/L$, $U_1^+ = U^+ = \hat{u}/\mathcal{U}$, and $U_2^+ = V^+ = \hat{v}/\mathcal{U}$; the macroscopic Reynolds number is $Re = \rho\mathcal{U}\,L/\mu$. Notice that all dependent variables in this upper region depend only upon the macroscale spatial coordinates. The intermediate region, across the dividing line/surface, is denoted by the superscript =; here we choose $l = \epsilon\,L, L/\mathcal{U}$, $\epsilon\mathcal{U}$, and $\mu\mathcal{U}/L$ to normalize, respectively, length, time, velocity and pressure. These are the same scales used in countless papers to model the flow over a textured wall wall (Bottaro and Naqvi (2020), Airiau and Bottaro (2020), and section 2.2.). The dimensionless equations in the y-elongated microscopic cell which traverses $y = 0$ are

$$\frac{\partial U_i^=}{\partial x_i} = 0, \quad \epsilon^2 Re\left(\frac{\partial U_i^=}{\partial t} + U_j^= \frac{\partial U_i^=}{\partial x_j}\right) = -\frac{\partial P^=}{\partial x_i} + \frac{\partial^2 U_i^=}{\partial x_j^2}, \tag{2.89}$$

with $x_1 = x = \hat{x}/l$, $x_2 = y = \hat{y}/l$, $U_1^= = U^= = \epsilon^{-1}\hat{u}/\mathcal{U}$, and $U_2^= = V^= = \epsilon^{-1}\hat{v}/\mathcal{U}$. All dependent variables are assumed to be periodic along x (and along z when in three-dimensions); around the dividing line/surface they are function of both microscale and macroscale coordinates and the latter dependence is immediately apparent upon matching velocity and traction vectors at the upper boundary of the = region, i.e.

$$\lim_{y\to+\infty}(U^=, V^=) = \frac{1}{\epsilon}\lim_{Y\to 0^+}(U^+, V^+) \tag{2.90}$$

and

$$\lim_{y\to+\infty}\left(\frac{\partial U^=}{\partial y} + \frac{\partial V^=}{\partial x}, -P^= + 2\frac{\partial V^=}{\partial y}\right) = \lim_{Y\to 0^+}\left(\frac{\partial U^+}{\partial Y} + \frac{\partial V^+}{\partial X}, -Re\,P^+ + 2\frac{\partial V^+}{\partial Y}\right). \tag{2.91}$$

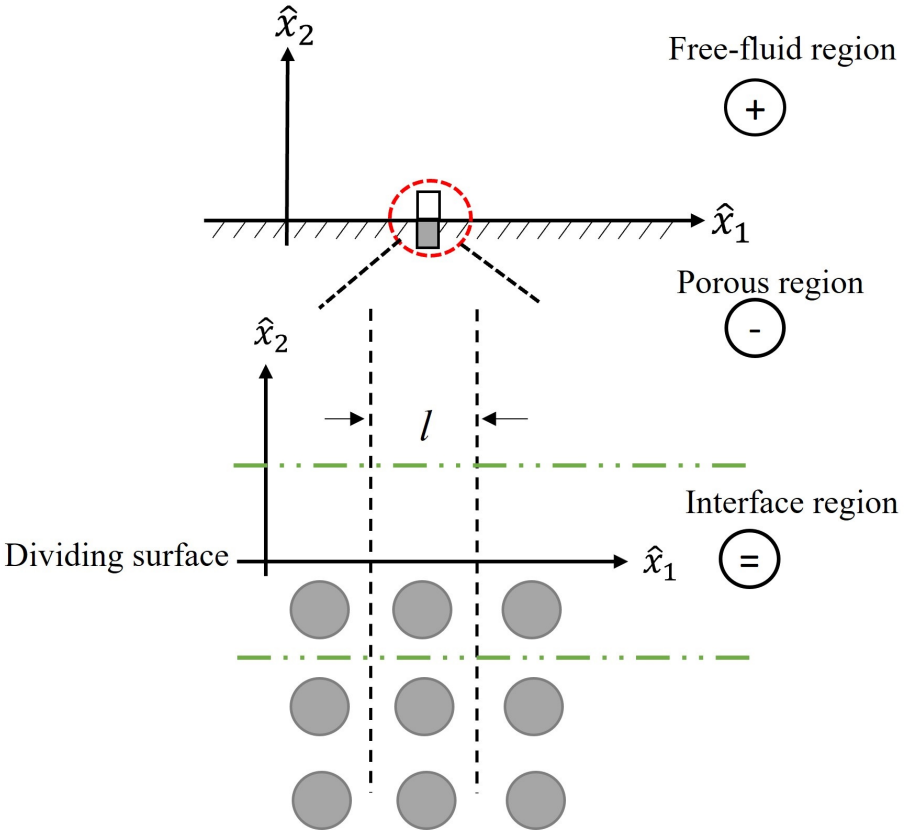

Figure 2.10: Two-dimensional macroscopic domain together with microscopic cell (enclosed in red circle). The latter is shown in its dimensional settings right below.

The flow in the lower $(-)$ inter-pore space, sufficiently below the dividing line/surface, is assumed steady and the equations are rendered dimensionless by the same scales as in the interface region, except for replacing $\epsilon\mathcal{U}$ by $\epsilon^2\mathcal{U}$ when normalizing the velocity. This choice of scales stems from assuming that the macroscopic pressure gradient is balanced by viscous dissipation within the pores (Mei and Vernescu, 2009). Eventually, in a square unit cell within the porous medium and away from boundaries we should solve

$$\epsilon \frac{\partial U_i^-}{\partial x_i} = 0, \quad \epsilon^4 Re\, U_j^- \frac{\partial U_i^-}{\partial x_j} = -\frac{\partial P^-}{\partial x_i} + \epsilon \frac{\partial^2 U_i^-}{\partial x_j^2}, \tag{2.92}$$

subject to periodicity along all spatial directions. This latter system leads to Darcy's equation, after the variables are expanded in power series of ϵ, and the leading order terms are retained. The procedure is described in details by Mei and Vernescu (2009); we will not carry it out here, but will develop a composite system valid across the dividing line/surface and below.

2.3.2. The *Composite* Description

Here we couple the three regions identified above. Assuming that $\epsilon^2 Re \ll 1$, the leading order system in the intermediate domain turns out to be simply Stokes' system. This stems from expanding the generic = variable as

$$F^{=}(x_i, X_i, t) = F_0^{=} + \epsilon\, F_1^{=} + \epsilon^2\, F_2^{=} + ... \tag{2.93}$$

and substituting the expansion into system (2.89). Since each dependent variable is function of both microscopic and macroscopic coordinates, it is important also to replace

$$\frac{\partial}{\partial x_j} \to \frac{\partial}{\partial x_j} + \epsilon \frac{\partial}{\partial X_j}, \tag{2.94}$$

to obtain

$$\mathcal{O}(\epsilon^0): \qquad \frac{\partial U_{0_i}^{=}}{\partial x_i} = 0, \qquad -\frac{\partial P_0^{=}}{\partial x_i} + \frac{\partial^2 U_{0_i}^{=}}{\partial x_j^2} = 0, \tag{2.95}$$

$$\mathcal{O}(\epsilon^1): \quad \frac{\partial U_{1_i}^{=}}{\partial x_i} = -\frac{\partial U_{0_i}^{=}}{\partial X_i}, \qquad -\frac{\partial P_1^{=}}{\partial x_i} + \frac{\partial^2 U_{1_i}^{=}}{\partial x_j^2} = \frac{\partial P_0^{=}}{\partial X_i} - 2\frac{\partial^2 U_{0_i}^{=}}{\partial x_j \partial X_j}. \tag{2.96}$$

In the $-$ region each generic F^{-} variable is expanded as

$$F^{-}(x_i, X_i) = F_0^{-} + \epsilon\, F_1^{-} + \epsilon^2\, F_2^{-} + ... \tag{2.97}$$

and the expansions are substitute into system (2.92), to obtain

$$\mathcal{O}(\epsilon^0): \qquad \frac{\partial P_0^{-}}{\partial x_i} = 0, \tag{2.98}$$

$$\mathcal{O}(\epsilon^1): \qquad \frac{\partial U_{0_i}^{-}}{\partial x_i} = 0, \qquad -\frac{\partial P_1^{-}}{\partial x_i} + \frac{\partial^2 U_{0_i}^{-}}{\partial x_j^2} = \frac{\partial P_0^{-}}{\partial X_i}, \tag{2.99}$$

$$\mathcal{O}(\epsilon^2): \quad \frac{\partial U_{1_i}^{-}}{\partial x_i} = -\frac{\partial U_{0_i}^{-}}{\partial X_i}, \qquad -\frac{\partial P_2^{-}}{\partial x_i} + \frac{\partial^2 U_{1_i}^{-}}{\partial x_j^2} = \frac{\partial P_1^{-}}{\partial X_i} - 2\frac{\partial^2 U_{0_i}^{-}}{\partial x_j \partial X_j}. \tag{2.100}$$

It is a well-established fact that the pressure at leading order in the porous matrix, P_0^{-}, does not fluctuate on the pore scale (cf. equation 2.98), Naqvi and Bottaro (2021).
We now define the *composite* velocity and pressure fields

$$u_i = u_i^{(0)} + \epsilon\, u_i^{(1)} + \mathcal{O}(\epsilon^2), \tag{2.101}$$

$$p = p^{(0)} + \epsilon\, p^{(1)} + \mathcal{O}(\epsilon^2), \tag{2.102}$$

with

$$u_i^{(0)} = \begin{cases} U_{0_i}^{=} & y > 0, \\ \epsilon\, U_{0_i}^{-} & y < 0, \end{cases} \tag{2.103}$$

$$p^{(0)} = \begin{cases} P_0^{=} & y > 0, \\ P_0^{-} + \epsilon\, P_1^{-} & y < 0, \end{cases} \tag{2.104}$$

and

$$u_i^{(1)} = \begin{cases} U_{1_i}^{=} & y > 0, \\ \epsilon\, U_{1_i}^{-} & y < 0, \end{cases} \tag{2.105}$$

$$p^{(1)} = \begin{cases} P_1^{=} & y > 0, \\ \epsilon\, P_2^{-} & y < 0. \end{cases} \tag{2.106}$$

The Ansatz above implies that an abrupt transition is assumed between the $=$ and $-$ regions; this corresponds to what is referred to in the literature as the *two-domain approach*, leading to a jump in pressure across $y = 0$. The leading-order composite equations, valid in a neighborhood of $y = 0$ as well as throughout the porous medium, are

$$\frac{\partial u_i^{(0)}}{\partial x_i} = 0, \quad -\frac{\partial p^{(0)}}{\partial x_i} + \frac{\partial^2 u_i^{(0)}}{\partial x_j^2} = 0, \tag{2.107}$$

and at next order we have

$$\frac{\partial u_i^{(1)}}{\partial x_i} = -\frac{\partial u_i^{(0)}}{\partial X_i} \qquad -\frac{\partial p^{(1)}}{\partial x_i} + \frac{\partial^2 u_i^{(1)}}{\partial x_j^2} = \frac{\partial p^{(0)}}{\partial X_i} - 2\,\frac{\partial^2 u_i^{(0)}}{\partial x_j \partial X_j}. \tag{2.108}$$

The situation is schematized in figure 2.11.
For $y \to -\infty$ (i.e. sufficiently deep inside the porous medium) the solution of system (2.92) in a 1×1 periodic unit cell, eventually leading to the medium permeability, should be recovered. On the top boundary of the interface cell the matching outer-flow conditions (2.90) and (2.91) are

$$\lim_{y \to +\infty} (u, v) = \frac{1}{\epsilon} \lim_{Y \to 0^+} (U, V), \tag{2.109}$$

$$\lim_{y \to +\infty} \left(\frac{\partial u}{\partial y} + \frac{\partial v}{\partial x}, -p + 2\frac{\partial v}{\partial y} \right) = \lim_{Y \to 0^+} \left(\frac{\partial U}{\partial Y} + \frac{\partial V}{\partial X}, -Re\, P + 2\frac{\partial V}{\partial Y} \right). \tag{2.110}$$

Note that from now on we omit the $+$ superscript when referring to dependent variables in the free-fluid region. Also, to simplify notations, we will indicate with S_{12} and S_{22} the tangential and normal components of the dimensionless macroscopic stress for $Y \to 0^+$, i.e.

$$S_{12} = \frac{\partial U}{\partial Y} + \frac{\partial V}{\partial X}\bigg|_{Y \to 0^+}, \quad S_{22} = -Re\, P + 2\,\frac{\partial V}{\partial Y}\bigg|_{Y \to 0^+}. \tag{2.111}$$

The boundary conditions for (2.107) at $y \to \infty$ become

$$\frac{\partial u^{(0)}}{\partial y}\bigg|_{y \to +\infty} = S_{12}, \qquad -p^{(0)}\big|_{y \to +\infty} = S_{22}, \tag{2.112}$$

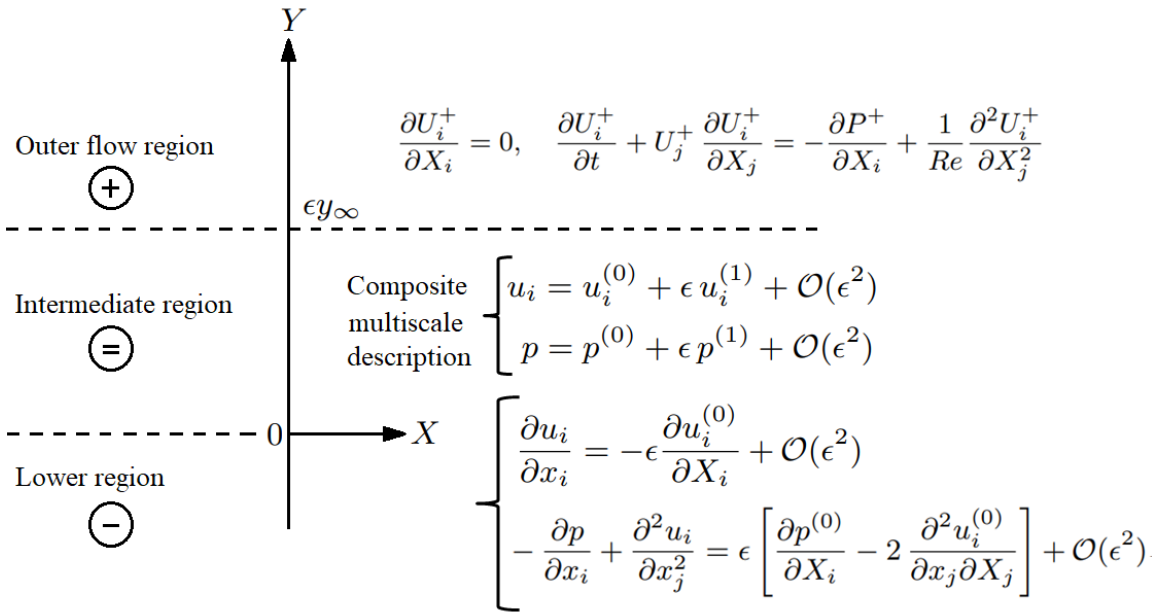

Figure 2.11: Schematic of the mathematical description of the interface problem, together with equations in the free-flow (+) region and composite, multiscale equations which apply in the = and − regions. In the numerical application, the matching between the flow in the region described by the composite equations and that in the free-fluid region is done at a finite value of y, i.e. $y = y_\infty$.

on account of the fact that on the top boundary of the interface cell, by construction, $u^{(0)} = u_1^{(0)}$, $v^{(0)} = u_2^{(0)}$, and $p^{(0)}$ loose memory of the porous matrix microstructure to become independent of x. The corresponding conditions for the variables at order ϵ are:

$$\left.\frac{\partial u^{(1)}}{\partial y}\right|_{y\to+\infty} = -\left.\frac{\partial u^{(0)}}{\partial Y}\right|_{y\to+\infty} - \left.\frac{\partial v^{(0)}}{\partial X}\right|_{y\to+\infty}, \tag{2.113}$$

$$-\left.p^{(1)}\right|_{y\to+\infty} + 2\left.\frac{\partial v^{(1)}}{\partial y}\right|_{y\to+\infty} = -2\left.\frac{\partial v^{(0)}}{\partial Y}\right|_{y\to+\infty}. \tag{2.114}$$

Sample solutions of the leading order composite system: Linearity of system (2.107) permits to express the velocity components and the pressure using separation of variables, i.e.

$$u_i^{(0)} = u_i^\dagger\, S_{12} + u_i^\ddagger\, S_{22}, \tag{2.115}$$

and

$$p^{(0)} = p^\dagger\, S_{12} + p^\ddagger\, S_{22} + C(X_j). \tag{2.116}$$

The fields $u_i^\dagger$, $p^\dagger$, $u_i^\ddagger$, and $p^\ddagger$ depend only on x_j; conversely, the *integration constant* C is only a function of macroscopic coordinates. Plugging (2.115-2.116) into (2.107) and (2.112) permits to find the two systems below, subject to periodicity along x (and

eventually z, in three-dimensional settings) and to the no-slip condition on the solid grains of the porous medium.

Forcing by S_{12}:

$$\frac{\partial u_i^\dagger}{\partial x_i} = 0, \quad -\frac{\partial p^\dagger}{\partial x_i} + \frac{\partial^2 u_i^\dagger}{\partial x_j^2} = 0, \tag{2.117}$$

$$\lim_{y\to+\infty} \frac{\partial u^\dagger}{\partial y} = 1, \quad \lim_{y\to+\infty} p^\dagger = 0. \tag{2.118}$$

Forcing by S_{22}:

$$\frac{\partial u_i^\ddagger}{\partial x_i} = 0, \quad -\frac{\partial p^\ddagger}{\partial x_i} + \frac{\partial^2 u_i^\ddagger}{\partial x_j^2} = 0, \tag{2.119}$$

$$\lim_{y\to+\infty} \frac{\partial u^\ddagger}{\partial y} = 0, \quad \lim_{y\to+\infty} p^\ddagger = -1. \tag{2.120}$$

This latter system admits the trivial solution $u_i^\ddagger = 0$ and $p^\ddagger = -1$.
Solutions of the $\bullet^\dagger$ problem are pursued for both two- and three-dimensional porous media, with either circular or spherical grains, for both in-line or regularly staggered solid inclusions, and for varying porosities. The porosity is defined as $\theta = \mathcal{V}_{fluid}/\mathcal{V}_{total}$, with $\mathcal{V}_{fluid}$ the fluid's volume in a square unit cell (in a two-dimensional case the volume is meant per unit depth) within the porous domain and $\mathcal{V}_{total}$ the corresponding total (fluid plus solid) volume. By defining the superficial (or phase) average,

$$\langle a \rangle := \frac{1}{\mathcal{V}_{total}} \int_{\mathcal{V}_{fluid}} a \, \mathrm{d}V, \tag{2.121}$$

the porosity is also $\theta = \langle 1 \rangle$. The intrinsic average can also be defined as

$$\langle a \rangle^f := \frac{1}{\mathcal{V}_{fluid}} \int_{\mathcal{V}_{fluid}} a \, \mathrm{d}V, \tag{2.122}$$

to be used later on.
Since only the gradient of $p^\dagger$ appears in equations (2.117), uniqueness of the solution is guaranteed by imposing

$$\langle p^\dagger \rangle_\infty = 0, \tag{2.123}$$

with the phase average now taken on the top 1×1 square (or cubic) cell of the elongated interfacial domain (this is indicated by the subscript ∞). This implies that

$$p^{(0)}\Big|_\infty = \langle p^{(0)} \rangle_\infty = -S_{22} + C, \tag{2.124}$$

so that by the second equation in (2.112) it is finally found

$$C = 0. \tag{2.125}$$

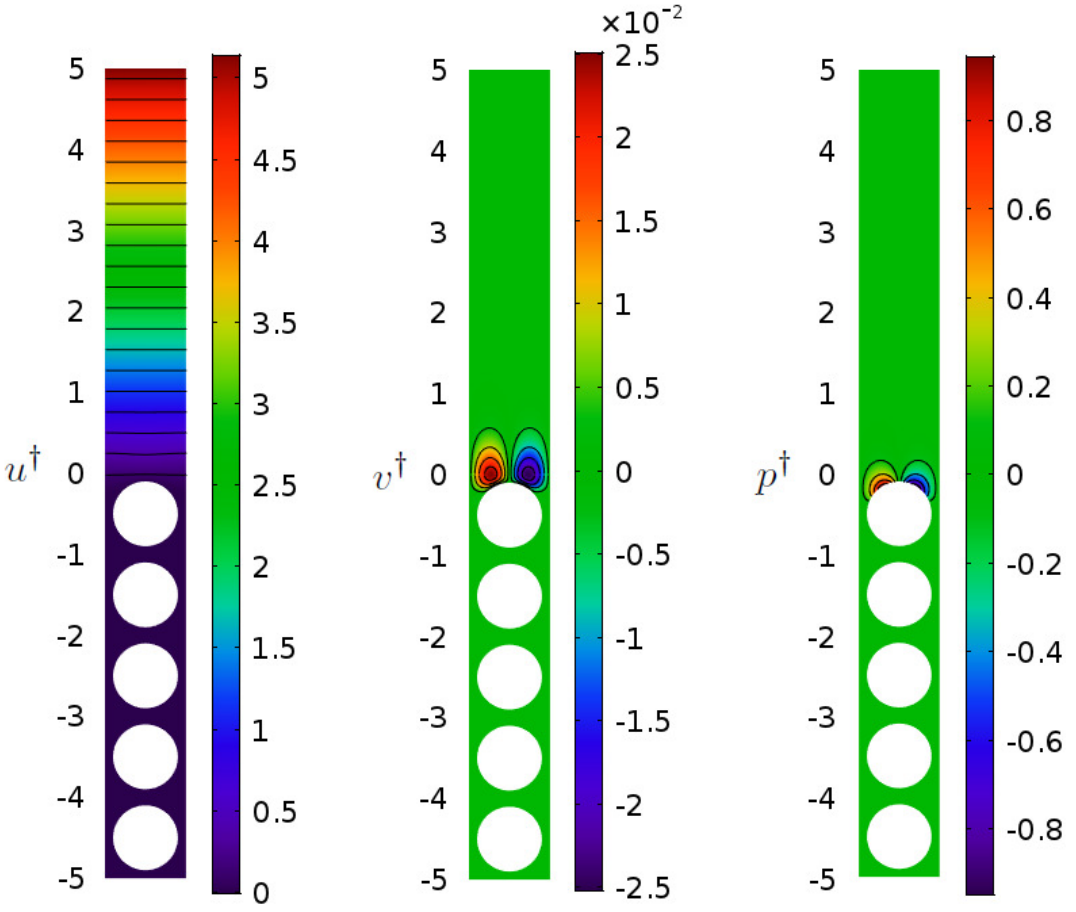

Figure 2.12: Fields of $u^\dagger$, $v^\dagger$ and $p^\dagger$ for $\theta = 0.4973$, regularly arranged two-dimensional solid grains.

Solutions of the auxiliary problem (2.117-2.118) are carried out using the finite elements method based COMSOL Multiphysics (2019) software, progressively refining the mesh until grid-converged solutions are found. Sample results are first provided below, the parametric variation is discussed later. Figures 2.12 and 2.13 display isolines of the unknowns for two values of θ in the full domain considered in the two-dimensional in-line case, domain which ranges in y from $-y_\infty = -5$ to $y_\infty = +5$. Such a vertical extent has been verified against larger values of y_∞ and it has been found to be sufficient to yield domain-independent results for all porosities tested. In particular, y_∞ must be sufficiently large for all fields computed to become homogeneous in x when $y = +y_\infty$. The larger value of the porosity considered in figure 2.13 ($\theta = 0.9999$) is not representative of a realistic porous medium, except perhaps for the case of sparse canopies and, as a consequence, it will be shown that slip velocities (at the dividing line/surface) and permeability coefficients are much larger than for lower porosities. It should also be observed that $v^\dagger$ and $p^\dagger$ are antisymmetric around a vertical mid-line (through $x = 0.5$). Thus, for isotropic grains it is $\int_0^1 v^\dagger \mathrm{d}x = 0$ at any y, and likewise for $p^\dagger$.

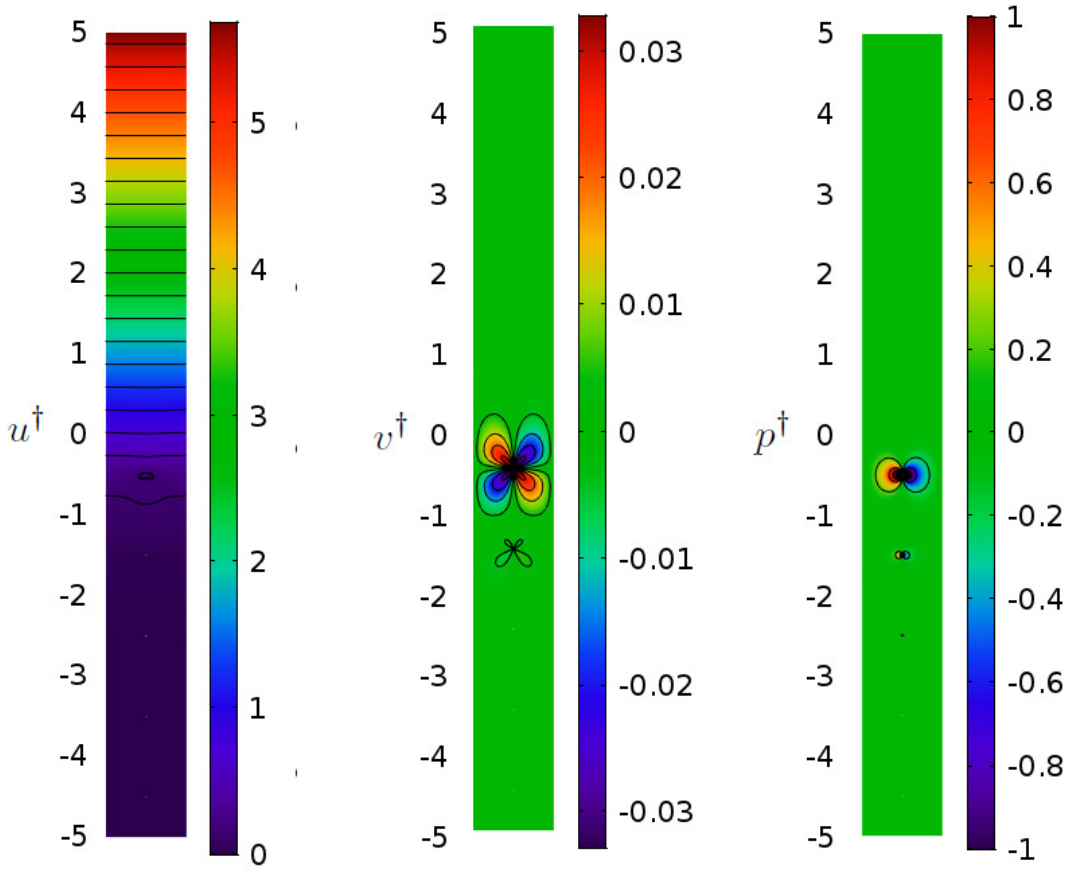

Figure 2.13: Same as figure 2.12 for $\theta = 0.9999$. The solid inclusions are so small that they are not visible on the scale of the plot.

Just like in the case of the flow over a rough wall (Bottaro and Naqvi, 2020) it is found that

$$u^\dagger|_{y_\infty} = y_\infty + \lambda, \tag{2.126}$$

with λ a slip length which, for in-line solid inclusions of $\theta = 0.4973$, is equal to 1.451×10^{-1}, while $\lambda = 6.188 \times 10^{-1}$ when the porosity is 0.9999. It is reasonable to expect the slip length (and, as a consequence, the slip velocity) to increase as the solid inclusions become of smaller dimensions. The same values of λ are recovered also by

$$\lambda = \int_0^1 u^\dagger|_{y=0} \, \mathrm{d}x. \tag{2.127}$$

As in the case of the flow past a rough solid surface (Bottaro and Naqvi, 2020), the outer flow matching

$$u|_{y=y_\infty} = (y_\infty + \lambda)\, S_{12} + \mathcal{O}(\epsilon), \qquad v|_{y=0^+} = \mathcal{O}(\epsilon). \tag{2.128}$$

can be transferred to a dividing surface in $y = 0^+$ and expressed in terms of macroscopic variables (cf. equation 2.109), for the boundary conditions of the free-fluid variables to

read:

$$U|_{Y=0^+} = \epsilon\lambda\, S_{12} + \mathcal{O}(\epsilon^2), \qquad V|_{Y=0^+} = \mathcal{O}(\epsilon^2). \tag{2.129}$$

This is a simple Navier slip condition, aside from the fact that a $\partial V/\partial X$ term appears in the condition (*via* S_{12}).

The first correction to the leading order composite description: On account of the results obtained for $u_i^{(0)}$ and $p^{(0)}$, system (2.113) equipped with boundary conditions (2.113) and (2.114) becomes

$$\frac{\partial u_i^{(1)}}{\partial x_i} = -u_i^\dagger \frac{\partial S_{12}}{\partial X_i}, \tag{2.130}$$

$$-\frac{\partial p^{(1)}}{\partial x_i} + \frac{\partial^2 u_i^{(1)}}{\partial x_j^2} = p^\dagger \frac{\partial S_{12}}{\partial X_i} - \frac{\partial S_{22}}{\partial X_i} - 2\,\frac{\partial u_i^\dagger}{\partial x_j}\frac{\partial S_{12}}{\partial X_j}, \tag{2.131}$$

together with

$$\left.\frac{\partial u^{(1)}}{\partial y}\right|_{y\to\infty} = -u^\dagger \frac{\partial S_{12}}{\partial Y} - v^\dagger \frac{\partial S_{12}}{\partial X}, \tag{2.132}$$

$$-p^{(1)} + 2\left.\frac{\partial v^{(1)}}{\partial y}\right|_{y\to\infty} = -2\,v^\dagger \frac{\partial S_{12}}{\partial Y}. \tag{2.133}$$

The Ansatz for the new variables is

$$u_i^{(1)} = \tilde{u}_{ij}\frac{\partial S_{12}}{\partial X_j} + \breve{u}_{ij}\frac{\partial S_{22}}{\partial X_j}, \tag{2.134}$$

$$p^{(1)} = \tilde{p}_j\frac{\partial S_{12}}{\partial X_j} + \breve{p}_j\frac{\partial S_{22}}{\partial X_j}, \tag{2.135}$$

with the microscopic coefficients arising from the solutions of the two sets of microscopic problems given below.

Forcing by $\dfrac{\partial S_{12}}{\partial X_j}$:

$$\frac{\partial \tilde{u}_{ij}}{\partial x_i} = -u_i^\dagger\,\delta_{ij}, \quad -\frac{\partial \tilde{p}_j}{\partial x_i} + \frac{\partial^2 \tilde{u}_{ij}}{\partial x_k^2} = p^\dagger\,\delta_{ij} - 2\,\frac{\partial u_i^\dagger}{\partial x_j}, \tag{2.136}$$

$$\lim_{y\to+\infty}\frac{\partial \tilde{u}_{1j}}{\partial y} = -u^\dagger\,\delta_{j2} - v^\dagger\,\delta_{j1}, \quad \lim_{y\to+\infty} -\tilde{p}_j + 2\,\frac{\partial \tilde{u}_{2j}}{\partial y} = -2\,v^\dagger\,\delta_{j2}. \tag{2.137}$$

Forcing by $\dfrac{\partial S_{22}}{\partial X_j}$:

$$\frac{\partial \breve{u}_{ij}}{\partial x_i} = 0, \quad -\frac{\partial \breve{p}_j}{\partial x_i} + \frac{\partial^2 \breve{u}_{ij}}{\partial x_k^2} = -\delta_{ij}, \tag{2.138}$$

$$\lim_{y\to+\infty}\frac{\partial \breve{u}_{1j}}{\partial y} = 0, \quad \lim_{y\to+\infty} -\breve{p}_j + 2\,\frac{\partial \breve{u}_{2j}}{\partial y} = 0. \tag{2.139}$$

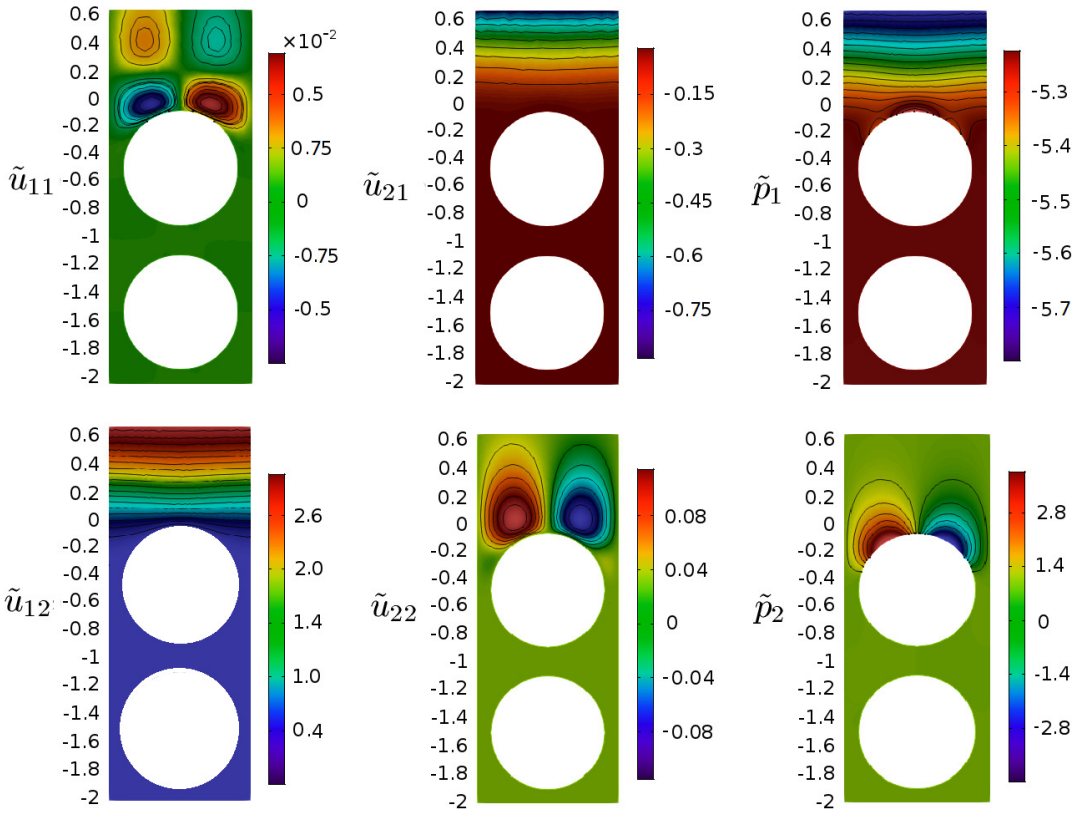

Figure 2.14: Fields of $\tilde{u}_{ij}$ and $\tilde{p}_j$ in the neighborhood of the dividing surface for regularly arranged two-dimensional solid grains, porosity $\theta = 0.4973$.

These two systems, like the ones solved earlier, require periodicity along the interface-parallel direction(s); furthermore, the fields deep within the porous domain ($y \to -\infty$) must repeat themselves with a dimensionless y-periodicity equal to 1. Numerical solutions of these systems can be easily carried out by the same technique used before; the $\tilde{\bullet}$ and $\breve{\bullet}$ terms yield all of the $\mathcal{O}(\epsilon^2)$ terms in the expressions of the macroscopic fields at the interface.

The solution of systems (2.136-2.137) and (2.138-2.139) is carried out for varying values of y_∞, and results are displayed in figures 2.14 and 2.15 in the vicinity of the interface, when using $y_\infty = 5$. For the system driven by the gradient of S_{12} the coefficient of concern here is $\tilde{u}_{21}$ whereas for that driven by the gradient of S_{22} we are interested in $\breve{u}_{11}$ and $\breve{u}_{11}$. Other coefficients either vanish at y_∞ or are antisymmetric about the vertical mid-line so that their x-averaged value at any y vanishes. For y_∞ sufficiently large (larger than about 4), it is found that

$$-\tilde{u}_{21}\big|_{y_\infty} = \breve{u}_{11}\big|_{y_\infty} = \frac{y_\infty^2}{2} + \lambda\, y_\infty + \mathcal{K}^{itf}, \tag{2.140}$$

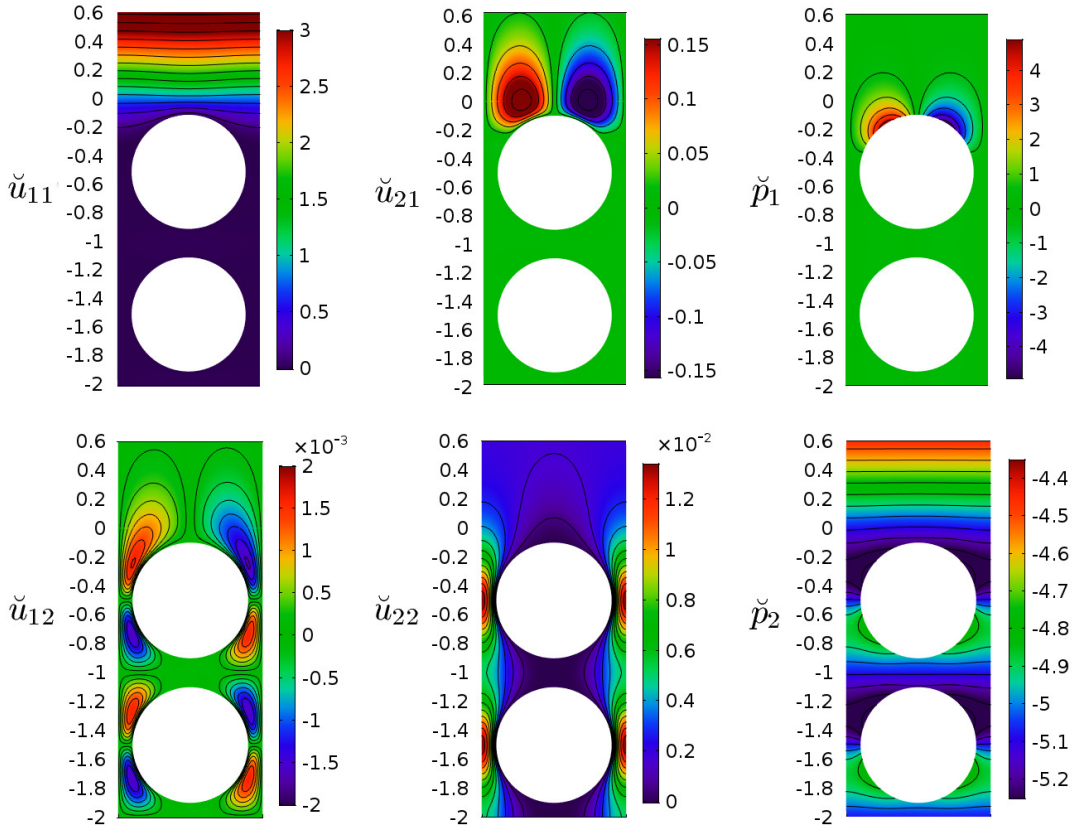

Figure 2.15: Same as figure 2.14 for $\breve{u}_{ij}$ and $\breve{p}_j$.

$$\breve{u}_{22}|_{y_\infty} = \mathcal{K}, \tag{2.141}$$

with λ the slip length. The other two parameters introduced above are the porous system permeability, $\mathcal{K}$, and the interface permeability, $\mathcal{K}^{itf}$. For the case reported in figures 2.14 and 2.15 it is found that

$$\mathcal{K} = 1.830 \times 10^{-3} \qquad \text{and} \qquad \mathcal{K}^{itf} = 1.173 \times 10^{-2}.$$

A result similar to that expressed by (2.140) was obtained before for the case of the flow past a regularly microstructured, impermeable surface. We also note that the same values of the parameters λ, $\mathcal{K}$ and $\mathcal{K}^{itf}$ can be found by the alternative adjoint approach proposed by Bottaro (2019).

If the matching condition (which normally is enforced at y_∞) is conveniently transferred to the dividing surface in $y = 0^+$, only $\mathcal{K}$ and $\mathcal{K}^{itf}$ enter the interface conditions at second order. The velocity of the macroscopic problem at $Y = 0^+$, correct up to order ϵ^2 (i.e. including $u_i^{(0)}$ and $u_i^{(1)}$), has components:

$$U|_{Y=0^+} = \epsilon\,\lambda\; S_{12}|_{Y=0^+} + \epsilon^2\,\mathcal{K}^{itf}\; \left.\frac{\partial S_{22}}{\partial X}\right|_{Y=0^+} + \mathcal{O}(\epsilon^3), \tag{2.142}$$

$$V|_{Y=0^+} = -\epsilon^2 \, \mathcal{K}^{itf} \left. \frac{\partial S_{12}}{\partial X} \right|_{Y=0^+} + \epsilon^2 \, \mathcal{K} \left. \frac{\partial S_{22}}{\partial Y} \right|_{Y=0^+} + \mathcal{O}(\epsilon^3). \tag{2.143}$$

Equations (2.142) and (2.143) represent the most important result of the present contribution: the outer flow is coupled to the motion in the porous medium through the coefficients λ, $\mathcal{K}$, and $\mathcal{K}^{itf}$, available via the solutions of Stokes-like problems in a y-elongated cell, periodic along the interface-parallel direction(s). In the expressions above the terms of order ϵ^2 arise from streamwise and normal variations of the components of the outer traction vector. Equations (2.142) and (2.143) coincide with those given in the previous section for the case of the flow over a rough, impermeable wall, provided the permeability $\mathcal{K}$ is set to zero; the first term in equation (2.143) is related to transpiration at the surface in $Y = 0$ because of shear variations.

The condition for $U|_{Y=0^+}$ does not seem to match that by Saffman (1971), given in dimensional form in (1.7), since the streamwise velocity at the dividing surface appears to be decoupled from the pore pressure gradient $\partial P_0^- / \partial Y$ at $Y = 0^-$. A further look at the pressure condition is thus needed.

2.3.3. The Pressure Condition

Continuity of pressure has often been used at the dividing surface (e.g. (Lācis and Bagheri, 2017; Zampogna et al., 2019a; Ochoa-Tapia et al., 2017; Whitaker, 1986)); however, the interstitial pressure is a pore-averaged value and, even if the microscopic pressure is indeed continuous at $y = 0$, it is now accepted that a pressure jump exists between the fluid pressure and the pore pressure, when crossing the interface (Carraro et al., 2013; Lācis et al., 2020). To evaluate such a pressure jump, the starting point is the expression of p in the interfacial domain, i.e.

$$p = p^\dagger \, S_{12} - S_{22} + \epsilon \, \tilde{p}_j \, \frac{\partial S_{12}}{\partial X_j} + \epsilon \, \breve{p}_j \, \frac{\partial S_{22}}{\partial X_j} + \mathcal{O}(\epsilon^2). \tag{2.144}$$

Within the porous region the coefficients $\tilde{p}_j$ and $\breve{p}_j$ attain a y-periodic behavior when we are sufficiently below the dividing surface. The intrinsic average value of the pressure in a $1{\times}1$ unit cell for $y \to -\infty$ is indicated by $\langle p \rangle^f_{-\infty}$. We have

$$\langle p \rangle^f_{-\infty} = -S_{22} + \epsilon \, \langle \tilde{p}_1 \rangle^f_{-\infty} \, \frac{\partial S_{12}}{\partial X} + \epsilon \, \langle \breve{p}_2 \rangle^f_{-\infty} \, \frac{\partial S_{22}}{\partial Y} + \mathcal{O}(\epsilon^2). \tag{2.145}$$

Furthermore, from the definition of p in the porous domain we have

$$\langle p \rangle^f_{-\infty} = P_0^-|_{Y=0^-} + \epsilon \, \langle P_1^- \rangle^f_{-\infty} + \mathcal{O}(\epsilon^2), \tag{2.146}$$

so that it is simple to conclude that the normal stress exerted by the outer fluid is impressed onto the pore pressure, i.e.

$$P_0^-|_{Y=0^-} = -S_{22} + \mathcal{O}(\epsilon) \tag{2.147}$$

This condition on the leading-order interstitial pressure is sufficient to close the problem and there is no need to find the order one correction to the pressure, $\langle P_1^- \rangle_{-\infty}^f$, nor to evaluate the pressure jump across the dividing surface. If the solution in the + domain is known at iteration n, boundary condition (2.147) can be used at the interface for the equation $\partial^2 P_0^- / \partial X_j^2 = 0$ which describes the behavior of the pore pressure in the bulk of the porous medium. The same condition permits also writing the macroscopic free-fluid streamwise velocity at $Y = 0^+$ (equation (2.142)) in terms of the pore pressure, i.e. in Saffman's form (cf. equation (1.7)):

$$U|_{Y=0^+} = \epsilon\,\lambda\; S_{12}|_{Y=0^+} - \epsilon^2\,\mathcal{K}^{itf}\;\left.\frac{\partial P_0^-}{\partial X}\right|_{Y=0^-} + \mathcal{O}(\epsilon^3). \tag{2.148}$$

The vertical velocity at $Y = 0^+$ can also be expressed in terms of P_0^- by using Darcy's law, enforcing mass conservation across the interface and accounting for periodicity along the interface-normal cell boundaries. It reads:

$$V|_{Y=0^+} = -\epsilon^2\,\mathcal{K}\;\left.\frac{\partial P_0^-}{\partial Y}\right|_{Y=0^-} + \mathcal{O}(\epsilon^3). \tag{2.149}$$

If (2.148) and (2.149) are used at the interface instead of (2.142) and (2.143) the motion in the free-fluid region is coupled to that in the porous matrix, i.e. the problems in the two domains must be solved together. Comparison of the two proposed (and equivalent) forms of interface conditions permits to state that also the pressure gradient is discontinuous at the interface; in particular it is easy to find that

$$Re\;\left.\frac{\partial P}{\partial X}\right|_{Y=0^+} - \left.\frac{\partial P_0^-}{\partial X}\right|_{Y=0^-} = 2\;\left.\frac{\partial^2 V}{\partial X \partial Y}\right|_{Y=0^+} + \mathcal{O}(\epsilon), \tag{2.150}$$

$$Re\;\left.\frac{\partial P}{\partial Y}\right|_{Y=0^+} - \left.\frac{\partial P_0^-}{\partial Y}\right|_{Y=0^-} = -\frac{\mathcal{K}^{itf}}{\mathcal{K}}\frac{\partial}{\partial X}\left.\left(\frac{\partial U}{\partial Y} + \frac{\partial V}{\partial X}\right)\right|_{Y=0^+} + 2\;\left.\frac{\partial V}{\partial Y}\right|_{Y=0^+} + \mathcal{O}(\epsilon). \tag{2.151}$$

Before closing this subsection it is useful to write all the coupling conditions in terms of dimensional variables. The slip and transpiration conditions to be used in the resolution of the outer flow are:

$$\hat{u}|_{0^+} \approx \hat{\lambda}\,\left.\left(\frac{\partial \hat{u}}{\partial \hat{y}} + \frac{\partial \hat{v}}{\partial \hat{x}}\right)\right|_{0^+} + \frac{\hat{\mathcal{K}}^{itf}}{\mu}\,\frac{\partial}{\partial \hat{x}}\left.\left(-\hat{p} + 2\,\mu\,\frac{\partial \hat{v}}{\partial \hat{y}}\right)\right|_{0^+}, \tag{2.152}$$

$$\hat{v}|_{0^+} \approx \frac{\hat{\mathcal{K}}}{\mu}\,\frac{\partial}{\partial \hat{y}}\left.\left(-\hat{p} + 2\,\mu\,\frac{\partial \hat{v}}{\partial \hat{y}}\right)\right|_{0^+} - \hat{\mathcal{K}}^{itf}\,\frac{\partial}{\partial \hat{x}}\left.\left(\frac{\partial \hat{u}}{\partial \hat{y}} + \frac{\partial \hat{v}}{\partial \hat{x}}\right)\right|_{0^+}. \tag{2.153}$$

And one could easily recover the boundary condition for isotropic impermeable roughness if we set meadium $\mathcal{K} = 0$ in the above equations.

Alternatively, we can also write

$$\hat{u}|_{0^+} \approx \hat{\lambda}\,\left.\left(\frac{\partial \hat{u}}{\partial \hat{y}} + \frac{\partial \hat{v}}{\partial \hat{x}}\right)\right|_{0^+} - \frac{\hat{\mathcal{K}}^{itf}}{\mu}\,\left.\frac{\partial \hat{p}}{\partial \hat{x}}\right|_{0^-}. \tag{2.154}$$

$$\hat{v}|_{0^+} \approx -\frac{\hat{\mathcal{K}}}{\mu}\frac{\partial \hat{p}}{\partial \hat{y}}\bigg|_{0^-}. \tag{2.155}$$

The Dirichlet condition for the pore pressure at the interface is

$$\hat{p}\big|_{0^-} \approx \hat{p} - 2\,\mu\,\frac{\partial \hat{v}}{\partial \hat{y}}\bigg|_{0^+}. \tag{2.156}$$

The dimensional coefficients are $\hat{\lambda} = \lambda l$, $\hat{\mathcal{K}}^{itf} = \mathcal{K}^{itf} l^2$, and $\hat{\mathcal{K}} = \mathcal{K} l^2$. It is important to stress once more that no empirical coefficients are present in the matching conditions (2.152-2.156); the coefficients of interest, homogeneous to either a length or an area, are all available through the solution of simple microscopic problems. Such coefficients are discussed in the section 2.3.5., for both two- and three-dimensional isotropic porous media.

2.3.4. Randomly Arranged Grains

Two dimensional circular grains are arranged at random fashion (randomness is periodic after 10 unites of microscopic length scale l), such as those shown in figure 2.17 are also considered for completeness by perturbing the position of each grain (starting from the staggered configuration) by its reference value. The extension of three dimensions is trivial and not pursued here. The figure 2.17 shows the results obtained in the domain 10×10 $x-$periodic; the left image shows $u^\dagger$ (eventually leading to λ) and the right image shows $\breve{u}11$ (eventually returning $\mathcal{K}^{itf}$). The values of the permeability of the anisotropic medium is obtained from the method described by Mei and Vernescu (2009)), computing all components of the permeability tensor by solving the following auxiliary Stokes system forced by δ_{ij} (Kronecker delta):

$$\frac{\partial u_i^*}{\partial x_i} = 0, \quad -\frac{\partial p_j^*}{\partial x_i} + \frac{\partial^2 u_{ij}^*}{\partial x_k^2} = -\delta_{ij}, \tag{2.157}$$

in a unit cell of 10×10 fully periodic domain, and no-slip condition on the boundaries of grains is imposed. The solution of first problem yields the horizontal component of the seepage velocity $\langle u_1^* \rangle = -\mathcal{K}_{xx}\frac{\partial p}{\partial X_1} - \mathcal{K}_{xy}\frac{\partial p}{\partial X_2}$ and the solution of second problem yields the vertical component of seepage velocity $\langle u_2^* \rangle = -\mathcal{K}_{yx}\frac{\partial p}{\partial X_1} - \mathcal{K}_{yy}\frac{\partial p}{\partial X_2}$ and $\mathcal{K}_{ij}$ are the entities of the permeability tensor $\mathcal{K}$. Figure 2.16(bottom) displays the sample system solutions of system 2.157 in the form of color contours. Once the system 2.157 is solved twice in the unit cell, four components of of the tensor $\mathcal{K}$ are available Once this is done, we need to compute the two eigenvalues $\mathcal{K}_{max}$ and $\mathcal{K}_{min}$ of the tensor $\mathcal{K}$, and then their geometric average, $\mathcal{K}_{mean}=\sqrt{\mathcal{K}_{max}\mathcal{K}_{min}}$ (see (Airiau and Bottaro, 2020)). Note that $\mathcal{K}_{max}$ and $\mathcal{K}_{min}$ are the eigen value of the tensor $\mathcal{K}$ and are slightly different form $\mathcal{K}_{xx}$ and $\mathcal{K}_{yy}$. For randomly arranged grains, this average value of $\mathcal{K}$ is reported in figure 2.17 (central frame) with diamond symbols and compared to values for in-line and staggered solid

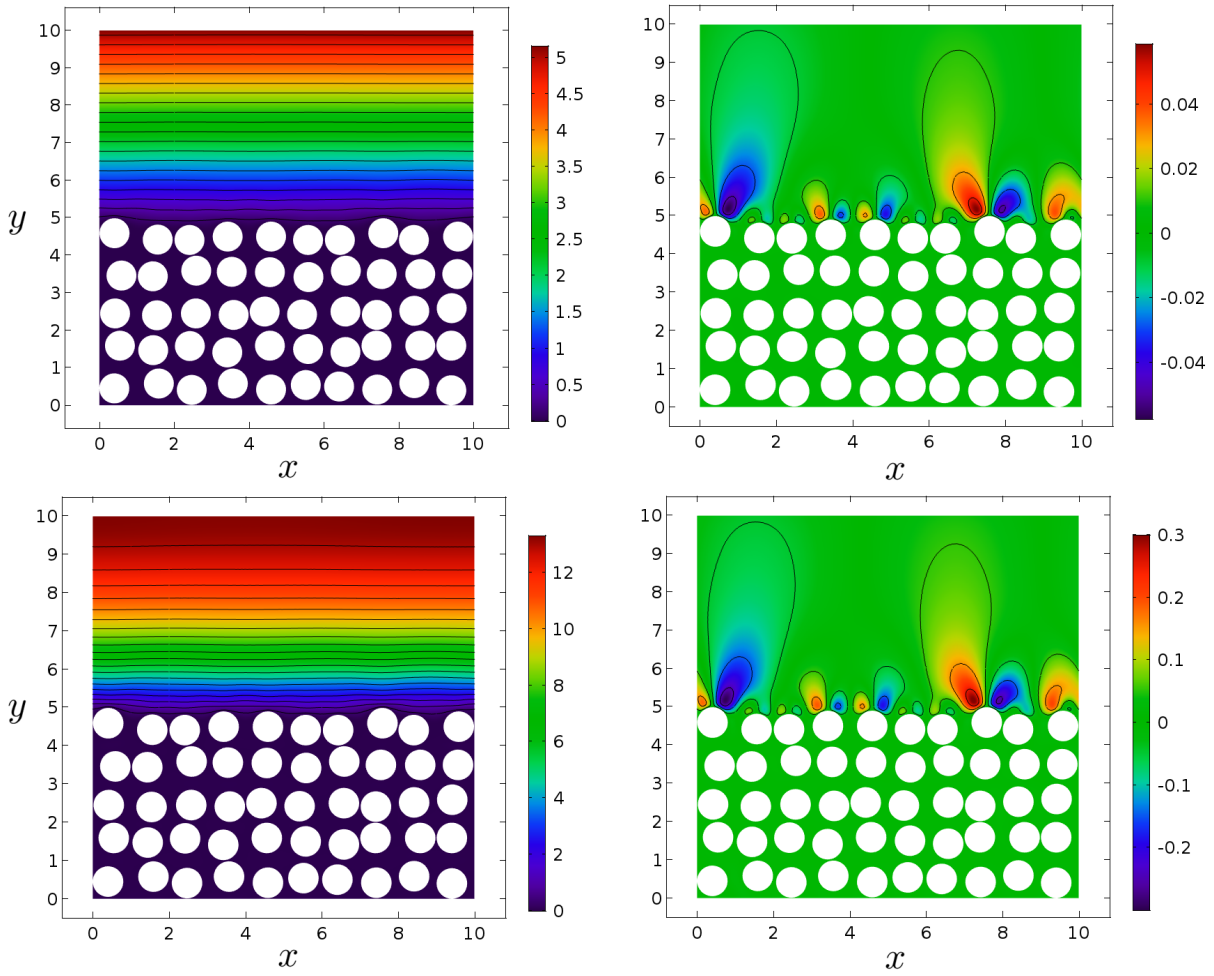

Figure 2.16: Fields of $u^\dagger$ (top left) $v^\dagger$ (top right) and $\breve{u}_{11}$(bottom left) and $\breve{u}_{21}$(bottom right) for $\theta = 0.4973$, randomly arranged two-dimensional solid grains.

inclusions/grains. It is interesting to observe that the coefficients found, λ, $\mathcal{K}_{mean}$ and $\mathcal{K}^{itf}$, are typically included between the staggered and the in-line values, while remaining closer to the former as the porosity varies.

2.3.5. Variation of Coupling Coefficients as a Function of Porosity

Results for two-dimensional circular and three-dimensional spherical grains are summarized in figures 2.17 and 2.18, respectively, for both in-line (solid lines) and staggered (dashed) arrangements of the solid inclusions, and for varying values of the porosity. The two-dimensional case of randomly arranged grains is also included in the figure.
In both two-dimensional and three-dimensional configurations the coefficients have a monotonic behavior with θ; both slip length and interface permeability are systemati-

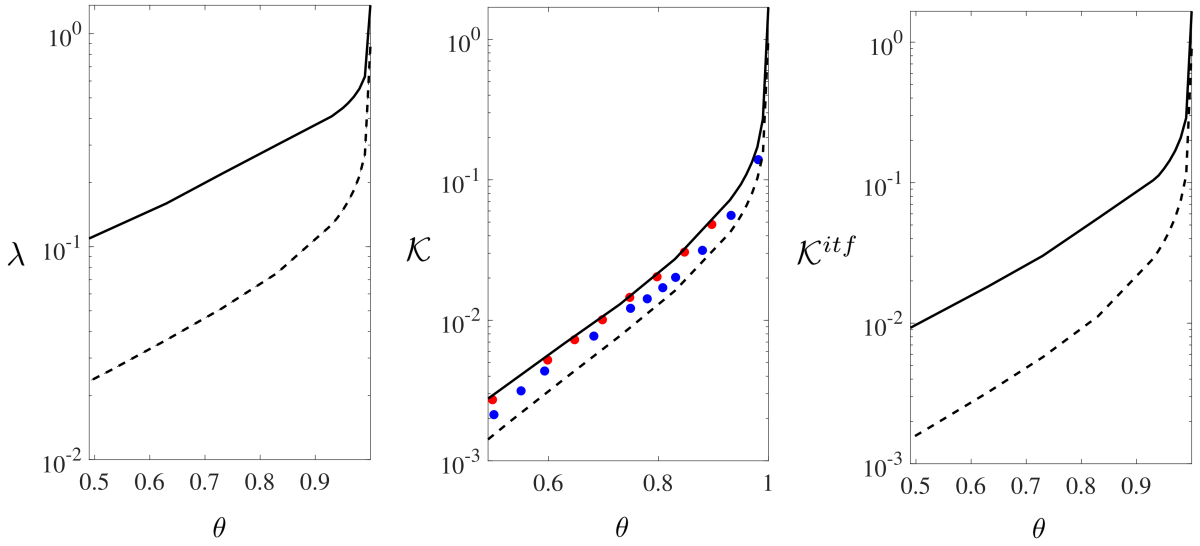

Figure 2.17: Comparison between regularly arranged grains (solid lines) and staggered grains (dashed lines) for two-dimensional isotropic porous media of varying porosity θ (plotted in abscissa in all frames). From left to right: λ, $\mathcal{K}$ and $\mathcal{K}^{itf}$. In the central frame the medium permeabilities for in-line and staggered cases are validated, respectively, against Zampogna and Bottaro (2016) (red circles) and Bottaro (2019) (black circles). The case of randomly arranged grains is also considered (diamond symbols).

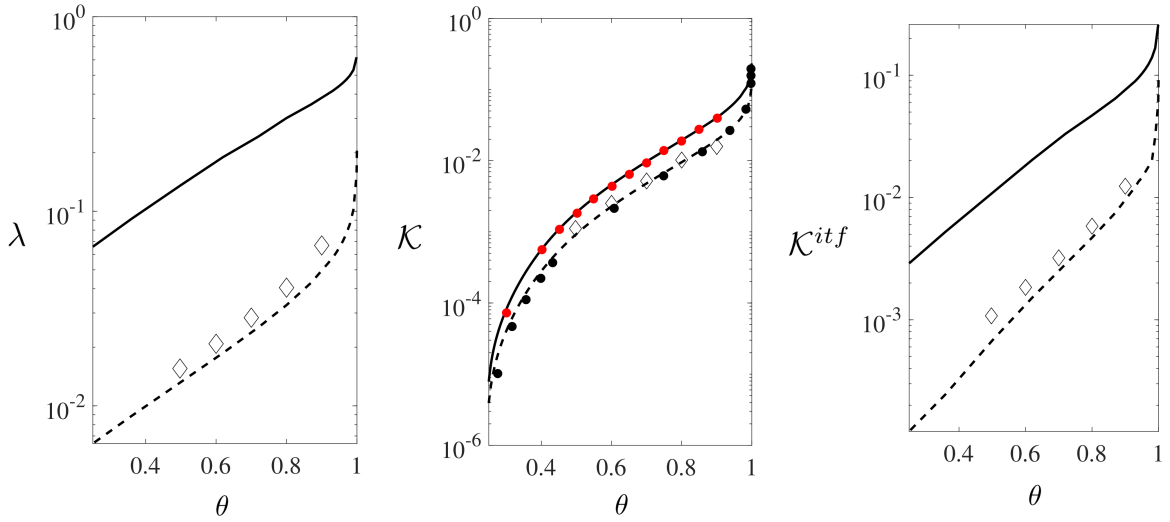

Figure 2.18: Same as figure 2.17 (solid line for uniformly arranged and dashed line for staggered) three-dimensional spherical grains. In the central frame the permeability for the in-line arrangement of spheres is compared to results in Zampogna and Bottaro (2016) (red circles). The permeability results for Wigner-Seitz grains (Lee et al. (1996)) are given with blue filled symbols.

cally one order of magnitude larger in the regularly arranged case than in the staggered configuration (at the same value of θ), to be ascribed to the fact that the unit cell right below the interface ($0 \leq x \leq 1$, $-1 \leq y \leq 0$) in the staggered case presents a sizeable portion in $y = 0$ where the fluid cannot slip and through which it cannot penetrate (cf. figure 2.10). Conversely, the deviation in $\mathcal{K}$ between the two arrangements of solid grains examined is rather small. In the two-dimensional case (figure 2.17) for both grains arrangements the present procedure yields results in excellent agreement with those reported in the past (Zampogna and Bottaro, 2016; Bottaro, 2019), obtained from the *conventional* approach described by Mei and Vernescu (2009).
For three-dimensional spherical grains, conditions (2.152-2.156) remain unchanged, and must be supplemented by the following spanwise slip condition:

$$\hat{w}|_{0^+} = \hat{\lambda} \left(\frac{\partial \hat{w}}{\partial \hat{y}} + \frac{\partial \hat{v}}{\partial \hat{z}} \right) \Bigg|_{0^+} - \frac{\hat{\mathcal{K}}^{itf}}{\mu} \frac{\partial \hat{p}}{\partial \hat{z}} \Bigg|_{0^-}, \tag{2.158}$$

with the same coefficients used in $\hat{u}$. The results for $\mathcal{K}$ in figure 2.18 coincide with those computed by Zampogna and Bottaro (2016), cf. solid line and red dots in the central frame of the figure. It is also instructive to compare the permeability found to that of the Wigner-Seitz grain Lee et al. (1996), a polyhedron with 14 sides in a cubically packed array, with contact among grains on the six faces of the unit cell. The results of the Wigner-Seitz grain are contained between those of in-line and staggered spherical inclusions, and this denotes the low sensitivity of $\mathcal{K}$ to the arrangement (and to the exact shape) of the solid grains.
As anticipated in the introduction, all the coefficients computed are tabulated in the tables 2.5 (for two-dimensional) and 2.6 (for three-dimensional).

2.3.6. Two-Dimensional Interface Conditions

Let us now assume that all dimensional variables, throughout the whole domain, are rendered dimensionless with the same scales used in the free-fluid region. In particular, from now on we denote by P_0^- the pore pressure non-dimensionalized with $\rho \mathcal{U}^2$. If the dividing surface is positioned in $Y = 0$ the conditions to be imposed there for a two-dimensional macroscopic flow problem, correct up to order 2 in ϵ, are:

$$U|_{Y=0^+} \approx \epsilon \, \lambda \left(\frac{\partial U}{\partial Y} + \frac{\partial V}{\partial X} \right) \Bigg|_{Y=0^+} + \epsilon^2 \, \mathcal{K}^{itf} \, \frac{\partial}{\partial X} \left(-Re \, P + 2 \frac{\partial V}{\partial Y} \right) \Bigg|_{Y=0^+}, \tag{2.159}$$

$$V|_{Y=0^+} \approx -\epsilon^2 \, \mathcal{K}^{itf} \, \frac{\partial}{\partial X} \left(\frac{\partial U}{\partial Y} + \frac{\partial V}{\partial X} \right) \Bigg|_{Y=0^+} + \epsilon^2 \, \mathcal{K} \, \frac{\partial}{\partial Y} \left(-Re \, P + 2 \frac{\partial V}{\partial Y} \right) \Bigg|_{Y=0^+}. \tag{2.160}$$

With the conditions above there is no direct coupling between the Navier-Stokes and the Darcy regions: once the outer flow problem is solved for, the pore pressure at leading

Table 2.5: Values of effective coefficients for two-dimensional circular grains as a function of porosity.

	In-line			Staggered		
θ	λ	$\mathcal{K}$	$\mathcal{K}^{itf}$	λ	$\mathcal{K}$	$\mathcal{K}^{itf}$
0.2500	6.571×10^{-2}	8.918×10^{-6}	2.896×10^{-3}	6.400×10^{-3}	3.920×10^{-6}	1.223×10^{-4}
0.3600	9.147×10^{-2}	2.962×10^{-4}	5.268×10^{-3}	8.872×10^{-3}	1.479×10^{-4}	2.469×10^{-4}
0.4973	1.451×10^{-1}	1.830×10^{-3}	1.173×10^{-2}	1.315×10^{-2}	9.100×10^{-4}	6.600×10^{-4}
0.5000	1.362×10^{-1}	1.877×10^{-3}	1.089×10^{-2}	1.325×10^{-2}	9.348×10^{-4}	6.775×10^{-4}
0.6200	1.899×10^{-1}	5.378×10^{-3}	2.032×10^{-2}	1.871×10^{-2}	2.665×10^{-3}	1.516×10^{-3}
0.7200	2.420×10^{-1}	1.120×10^{-2}	3.319×10^{-2}	2.531×10^{-2}	5.518×10^{-3}	2.848×10^{-3}
0.8000	3.013×10^{-1}	1.945×10^{-2}	4.691×10^{-2}	3.294×10^{-2}	9.530×10^{-3}	4.694×10^{-3}
0.8700	3.542×10^{-1}	3.201×10^{-2}	6.456×10^{-2}	4.293×10^{-2}	1.559×10^{-2}	7.496×10^{-3}
0.9300	4.144×10^{-1}	5.798×10^{-2}	8.957×10^{-2}	5.729×10^{-2}	2.547×10^{-2}	1.224×10^{-2}
0.9500	4.410×10^{-1}	7.268×10^{-2}	1.030×10^{-1}	6.504×10^{-2}	3.214×10^{-2}	1.453×10^{-2}
0.9700	4.752×10^{-1}	9.879×10^{-2}	1.233×10^{-1}	7.675×10^{-2}	4.027×10^{-2}	4.027×10^{-2}
0.9900	5.323×10^{-1}	1.256×10^{-1}	1.670×10^{-1}	1.019×10^{-1}	6.264×10^{-2}	3.157×10^{-2}
0.9999	6.188×10^{-1}	2.166×10^{-1}	2.585×10^{-1}	1.545×10^{-1}	1.039×10^{-1}	5.989×10^{-2}

Table 2.6: Values of effective coefficients for three-dimensional spherical grains as a function of porosity.

	In-line			Staggered		
θ	λ	$\mathcal{K}$	$\mathcal{K}^{itf}$	λ	$\mathcal{K}$	$\mathcal{K}^{itf}$
0.4900	1.093×10^{-1}	2.769×10^{-3}	9.280×10^{-3}	2.333×10^{-2}	1.421×10^{-3}	1.507×10^{-3}
0.6300	1.597×10^{-1}	6.901×10^{-3}	1.818×10^{-2}	3.648×10^{-2}	3.864×10^{-3}	3.213×10^{-3}
0.7300	2.196×10^{-1}	1.302×10^{-2}	3.019×10^{-2}	5.112×10^{-2}	7.747×10^{-3}	5.735×10^{-3}
0.8300	3.002×10^{-1}	2.727×10^{-2}	5.580×10^{-2}	7.497×10^{-2}	1.623×10^{-2}	1.120×10^{-2}
0.9300	4.098×10^{-1}	7.172×10^{-2}	5.580×10^{-2}	1.267×10^{-1}	4.209×10^{-2}	2.876×10^{-2}
0.9500	4.478×10^{-1}	9.287×10^{-2}	1.260×10^{-1}	1.486×10^{-1}	5.537×10^{-2}	3.828×10^{-2}
0.9700	5.061×10^{-1}	1.330×10^{-1}	1.686×10^{-1}	1.842×10^{-1}	7.963×10^{-2}	5.639×10^{-2}
0.9900	6.291×10^{-1}	2.708×10^{-1}	2.893×10^{-1}	2.713×10^{-1}	1.507×10^{-1}	1.130×10^{-1}
0.9999	1.361	1.691	1.658	8.687×10^{-1}	1.020	8.966×10^{-1}

order within the isotropic porous medium is a harmonic function which satisfies

$$\frac{\partial P_0^-}{\partial X_i}\, n_i = 0, \tag{2.161}$$

at solid surfaces of unit normal n_i, and

$$P_0^-\Big|_{Y=0^-} = P\Big|_{Y=0^+} - \frac{2}{Re}\,\frac{\partial V}{\partial Y}\bigg|_{Y=0^+} \tag{2.162}$$

at the dividing surface.
An alternative to conditions (2.159-2.160), formally correct up to the same order in ϵ, is constituted by the following dimensionless conditions:

$$U|_{Y=0^+} \approx \epsilon\,\lambda\,\left(\frac{\partial U}{\partial Y} + \frac{\partial V}{\partial X}\right)\bigg|_{Y=0^+} - \epsilon^2\,\mathcal{K}^{itf}\,Re\;\frac{\partial P_0^-}{\partial X}\bigg|_{Y=0^-}, \tag{2.163}$$

$$V|_{Y=0^+} \approx -\epsilon^2\,\mathcal{K}\,Re\;\frac{\partial P_0^-}{\partial Y}\bigg|_{Y=0^-}. \tag{2.164}$$

Conditions (2.163-2.164) are, respectively, a Beavers-Joseph-like condition for the velocity along the direction tangent to the interface, and an expression of mass conservation across the two domains; they must be coupled to the Laplace equation for the pore pressure in the porous medium, using equation (2.162) which expresses the balance of normal forces at the interface. This latter system is closer to what is often found in the literature (cf. Eggenweiler and Rybak (2020) and references therein). We have employed both sets of conditions to compute the macroscopic results presented below, finding negligible differences.
It is important to notice that Saffman's result, see equation (1.7), is equivalent to (2.163). In dimensionless form, the result by Saffman, including Jones (1973) correction[2], reads:

$$U|_{Y=0^+} \approx \epsilon\,\lambda\,\left(\frac{\partial U}{\partial Y} + \frac{\partial V}{\partial X}\right)\bigg|_{Y=0^+} - \epsilon^2\,B\,\mathcal{K}\,Re\;\frac{\partial P_0^-}{\partial X}\bigg|_{Y=0^-}. \tag{2.165}$$

Equations (2.163) and (2.165) coincide once the constant B is set equal to $\mathcal{K}^{itf}/\mathcal{K}$. The important result of the present contribution is that microscopic problems have been derived and solved for isotropic porous media which yield directly the required constants, λ, $\mathcal{K}$, and $\mathcal{K}^{itf}$. The approach proposed here can be used to solve cases in which the fluid flows parallel to the porous layer or infiltrates the porous medium. Whereas the first case has been much examined in the literature, the latter has been scarcely focused upon. A recent paper by Eggenweiler and Rybak (2020) shows that the Beavers and Joseph condition is unsuited for filtration problems, and that the parameters of the Beavers-Joseph condition cannot be fitted for arbitrary flow direction.

[2]Jones replaced the scalar product of the interface-normal unit vector times the free-fluid velocity gradient with the scalar product of the same unit normal vector times the rate of strain tensor.

2.3.7. Three-Dimensional Interface Conditions

The interface conditions for the porous medium consisting of evenly spaced micro-structured cylinders aligned along the spanwise or the streamwise direction with inline and staggered patterns, enabling direct measurement of the flow inside the porous structure, are given below. Here, the interface between the free-fluid region and porous medium is located at the crest of the cylinder.
As before, these conditions can be enforced at the dividing surface (interface) ($Y = 0$). We will not explain the full development of these conditions again as it is straightforward but directly write the conditions which are given below:

$$U|_{Y=0^+} = \epsilon\,\lambda_x\ S_{12}|_{Y=0^+} + \epsilon^2\,\mathcal{K}_{12}^{itf}\ \left.\frac{\partial S^{22}}{\partial X}\right|_{Y=0^+} + \mathcal{O}(\epsilon^3), \tag{2.166}$$

$$V|_{Y=0^+} = -\epsilon^2\,\mathcal{K}_{12}^{itf}\left.\frac{\partial S_{12}}{\partial X}\right|_{Y=0^+} - \epsilon^2\,\mathcal{K}_{32}^{itf}\left.\frac{\partial S_{32}}{\partial Z}\right|_{Y=0^+} + \epsilon^2\,\mathcal{K}_{22}\ \left.\frac{\partial S_{22}}{\partial Y}\right|_{Y=0^+} + \mathcal{O}(\epsilon^3), \tag{2.167}$$

$$W|_{Y=0^+} = \epsilon\,\lambda_z\ S_{32}|_{Y=0^+} + \epsilon^2\,\mathcal{K}_{32}^{itf}\ \left.\frac{\partial S_{22}}{\partial Z}\right|_{Y=0^+} + \mathcal{O}(\epsilon^3), \tag{2.168}$$

where

$$S_{12} = \left.\frac{\partial U}{\partial Y} + \frac{\partial V}{\partial X}\right|_{Y=0^+}, \quad S_{32} = \left.\frac{\partial W}{\partial Y} + \frac{\partial V}{\partial Z}\right|_{Y=0^+}, \quad S_{22} = -Re\,P + 2\left.\frac{\partial V}{\partial Y}\right|_{Y=0^+}.$$

and $\mathcal{K}_{ij}^{itf}$ denoting the components of interface permeability tensor, $\mathcal{K}_{ij}$ are the component of medium permeability tensor, and λ_i are the components of the slip length tensor as defined in Bottaro (2019).
It is simple to transform the conditions above to the following ones, probably more manageable numerically:

$$U|_{Y=0^+} = \epsilon\,\lambda_x\ \left.\frac{\partial U}{\partial Y}\right|_{Y=0^+} + \epsilon^2\,\mathcal{K}_{12}^{itf}\ \left.\frac{\partial S_{22}}{\partial X}\right|_{Y=0^+} + \mathcal{O}(\epsilon^3), \tag{2.169}$$

$$V|_{Y=0^+} = -\epsilon\,\frac{\mathcal{K}_{12}^{itf}}{\lambda_x}\left.\frac{\partial U}{\partial X}\right|_{Y=0^+} - \epsilon\,\frac{\mathcal{K}_{32}^{itf}}{\lambda_z}\left.\frac{\partial W}{\partial Z}\right|_{Y=0^+} + \epsilon^2\,\mathcal{K}_{22}\ \left.\frac{\partial S_{22}}{\partial Y}\right|_{Y=0^+} + \mathcal{O}(\epsilon^3), \tag{2.170}$$

$$W|_{Y=0^+} = \epsilon\,\lambda_z\ \left.\frac{\partial W}{\partial Y}\right|_{Y=0^+} + \epsilon^2\,\mathcal{K}_{32}^{itf}\ \left.\frac{\partial S_{22}}{\partial Z}\right|_{Y=0^+} + \mathcal{O}(\epsilon^3). \tag{2.171}$$

2.3.8. The Coupling Coefficients

The coupling coefficients involved in the interface conditions are computed and are given in graphical form (figure 2.20, 2.19) as well as tabular form (table 2.7 and 2.8) for spanwise cylinder case. In the figure 2.20, we are only representing the solutions of † variables microscopic problem as contours plots as it is the only microscopic problem that needs to be solved if we employ Navier's conditions at the dividing surface, providing the information about slip length. From figure 2.19, it is shown that the coefficients increase as θ increases. Alternatively, the constitutive coefficients of the case when cylinders are arranged in the longitudinal direction (direction of the flow) can be easily found by simply switching the streamwise and spanwise coordinates. This alignment of the porous structures along x is expected to provide a better outcome in terms of skin friction drag reduction as also reported by Gómez-de Segura et al. (2018).

The component of the permeability tensor $\mathcal{K}_{ij}$ computed over the unitary cubic cell (fully periodic) for the inline and staggered arrangement of cylinders, respectively by the classical procedure described by Mei and Vernescu (2009) using phase averaging of the velocities just like in a case of two-dimensional case, where we found that $\mathcal{K}_{11} = \mathcal{K}_{22}$ (spanwise aligned cylinders) and $\mathcal{K}_{22} = \mathcal{K}_{33}$ (longitudinally aligned cylinders) when the cylinders are either arranged with inline or staggered patterns. The rest of the components are either anti-symmetric or zero about the vertical mid-plane in the respective cases.

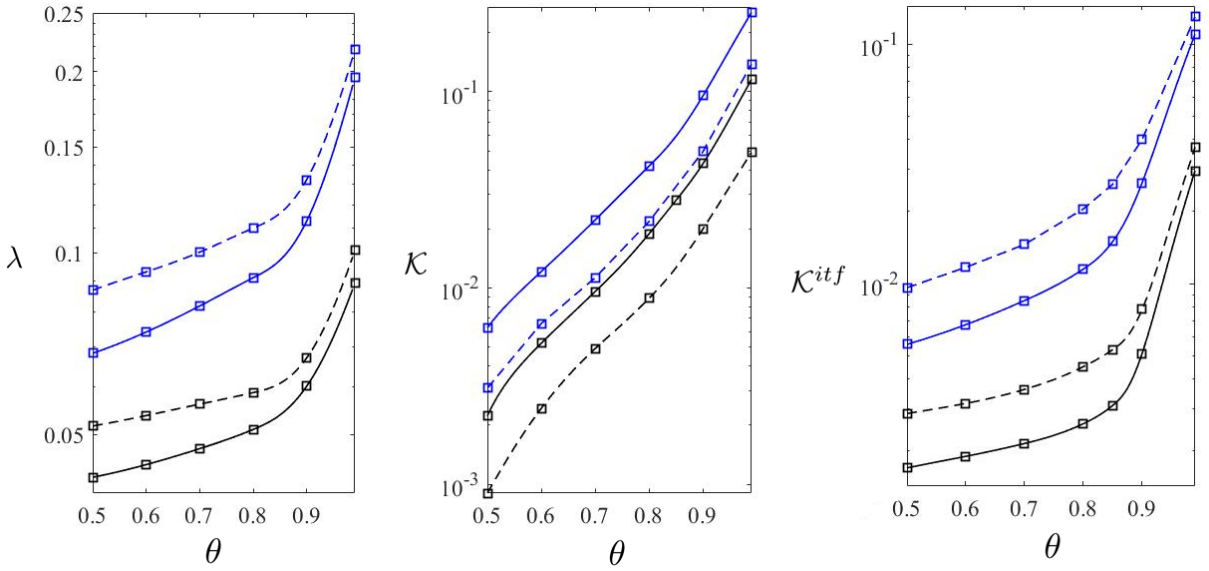

Figure 2.19: Comparison between regularly arranged cylinders (solid lines) and staggered cylinders (dashed lines) for three-dimensional porous media of varying porosity θ (plotted in abscissa in all frames). From left to right: λ_x, $\mathcal{K}_{22}$ and $\mathcal{K}_{12}^{itf}$ (black color) and λ_z, $\mathcal{K}_{33}$ and $\mathcal{K}_{32}^{itf}$ (blue color). The component $\mathcal{K}_{11}$ is not added in the figure because $\mathcal{K}_{11}$=$\mathcal{K}_{22}$. The values for $\mathcal{K}_{11}$ are given in tabular form for future use.

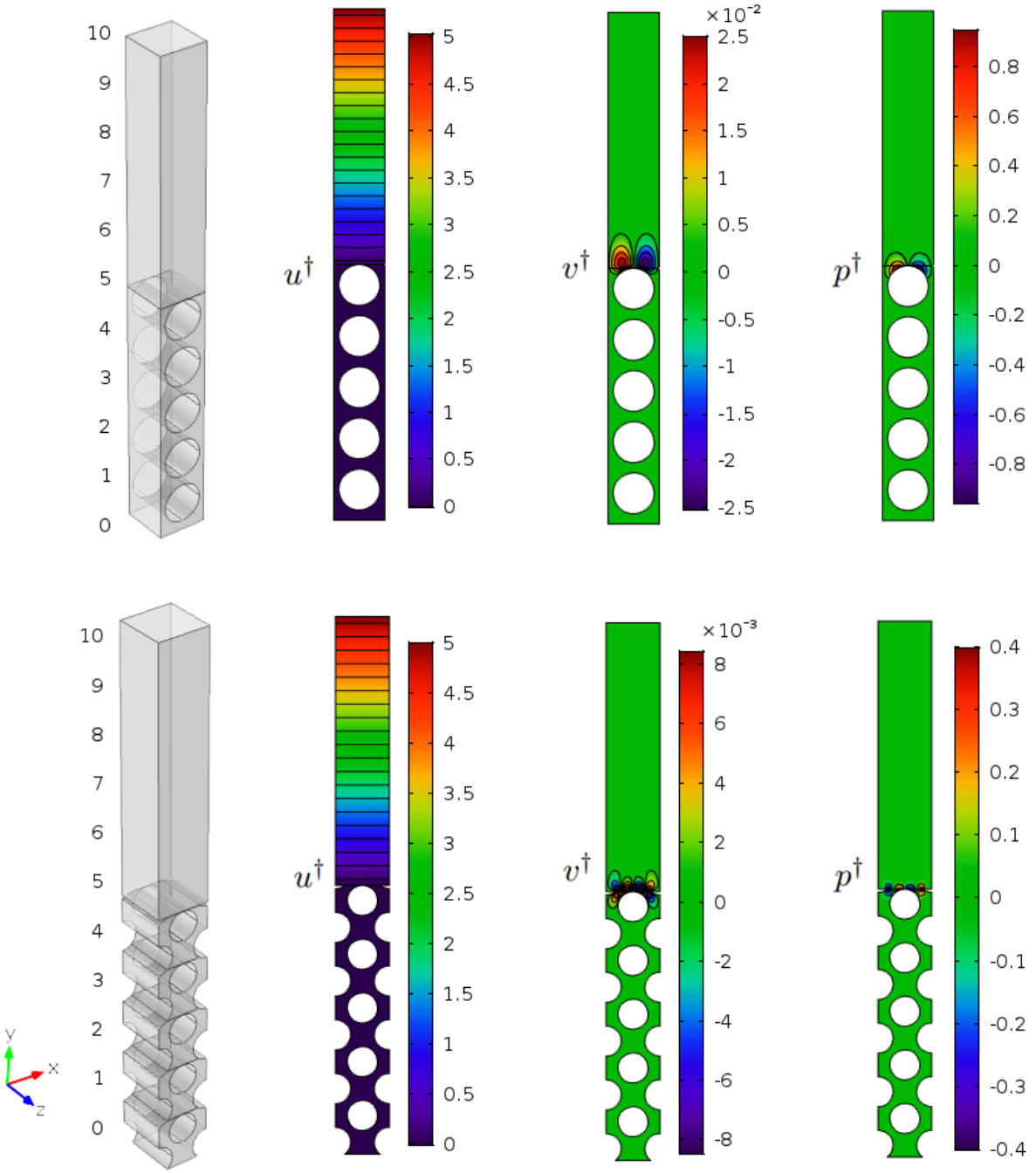

Figure 2.20: Fields of $u^\dagger$, $v^\dagger$, and $p^\dagger$ are displayed on a cut plane xy located at $z = 0$ for inline (top) and staggered (right) configurations of cylinders aligned in the spanwise direction for $\theta = 0.5$. From this solution, one can easily obtain the coefficients λ_x and $\mathcal{K}_{12}^{itf}$ used in the effective conditions (2.169-2.171) by following the procedure used in the previous section.

Table 2.7: Coefficients of three dimensional wall conditions for cylindrical inline porous media aligned in a spanwise direction

θ	λ_x	λ_z	$\mathcal{K}_{11} = \mathcal{K}_{22}$	$\mathcal{K}_{33}$	$\mathcal{K}_{12}^{itf}$	$\mathcal{K}_{32}^{itf}$
0.5	4.513×10^{-2}	6.895×10^{-2}	1.831×10^{-3}	6.968×10^{-3}	2.220×10^{-3}	5.575×10^{-3}
0.6	4.710×10^{-2}	7.398×10^{-2}	4.331×10^{-3}	1.212×10^{-2}	2.410×10^{-3}	6.737×10^{-3}
0.7	4.990×10^{-2}	8.170×10^{-2}	9.587×10^{-3}	2.222×10^{-2}	2.657×10^{-3}	9.042×10^{-3}
0.8	5.386×10^{-2}	9.347×10^{-2}	1.990×10^{-2}	4.179×10^{-2}	2.965×10^{-3}	1.410×10^{-2}
0.9	6.011×10^{-2}	1.130×10^{-1}	3.970×10^{-2}	8.031×10^{-2}	4.113×10^{-3}	2.638×10^{-2}
0.99	8.910×10^{-2}	1.953×10^{-1}	1.255×10^{-1}	2.534×10^{-1}	2.960×10^{-2}	1.075×10^{-1}

Table 2.8: Coefficients of three dimensional wall conditions for cylindrical staggered porous media aligned in a spanwise direction

θ	λ_x	λ_z	$\mathcal{K}_{11}$	$\mathcal{K}_{22}$	$\mathcal{K}_{33}$	$\mathcal{K}_{12}^{itf}$	$\mathcal{K}_{32}^{itf}$
0.5	5.017×10^{-2}	1.676×10^{-2}	1.101×10^{3}	1.101×10^{3}	3.693×10^{-3}	2.866×10^{-3}	7.625×10^{-4}
0.6	5.378×10^{-2}	9.305×10^{-2}	2.457×10^{-3}	2.435×10^{-3}	6.591×10^{-3}	3.160×10^{-3}	1.168×10^{-2}
0.7	5.618×10^{-2}	1.004×10^{-1}	5.070×10^{-3}	4.314×10^{-3}	1.128×10^{-2}	3.618×10^{-3}	1.457×10^{-2}
0.8	5.998×10^{-2}	1.122×10^{-1}	1.153×10^{2}	7.358×10^{-3}	2.180×10^{-2}	4.699×10^{-3}	2.051×10^{-2}
0.9	6.656×10^{-2}	1.323×10^{-1}	2.760×10^{-2}	1.342×10^{-2}	2.958×10^{-2}	7.806×10^{-3}	3.376×10^{-2}
0.99	1.010×10^{-1}	2.173×10^{-1}	8.475×10^{-2}	4.897×10^{-2}	1.382×10^{-1}	3.712×10^{-2}	1.056×10^{-1}

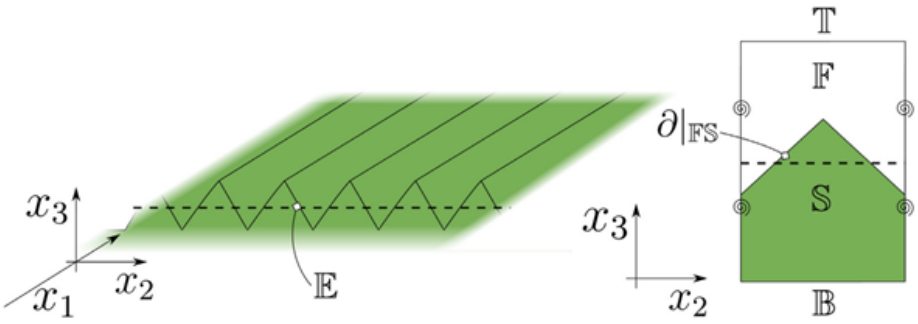

Figure 2.21: Sketch of a deformable, regularly micro-structured surface. Right frame: a periodic unit cell is identified to apply the homogenization technique.

2.4. Compliant Riblets: Problem Formulation and Effective Macrostructural Properties[3]

Based on the idea given in subsection 1.4.7. justify the interest in examining the interaction between elastic, streamwise-elongated wall corrugations and the overlying fluid. We call these indentations compliant riblets. The goal of this work is to develop the mathematical tools to describe compliant riblets, to set the framework in order to optimize their geometrical and structural properties, for drag reduction purposes. The present contribution is thus dedicated to the study of the interface problems, in both the fluid and the solid domains, for prototypical triangular and blade riblets such as those shown in figure 2.21, made of a linearly elastic material and can undergo small deformations; their collective behavior is assumed to occur over a large, elastic wavelength. The presence of two length scales allows for the use of a multiscale homogenization approach yielding microscopic problems for convolution kernels and parameters, which must then be employed in macroscopic boundary conditions to be enforced at a virtual wall through the riblets. The main outcome of the work will be the macroscopic equations ruling the fluid–solid interactions, plus the effective coefficients (or convolution kernels, by virtue of the time dependent nature of the fluid–solid coupling) required to close the macroscopic problem. The results found suggest that, in analogy to the case of rigid riblets, compliant, blade-like wall corrugations are more effective than triangular riblets in reducing skin friction drag, provided the spanwise periodicity of the indentations is sufficiently small for the creeping flow approximation to be tenable. Clearly this work is but the first step of a more comprehensive examination on the effect and design of compliant riblets; the considerations made possible by the analysis reported herein represent a promising path for future investigations.

[3]Zampogna et al. (2019d)

2.4.1. Mathematical Formulation

An incompressible Newtonian fluid of density ρ_f and viscosity μ is assumed to flow over a micro-patterned surface made of a linearly elastic material of density ρ_s, Poisson's ratio v_P and Young's modulus E. A sketch of the surface being considered is represented in 2.21. The objective of this model is to simulate the fluid flow and solid structure deformation without the need of large computational efforts to describe the details of the solid surface and solve the small-scale fluid-solid interactions. The procedure shown in the present section gives rise to equivalent boundary conditions for the macroscopic fields associated with the solid displacement and fluid flow. These boundary conditions must be imposed on an equivalent smooth surface (denoted with $\mathbb{E}$ in 2.21) which is located at a certain (small) distance from the tip of the small-scale protrusions. To proceed with the development of these conditions, we introduce the fluid domain, denoted by $\mathbb{F}$ in 2.21 , in which the incompressible Navier-Stokes equations are valid and write in dimensional form

$$\rho_f \left(\frac{\partial \hat{u}_i}{\partial \hat{t}} + \hat{u}_j \frac{\partial \hat{u}_i}{\partial \hat{x}_j} \right) = \frac{\partial \hat{\Sigma}_{ij}}{\partial \hat{x}_j} \frac{\partial \hat{u}_i}{\partial \hat{x}_i} = 0, \tag{2.172}$$

where $\hat{\Sigma}_{ij}$ is the canonical fluid stress tensor of a Newtonian fluid

$$\hat{\Sigma}_{ij} = -\hat{p}\delta_{ij} + 2\mu\hat{\varepsilon}_{ij}(\hat{\mathbf{u}}), \tag{2.173}$$

and $\hat{\varepsilon}_{ij}(\hat{\mathbf{u}})$ is the strain-rate tensor, formally defined as

$$\hat{\varepsilon}_{ij}(\hat{\mathbf{u}}) = \frac{1}{2} \left(\frac{\partial \hat{u}_i}{\partial \hat{x}_j} + \frac{\partial \hat{u}_j}{\partial \hat{x}_i} \right). \tag{2.174}$$

In the domain $\mathbb{S}$ occupied by the linearly elastic solid, the governing equations read

$$\rho_s \frac{\partial^2 \hat{v}_i}{\partial \hat{t}^2} = \frac{\partial \hat{\sigma}_{ij}}{\partial \hat{x}_j}, \tag{2.175}$$

where $\hat{v}_i$ denote the components of the displacement vector, $\hat{\mathbf{v}}$, and $\hat{\sigma}_{ij}$ is the generic component of the stress tensor. Under the assumption that the structure is elastic, the stress and strain tensors are linearly related through the relation

$$\hat{\sigma}_{ij} = \hat{C}_{ijk}\hat{\varepsilon}_{kl}(\hat{\mathbf{v}}) = \frac{1}{2}\hat{C}_{ijkl} \left(\frac{\partial \hat{v}_k}{\partial \hat{x}_l} + \frac{\partial \hat{v}_l}{\partial \hat{x}_k} \right), \tag{2.176}$$

where $\hat{C}_{ijkl} = \hat{\lambda}\delta_{ij}\delta_{kl} + \hat{G}\left(\delta_{ik}\delta_{jl} + \delta_{il}\delta_{jk}\right)$ are the components of the stiffness tensor, and $\hat{\lambda}$ and $\hat{G}$ are the two Lamé coefficients. These coefficients are related to the Young modulus, E, and Poisson's ratio, v_p, by $\hat{\lambda} = \dfrac{v_p E}{(1+v_p)(1-2v_p)}$ and $\hat{G} = \dfrac{E}{2(1+v_p)}$. The fluid and solid equations are coupled through the matching of velocities and tractions across the microscopic fluid-solid interface denoted with $\partial|_{\mathrm{Es}}, viz.$

$$\hat{u}_i = \frac{\partial \hat{v}_i}{\partial \hat{t}}, \tag{2.177}$$

and

$$\hat{\Sigma}_{ij} n_j = \hat{\sigma}_{ij} n_j, \tag{2.178}$$

with $\mathbf{n} = \{n_j\}$ the unit vector normal to the considered surface, always taken to point into the fluid cell. We also need to specify the boundary conditions at the bottom $\mathbb{B}$, and top $\mathbb{T}$ of the unit cell sketched in 2.21. Continuity of fluid tractions and velocity is imposed on $\mathbb{T}$, i.e.

$$\hat{\Sigma}_{ij} n_j = \hat{\Sigma}^{\text{out}}_{ij}\, n_j \quad \text{and} \quad \hat{u}_i = \hat{u}^{\text{out}}_i\,, \tag{2.179}$$

where the superscript $^{\text{out}}$ denotes the variables on the external side of the cell, cf. Zampogna et al. (2019c). On $\mathbb{B}$ we impose that

$$\hat{v}_i = 0, \tag{2.180}$$

which is equivalent to assuming that the elastic layer is anchored to a rigid, undeformable substrate.

2.4.2. Scaling Relations

We start by assuming that the continuum layer made up by fluid and solid is characterized by a frequency, f, sufficiently large for dynamic effects to be felt at leading order. Then, it can be argued that in the fluid domain

$$\rho_f U \mathrm{f} \sim \frac{P}{l} \sim \mu \frac{U}{l^2}, \tag{2.181}$$

with U the velocity scale, P the pressure scale, and I the microscopic length scale. From the above, we can choose the velocity scale to normalize the governing equations, i.e.

$$U = \frac{Pl}{\mu}. \tag{2.182}$$

We further have a relation between the microscale l and the frequency f, which states that, for viscous effects to balance inertia, l must be of the order of the Stokes layer thickness, i.e.

$$I \sim \sqrt{\frac{\mu}{\rho_f}}. \tag{2.183}$$

The small displacement of the elastic riblets is assumed to occur coherently over a macroscopic length L. This is the case for instance, of honami waves of canopy flows (Dupont et al. (2010)). By equilibrating inertia and diffusion in Cauchy's equation for the solid, we have

$$\rho_s \mathcal{V} \mathbf{f}^2 \sim E \frac{\mathcal{V}}{L^2}, \tag{2.184}$$

so that the macroscale L can be taken to coincide with the elastic wavelength, i.e.

$$L = \frac{1}{f}\sqrt{\frac{E}{\rho_s}}. \tag{2.185}$$

The interface condition (2.177) is useful since it permits to relate the displacement and the velocity scales through

$$U = f\mathcal{V}. \tag{2.186}$$

We are now ready to introduce the relations between the dimensional and dimensionless variables (the latter without hat), setting

$$\hat{t} = \frac{t}{f}, \quad \hat{\mathbf{x}} = l\mathbf{x}, \quad \hat{p} = Pp, \quad \hat{\mathbf{u}} = \frac{Pl}{\mu}\mathbf{u}, \quad \hat{\mathbf{v}} = \frac{Pl}{\mu f}\mathbf{v}. \tag{2.187}$$

Substituting these definitions in the continuity and momentum equations for the fluid phase, we obtain

$$\frac{\partial u_i}{\partial x_i} = 0; \quad \frac{\partial u_i}{\partial t} + \mathrm{Re}\, u_j \frac{\partial u_i}{\partial x_j} = -\frac{\partial p}{\partial x_i} + 2\frac{\partial \varepsilon_{ij}(\mathbf{u})}{\partial x_j} \text{ in } \mathbb{F}, \tag{2.188}$$

where $\varepsilon_{ij}(\mathbf{u}) = \frac{1}{2}\left(\frac{\partial u_i}{\partial x_j} + \frac{\partial u_j}{\partial x_i}\right)$ and $\mathrm{Re} = \frac{\rho_f U l}{\mu} = \epsilon\mathcal{R}$, with $\mathcal{R} = \frac{\rho_f U L}{\mu}$, assuming the microscale Reynolds number Re to be of order ϵ (or possibly smaller). Applying the same procedure to the Cauchy's equation in the solid, we obtain

$$\epsilon^2 \frac{\partial^2 v_i}{\partial t^2} = \frac{\partial \sigma_{ij}}{\partial x_j} \quad \text{in } \mathbb{S}, \tag{2.189}$$

with $\sigma_{ij} = C_{ijkA}\varepsilon_{kl}(\mathbf{v})$ and $C_{ijkl} = \hat{C}_{ijkl}/E$. The continuity of tractions on $\partial|_{\mathbb{E}S}$ becomes

$$-pn_i + 2\varepsilon_{ij}(\mathbf{u})n_j = \epsilon^{-2}\frac{\rho_s}{\rho r} C_{ijkl}\varepsilon_{\mathrm{k}I}(\mathbf{v})n_j, \tag{2.190}$$

and the kinematic condition reads

$$u_i = \frac{\partial v_i}{\partial t}. \tag{2.191}$$

The periodicity condition along x_1 and x_2 in the unit cell (2.21, right frame) must also be enforced, together with $v_i = 0$ at $\mathbb{B}$ and $\Sigma_{ij}n_j = \Sigma_{ij}^{\mathrm{out}}\, n_j$ at $\mathbb{T}$.
Within the micro-patterned elastic layer, we can use the multiscale homogenization approach described by Mei and Vernescu (2010). We introduce the fast (microscopic) and slow (macroscopic) variables, $\mathbf{x} = (x_1, x_2, x_3)$ and $\mathbf{x}' = \epsilon\,(x_1, x_2)$ and the expansions

$$\mathcal{F} = \sum_{i=0}^{\infty} \epsilon^i \mathcal{F}^{(i)}, \tag{2.192}$$

where $\mathcal{F}^{(i)} = \left(\mathbf{u}^{(i)}, \mathbf{v}^{(i)}, p^{(i)}\right)$ is a function of $(\mathbf{x}, \mathbf{x}', t)$. The spatial derivatives become

$$\frac{\partial}{\partial x_i} \to \frac{\partial}{\partial x_i} + \epsilon\frac{\partial}{\partial x_i'} \quad \text{for } i = 1, 2, \tag{2.193}$$

so that

$$\varepsilon_{ij}(\mathbf{u}) \to \varepsilon_{ij}(\mathbf{u}) + \epsilon\varepsilon_{ij}'(\mathbf{u}), \tag{2.194}$$

with $\varepsilon'_{ij}(\mathbf{u}) = \frac{1}{2}\left(\frac{\partial u_i}{\partial x'_j} + \frac{\partial u_j}{\partial x'_i}\right)$. The slow variable has a missing third entry because the micro-structured layer does not extend macroscopically along the normal-to-the-surface direction, x_3 (cf. 2.21). For simplicity, we maintain the notation x'_i, with the understanding that i can only be equal to 1 or 2 . The fluid equations at order ϵ^0 and ϵ^1 in F then read

$$\frac{\partial u_{\mathrm{i}}^{(0)}}{\partial x_i} = 0, \tag{2.195}$$

$$\frac{\partial u_i^{(1)}}{\partial x_i} + \frac{\partial u_i^{(0)}}{\partial x'_i} = 0, \tag{2.196}$$

$$\frac{\partial u_i^{(0)}}{\partial t} = \frac{\partial \Sigma_{ij}^{(0)}}{\partial x_j} = -\frac{\partial p^{(0)}}{\partial x_i} + \frac{\partial^2 u_i^{(0)}}{\partial x_k^2}, \tag{2.197}$$

$$\frac{\partial u_i^{(1)}}{\partial t} + \mathcal{R} u_j^{(0)} \frac{\partial u_i^{(0)}}{\partial x_j} = \frac{\partial \Sigma_{ij}^{(0)}}{\partial x'_j} + \frac{\partial \Sigma_{ij}^{(1)}}{\partial x_j} \tag{2.198}$$

In (2.197) and (2.198) we have used the definition

$$\Sigma_{ij}^{(n)} = -p^{(n)}\delta_{ij} + 2\left[\varepsilon_{ij}\left(\mathbf{u}^{(n)}\right) + \varepsilon'_{ij}\left(\mathbf{u}^{(n-1)}\right)\right], \tag{2.199}$$

for each $n \geq 0$, with $\mathbf{u}^{(-1)} = 0$ for consistency. Similarly, the equations describing the motion of the solid structure at

$$\frac{\partial \sigma_{ij}^{(0)}}{\partial x_j} = 0, \tag{2.200}$$

$$0 = \frac{\partial \sigma_{ij}^{(1)}}{\partial x_j} + \frac{\partial \sigma_{ij}^{(0)}}{\partial x'_j}, \tag{2.201}$$

$$\frac{\partial^2 v_i^{(0)}}{\partial t^2} = \frac{\partial \sigma_{ij}^{(2)}}{\partial x_j} + \frac{\partial \sigma_{ij}^{(1)}}{\partial x'_j}, \tag{2.202}$$

In (2.201) and (2.202) the stress tensor at each order, $\sigma_{ij}^{(n)}$, is defined as

$$\sigma_{ij}^{(n)} = C_{ijkl}\left[\varepsilon_{kl}\left(\mathbf{v}^{(n)}\right) + \varepsilon'_{kl}\left(\mathbf{v}^{(n-1)}\right)\right], \tag{2.203}$$

for each $n \geq 0$, with $\mathbf{v}^{(-1)} = 0$ for consistency. On $\partial|_{\mathrm{ss}}$ the interface conditions read

$$u_i^{(0)} = \frac{\partial v_i^{(0)}}{\partial t}, \tag{2.204}$$

$$u_i^{(1)} = \frac{\partial v_i^{(1)}}{\partial t}, \tag{2.205}$$

$$\sigma_{ij}^{(0)} n_j = 0, \tag{2.206}$$

$$\sigma_{ij}^{(1)} n_j = 0, \tag{2.207}$$

$$\frac{\rho_s}{\rho_f}\sigma_{ij}^{(2)} n_j = \Sigma_{ij}^{(0)} n_j = -p^{(0)} n_i + 2\varepsilon_{ij}\left(\mathbf{u}^{(0)}\right) n_j. \tag{2.208}$$

To manage the stress boundary condition in Eq. (2.179) on the top side of the cell, T, we follow the same procedure as in Zampogna et al. (2019c), by truncating the continuity of tractions at order ϵ, which in the present case yields

$$\Sigma_{ij}^{(0)} n_j + \epsilon \Sigma_{ij}^{(1)} n_j = \Sigma_{ij}^{out} n_j \quad \text{on } \mathbb{T}. \tag{2.209}$$

The outer stress tensor depends on the outer quantities defined in Zampogna et al. (2019c) (i.e. $\mathbf{x}^{\text{out}} = (x_1', x_2', x_3^{\text{out}})$ with $x_2^{\text{out}} = \epsilon X_3$) and is assumed not to be influenced by small-scale effects (this assumption applies if $\mathbb{T}$ is sufficiently far from the elastic, microstructured wall). Collecting terms at each order in (2.209), we obtain

$$\Sigma_{ij}^{(0)} n_j = \Sigma_{ij}^{\text{out}}\, n_j \quad \text{on } \mathbb{T}, \tag{2.210}$$

and

$$\Sigma_{ij}^{(1)} n_j = 0 \quad \text{ on } \mathbb{T}. \tag{2.211}$$

Using arguments similar to those employed in Zampogna et al. (2019c), one also has $\epsilon u_i^{(0)} = u_i^{\text{out}}$ on the upper boundary. Finally, the boundary condition (2.180) on $\mathbb{B}$ is merely a homogeneous Dirichlet condition for the displacement at each order. Other boundary conditions can be used on $\mathbb{B}$, such as prescribed shear or normal stress to impose a specific time-varying deformation of the elastic layer.

2.4.3. The Macroscopic Model

Eq. (2.200) and the homogeneous boundary condition (2.206) imply that $v^{(0)}$ does not depend on the microscopic variable, i.e. $v^{(0)} = v^{(0)}(\mathbf{x}', t)$, so that $\sigma_{ij}^{(0)} = 0$. Eqs. (2.195) and (2.197) can then be written in terms of the velocity of the fluid relative to that of the solid, as

$$\frac{\partial}{\partial x_i}\left(u_i^{(0)} - \dot{v}_i^{(0)}\right) = 0, \tag{2.212}$$

$$\frac{\partial}{\partial t}\left(u_i^{(0)} - \dot{v}_i^{(0)}\right) = -\ddot{v}_i^{(0)} - \frac{\partial p^{(0)}}{\partial x_i} + \frac{\partial^2}{\partial x_k^2}\left(u_i^{(0)} - \dot{v}_i^{(0)}\right). \tag{2.213}$$

Because of linearity, the solution of (2.212) and (2.213) with boundary conditions (2.204) and (2.210) can be expressed with four convolution kernels, $L_{i,k}(\mathbf{x}, t), H_{ij}(\mathbf{x}, t), B_{jk}(\mathbf{x}, t)$ and $A_j(\mathbf{x}, t)$, as

$$u_i^{(0)} - \dot{v}_i^{(0)} = \int_0^t L_{ijk}(\mathbf{x}, t-t')\, \varepsilon_{jk}'\left(\mathbf{u}^{\text{out}}; t'\right) dt' + \int_0^t H_{ij}(\mathbf{x}, t-t')\, \ddot{v}_j^{(0)}(\mathbf{x}', t')\, dt', \tag{2.214}$$

$$p^{(0)} = \bar{p}^{(0)}\left(\mathbf{x}', t\right) + \int_0^t B_{jk}\left(\mathbf{x}, t-t'\right)\varepsilon'_{jk}\left(\mathbf{u}^{\text{out}}\,; t'\right)dt' + \int_0^t A_j\left(\mathbf{x}, t-t'\right)\ddot{v}_j^{(0)}\left(\mathbf{x}', t'\right)\mathrm{dt}', \tag{2.215}$$

where $\bar{p}^{(0)}$ is the macroscopic reference pressure which can be set thanks to the third component of (2.210). By substituting (2.214) and (2.215) into ((2.212), (2.213), (2.204) and (2.210), the tensors L_{ijk}, H_{ij}, B_{jk} and A_j are found to satisfy the following microscopic problems:

$$\begin{cases} \dfrac{\partial L_{ijk}}{\partial t} = -\dfrac{\partial B_{jk}}{\partial x_i} + \nabla^2 L_{ijk} \text{ in } \mathbb{F}, \\ \dfrac{\partial L_{ijk}}{\partial x_i} = 0 \text{ in } \mathbb{F}, \\ L_{ijk} = 0 \text{ on } \partial|_{\mathbb{FS}}\,, \\ \mathcal{U}\left(t'\right)\mathcal{U}\left(t-t'\right)\varepsilon_{ij}\left(L_{\cdot pq}\left(t-t'\right)\right)n_j = \delta\left(t'-t\right)\delta_{ip}\delta_{jq}n_j \text{ on } \mathbb{T}, \\ L_{ijk}, B_{jk} \text{ periodic along the tangential directions 1 and 2,} \end{cases} \tag{2.216}$$

$$\begin{cases} \dfrac{\partial H_{ij}}{\partial t} = -\dfrac{\partial A_j}{\partial x_i} + \nabla^2 H_{ij} \quad \text{in } \mathbb{F}, \\ \dfrac{\partial H_{ij}}{\partial x_i} = 0 \text{ in } \mathbb{F}, \\ H_{ij} = 0 \text{ on } \partial|_{\mathbb{FS}}\,, \\ \varepsilon_{ij}\left(H_{\cdot p}\right)n_j = 0 \text{ on } \mathbb{T}, \\ H_{ij}, A_j \quad \text{periodic along the tangential directions 1 and 2,} \end{cases} \tag{2.217}$$

subject to the initial condition $L_{ijk}(\mathbf{x}, 0) = 0$ and $H_{ij}(\mathbf{x}, 0) = -\delta_{ij}$. In the boundary condition at the top of the domain, $\mathbb{T}$, for system (2.216), $\mathcal{U}(t)$ is the unit step function and $\delta(t)$ is the Dirac delta function. The solutions of interest are transients. In particular, since $\boldsymbol{L}$ solves the problem (2.216) for each t' greater than 0 , it is univocally defined up to a temporal translation in t'. To obtain a numerical solution we set $t' = 0$.
At this point we introduce the spatial average over a unit cell to deduce macroscopic equations valid over the homogenized domain. This average is defined using an integral over either the fluid, $\mathbb{F}$, or the solid, $\mathbb{S}$, domain as:

$$\langle f \rangle := \frac{1}{|\mathbb{F} \cup \mathbb{S}|}\int_{\mathbb{F}|\mathbb{S}} f dV, \tag{2.218}$$

where $|\cdot|$ denotes the volume of the corresponding domain. It could be alternatively defined with an integral over the total volume of the unit cell, introducing a filter function to discern whether the integrand refers to the fluid or the solid. After (2.218) is applied, the microscopic three-dimensional cell reduces to a single macroscopic point lying on a 2-manifold located at a constant distance, d, from a reference (x_1, x_2) plane through the micro-patterned surface. Macroscopically speaking, since d is of order ϵ and spatial variations smaller than ϵ cannot be measured by the slow variable $\mathbf{x}'$, we are allowed to take $d = 0$. As shown in Zampogna et al. (2019c), the present theory is not able to estimate the value of d better than $d = 0$, since we are approximating the physical phenomenon at leading order in ϵ. Directly linked to this fact is also the choice of $\hat{h}$, the

normal-to-the-surface height of the unit cell over which the variables must be averaged. Since $\hat{h}$ must be of order $l = \epsilon L$ in the present theory, we do not introduce any error by taking $h = 2$ to include a balanced fraction of solid and fluid in the cell. Other definitions of averages can be used in order to deduce effective properties starting from the microscopic tensors.
The macroscopic equations for the fluid quantities are found by applying the spatial average over the fluid domain $\mathbb{F}$ to (2.214) and (2.215), leading to

$$\left\langle u_i^{(0)} \right\rangle - \theta \frac{\partial v_i^{(0)}}{\partial t} = \int_0^t \mathcal{L}_{ijk} \varepsilon'_{jk} \left(\mathbf{u}^{out}; t' \right) + \mathcal{H}_{ij} \ddot{v}_j^{(0)} \left(\mathbf{x}', t' \right) dt', \tag{2.219}$$

$$\left\langle p^{(0)} \right\rangle = \left\langle \bar{p}^{(0)} \left(\mathbf{x}', t \right) \right\rangle + \int_0^t \mathcal{B}_{jk} \varepsilon'_{jk} \left(\mathbf{u}^{out}; t' \right) + \mathcal{A}_j \ddot{v}_j^{(0)} \left(\mathbf{x}', t' \right) dt', \tag{2.220}$$

with $\theta = \frac{|\mathbb{F}|}{|\mathbb{F} \cup \mathbb{S}|}$. The quantities $\mathcal{L}_{ijk}, \mathcal{H}_{ij}, \mathcal{B}_{jk}$ and $\mathcal{A}_j$ are defined as

$$\mathcal{L}_{ijk} = \langle L_{ijk} \rangle, \quad \mathcal{H}_{ij} = \langle H_{ij} \rangle, \quad \mathcal{B}_{jk} = \langle B_{jk} \rangle \quad \text{and} \quad \mathcal{A}_j = \langle A_j \rangle, \tag{2.221}$$

where $\mathcal{L}_{ijk}$ is the dynamic slip tensor. To ensure uniqueness of the solution of problems (2.216) and (2.217), we also take $\langle B_{jk} \rangle = 0$ and $\langle A_j \rangle = 0$, so that Eq. (2.220) simplifies to $\left\langle p^{(0)} \right\rangle = \left\langle \bar{p}^{(0)} \left(\mathbf{x}', t \right) \right\rangle$.
We now consider the linearly elastic solid. Eq. (2.201) reduces to

$$\frac{\partial}{\partial x_j} C_{ijkl} \varepsilon_{kl} \left(\mathbf{v}^{(1)} \right) = 0, \tag{2.222}$$

and the interface condition (2.207) valid on $\partial|_{\mathrm{FS}}$ becomes

$$C_{ijkl} \varepsilon_{kl} \left(\mathbf{v}^{(1)} \right) n_j = -C_{ijk} \varepsilon'_{kl} \left(\mathbf{v}^{(0)} \right) n_j. \tag{2.223}$$

The solution of (2.222) and (2.223) can formally be written as

$$v_i^{(1)} \left(\mathbf{x}, \mathbf{x}', t \right) = \chi_i^{pq}(\mathbf{x}) \varepsilon'_{pq} \left(\mathbf{v}^{(0)} \right) \left(\mathbf{x}', t \right). \tag{2.224}$$

Replacing (2.224) into (2.222) and (2.223), χ^{pq} is found to satisfy the microscopic problem:

$$\begin{cases} \frac{\partial}{\partial x_j} \left\{ C_{ijkl} \left[\varepsilon_{kl} \left(\chi^{pq} \right) \right] \right\} = 0 \text{ in } \mathbb{S}, \\ \left\{ C_{ijkl} \left[\varepsilon_{kl} \left(\chi^{pq} \right) + \delta_{kp} \delta_{lq} \right] \right\} n_j = 0 \text{ on } \partial|_{\mathrm{RS}}, \\ \chi_i^{pq} \text{ periodic along tangential directions 1 and 2,} \\ \chi_i^{pq} = 0 \text{ on } \mathbb{B}. \end{cases} \tag{2.225}$$

Summing the dimensionless momentum equations of fluid and solid at the various orders, and retaining terms up to order ϵ^0 we have:

$$\epsilon^{-1} \left[\Xi \left(\frac{\rho_s}{\rho_f} \frac{\partial \sigma_{ij}^{(1)}}{\partial x_j} \right) \right] + \epsilon^0 \left[(1 - \Xi) \left(-\frac{\partial u_i^{(0)}}{\partial t} + \frac{\partial \Sigma_{ij}^{(0)}}{\partial x_j} \right) + \Xi \left(-\frac{\rho_s}{\rho_f} \frac{\partial^2 v_i^{(0)}}{\partial t^2} + \frac{\partial \sigma_{ij}^{(2)}}{\partial x_j} + \frac{\partial \sigma_{ij}^{(1)}}{\partial x'_j} \right) \right] = 0, \tag{2.226}$$

with Ξ a filter function, equal to 1 (or 0) when at each instant in time there is solid (or fluid) matter at any position $\mathbf{x}$. We can now average over the total volume of the unit cell and, making use of Gauss' theorem and of the boundary conditions, obtain the macroscopic momentum equation for the fluid-solid composite in the form:

$$\left\{\left[\frac{\rho_s}{\rho_f}+\theta\left(1-\frac{\rho_s}{\rho_f}\right)\right]\delta_{ij}+\mathcal{H}_{ij}\right\}\ddot{v}_j^{(0)}+\mathcal{L}_{ijk}\varepsilon'_{jk}\left(\mathbf{u}^{\text{out}}\right)=\frac{\rho_s}{\rho_f}\frac{\partial}{\partial x'_j}\mathfrak{c}_{ijkl}\varepsilon'_{kl}\left(\mathbf{v}^{(0)}\right)-\frac{1}{|\mathbb{F}\cup\mathbb{S}|}\int_{\mathbb{T}}\Sigma_{ij}^{\text{out}}\,n_j dA, \tag{2.227}$$

with the components of the effective stiffness tensor $\mathfrak{C}$ given by

$$\mathfrak{C}_{ijkl}=C_{ijpq}\left\langle\varepsilon_{pq}\left(\chi^{kl}\right)\right\rangle+\left\langle C_{ijpq}\delta_{pk}\delta_{ql}\right\rangle. \tag{2.228}$$

Finally, we need a third equation to formally close the macroscopic problem. This is linked to the mass balance of the composite medium and is found by taking the average of (2.196) over $\mathbb{F}$, yielding

$$\frac{\partial\left\langle u_i^{(0)}\right\rangle}{\partial x'_i}=\mathfrak{D}_{pq}\varepsilon'_{pq}\left(\dot{\mathbf{v}}^{(0)}\right), \tag{2.229}$$

with the components of the compression/dilatation tensor $\mathfrak{D}$ given by

$$\mathfrak{D}_{pq}=\frac{1}{|\mathbb{F}\cup\mathbb{S}|}\int_{\partial|\mathbb{E}\mathbb{S}}\chi_i^{pq}(\mathbf{x})n_i dA. \tag{2.230}$$

Eq. (2.219) represents a modified boundary condition for the velocity field in the outer fluid and requires the knowledge of the solid displacement field at leading order. Thus, at each time step, the solutions of (2.219),(2.227) and (2.229) must be pursued to yield the unknowns $\left\langle\mathbf{u}^{(0)}\right\rangle, \left\langle p^{(0)}\right\rangle$ and $\mathbf{v}^{(0)}$. Before being able to do this it is, however, necessary to evaluate the effective tensors $\mathcal{L}_{ijk}, \mathcal{H}_{ij}, \mathbb{C}_{ijkl}$ and $\mathfrak{D}_{pq}$ for given shapes and properties of the periodic surface micro-structure.

2.4.4. Solution of the Microscopic Problem and Effective Macroscopic Parameters

In order to apply the equivalent boundary condition (2.219), the microscopic problems (2.216), (2.217) and (2.225) have to be solved. Once their solution is computed, the averaged values over a unit cell (the so-called effective coefficients of the micro-structured elastic surface) are available. The computational microscopic domain used to find the solution of (2.216) (2.217) and (2.225) extends, along x_3, from -1 up to 5 (normalizing distances with l), and the near-interface solution does not change when the upper boundary is moved farther from the interface. For the purpose of volume averaging (definition (2.218)) the unit cell goes from -1 to $+1$ along x_3 (cf. figure A.4 where a typical grid is also shown), so that the total dimensionless volume in the denominator of Eq. (2.218) is $1\times 1\times 2$. The results discussed below correspond to both a triangular riblet-like surface with an opening angle of 90° (see figure A.4) and to blade riblets. The surface over which the riblets are positioned is a plane with tangent vectors $\hat{e}_1$ and $\hat{e}_2$ and normal vector $\hat{e}_3$.

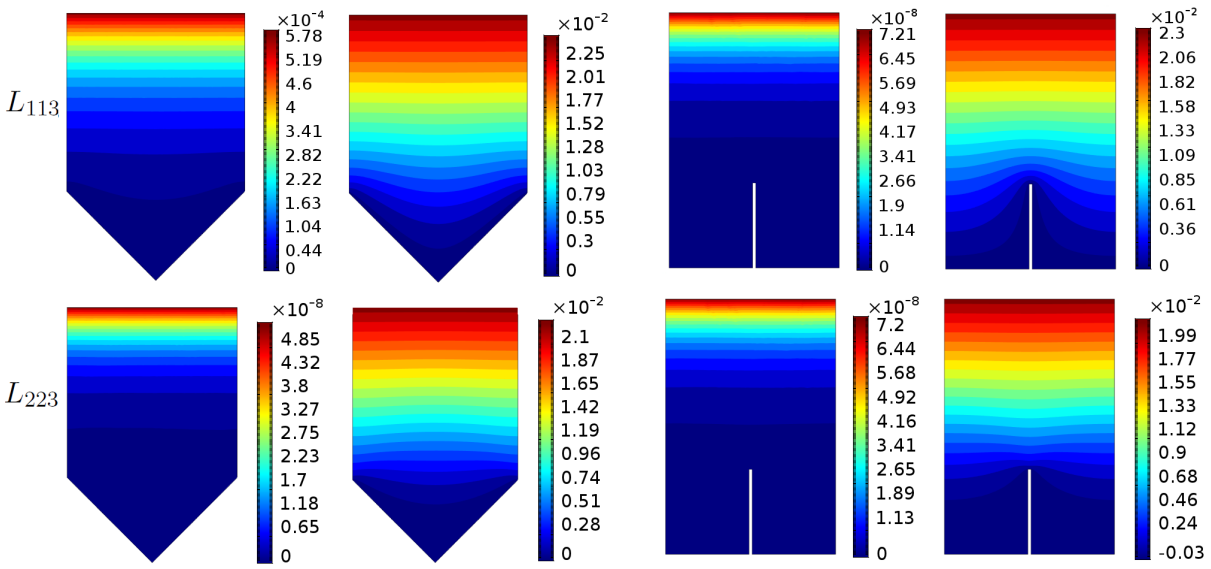

Figure 2.22: Isosurfaces of L_{113} (top row) and L_{223} (bottom row) at two instants in time ($t = 1$ and $t = 20$), for triangular and blade riblets.

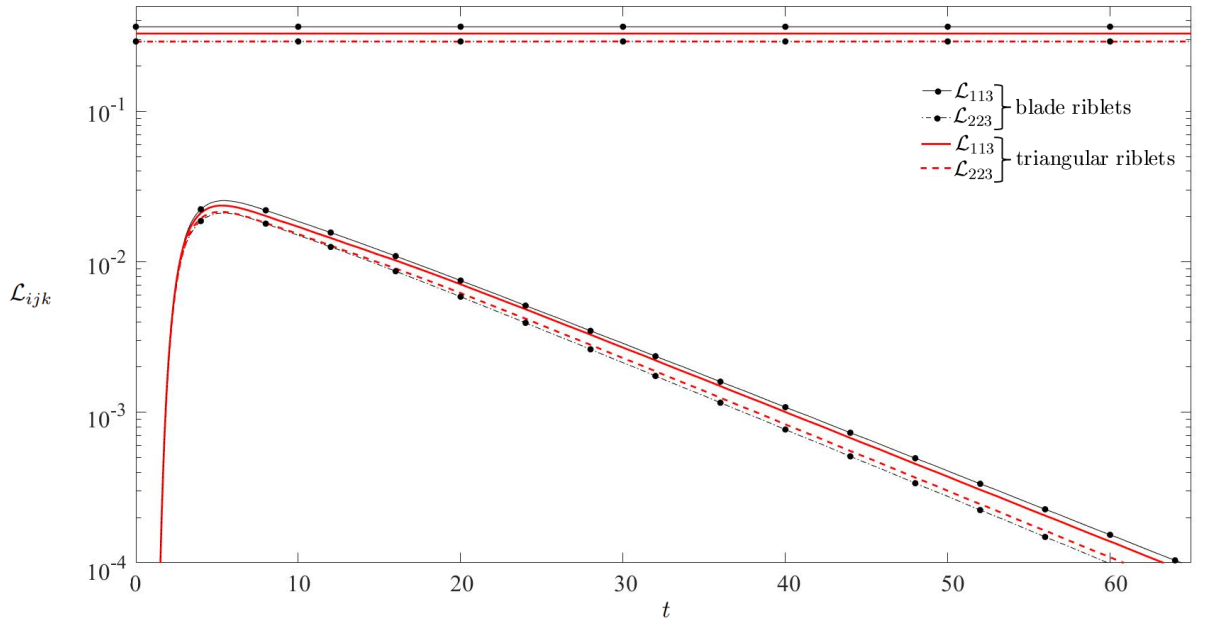

Figure 2.23: Variation in time of the nonzero components of the dynamic slip tensor $\mathcal{L}$ for a Gaussian impulse centered at $t' = 0$. The straight lines drawn for comparison purposes represent the corresponding values of the components of the slip tensor for the case of rigid riblets, normalized with the same volume used in the compliant case. Black solid lines represents $\mathcal{L}_{113}$ and dashed lines represents $\mathcal{L}_{223}$ for blade type riblets, and similarly red color denoted triangular riblets.

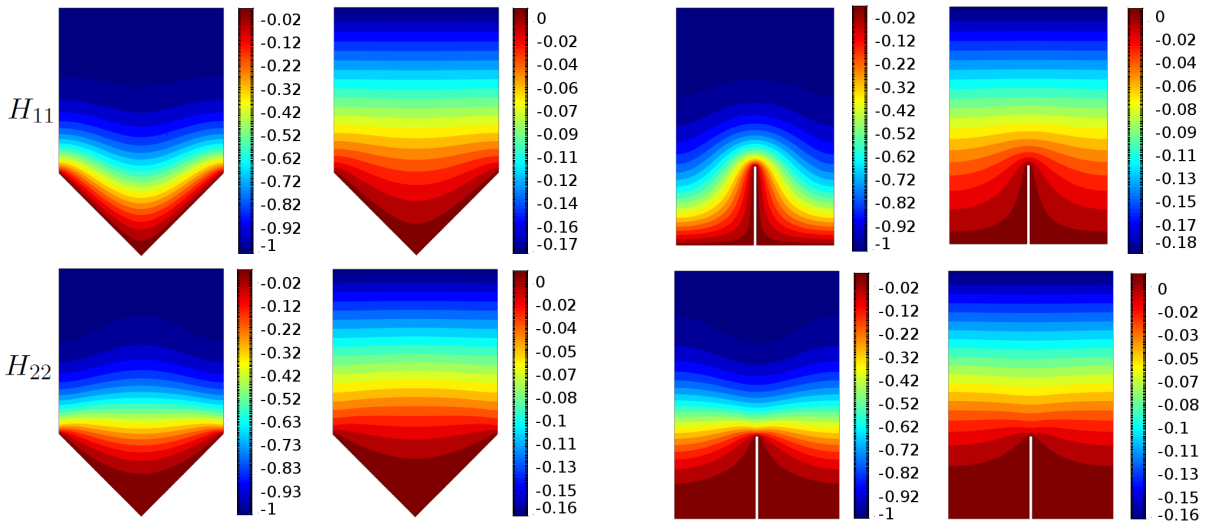

Figure 2.24: Nonzero components of $\mathcal{H}$ at two instants of time, $t = 0.05$ and $t = 20$, for triangular and blade riblets.

The elastic solid forming the rough layer is assumed to be made of an isotropic material, the Poisson's ratio of which, υ_P, is taken, by way of illustration, equal to 0.330. Hence the first and the second Iamé coefficients, $\hat{\lambda}$ and $\hat{\sigma}_1$, are 0.730 F and 0.376 F, respectively. The resulting dimensionless fourth-order isotropic stiffness tensor $\mathbf{C}$ of the material forming the wall indentations has components C_{ijkl} which read, in Voigt's notation (Voigt, 1889):

$$\mathbf{C} = \begin{pmatrix} C_{1111} & C_{1122} & C_{1133} & C_{1123} & C_{1113} & C_{1112} \\ C_{2211} & C_{2222} & C_{2233} & C_{2223} & C_{2213} & C_{2212} \\ C_{3311} & C_{3322} & C_{3333} & C_{3323} & C_{3313} & C_{3312} \\ C_{2311} & C_{2322} & C_{2333} & C_{2323} & C_{2313} & C_{2312} \\ C_{1311} & C_{1322} & C_{1333} & C_{1323} & C_{1313} & C_{1312} \\ C_{1211} & C_{1222} & C_{1233} & C_{1223} & C_{1213} & C_{1212} \end{pmatrix} = \begin{pmatrix} 1.482 & 0.730 & 0.730 & 0 & 0 & 0 \\ 0.730 & 1.482 & 0.730 & 0 & 0 & 0 \\ 0.730 & 0.730 & 1.482 & 0 & 0 & 0 \\ 0 & 0 & 0 & 0.376 & 0 & 0 \\ 0 & 0 & 0 & 0 & 0.376 & 0 \\ 0 & 0 & 0 & 0 & 0 & 0.376 \end{pmatrix}. \tag{2.231}$$

The independent entries of this matrix are at the most 21 , instead of 36, for the most general anisotropic linear elastic material, because of the symmetry properties $C_{ijkl} = C_{jikl} = C_{ijlk} = C_{klij}$. In the present case of isotropic material the independent entries reduce to two, $C_{1111} = C_{2222} = C_{3333}$ and $C_{1122} = C_{1133} = C_{2233}$, with $C_{1212} = C_{1313} = C_{2323} = (C_{1111} - C_{1122})/2$. We will see, however, that the effective stiffness is anisotropic.

2.4.5. The Convolution Kernels in the Fluid Domain

In this section we analyze the solution of problems (2.216) and (2.217). These are time-dependent linear Stokes problems valid over the $\mathbb{F}$ domain, with a inhomogeneous initial condition (problem (2.217)) or inhomogeneous boundary conditions imposed on $\mathbb{T}$ (problem (2.216)). The boundary condition on $\mathbb{T}$ for problem (2.216) involves a Dirac distri-

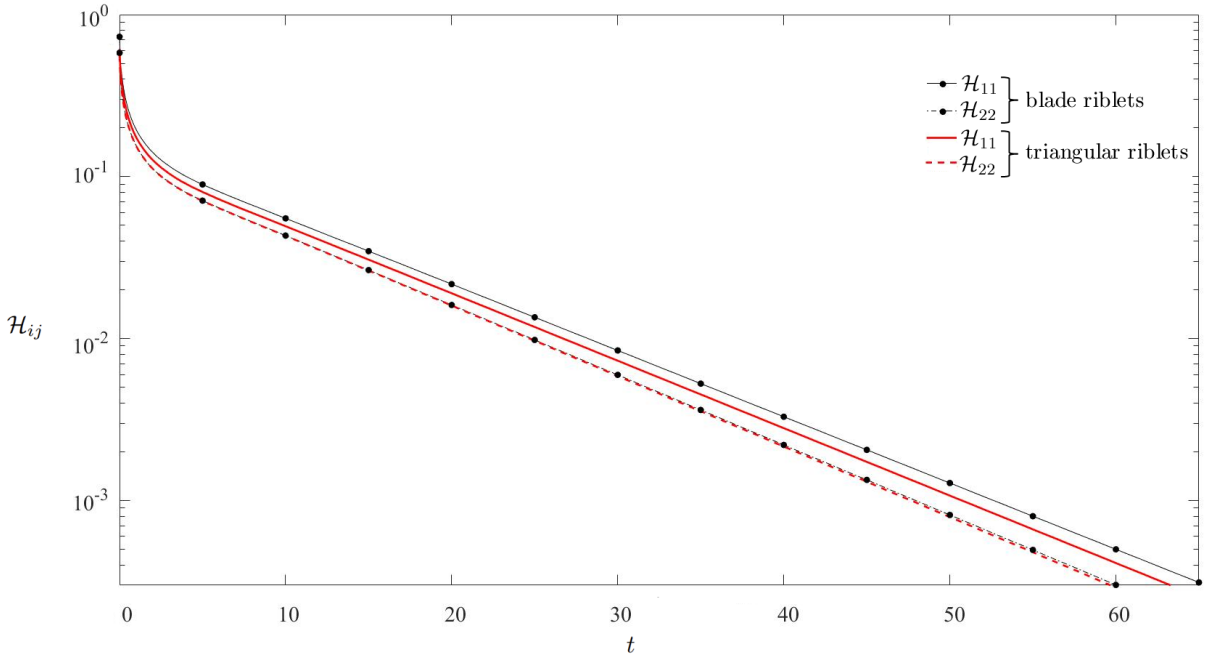

Figure 2.25: Time evolution of the nonzero components of $\mathcal{H}$ with the same color scheme as used in 2.23

bution which has been regularized numerically as a Gaussian impulse, $\mathcal{G}_\delta = \frac{1}{\sqrt{2\pi\delta}} e^{\frac{-t^2}{2\delta}}$. The convergence of the results by decreasing δ to zero has been checked. The fact that the micro-patterned elastic layer is placed over a planar surface with tangent and normal vectors that do not vary in space implies that only L_{i13} and L_{i23} differ from zero (this was shown in Zampogna et al., 2019 in the case of rigid micro-structures). In figure 2.22, the relevant components of $\boldsymbol{L}$ are shown for two successive instants of time. The volume average of $\boldsymbol{L}$ plays a central role in the macroscopic model developed in the previous section. as its components represent the instantaneous slip lengths associated with the relative fluid-solid tangential velocity. In contrast, $\boldsymbol{B}$ is identically zero within the microscopic domain. After volume averaging $\boldsymbol{L}$ over $\mathbb{F}$, the only nonzero components are $\langle L_{113} \rangle$ and $\langle L_{223} \rangle$; their behavior in time is shown in figure 2.23 , and displays an initial increase followed by an exponential decrease at the same rate for the two components when t exceeds 10 , for both riblets' shapes considered. The two components $\mathcal{L}_{113}$ and $\mathcal{L}_{223}$ are, respectively, the analogous of the longitudinal and transverse slip lengths, λ_x and λ_z, the definition of which can be found in Luchini et al. (1991). Similar to the conclusions of Luchini et al. (1991), they do not vary with the height of the computational cell (provided the average is always taken over the same volume, i.e. over a cell of dimensions $1 \times 1 \times 2$, in l-units). The fact that $\mathcal{L}_{113}$ is consistently larger than $\mathcal{L}_{223}$ suggests that compliant riblets reduce skin friction drag, furthermore, figure 2.23 suggests that compliant blade riblets are more effective as drag reducing agents than their triangular counterpart. For comparison purposes, also the time-invariant components of the slip tensor of the rigid

case, $\lambda_x = 0.3281$ and $\lambda_z = 0.2901$ for triangular riblets, $\lambda_x = 0.3642$ and $\lambda_z = 0.2907$ for blade riblets, are displayed in figure 2.23.

The calculations further show that the vector A is equal to zero within the computational domain, while H (whose components are shown for two different instants of time in figure 2.24) behaves similarly to $\boldsymbol{L}$ with one difference: it asymptotically approaches zero from the negative side. One should also note that $\mathcal{H}_{11} - \mathcal{H}_{22}$ is larger for the case of blade riblets than for triangular riblets, for any time, (cf. figure 2.25); the consequences of this are as yet undetermined, even if the monotonic decay of $|\mathcal{H}|$ could suggest that the acceleration of the structure holds a minor role.

2.4.6. The Tensors $\mathfrak{C}$ and $\mathfrak{D}$ in the Solid Domain

The tensor χ is the solution of the steady, second order partial differential equation (2.225) defined over the $\mathbb{S}$ domain. It informs on the microscopic displacement of the structure due to internal deformations, thus affecting the components of both the elasticity and the compression/dilatation tensors.

The spatial distribution of some components of χ may be observed in figure 8 for triangular and blade riblets; for both geometries it is found that $\chi_1^{13} = \chi_2^{23} = \chi_3^{33}$, which is the reason why only the latter component is shown in the figure. Other components not shown vanish after volume averaging, owing to their antisymmetry with respect to a vertical mid-line. All nonzero volume-averaged components are listed in 2.9 Once the tensor χ is available, the components $\mathfrak{C}_{ijkl}$ of the effective stiffness tensor ($cf.$ Eq. 2.228) can be computed, and the result, in Voigt's notation, is:

$$\boldsymbol{C} = \begin{pmatrix} 0.693 & 0.432 & 0.547 & 0 & 0 & 0 \\ 0.432 & 0.779 & 0.547 & 0 & 0 & 0 \\ 0.547 & 0.547 & 1.111 & 0 & 0 & 0 \\ 0 & 0 & 0 & 0.282 & 0 & 0 \\ 0 & 0 & 0 & 0 & 0.282 & 0 \\ 0 & 0 & 0 & 0 & 0 & 0.162 \end{pmatrix}, \tag{2.232}$$

$$\boldsymbol{C} = \begin{pmatrix} 0.470 & 0.279 & 0.373 & 0 & 0 & 0 \\ 0.279 & 0.475 & 0.373 & 0 & 0 & 0 \\ 0.373 & 0.373 & 0.756 & 0 & 0 & 0 \\ 0 & 0 & 0 & 0.192 & 0 & 0 \\ 0 & 0 & 0 & 0 & 0.192 & 0 \\ 0 & 0 & 0 & 0 & 0 & 0.098 \end{pmatrix}, \tag{2.233}$$

for, respectively, triangular and blade-like riblets. The volume of the solid portion for the triangular wall corrugations is 0.75; that for the blade riblets is 0.51 (against a total volume, fluid plus solid, used in Eq. (2.218) equal to 2). The values of the entries in (2.232) and (2.233) would change by changing the microscopic volume over which Eq. (2.227) is applied; however. the structure of the effective elasticity matrix would not change, and

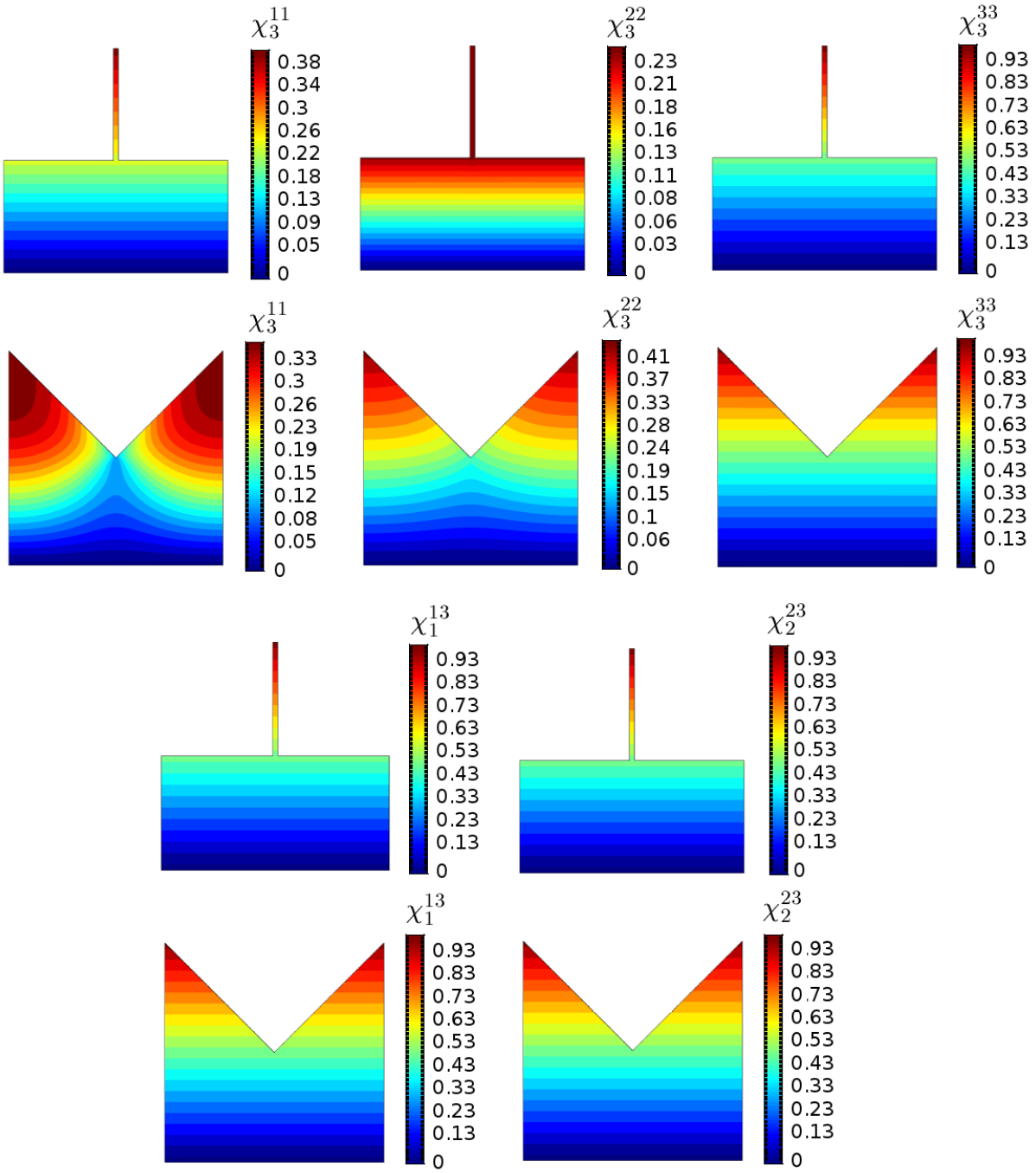

Figure 2.26: Relevant components of χ on the domain $\mathbb{S}$.

Table 2.9: Nonzero volume-averaged entries of the microscopic solid tensor.

Riblets' type	$\langle\chi_3^{11}\rangle$	$\langle\chi_3^{22}\rangle$	$\langle\chi_1^{13}\rangle$=$\langle\chi_2^{23}\rangle$=$\langle\chi_3^{33}\rangle$
Triangular	0.070	0.072	0.146
Blade	0.033	0.032	0.066

is the same in the two geometries considered. The effective stiffness tensor is orthotropic (Cowin (2013)), with three mutually orthogonal planes of reflection symmetry; however, only seven independent components are present (instead of nine) since $\mathfrak{C}_{1133} = \mathrm{C}_{2233}$ and $\mathrm{C}_{2323} = \mathrm{C}_{1313}$ and this stems from geometrical invariance in x_1 and periodicity in x_2. Finally, the compression/dilatation tensor of use in the mass conservation equation of the composite turns out to be diagonal, i.e.

$$\mathfrak{D} = \begin{pmatrix} 0.188 & 0 & 0 \\ 0 & 0.218 & 0 \\ 0 & 0 & 0.265 \end{pmatrix}, \tag{2.234}$$

$$\mathfrak{D} = \begin{pmatrix} 0.125 & 0 & 0 \\ 0 & 0.123 & 0 \\ 0 & 0 & 0.255 \end{pmatrix}. \tag{2.235}$$

for triangular and blade-like indentations, respectively. This tensor measures the compressibility of the elastic substrate and is the main responsible of a non-zero normal velocity, $\left\langle u_3^{(0)} \right\rangle$, which, in the case of rigid protrusions, has previously been set to zero at leading order (Zampogna et al., 2019).

MACROSCOPIC PROBLEMS

3.1. Summary

Effective and fully-feature simulations are conducted for following classical configurations:

- *Hiemenz stagnation point flow over a rough wall*: The high-order effective conditions apply to a steady, laminar flow case. In the Hiemenz flow over a rough wall is demonstrated. In this case, the differences between the exact results and those obtained using conditions of different asymptotic orders are highlighted. In particular, for the problem under consideration, a difference in the streamwise velocity is observed between the effective macroscopic conditions at orders one and two, whereas the terms of order three only slightly correct the order-two result by comparing with the results of feature resolving simulations.

- *Hiemenz stagnation point flow over a porous bed and flow over backward facing step with the step region made of a porous material*: This test case is to verify the accuracy of the interface conditions in which macroscopic solutions are compared to feature-resolving simulations. A good agreement is observed for a large value of the porosity, which results in significant infiltration of the fluid into the porous medium. In addition to this, excellent agreement is demonstrated even for the large values of Reynolds number for which the theory is not formally applicable.

- *Pressure-driven turbulent flow over a permeable walls in a rectangular periodic channel*: The application of the interface conditions developed for the permeable interface between the free-fluid region and porous media are also tested for a fully turbulent flow in a periodic channel, where a constant pressure gradient drives the flow. The findings suggest that the interface conditions influence near-wall turbulence similarly to the full features and the case of riblets. Results also suggested that the optimal design of the porous medium can be quickly obtained for the possible reduction of skin friction drag using the effective coefficients without full-feature resoling simulations. It is also observed that the homogenized model characterizing the flow over the microstructured porous media works well and is computationally cheap as compared to the full-featured simulations, even in the turbulent flow problems using the direct numerical simulations.

3.2. Hiemenz Stagnation Point Flow over a Rough Plate

To assess the accuracy of the effective wall conditions we have chosen to study a steady boundary layer flow past a rough wall; the configuration considered is the stagnation point flow, an exact solution of the Navier-Stokes equations when the wall is smooth. As

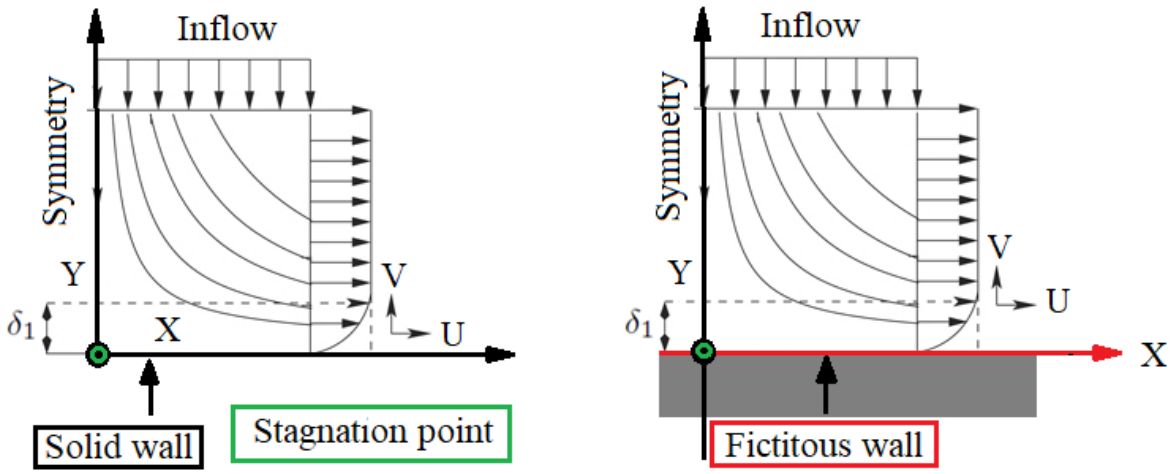

Figure 3.1: Schematic of the stagnation point flow on a smooth wall (left) and over a rough surface (right) where the grey color indicates the rough region.

it turns out, a similarity solution exists also when the wall is rough and this is addressed first.

3.2.1. Two-Dimensional Hiemenz Flow Over a Rough Wall: A Similarity Formulation

The ansatz behind Hiemenz similarity solution for viscous incompressible flow Hiemenz (1911) consists in writing the velocity components in (2.4) as

$$U = Xf'(Y), \quad V = -f(Y), \tag{3.1}$$

so that the continuity equation is automatically satisfied. The pressure is further expressed as (see Sin and Tong (2009) for further details on the pressure expression)

$$P = P_0 - \frac{1}{2}[X^2 + g(Y)], \tag{3.2}$$

with P_0 the stagnation pressure. These assumptions are also applied to the case of a regularly microstructured wall (see figure 3.1), with boundary conditions (2.57-2.58) on $Y = 0$, so that the two momentum equations become

$$\frac{1}{Re}f''' + ff'' - f'^2 + 1 = 0, \tag{3.3}$$

$$\frac{1}{Re}f'' + ff'' - \frac{g'}{2} = 0. \tag{3.4}$$

The first nonlinear ordinary differential equation above can be solved for $f(Y)$ and, once the solution is available, equation (3.4) can be solved for $g(Y)$, upon imposing that $P = P_0$

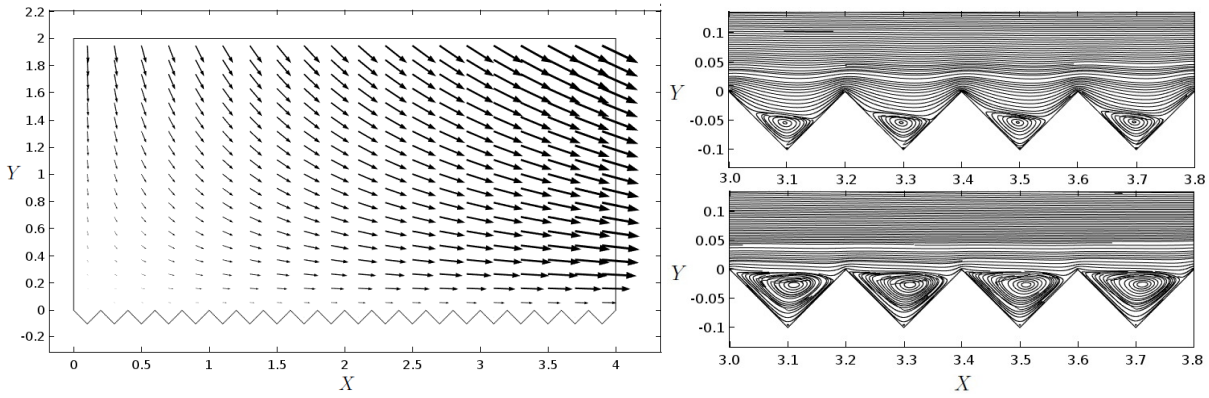

Figure 3.2: Stagnation point flow over a rough wall, visualized via velocity vectors (left.) In the images on the right the flow in the vicinity and within the micro-indentations is visualized by streamlines around $X = 3.4$, highlighting Moffatt eddies in the triangular cavities. Only for comparison purposes, such eddies are shown at two Reynolds numbers, $Re = 25$ (top) and 250 (bottom) (in both cases it is $\epsilon = l/L = 0.2$.)

at the stagnation point (which translates into $g(0) = 0$.) The boundary conditions up to $\mathcal{O}(\epsilon^3)$ to be used with equation (3.3) are

$$\epsilon\lambda^x f'' - f' + \epsilon^2 m_{12} Re = 0, \quad \epsilon^2 m_{21} f'' + f + \epsilon^3 q_{21} Re = 0 \quad \text{at} \quad Y = 0, \tag{3.5}$$

$$f' = 1 \quad \text{at} \quad Y \to \infty; \tag{3.6}$$

the second-order conditions are found by setting q_{21} to zero, while for those at first order it is sufficient to also impose $m_{12} = -m_{21} = 0$.

3.2.2. The Numerical Solution

Rather than solving equations (3.3-3.6), numerical simulation of the full Navier-Stokes equations is performed in this section, either resolving the flow field within the roughness elements, or modelling it with the effective conditions. We consider a domain of length equal to $10L$ along $\hat{x}$, and focus on the results over the first four units of length past the stagnation point. The outer edge of the domain is set at $\hat{y} = 2L$. Symmetry conditions are enforced along the $\hat{x} = 0$ axis, and the flow is considered to develop only in the positive $\hat{x}$ direction. The external potential flow is $\hat{u} = a\hat{x}, \hat{v} = -a\hat{Y}$; the constant a is the inverse of a time scale; the characteristic velocity can thus be chosen as aL and the dimensionless outer irrotational motion is thus of the form $(U, V) = (X, -Y)$. For the viscous near-wall flow we choose a Reynolds number $Re = aL^2/\nu$ (ν the fluid's kinematic viscosity) equal to 25; to account for the presence of a constant-thickness boundary layer, in enforcing the inflow condition the vertical coordinate must be shifted by a quantity equal to the

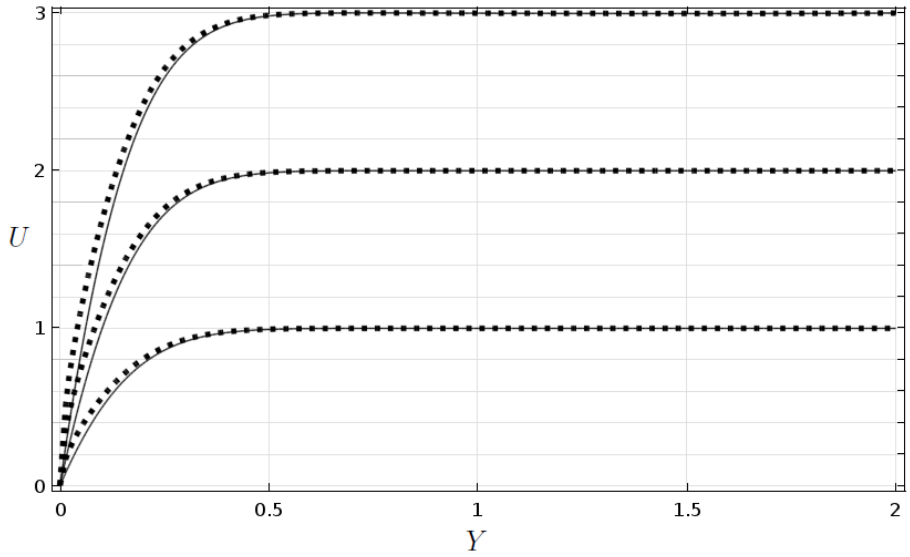

Figure 3.3: Comparison between the wall-parallel velocity profiles along Y evaluated at $X = 1$, 2 and 3 in the case of smooth wall (solid lines) and rough wall (dots) with $\epsilon = 0.2$, in correspondence to the roughness peaks. The rough-wall results displayed are those computed with a feature-resolving simulation; results for a microstructured wall simulated by employing effective conditions at order one, two or three are superimposed to the feature-resolving results and cannot be distinguished to graphical accuracy.

displacement thickness δ_1, i.e. at $Y = 2$, outer edge of the domain, the inflow conditions in dimensionless form must read:

$$U = X, \quad V = -Y + \delta_1. \tag{3.7}$$

Finally, at $X = 10$ boundary the usual "do-nothing" condition is employed, which corresponds to zeroing the traction components.

In the no-roughness case the computed solution compares very well with the similarity solution, and it is found $\delta_1 = 0.64795\, Re^{-1/2}$. When roughness is present on the lower wall, cf. figure 3.2, the solution changes slightly as shown in figure 3.3, and the displacement thickness decreases to $0.5680\, Re^{-1/2}$.

The case lends itself to being treated with the effective conditions (2.57-2.58) even if, on the one hand, the parameter ϵ is not so much smaller than one and, on the other, the microscopic Reynolds number, $\mathcal{R} = \epsilon^2 Re$, is equal to one so that the terms on the left-hand-side of the two momentum equations in 2.3 might appear to be leading order terms. This is thus a strenuous test for the theory.
The wall-normal velocity at the fictitious wall at $Y = 0$ is zero, by definition, at first order, but we find that it does not vanish when applying the effective conditions at higher orders. In particular, $V(X, 0, t)$ is approximately constant and equal to -0.0014 (-0.0017) when second (respectively, third) order effective conditions are used. This means that a net mass flux into the wall occurs and this might be due to two causes. On the one hand, ϵ is

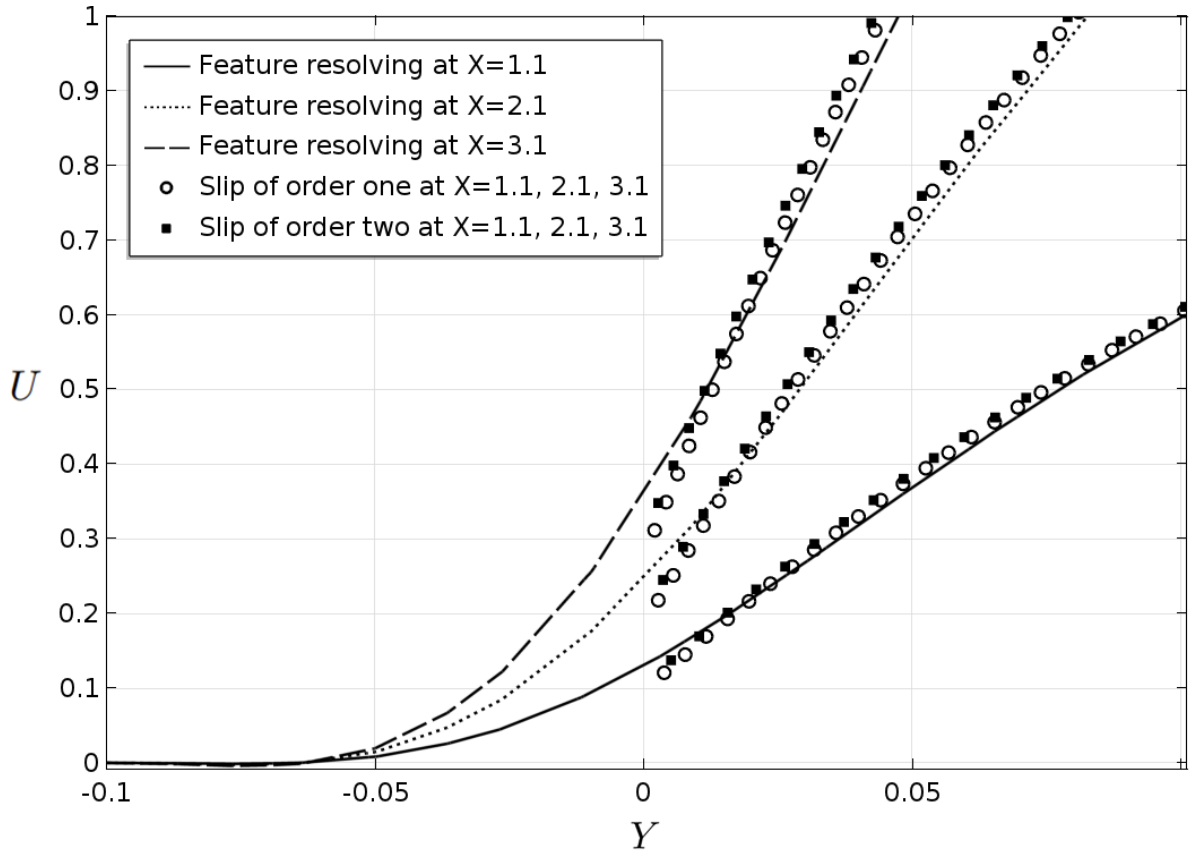

Figure 3.4: Close-up of the streamwise velocity near $Y = 0$, for $X = 1.1$, 2.1 and 3.1, i.e. on the troughs of the roughness elements. The solid lines represent the result of the feature-resolving simulation, the white bullets are the results of the Navier condition, the black square symbols correspond to the second-order condition, and the third-order results are shown with white triangles.

not infinitesimal in the problem considered here ($\epsilon = 0.2$) and thus the terms neglected in the expansion of the conditions at $Y = 0$ are not vanishingly small. On the other, when evaluating S_{12_X} and $S_{22_{XX}}$ to be used in (2.58) discretization errors are inevitable. Note, however, that the unphysical mass flux through the wall is less than 0.1% of the total mass flux which enters the domain from the upper boundary. An even more difficult test case for the condition on the vertical velocity at $Y = 0$ would be represented by a three-dimensional turbulent wall flow, because of the presence of violent near-wall events, such as ejections and sweeps. As shown by Bottaro (2019), the transpiration condition seems adequate in a turbulent channel flow when $\epsilon = 0.2$ and the friction Reynolds number is 180; however, a better approximation is necessary when $\epsilon = 0.4$ (cf. figures 17 and 20 in the cited reference.)

In figure 3.4 a close-up view of the U velocity component is shown near the surface where the effective conditions are enforced, highlighting the fact that the approximations made do a good job at representing the physics near the roughness (only in mean sense). Further

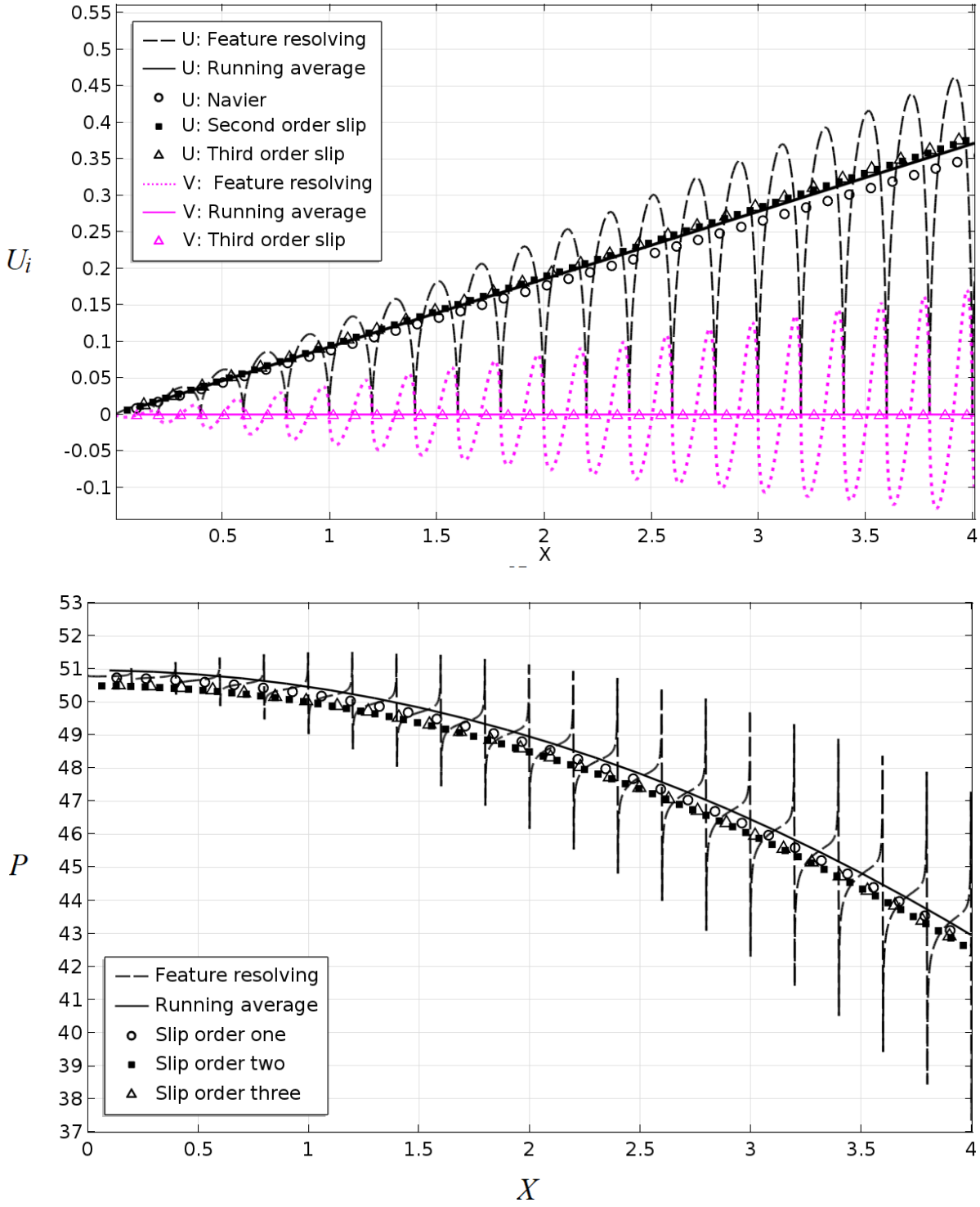

Figure 3.5: Top: slip velocity U (dashed black line) at $Y = 0$ for the feature-resolving solution, displaying typical oscillations; the results at different asymptotic orders are displayed using the same symbols as in figure 3.4. The second/third order conditions are very close to the running average of the "exact" slip velocity, displayed with a solid lines. The "exact" (dotted pink line) and the one with the third order conditions (pink symbols) of wall-normal velocity V at $Y = 0$ is plotted in the same image, where the average transpiration velocity is almost zero. Bottom: pressure at $Y = 0$, same symbols and line-styles as above. The parabolic behavior of the pressure with X agrees with ansatz (3.2).

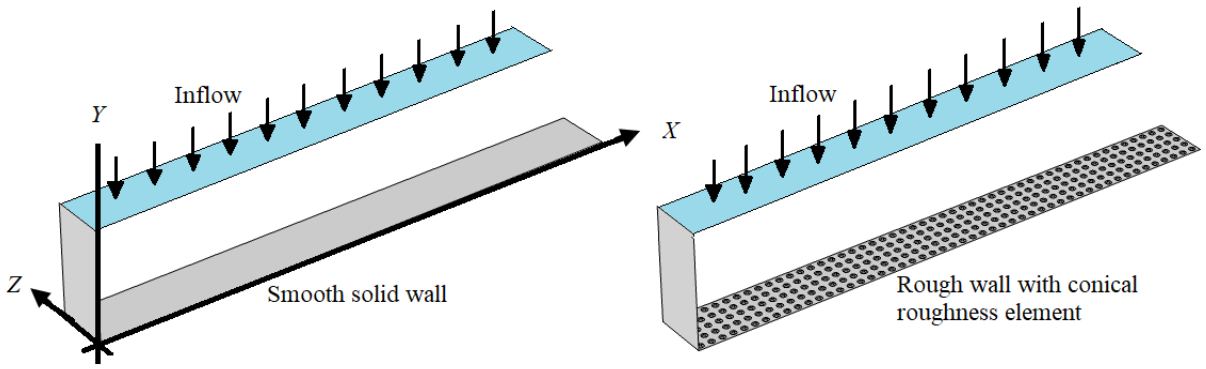

Figure 3.6: Schematic of the stagnation flow over smooth and rough wall.

away from the wall the disagreement with the "exact" solution cannot be ascertained, to graphical accuracy. The slip and transpiration velocity components at $Y = 0$ for the same cases are displayed in figure 3.5, together with the pressure. Whereas the vertical velocity at the fictitious wall oscillates around zero in the complete simulation, and is very close to zero when equation (2.58) is used, the streamwise velocity displays amplifying oscillations in the resolved case, and grows linearly in X when the effective conditions are employed, consistent with (3.1). The conditions at second and third orders almost coincide and are very close to the running average of the feature-resolving simulation (displayed with a solid line): the growth of the "exact" solution is more rapid than that found with simple Navier slip and the difference is appreciable.

3.3. Three-Dimensional Hiemenz Flow Over a Rough Wall

Like, in the two-dimensional case, in this subsection, stagnation point flow over a conical type roughness is considered for testing the three-dimensional effective conditions developed for rough walls with isotropic element in (x, z) plane. We are not presenting a similarity solution here as it is now straightforward but aims to present numerical solutions, where full Navier-Stokes equations are used in the computations, either resolving the flow field over the rough wall or solving the model case with effective conditions, in a similar manner as described previously.
Total domain dimensions in this case are $5L \times 1L \times 0.2L$ along the $\hat{x} \times \hat{y} \times \hat{z}$ directions. We chose two Reynolds numbers $Re = aL^2/\nu = 25$ and 500. The inflow condition are the same as those employed in the two-dimensional case with inclusion of spanwise component which is set to be zero and periodicity along the spanwise direction. The symmetric condition holds on the left wall and do-nothing condition holds at wall located at $\hat{x} = 5L$. The displacement thickness in this case for Reynolds numbers 25 and 500 are $\hat{\delta} = 0.55\sqrt{\nu/a}$ and $\hat{\delta} = 0.2\sqrt{\nu/a}$ respectively.
In figure 3.7 streamwise average velocity U is displayed versus X at the interface. The solutions are compared with the full feature resolving case and to the one with the first-

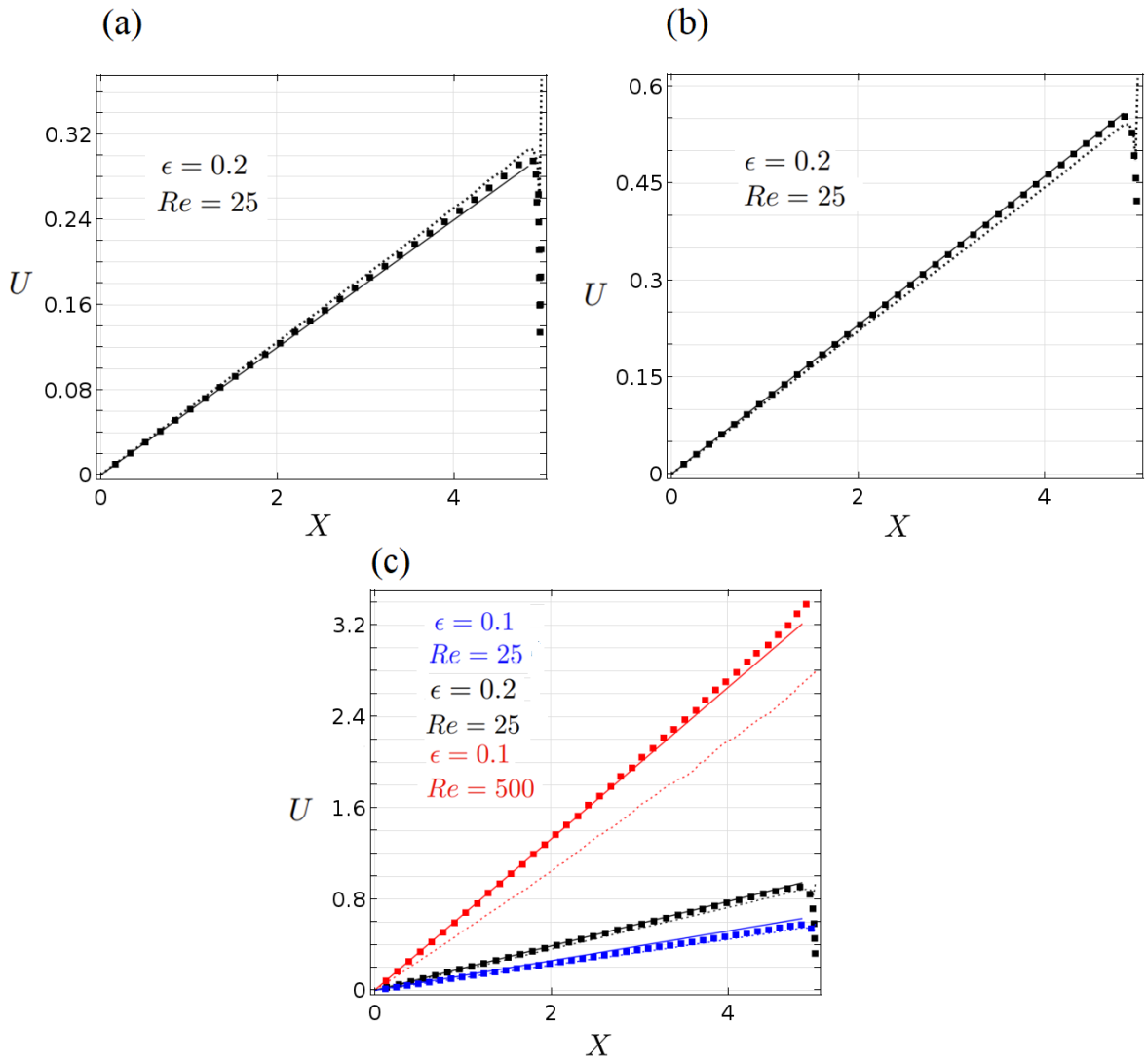

Figure 3.7: Streamwise average velocity plots verses varying height of cone, (a) $H = 0.1$, (b) 0.2, (c) 0.4 The solid lines are the running averages computed from the full feature resolving simulations; dotted line is presenting solution with effective velocity of order-one. The symbols denoted a solution of the model case with effective conditions of order-two.

order conditions for different Reynolds (low and moderate) numbers and for different roughness heights. It is noticed that the solutions of the model case at order two is comparatively closer to the running average as compared to the solutions with order one condition. The streamwise velocity plots are enough to validate the accuracy of high-order effective conditions developed for three-dimensional isotropic roughness, as we already discussed detailed solutions in a two-dimensional case. The average transpiration velocity at the bottom wall is zero.

3.4. Hiemenz Stagnation Point Flow Over Porous Bed

3.4.1. Two Dimensional Hiemenz Flow Over a Porous Bed

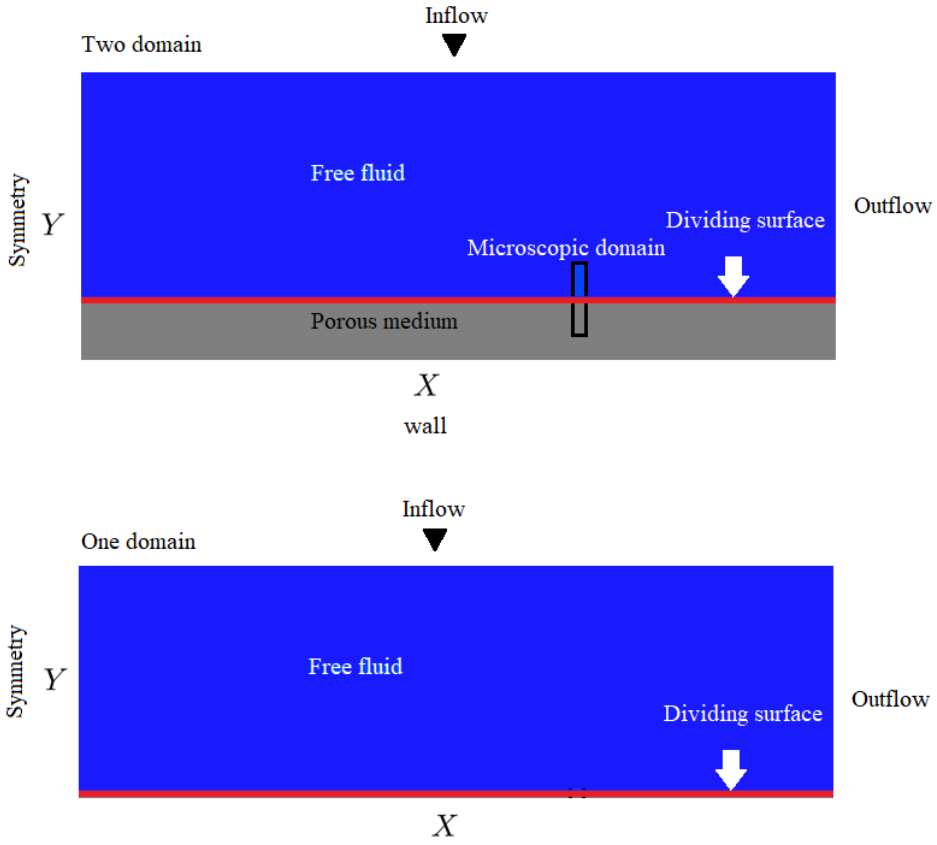

Figure 3.8: Schematic of the Hiemenz stagnation point flow for two (top) and one (bottom) approach.

The first configuration considered is that of the stagnation point flow, with the fluid impacting onto a permeable surface; the porous domain (in $\hat{y} < 0$) is assumed isotropic and the porosity is very large ($\theta = 0.9999$) to allow for large infiltration of the fluid within the porous domain. The small parameter ϵ is set to $\epsilon = 0.1$, i.e. there are 10^2 two-dimensional circular grains in every macroscopic 1×1 area.

In the inviscid, irrotational approximation the velocity components in the free fluid are:

$$\hat{u} = a\hat{x}, \quad \hat{v} = -a\hat{y}. \tag{3.8}$$

The irrotational outer motion is used in the Hiemenz similarity solution far from the (smooth or regularly micro-structured) wall. In the present configuration a general sim-

ilarity solution does not exist, because of the Navier-Stokes/Darcy coupling across the interface. In the expressions above, the constant a is the inverse of a time scale; the characteristic velocity can thus be chosen as aL. The length scale L is here the depth of the porous layer; the domain has length $15L$ along $\hat{x}$, and the outer edge is set in $\hat{y} = 5L$. Symmetry boundary conditions are employed on the $\hat{x} = 0$ axis so that the flow develops only in the positive $\hat{x}$ direction (cf. figure 3.9).

3.4.2. The Numerical Solutions

The full Navier-Stokes equations are used in the computations, either resolving the flow field over and within the porous bed, or coupling the solution in $Y > 0$ to the harmonic pressure field in the porous region, in the manner described before. The same finite elements method is employed for these macroscopic simulations as that used for the microscopic systems.
We choose a Reynolds number $Re = aL^2/\nu = 25$. To account for the presence of a boundary layer, in enforcing the inflow condition the vertical coordinate must be shifted by a quantity equal to the displacement thickness δ_1, i.e. at $Y = 5$, outer edge of the domain, the inflow conditions in dimensionless form reads:

$$U = X, \quad V = -Y + \delta_1. \tag{3.9}$$

The dimensionless displacement thickness δ_1 is *a priori* unknown and it arises as part of the solution. Just like in the case of the Hiemenz flow, also here we find that the boundary layer has a constant thickness, i.e. δ_1 is constant. On the $X = 15$ boundary the usual *do-nothing* condition is employed when the full Navier-Stokes conditions are employed, and this corresponds to zeroing the traction components. When using the two-domain approach, the condition for P_0^- in $Y < 0$ is $\partial^2 P_0^- / \partial X^2 = 0$ for $X = 15$. This amounts to setting to zero the Y-component of the phase-averaged velocity in the porous medium at the exit plane, an acceptable approximation if the exit boundary is sufficiently far away from the stagnation point.
In the smooth wall case, it is $\hat{\delta}_1 = 0.648\sqrt{\nu/a}$, while when the isotropic porous structures are present below the free-fluid region, the displacement thickness decreases to $0.425\sqrt{\nu/a}$.
The result in the feature-resolving simulation is displayed in fig. 3.9 in the vicinity of the point of symmetry ($X = Y = 0$) by the use of streamlines. It is immediately apparent that the fluid both slips at the fictitious wall and traverses it. This is thus a more difficult test case compared to the often used one of the flow is a plane channel bounded by one (or two) porous layers.
In fig. 3.11, the solution U is displayed as a function of Y, at three different positions, $X = 1, 2$ and 3, for both direct simulations and for the case in which slip/transpiration conditions are imposed. It is clear that the solution of the feature-resolving simulation, which oscillates along Y when $Y < 0$ because of the presence of solid grains, matches well the modeled case.
This result also shows that the velocity component U in the model problem has a discontinuity close to the interface because of the presence of reasonably large slip speed. The

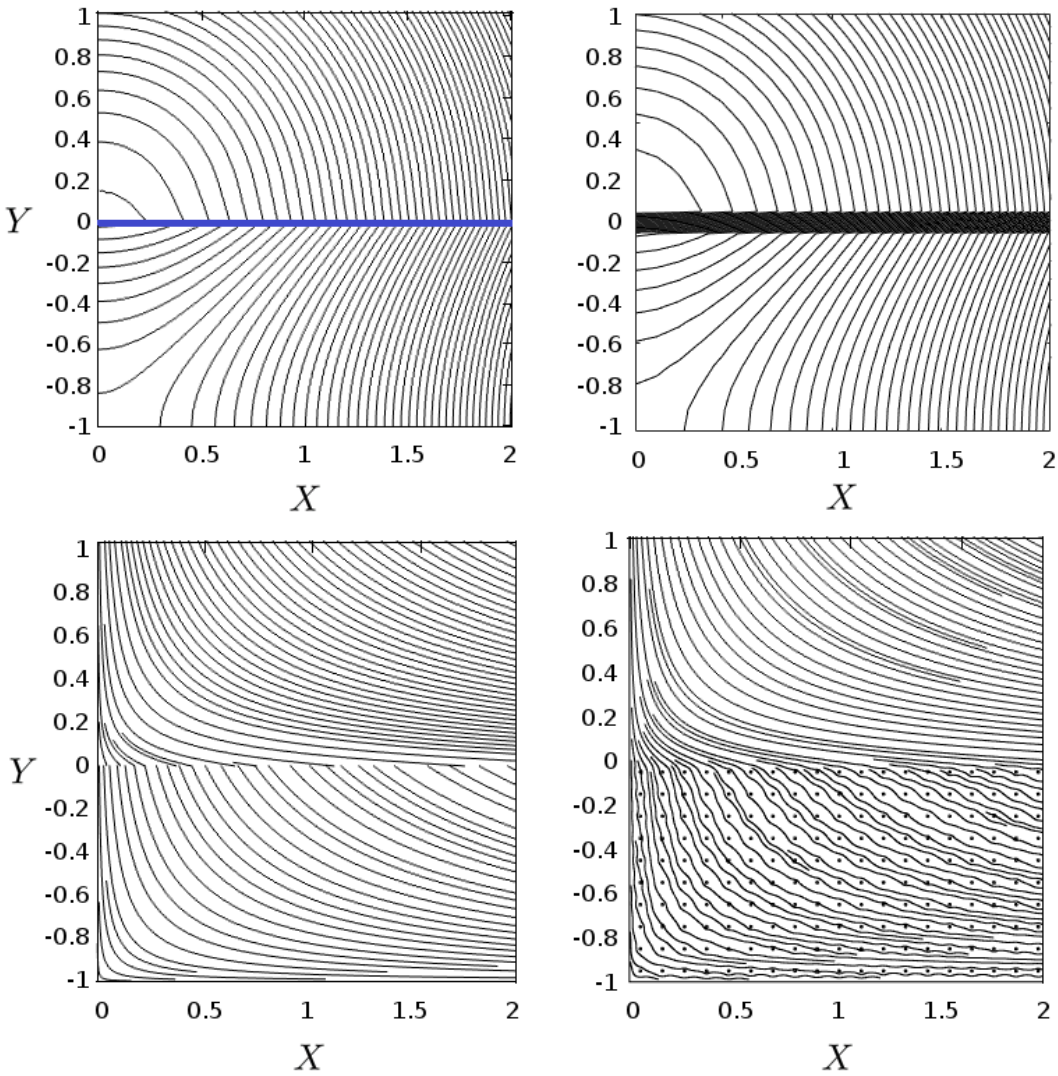

Figure 3.9: Streamlines (top row) and pressure contours (bottom row) close to the axes origin, both in the free-fluid and the porous region. The frames on the left correspond to solutions obtained with the two-domain approach; results on the right are obtained by fully resolving the flow, also through the solid inclusions. The pressure in the bottom right frame is the intrinsic averaged pressure.

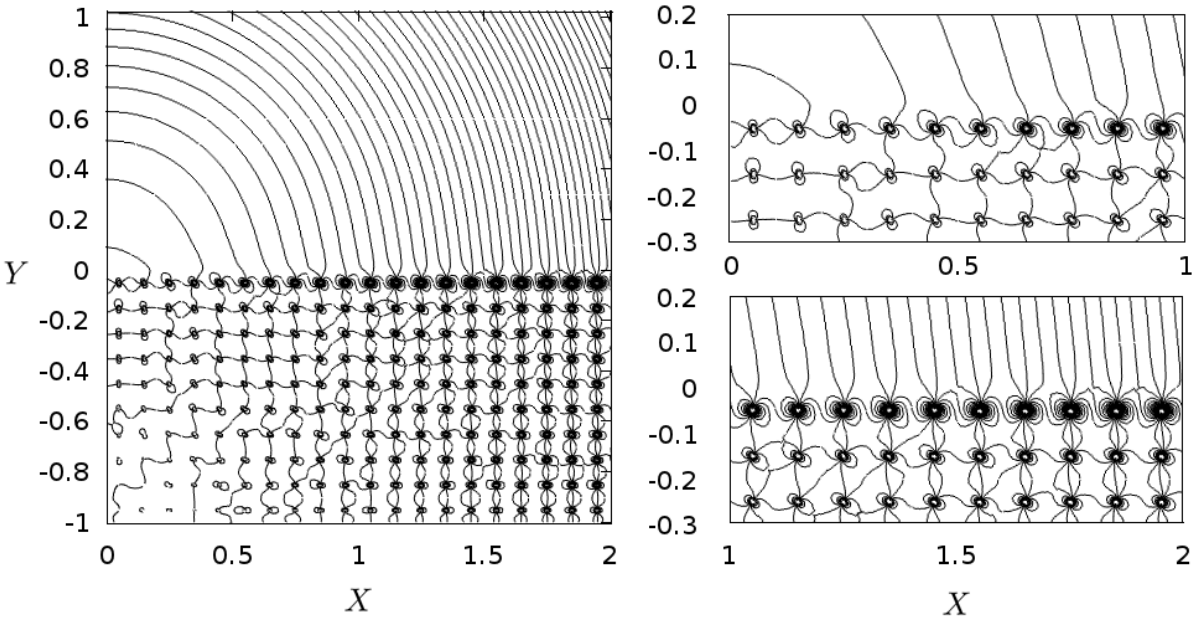

Figure 3.10: Pointwise pressure field (left), together with two close up views of the first two rows of grains (right)

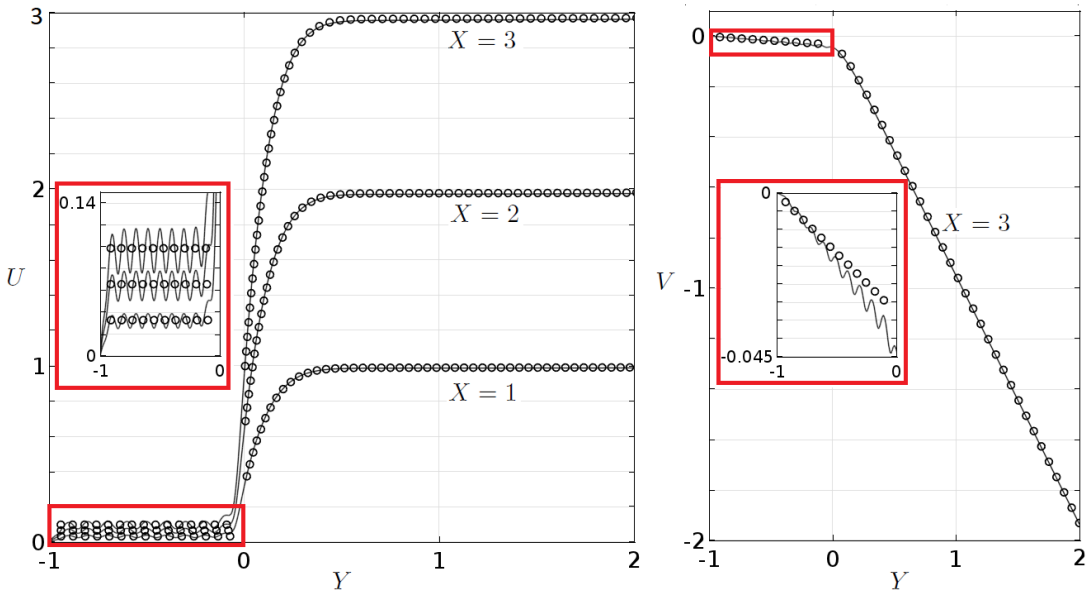

Figure 3.11: Comparison between complete simulation with full feature resolution (solid lines) and modeled with slip/transpiration velocity imposed at the dividing line/surface (empty circles). Longitudinal velocity component U (left) and normal velocity component V (right) as a function of Y. The insets highlight the velocity distributions in the porous domain.

right frame in the fig. 3.11 presents the normal velocity component V as a function of Y at $X = 3$ only, since all solutions at different X positions coincide with one another.
The intrinsic averaged pressure contours in both cases are displayed in fig. 3.9 (bottom row). The blue line in the left image corresponds to the dividing surface, across which a pressure jump occurs (cf. equation 3.9). In the image on the right, the intrinsic average pressure, computed over each unit cell $\mathcal{V}_f$ of the domain, is displayed for the feature-resolving simulation. The pressure field and its gradient are discontinuous at $Y = 0$ also in the right image; the computed pointwise pressure (cf. figure 3.10) is irregular around the dividing line/surface when the fluid enters the porous region because large local values of the pressure occur near the stagnation points of the uppermost solid grains. There is thus a transition region of dimensional size of order l (cf. figure 3.9, inset), highlighted with a black strip, across which a jump in intrinsic averaged pressure occurs.
We believe that the results presented in this section represents convincing evidence of the accuracy and applicability of the proposed methodology to treat the dividing surface between a free-fluid and a porous region, even when the fluid infiltrates significantly within the porous domain. The results are all the more significant after considering that they have been obtained for an extremely large value of the porosity ($\theta = 0.9999$) and a rather large value of the expansion parameter ($\epsilon = 0.1$). In the next section, another case is considered with two orthogonal intersecting Navier-Stokes/Darcy interfaces, and a value of θ smaller than that considered so far. We will also test reasonably large values of the Reynolds number, stretching the limits of applicability of the theory, to assess whether the conditions proposed can be employed for Re beyond order one.

3.5. Backward Facing Step With Porous Step Region

We now focus on testing the interfacial conditions between the free fluid and the porous domains for the case of the two-dimensional incompressible fluid flow past a backward-facing step, with the step region made of an isotropic porous material as sketched in figure 3.12.
The porous block occupies the area $2 \leq X \leq 3$ and $0 \leq Y \leq 1$. The domain is 15 units long in X, and the unit of length corresponds to either the inflow section or the step height. The horizontal interface, $itf1$, is located at $Y = 1$ and $2 \leq X \leq 3$; the vertical interface, $itf2$, is at $X = 3$ and $0 \leq Y \leq 1$. At the inflow of the domain ($X = 0$), the laminar, fully developed channel flow velocity distribution is imposed, i.e.

$$U = 4(Y - 1)(2 - Y) \qquad \text{and} \qquad V = 0; \tag{3.10}$$

thus, the centerline velocity at $X = 0$ and $Y = 1.5$ is the velocity scale, used in the definition of the Reynolds number Re. At the outflow ($X = 15$) the traction vector is set to zero. At the solid walls the usual no-slip conditions apply, except on the dividing surfaces, $itf1$ and $itf2$, where we apply the interface conditions derived here.
The case $\epsilon = 0.1$ and $\theta = 0.4973$ is considered and the first comparisons, in terms of isobars and streamlines, are made for both a Stokes flow (figure 3.13) and a case with significant inertial effects (figure 3.14).

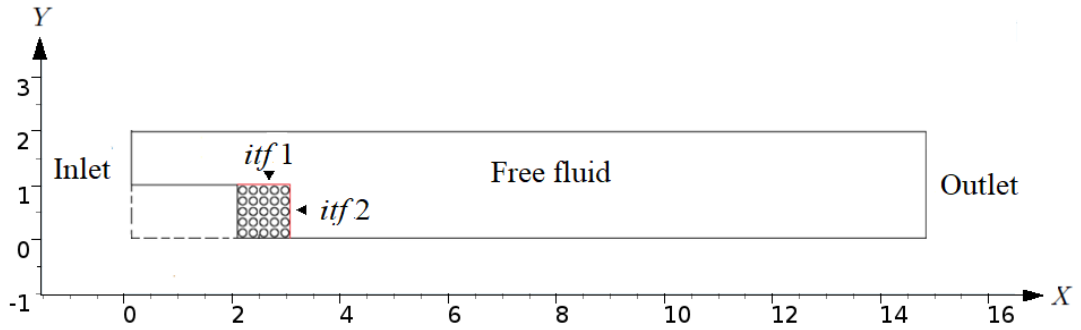

Figure 3.12: Computational domain of backward facing step case, with porous block at the step.

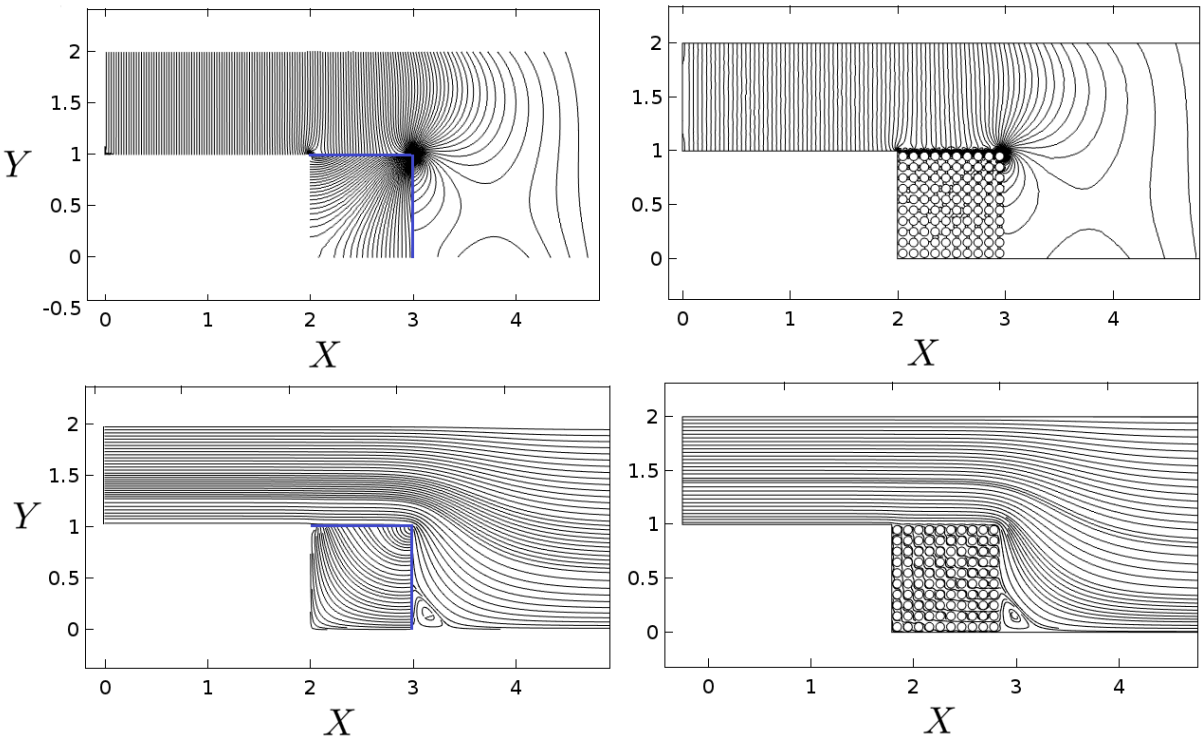

Figure 3.13: Comparison between the solutions for $Re = 0.0001$ of the two-domain approach (left frames, with blue lines denoting the dividing surfaces) and the *exact* feature-resolving numerical solution of the equations, also through the pores (right frames), focussing around the neighborhood of the step. The top row of images displays the pressure contours; streamlines are plotted in the second row.

At this latter value of Re ($Re = 500$) the flow is still two-dimensional and steady, according to Biswas et al. (2004), when the step is impermeable. The steady solutions we have computed for the permeable step, based on both fully feature-resolving simulations and the two-domain macroscopic approach, attest to the accuracy of the proposed interface conditions: both pressure and streamfunction show the same trends, also for the larger

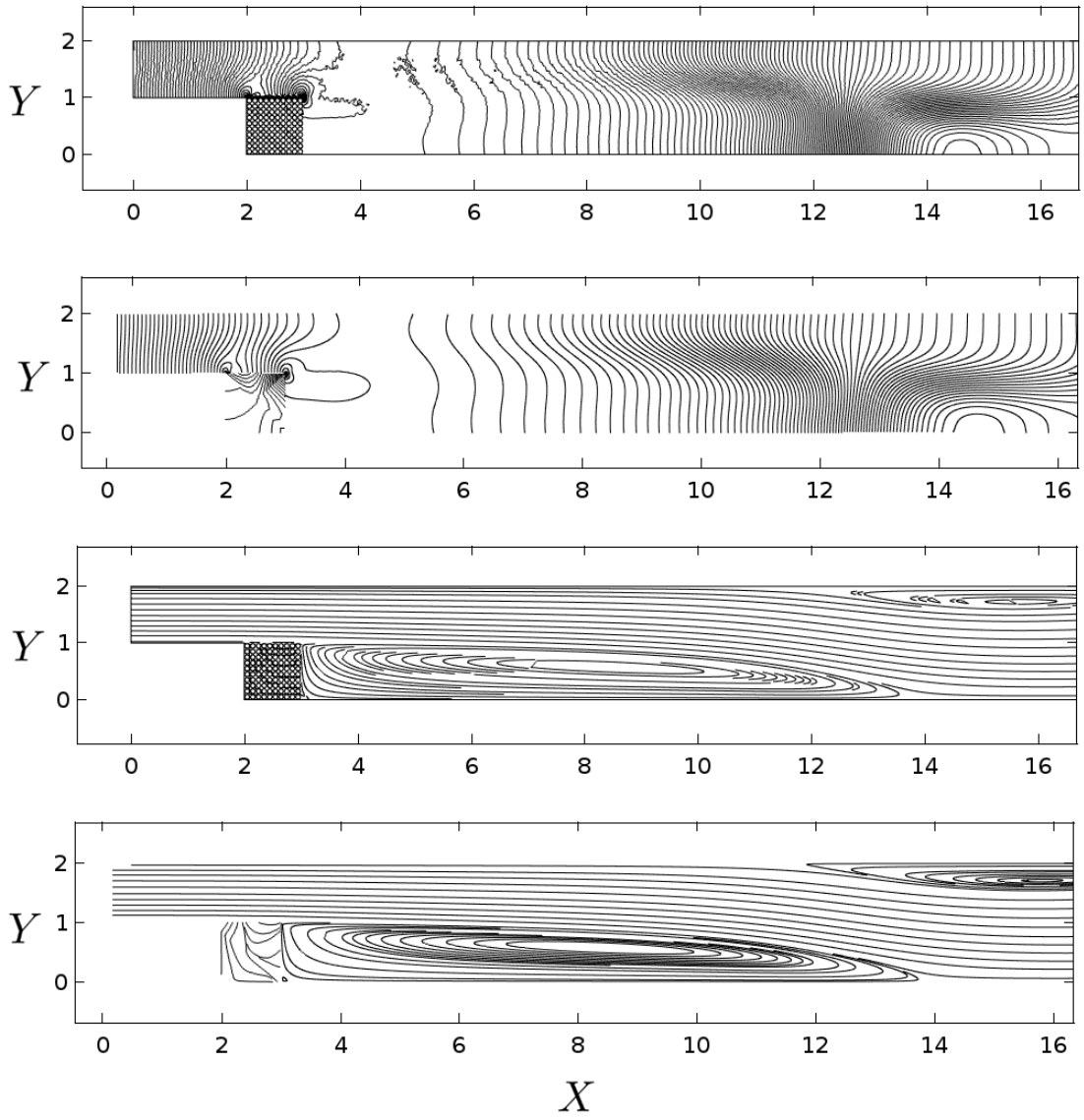

Figure 3.14: Pressure contours (first row: feature resolving, second row: model) and streamlines (third row: feature resolving, forth row: model) for $Re = 500$.

Re flow. In this latter case the primary recirculation region after the step extends almost up to the domain's exit, and a secondary bubble appears on the upper wall. On the contrary, in the Stokes' flow case the primary recirculating vortex is very small, with both approaches. Although these comparisons seem already to be sufficiently satisfactory, a closer look in the immediate vicinity of $itf1$ and $itf2$ is in order

The slip and transpiration velocity components along the two interfaces are plotted in figure 3.15, together with the pressure P, for the two Reynolds numbers already shown. The *exact* feature-resolving results and those obtained by using the interfacial conditions agree well with one another, with the former solutions displaying oscillations on the pore scale, of increasing amplitude with Re. Such oscillations clearly cannot be captured

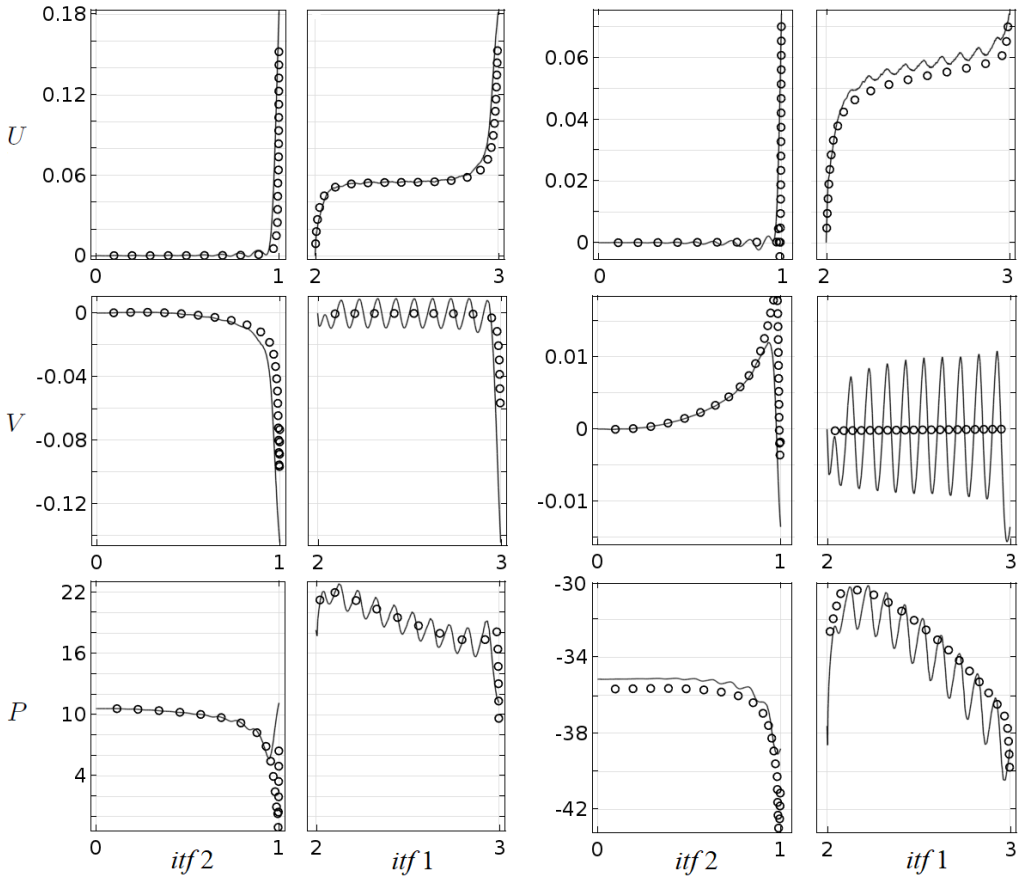

Figure 3.15: Comparison of velocity components U, V and pressure P for $Re = 0.0001$ (six frames on the left) and $Re = 500$ (six frames on the right), for the two interfaces. The feature-resolving solutions are shown with solid lines and results of the two-domain approach are displayed with symbols.

by the homogenization approach. Notable differences occur, not unexpectedly, at the corner point in $(X, Y) = (3, 1)$, where the approximations made break down. The level of accuracy of the model derived here is, however, surprising, particularly for the larger value of the Reynolds number.

A last comparison is made on the primary recirculating vortex after the step, comparing the two approaches in terms of reattachment point and abscissa of the vortex center. Both quantities are measured with respect to the base of the step, in $X = 3$. Such comparisons are displayed in figure 3.16. Also on this macroscopic measure the model performs very well, with the results being practically superposed (to graphical accuracy) to those available by carrying out fully resolved numerical simulations. In the figure a further comparison is made for the case $\theta = 0$, i.e. when the porous block is impermeable. The results we have obtained match very well those reported by Biswas et al. (2004), obtained for a slightly lower expansion ratio, confirming the validity of our numerical approach.

When the step is porous the recirculation length is slightly shorter (and so is the abscissa

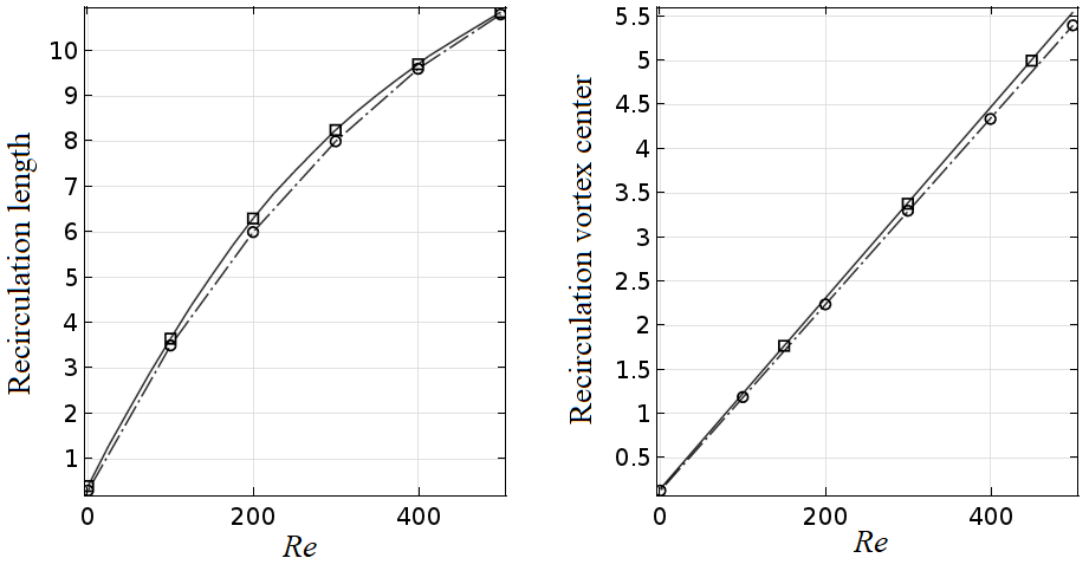

Figure 3.16: Recirculation length and distance of the primary vortex center from the backward-facing step as a function of Reynolds numbers, for the *exact* solutions (dash-dotted lines) and those obtained by using the homogenization approach (circles). Results of simulations without the porous block are shown with solid lines and are compared to reference values by Biswas et al. (2004) (square symbols).

of the vortex center) at each Reynolds number. Although the reduction is very small since no attempt has been made to optimize porosity, permeability, or length-scale ratio, this observation provides support on the use of porous panels to mitigate vortex shedding behind bodies.

3.6. Application of Turbulent Flow Across a Permeable Interface: Direct Numerical Simulation in a Channel Bounded by a Porous Wall

The flow mechanism around and inside a permeable porous layer are often encountered in industrial devices and environmental fields such as catalytic converters, metal foam heat exchangers, natural and urban canopies (Kuwata and Suga (2016), Kuruneru et al. (2020), Meroney (2007)). For enhancing the heat and mass transfer performance of industrial devices and alleviating urban heat island effects, understanding flow physics over porous media is a primarily important issue (see chapter 1 for references). Since flows over porous media are very different from impermeable-wall flows, many studies have been historically performed to understand the reason why such difference occurs especially the mechanism of turbulence transportation across the interface, and the role of turbulent flow motions of different scales in the transport process is rarely inspected (Abderrahaman-Elena and García-Mayoral (2017), Gómez-de Segura et al. (2018), Chavarin et al. (2021)).

It is clear that the accurate simulations of turbulent flows are difficult with respect to computational power. They require resolving a wide range of lengths and time scales as well as predicting chaotic behavior. There is a variety of approaches to dealing with turbulence transport through porous media and across permeable interfaces. For example, Reynolds Averaged Navier-Stokes (RANS) solve the average turbulent flow evolution. At the same time, Large Eddy Simulations (LES) compute only the turbulent flow at large scales (see references in the introductory chapter). On the one hand, these methods suffer from a lack of closure because the evolution equations contain terms that require modeling; on the other hand, RANS and LES simulate complex turbulent flows geometries. However, it is possible to simulate accurately turbulent flows in simple geometries using a direct numerical simulation (DNS). DNS has the advantage of permitting to observe and analyze turbulent physics in a confined small space, such as turbulent flow within a representative elementary volume (REV) of a porous medium (Chu et al. (2018),Chu et al. (2019) and He et al. (2018)). Jiménez et al. (2001) was a pioneering work describing results of DNS with a particular boundary condition. However, sufficient resolution of the flow's smallest length scales in the interface region requires massive computational resources. Thus, we simulated the model problems with the effective conditions employed at a smooth bottom wall (dividing surface) to reduce the massive computational issues. The porous media part has been discarded in all effective simulations as effective conditions replace the influence of porous media through effective coefficients (computed from microscopic closure problems). In the following subsection, a detailed summary of the effective DNS is described

The current study is intended to explore the process of turbulence transport over the permeable surface through the use of the homogenization approach. The ultimate purpose is to find the physical links between the geometrical feature of the porous medium through the use of effective conditions and the characteristics of the turbulence transfer process above the dividing surface without resolving the interface region. A specific porous structure could be designed to generate flow characteristics for possible industrial use without extensive computations. The turbulent statistics acquired here can also be used to support different levels of modeling in the future as well.

3.6.1. Simulations Details

DNS of incompressible channel flow with the permeable lower walls (porosity $\theta = 0.5$) has been performed here. The top surface of the channel is a solid wall with no-slip/no-penetration boundary conditions, whereas the lower wall (bottom surface at $Y = 0$) of the channel is acting as an interface between the free-fluid region and a porous medium, over which interface conditions (2.169-2.171) are employed. The effective coefficients involved in the interface conditions are obtained from the solution of auxiliary Stokes-like problems (see section) 2.3.7.. Periodic boundary conditions are applied in the streamwise (X) and spanwise (Z) directions. In the discussion to follow, the dimensionless streamwise, wall-normal, and spanwise velocities will be denoted U, V, and W, respectively, with the mean

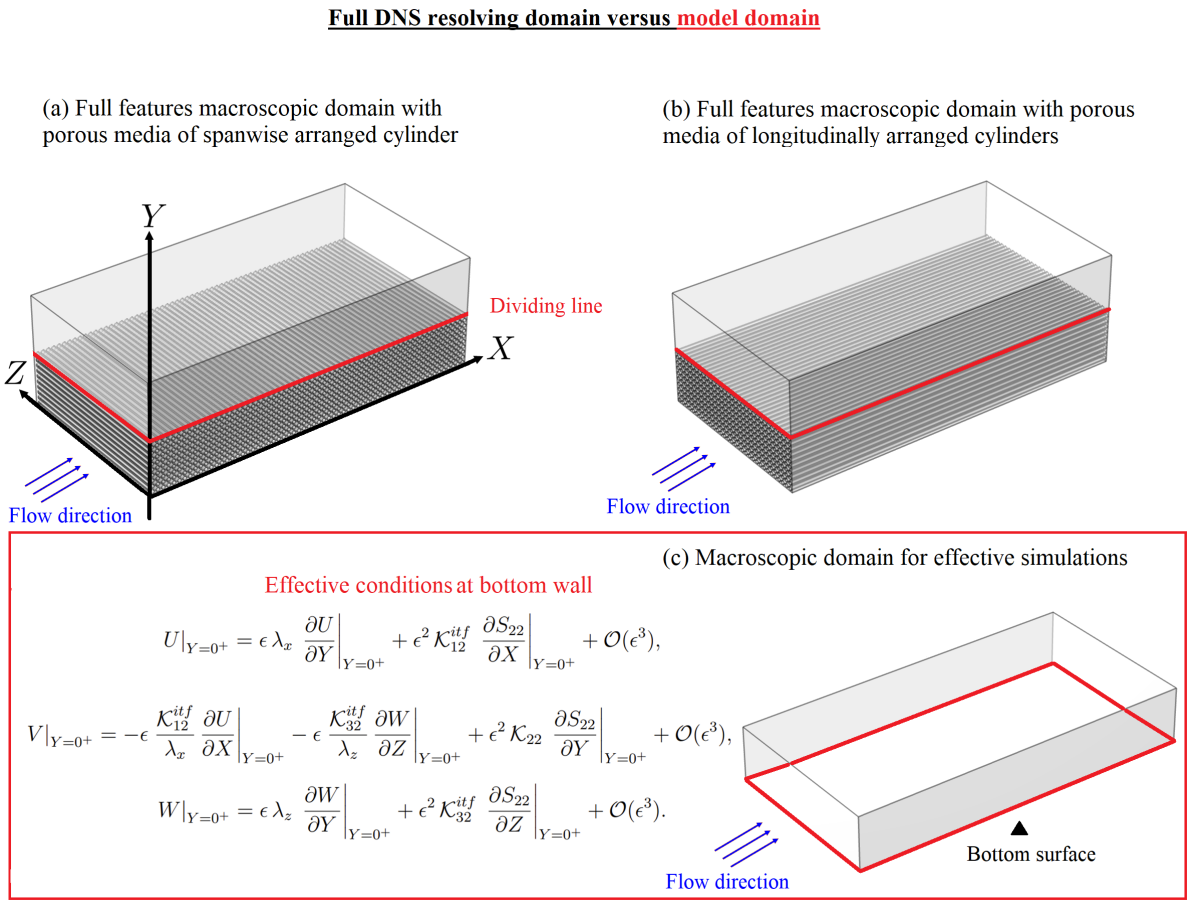

Figure 3.17: Schematic and cinematic view of full DNS turbulent channel flow featuring a pattern of cylinders aligned in a (a) spanwise and (b) longitudinal directions. A macroscopic domain without porous region is used for all simulations is given in (c), where the interface conditions (highlighted in a red box) are used at the bottom surface located at $Y = 0$. The effective coefficients λ_x, λ_z, $\mathcal{K}^itf_{xy}$, $\mathcal{K}^itf_{zy}$, and $\mathcal{K}yy$ appearing in the interface conditions are obtained from the closure problems (associated with spanwise and longitudinally aligned cases).

values, indicated with over bar sign, and fluctuations by a prime.
A sketch of the computational domain used in the model simulations is illustrated in the figure 3.17 (c), where the domain size in non-dimensional form for streamwise (L_x) and spanwise (L_z) direction is given in table A.4. The non-dimensional height of the domain is set to be 2. The domain size is made dimensionless with half channel height "H". An arbitrary instantaneous flow variable "ψ" is decomposed as follows:

$$\psi(X,Y,Z,t) = \overline{\psi}(X,Y,Z) + \psi'(X,Y,Z,t). \tag{3.11}$$

Equation 3.11 denotes Reynolds decomposition and is comparable to the triple decomposition introduced by Hussain and Reynolds (1970), where the over bar denotes temporal average i.e. $\frac{1}{T}\int_0^T \psi \mathrm{dt}$ and the prime denotes the instantaneous turbulent fluctuation.

From the time-averaged momentum equation, the total shear stress at the porous interface can be written as:

$$\tau_{wall} = \mu \frac{\partial \overline{U}}{\partial Y} - \rho(\overline{u'v'}), \tag{3.12}$$

where $\overline{U}$ is the mean (spatial and temporal) streamwise velocity. The first term in the above expression "$\mu \frac{\partial U}{\partial Y}$" is the viscous stress whereas the second term "$\rho(\overline{u'v'})$" is the Reynolds stress. For the top wall, the shear stress can be simply computed as $\tau_{wall}(y) = \mu \dfrac{\partial \overline{U}}{\partial Y}$ which is identical with wall bounded turbulence channel flow, and the friction velocity can be obtained by using the expression $\sqrt{\tau_{wall}/\rho}$. The other characteristic parameters of the boundary layer for the simulation are u_τ^{bot}, u_τ^{top}, $Re_\tau^{bot} = u_\tau^{bot} H/\nu$, and $Re_\tau^{top} = u_\tau^{top} H/\nu$, where u_τ^{bot} and u_τ^{top} are the friction velocities depending on the friction force τ_{wall}. Note that the superscripts "*bot*" and "*top*" indicate the quantities computed at the bottom and top surfaces respectively. Since the mass flux in the channel is kept constant, the bulk Reynolds number , $Re = U_b H/\nu$ can be specified directly for a simulation, where ρ is density of the fluid, and H is half channel thickness, ν is viscosity, and U_b is bulk velocity. The friction Reynolds number for the top and bottom are computed and listed in the table A.5 together with other parameters from the simulations conducted.

The flow is driven by a uniform pressure gradient varying in time to ensure that the mass flux through the channel remains constant. This condition leads to a friction Reynolds number $Re_\tau^{top} = 193$. A commercial software StarCCM+ v. 2021.1.1 is used for numerical solutions in which an implicit unsteady solver (with second order temporal discretization) is used. The uniform grid distribution is used in the tangential directions, whereas, in the normal direction, grid is not uniform but symmetric to the centerline. To fully resolve turbulence in near-wall regions, the first grid level near the bottom wall is located at $y^+ = 0.143$ (which corresponds to $\Delta y^+_{min} = 2 \times 0.143$), and more than 21 grids are used in $y^+ < 10$, where y^+ is the normalized grid distance from the wall. Note that the superscript "+" indicates viscous unit. Maximum grid resolution details are given in the table A.4. In terms of computational procedures, after reaching statistical equilibrium, flow statistics are accumulated over an average time $T = 20$ normalized by H/u_τ. The time step is set at $t = 1.5 \times 10^{-3}$ (for smooth wall case) corresponding to an average CFL number ≈ 1.1 and $t = 1 \times 10^{-3}$ (for model cases) corresponding to an average CFL number ≈ 1.06 . Once the flow becomes fully turbulent, we replaced no-slip and non-penetration conditions at the bottom wall with our effective conditions and simulated the same non-dimensional time to collect the required turbulent statistics.

3.6.2. Instantaneous and Mean Flow Fields

This section has started with a qualitative picture of the flow over a permeable and impermeable walls by analyzing mean and instantaneous fields. Figure 3.18 portraits vertical profiles of the streamwise mean velocity u^+ (top frame) and $\overline{u}$ (bottom frame).

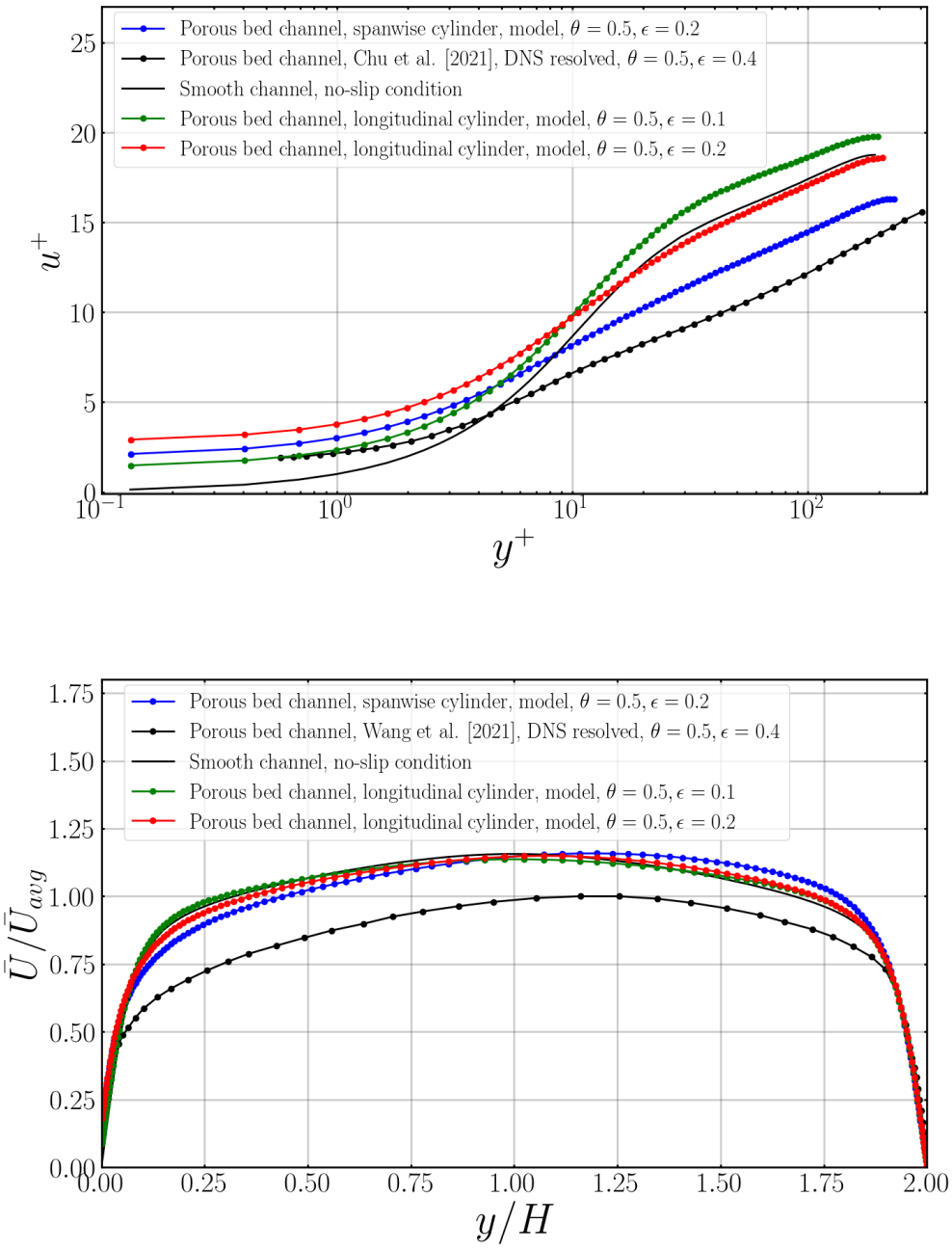

Figure 3.18: Top: Mean streamwise velocity profiles above permeable and impermeable walls i.e. u^+, (noted that + notation indicating viscous units) normalized by u_τ^{bot} and u_τ^{top} respectively. Profile of u^+ from Chu et al. (2021) (symbols) above permeable wall for $Re_\tau \approx 193$ is used for comparison. Bottom: Mean streamwise velocity in global units (i.e. $\langle \bar{U} \rangle$) above permeable wall normalized by u_τ^{top}. Profile of $\langle \bar{U} \rangle$ from Wang et al. (2021) (symbols) above permeable wall for $Re_\tau \approx 180$ is superimposed in form of symbols for comparison.

It is noticed that the result of a mean profile $\overline{u}^+$ over the permeable wall does not follow the linear and log law as compared to the profile obtained from smooth wall channel case. In the profile of u^+ verses y^+ above permeable wall, a shift of the logarithmic part of the velocity distribution is noted (Millikan (1939); Luchini (2013)) and can be calculated by the following relation:

$$u^+ = \frac{1}{\kappa}\log(y^+) + b - \Delta u^+ \tag{3.13}$$

where $\kappa = 0.392$, $b = 4.48$, u^+ is a streamwise mean velocity (mean in both temporal and spatial sense) in a viscous units normalized by u_τ^i (where i corresponds to the shear velocity of bottom wall in each case). In addition, Δu^+ is the function that measures the change in the mean velocity profile.

The effective simulations with slip and transpiration predict the higher shear velocity at the interface is observed as compare to the top shear velocity (see A.5) as also reported by Orlandi and Leonardi (2006). To check the accuracy of the model (using effective conditions) of the channel flow bounded by a permeable wall with spanwise arranged cylinder where $\epsilon = 0.2$, the solution of (u^+) is compared with DNS resolved simulation for $Re_\tau^{top} = 193$ and $\epsilon = 0.4$ by Chu et al. (2021). Since $\epsilon = 0.4$ is very large, this leads to high permeability; thus, we cannot have a converged solution for this case using effective conditions. However, a good agreement of the u^+ profile trend is found even for a very coarse mesh (around 2 million cells only). Recently, Chavarin et al. (2021) addressed that the anisotropic permeable substrate can hamper the near-wall turbulence cycle, leading to the drag reduction, like that of riblets, producing an offset between the virtual origin felt by the mean flow and that by the turbulent fluctuations. Therefore, channel flow bounded by a porous bed of longitudinally aligned cylinders for two different values of $\epsilon = 0.1, 0.2$ is also simulated under the same conditions. The obtained results of u^+ are plotted in the same figure. It is observed that the solution of u^+ for $\epsilon = 0.2$ sits below the solution of smooth wall case in the log law region, while for $\epsilon = 0.2$, it sits above. This behavior is also noticed in the second frame showing $\bar{U}/\bar{U}_{avg}$ profile versus y/H, concluding that:

- In a spanwise case ($\epsilon = 0.2$), the maximum velocity is displaced towards the impermeable wall; thus, losses on the upper wall, obtained with no additional power, may increase the global drag for the whole channel containing the porous wall.
- In contrast, an opposite behavior is observed in a case of longitudinally aligned cylinders, especially for $\epsilon = 0.1$.
- A mean vertical profile of $\bar{U}/\bar{U}_{avg}$ of the spanwise arranged cylindrical bed for $\epsilon = 0.2$ is compared with full DNS resolved case by Wang et al. (2021) for $\epsilon = 0.4$ and found that solution trend matches well and close to the reference case. Note that we are keeping the same porosity value (i.e., $= 0.5$) in all cases.

The role of the porous medium on the overlying turbulent flow modifying the near-wall turbulence significantly can be seen more clearly in the root mean square velocity plots

(top frame) drawn at the vertical center line of the channel, see figures 3.19, 3.20, and 3.21. The effect of the porous medium using interface conditions (porosity $\theta = 0.5$, $\epsilon = 0.1, 0.2$) is appreciated for all cases as it increases overall turbulence at the wall. It is seen that the value of streamwise root mean square velocity for longitudinal case with $\epsilon = 0.1$ next to the wall is higher than the other cases where the values of spanwise and wall-normal room mean square velocities for the same case are found lower. The normal τ_{xy}^R component of the Reynolds stress tensor normalized by u_τ^2 in each case is illustrated in the figure 3.22. A significant changes in τ_{xy}^R/u_τ^2 obtained from the simulations of model cases as compared to the smooth wall channel case are noticed.

Despite sharing similar mean profiles above, the high and low periodicity cases as a flow rate above the interface show clear differences, see figure 3.23, depicting that the flow rate increases for $\epsilon = 0.1$ (giving $l_{max}^+ \approx 20$) of a longitudinally arranged case, whereas for $\epsilon = 0.2$ it is nearly equal to zero, same as in a smooth channel case. Alternatively, the flow rate obtained from a spanwise arranged cylindrical case is much lower as compared to longitudinal cases.

A further look at the instantaneous streamwise (top) and wall-normal (bottom) velocity components are shown in figure 3.24, amplifies the above differences written above. These results concluded that when cylinders are longitudinally aligned, they behave like riblets since relatively minor fluctuations in $XZ-$plane are noticed compared to the longitudinally aligned case (for $\epsilon = 0.1$). In this longitudinally aligned case, the flow becomes almost laminar (a possible case of drag reduction), which is much more reasonable and organized than the spanwise arranged cylinder for $\epsilon = 0.2$. In addition, positive fluctuations of v (i.e., related to pockets of fluid being ejected outwards towards the bulk flow) are more vigorous than negative ones in the bottom frame.

The results obtained from the simulations demonstrated following conclusions:

- The model with effective condition works well even if the effective coefficients arising in the interface conditions computed from the Stokes like auxiliary problems.
- The porous media, which has been used for many years to analyze its effect on drag, specifically drag reduction, thus can be used as a drag reducing surface if design cleverly, and this can be achieved very quickly using the effective conditions under the same pattern as reported in the cases of the rough surfaced (such as riblets). In this way, an optimal anisotropic porous layer design can be available without having fully resolved simulations to check what is happening within the pores near the interface.
- The limitation of this homogenized model with interface condition is that it is effective only when $l^+ = \mathcal{O}(10)$ and it does not work well it the value of l^+ is higher then this limit.
- Using effective conditions, the model simulations of the flow over microstructured surfaces are computationally less expensive than full DNS resolving cases.

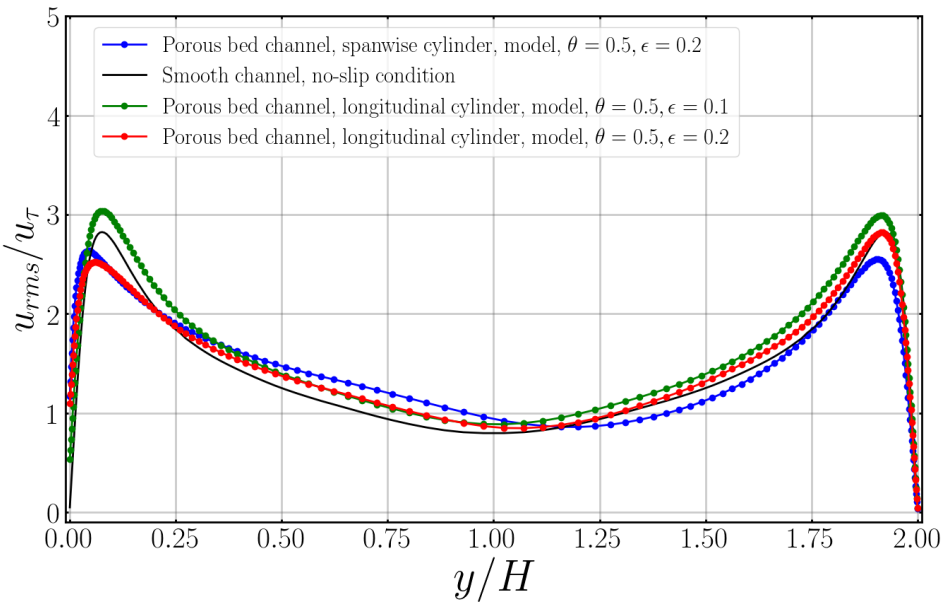

Figure 3.19: Streamwise RMS velocity profiles above permeable and impermeable walls.

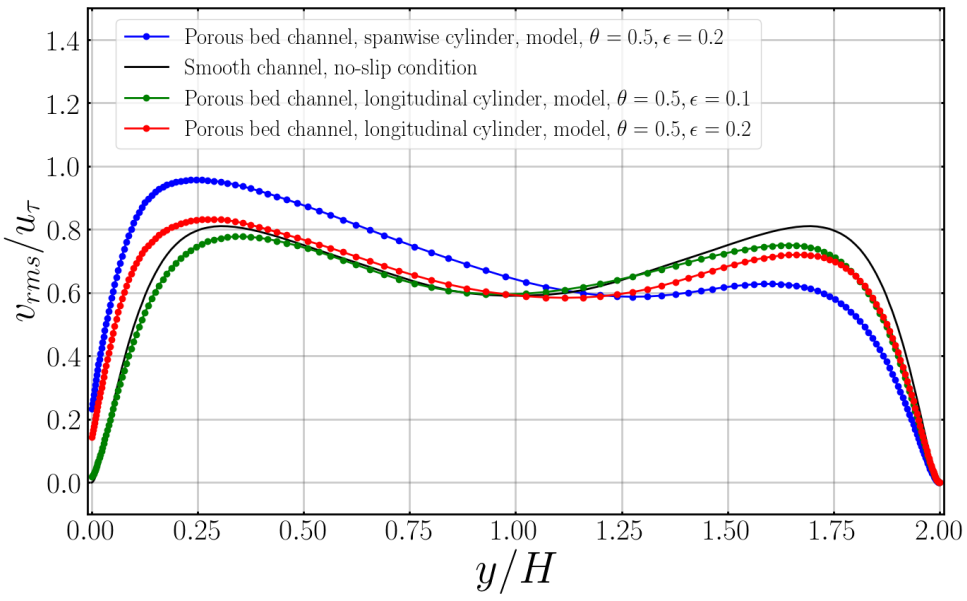

Figure 3.20: Wall-normal RMS velocity profiles above permeable and impermeable walls.

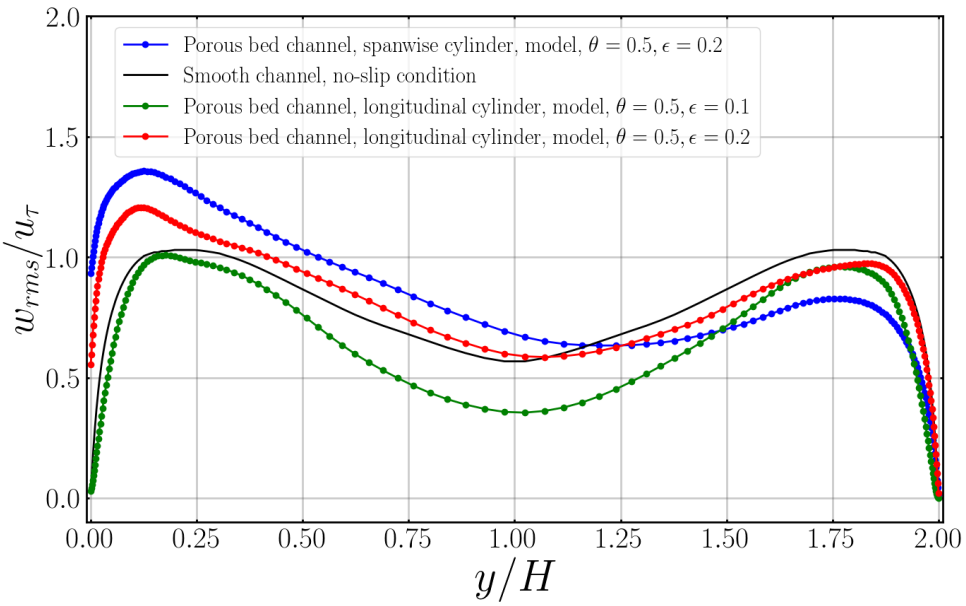

Figure 3.21: Spanwise RMS velocity profiles above permeable and impermeable walls.

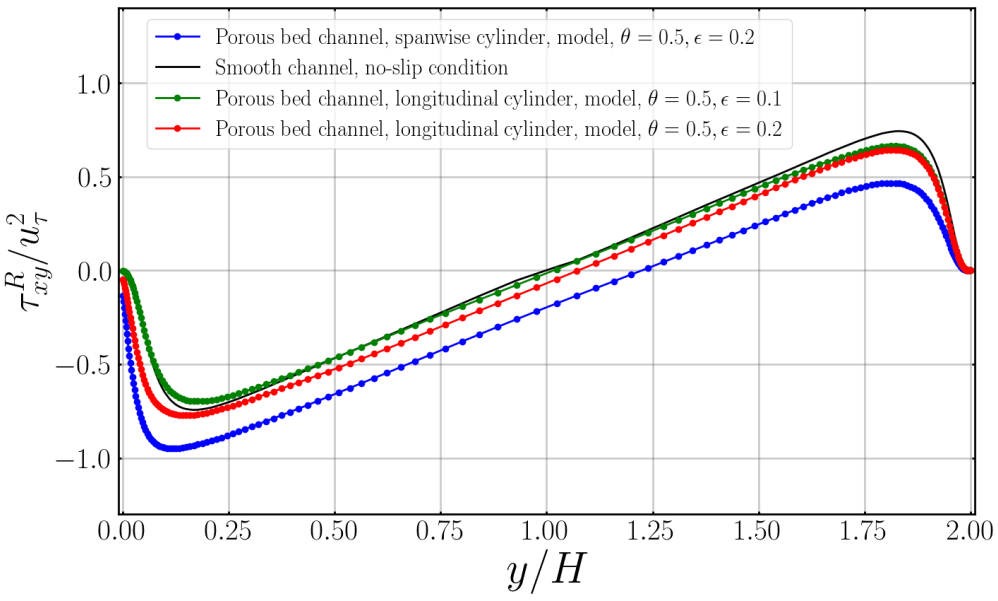

Figure 3.22: Mean Reynolds stress component profiles above permeable and impermeable walls.

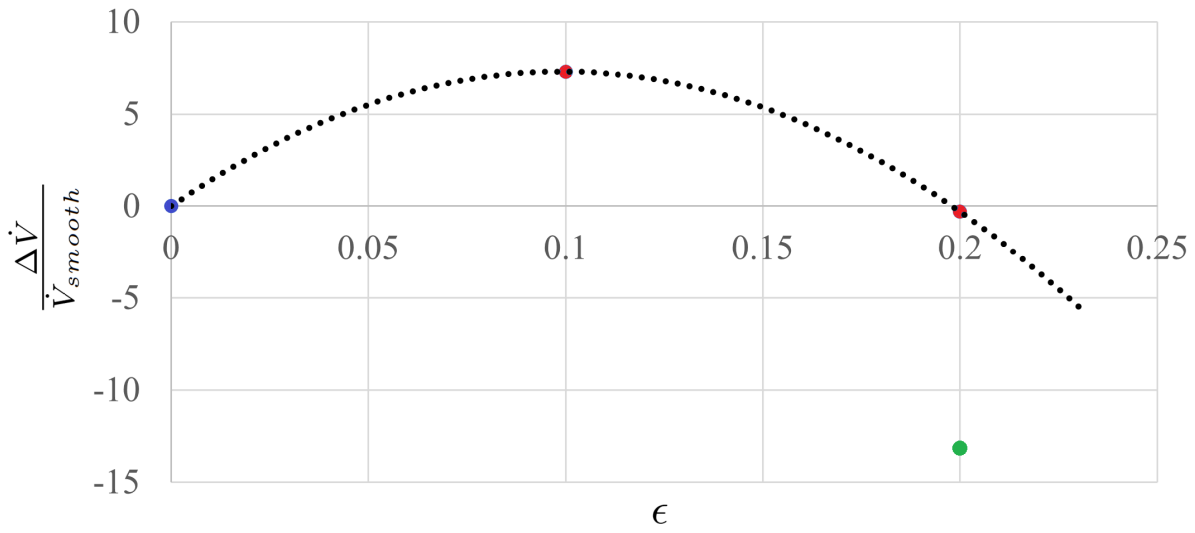

Figure 3.23: Flow rate of different channel flow cases using interface conditions as a function of ϵ. Blue symbol corresponds to the result of smooth wall case, red symbol denotes the solution of the flow above the longitudinally aligned cylindrical bed and green represents a solution of the flow above the spanwise arranged cylindrical bed.

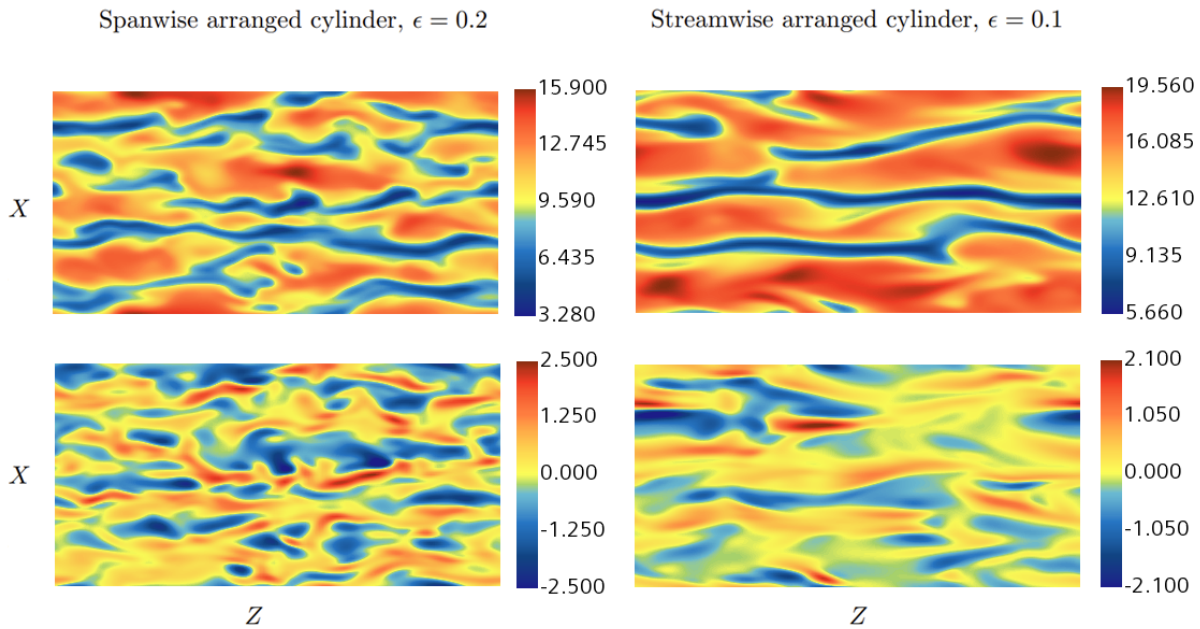

Figure 3.24: Comparison between instantaneous velocities obtained using model cases for $\epsilon = 0.2$ (spanwise) and $\epsilon = 0.1$ (streamwise), $Re_\tau = 193$.

Conclusions and Outlook

Homogenization theory is a powerful tool to be employed when small-scale features coexist with macroscopic ones. By using the homogenization approach, three flow problems have been formulated in this thesis. Therefore, the following conclusions are drawn from each case.

1. In the first example, two separate approaches to deriving effective boundary conditions beyond the usual Navier—slip paradigm have been presented to model regularly microstructured walls without the need to resolve fine-scale near-wall details numerically. The techniques used here differ in the details of the small-scale formulation but yield the same results as described in previous studies (Luchini et al. (1991); Sudhakar et al. (2019)). They are based on matching the outer flow solution, which is only affected by macroscopic spatial variables and time, to the inner flow state, which is assumed to be affected by small and large-scale variables. The effect of roughness shape and periodicity is thus captured by the inner equations and transferred to the outer flow through a set of coefficients at the matching position (set at $Y = \mathcal{Y} = \epsilon\bar{y}$). The solution to the inner, microscopic equations is found at orders zero, one, and two using an asymptotic expansion of the variables. For the wall-tangent velocity, Navier-slip is recovered at leading order, along with a no-transpiration condition. Note that the tangential gradient of the normal stress appears in the wall-parallel velocity component(s) at the next order, while the tangential gradient of the tangential stress appears in the wall-normal velocity component(s). This could result in suction and blowing through the inner-outer interface.

   The choice of the interface position can be changed at any time, but we fixed it at $Y = 0$ (the rim of the roughness components) in the macroscopic case. Any other value for $Y = \epsilon\bar{y}$ would have been suitable and yielded results of the same order of precision. A *single* solution of the homogeneous Stokes system of equations in a x-periodic unit cell, equipped with no-slip at the wall and forced at the outer edge by conditions (2.26), is sufficient to recover the coefficients γ_x and n_{12} in a two-dimensional configuration, and this is all we need in the effective conditions at order ϵ^2, (cf. equations (2.32) and (2.33)). The analysis that follows equation (2.33) discusses how these coefficients must be modified to enforce inner-outer matching elsewhere. (equations (2.37) and (2.38)). Finally, it is shown how the macroscopic matching equations ((2.57)-(2.57)), correct to $\mathcal{O}(\epsilon^3)$, develop at the next higher-order in ϵ, accounting for convective terms at the microscale.

2. In the second example, it is considered how an idealized porous medium, formed by isotropic (circular or spherical, inlined or staggered) solid grains of small dimensions, affects the free-fluid flow in its proximity. To achieve this goal, the whole domain was divided into three regions: an *outer* or *upper* region, where only macroscopic

variables are present; an *intermediate* region, across a dividing line/surface, whose dependent variables are function of both micro- and macro-scale variables; a *inner* or *lower* region, deep within the porous medium. The microscopic cell of the intermediate region spans, along the interface-normal direction, from the inner to the outer domain, where the behaviors are either known or can be computed. Such behaviors provide the boundary conditions to be enforced on the dependent variables of the intermediate reference cell, which has unit length along the interface-parallel, periodic directions. Expanding the unknowns in powers of the small parameter ϵ, ratio of microscopic to macroscopic length scales, Stokes-like systems arise at leading order and at next higher order in the intermediate reference cell. These linear systems can be expressed in terms of the forcing terms, related to the traction exerted by the outer flow and its gradient. The auxiliary problems thus arising in the intermediate cell permit to identify three important parameters: a slip length tensor, an interface permeability tensor, and a medium permeability tensor. These parameters represent the effect of the porous domain on the outer, large-scale flow and enter the interface conditions (2.142) and (2.142). Of note is the fact that the interface permeability, $\mathcal{K}^{itf}$, has a different behavior from the porous medium permeability, $\mathcal{K}$, particularly at low values of the porosity; this is because a tight packing of the grains affects the flow through the inner region more than it does near the dividing surface. Interface boundary conditions for three-dimensional flow over a porous medium consisting of cylindrical structures aligned in cross-flow direction. Effective parameters λ_i and $\mathcal{K}_{ij}^{itf}$ of interface conditions are computed over a microscopic domain of height $y_{-\infty} = -5$ to $y_{\infty} = 5$, where the medium permeability is computed over a fully periodic unit cell using the phase averaging of the velocity components using the conventional approach of Mei and Vernescu (2009).

Two cases have been reported for this example related to the location of interface. One is two- and three- dimensional flow over circular and spherical porous grains where the interface is located slightly above the crest of the grains, and second is three dimensional flow over cylindrical grains arranged spanwise and longitudinally with respect to the direction of the flow. In the second case, the interface is located at the crest of the cylinder. Different types of arrangement have been taken in each case for example; (i) inline and (ii) staggered, and (iii) random in the first case, where only (i) inline, and (ii) staggered arrangement is considered in the second case. All parameters are examined as functions of porosity and it is observed that, in the cross-flow alignment of the cylinders, effective parameters has a dramatic increase versus porosity increases specifically for a non-operational value of a porosity. The coupling coefficients for the interface conditions of longitudinally aligned cylinders case are obtained by just switching the coefficients linked with streamwise direction with the spanwise direction.

3. In the third example, a general framework aimed at analyzing micro-structured, elastic coatings anchored onto a rigid, solid substrate has been developed. The lack of geometrical limitations for both the macroscopic surface and the microscopic structure makes this model suitable to explore, at a reasonable computational cost,

a large number of situations involving interactions between a viscous fluid and a linearly elastic, micro-patterned surface. Eq.2.219 represents a generalization of the Navier slip boundary condition for the case of deformable surfaces, expressed here through a time convolution between the slip and strain tensors. In this equation, the components of the tensor L are the slip lengths allowing for the non-zero relative fluid–solid velocity at the equivalent surface $\mathbb{E}$ to be expressed in terms of the shear exerted by the outer flow. Such components of the slip tensor have been examined here for a specific texture of the wall, together with other components of relevant tensors, H, $\mathcal{C}$ and $\mathcal{D}$, which hold a role when the wall is elastic.Clearly, we need to examine other surface micro-patterns and other properties of the solid material, before a thorough understanding of the fluid–solid interaction can be gained. The results shown here, in particular figure 2.23, constitute already sufficient evidence to argue on the effectiveness of flexible micro-grooves in reducing skin friction drag. In future work macroscopic simulations of turbulence with conditions at the fictitious wall which employ the derived effective parameters will be carried out.

After solving the microscopic problems obtained via asymptotic development, the effective conditions have been derived in each case, and thus applied in the macroscopic problem except the third problem. The purpose of the developments are listed below:

1. In the first problem, the primary purpose of the formulations is to highlight the fact that the nominally higher-order terms can produce sizable effects in the flow over rigid rough surfaces and thus should not be negligible.

2. In the second case, interface conditions like classical Beavers-Joseph-Saffman conditions are developed. The difference is that the coefficients which appear in the interface relationship stem from the solution of auxiliary Stokes-like problems valid in a cell around the dividing surface with periodic conditions along with the interface-parallel directions and do not need to be fixed ad-hoc. The idealized patterns of porous media have been considered. The model coefficients are provided as a function of varying porosity for both two- and three-dimensional porous media and are given in section 2.3.. The primary purpose of these conditions is to cut the computational cost needed to analyze the flow behavior close to the microstructured surfaces and its impact on the far fields. The secondary purpose of the development is to provide a model which should be less expensive computations for industrial use to design the functional (drag reducing) engineered surfaces for aerodynamics and marine dynamics applications.

The important results drawn from the macroscopic tests are :

1. The effective conditions obtained from the first problem are then applied to the steady laminar test case to check the accuracy and viability of these conditions compared to the full feature resolving case and the classical Navier conditions. The problem examined highlights a difference between the macroscopic effective conditions at order one and two, whereas the terms of order three correct the order-two result by very little. The $\mathcal{O}(\epsilon^3)$ terms may become important in more complex flow

configurations, possibly three dimensional and unsteady. In this latter case, after naming the two tangential stress components $S^{T_x} = U_Y + V_X$ and $S^{T_z} = W_Y + V_Z$, the effective slip/transpiration conditions read:

$$\begin{aligned}\begin{bmatrix} U \\ W \end{bmatrix} = \epsilon \mathbf{\Lambda} \begin{bmatrix} S^{T_x} \\ S^{T_z} \end{bmatrix} + \epsilon^2 \mathbf{M} \begin{bmatrix} S^N_X \\ S^N_Z \end{bmatrix} + \epsilon^3 \mathbf{\Theta^x} \begin{bmatrix} S^{T_x}_{XX} \\ S^{T_x}_{XZ} \\ S^{T_x}_{ZZ} \end{bmatrix} \\ + \epsilon^3 \mathbf{\Theta^z} \begin{bmatrix} S^{T_z}_{XX} \\ S^{T_z}_{XZ} \\ S^{T_z}_{ZZ} \end{bmatrix} + \epsilon^3 \, Re \, \mathbf{Q} \begin{bmatrix} S^{T_x}_t \\ S^{T_z}_t \end{bmatrix} + \mathcal{O}(\epsilon^4),\end{aligned} \tag{4.1}$$

$$V = \epsilon^2 \mathbf{m_1} \begin{bmatrix} S^{T_x}_X \\ S^{T_x}_Z \end{bmatrix} + \epsilon^2 \mathbf{m_2} \begin{bmatrix} S^{T_z}_X \\ S^{T_z}_Z \end{bmatrix} + \epsilon^3 \mathbf{p} \begin{bmatrix} S^N_{XX} \\ S^N_{XZ} \\ S^N_{ZZ} \end{bmatrix} + \mathcal{O}(\epsilon^4). \tag{4.2}$$

$\mathbf{\Lambda}$, $\mathbf{M}$ and $\mathbf{Q}$ are 2×2 matrices; $\mathbf{\Theta^x}$ and $\mathbf{\Theta^z}$ are 2×3 matrices; $\mathbf{m_1}$ and $\mathbf{m_2}$ are 1×2 while $\mathbf{p}$ is 1×3. In principle, obtaining all coefficients of the matrices above would require a large number of numerical resolutions of differently forced three-dimensional Stokes systems. It is expected, however, that the effective number of auxiliary problems to be solved is significantly lower, in analogy to the two-dimensional case. It is indeed a nice and unexpected surprise to observe (Bottaro (2019); Sudhakar et al. (2019)) that a model of the rough surface based on only the leading order, non-trivial terms for the velocity components (i.e. those including only the factors $\mathbf{\Lambda}$, $\mathbf{m_1}$ and $\mathbf{m_2}$ produces good results for both mean flows and second order statistics, in a large-Re turbulent channel flow. The issue appears to be related to the effect of the wall normal velocity fluctuations (Orlandi and Leonardi (2006)).

2. The tests of interface conditions and coefficients have been carried out in simple two- and three-dimensional setting, under rather straining conditions: significant fluid infiltration through the pores, values of ϵ not so small, Reynolds number beyond the Stokes regime. Despite these difficulties, the conditions given have performed very well, even beyond expectations, when model computations are compared against simulations that resolve microscopic details also within the porous medium. The cases considered are *i*) the incompressible Hiemenz boundary layer flow over the porous bed and *ii*) the backward-facing step, with a porous step region. The extension of the theory to the case of anisotropic porous media does not present fundamental nor numerical difficulties. Another important observation concerns the pressure: the pressure (the outer pointwise value and the inner interstitial value) is not continuous nor differentiable at the interface.

3. Direct numerical simulation of turbulent flow over permeable-walled channel flows are performed to examine the influence of porous media on the overlaying fluid by using the commercial software StarCCM+ based on finite-volume method. The

bottom surface of the channel is suppose to be a dividing surface where the interface conditions (2.169-2.171) are enforced. Effective simulations (the model) are compared with full simulations of turbulent flow over permeable and impermeable walls for different periodicity. It is found that turbulence is affected by transpiration velocity, and it can be seen from the solution of root mean square velocities and Reynolds stress component ($\overline{u'v'}$) near the wall. Moreover, root-mean velocity fluctuations demonstrated that the near-wall turbulence is modified overall by the interface conditions, including the streamwise and spanwise slippage effect together with the large vertical transpiration effect. By comparing the friction Reynolds number, it is clear that the wall-shear stress over the porous wall increases by almost 16% in the spanwise case and increases by almost ...% in the longitudinally case compared to the smooth wall case, thus cause an increase and decrease respectively in the skin friction drag.

The multiscale homogenization approach is adapted to provide a homogenized framework that is capable of analyzing the fluid flow over and through the microstructured media. The present study found how various structures affect the free-fluid flow in its proximity. The solutions of different scales, such as inner and outer, are matched via matching conditions developed using the multiscale asymptotic approach. The results show that homogenization theory is a powerful tool to use when small-scale features coexist with macroscopic ones. Results provide insights for designing novel isotropic and anisotropic microscopic structural such as solid indentations, elastic rough inclusions, porous media with low porosity, and small permeability for industrial and engineering applications without performing expensive computations. Further, it is essential to highlight that the current homogenized framework is independent of empirical parameters/coefficients and provides accurate measurements of the effective coefficients from the microscopic simulations. The substantial freedom for choosing the appropriate parameters is left for the audience. It allows selecting the composition and structure that better fit the potential applications and mechanical requirements. For this purpose, all effective parameters are provided in tabular form in each case.

Complex cases will be considered in the future to take advantage of the current high-order homogenized framework to test further applications, such as turbulent flow over elastically deforming microstructures (third example of the work) and over the rigid roughness elements impregnated by a lubricant fluid. It is important to note that the coefficients obtained stem from the solution of microscopic Stokes-line problems; as such the parameters found apply to the reasonably low Reynolds number flows and to situations for which the expansion parameter ϵ is indeed small. The case of surface indentation of large amplitude or of strong advective near-wall effects is not corrected by the present theory; however, extension of the theory are currently being envisaged to try and account for dispersive stresses within the roughness elements, possibly by using a Oseen-like linearization. Such efforts will be reported in the future.

A.1. Numerical Approximations

In this chapter, numerical details used in the thesis are described.

A.1.1. Finite Element Method (FEM) and its Typical Procedure

The origin of the finite element method can be traced back to the 1950s, when engineers started solving structural mechanics problems in aeronautics using numerical tools. The technique has been very successful for the solution of partial differential equations (PDEs). The interpolation capability of the finite element is the approximation of scalar- and vector-valued functions, as well as the ability to approximate a mathematical model given in terms of PDEs within a proper mathematical framework (Ern (2004)). Many problems in physics and mechanics are described as a set of partial differentials and initial/boundary conditions. This set is called the strong form of the problem. However, a finite element analogous follows two main approaches, namely weighted residual and weak formulation (the detail given in the subsequent sections and subsection). After this, the local element equations for all finite elements are assembled and resolved simultaneously, with appropriate loadings, boundaries, and initial conditions applied for elements/nodes so that their values can be continuously solved at the nodes. The equations are solved in each finite element by assuming basis functions that interpolate the unknown variables over the element to approximate the problem's solution.

The idea behind FEM is to discretize the domain of interest in first, where the PDE is defined so that a linear combination of basis functions defined within each subdomain can approximate the PDE's solution. The assembly of subdomains, which is based on repositioning the finite elements, produces a discrete set of equations similar to the original mathematical problem. An assembly of discrete elements to approximate the whole domain is called finite elements, interconnected at points common to two or more elements, called nodes. The unknown variable values at the nodes are used to describe the basis function within the finite element. An approximated solution to the problem within the element is a linear combination between the nodal values of the variables and the element's base functions. The finite element equations connect the nodal values of the variables to other parameters.

A.1.2. The Weak Formulation of FEM

The approach to solving the problems with the Finite Element Method is based upon writing it in a different form, which is sometimes called weak or variational form. Green's theorem is the most important element in this process of reformatting of the problems. The formula used is also called the *first Green's formula* from Green sometimes. It is stated that:

$$\int_\Omega (\nabla^2 u)v + \int_\Omega (\nabla u)\cdot(\nabla v) = \int_\Gamma (\partial_n u)v. \tag{A.1}$$

Note that this formula contains two kinds of integrals. On the left-hand side, both are domain integrals, whereas, on the right-hand, the integral part is a part of the boundary. Moreover, in three dimensions, the result is also applicable, and in that case, domain components are integrals of volume, and boundary components are surface components. The dot between the gradients denotes the Euclidean product of two vectors. Green's Theorem is a simple result of the following divergence theorem:

$$\int_\Omega (\mathrm{div} p)v + \int_\Omega p\cdot(\nabla v) = \int_\Gamma (p\cdot n)v. \tag{A.2}$$

where div$p$ is the divergence of vector field $\mathbf{p}$ with $\mathbf{p} = (p_1, p_2, p_3)$. The Green's theorem can be recovered if p is replaced by ∇u. Green's theorem is the starting point for the weak or variational formulation. The v in the context of Green's theorem is nothing but a test function. It tests the equation that is satisfied by u. The central idea is to have an averaged version of the equation instead of looking at the equations point–by–point in the domain. Then v acts as a weight function, which is used to average the equation. In several places (books on mechanics, engineering, or physics), v is referred to as a virtual displacement (or virtual work, or virtual whatever), stressing the fact that v is not the system's unknown, but rather something that exists only in the mind's eye to write down the issue. In that sense, the weak formulation is a theory of virtual displacements (principle of virtual work).

Details on the weak formulation of each microscopic solutions are given in the following subsections.

A.1.3. Numerical Settings Using Weak Formulation: Two- and Three-Dimensional Flows Over Rough Walls

To construct the solution of the microscopic problems of the flow over rough wall, two different software based on finite element method are used. In the two dimensional case, finite element based toolbox FreeFEM (an open source code, Hecht (2012)), in which the incompressible two-dimensional slow flow equations for the generic unknown ($\mathbf{u}$, p) are solved. The approach used in this context is based on a weak formulation of the governing equations as discussed above, which means two regular test functions v and q

are introduced, and integrateD over the domain

$$\int_0^1 \int_{y_{wall}}^{y_\infty} -\mathbf{v}\cdot\nabla p - \nabla\mathbf{v}\cdot\nabla\mathbf{u} + q\nabla\cdot\mathbf{u}\ \mathrm{d}y\,\mathrm{d}x = \text{r.h.s}, \tag{A.3}$$

with the variables approximated by triangular P_1-P_2 Taylor-Hood elements. Taylor-Hood finite element consists of approximating the velocity by P2-Lagrange finite element and the pressure by P1-Lagrange finite element. Depending on the system being addressed, the term denoted as r.h.s. can contain contributions from volume source terms, boundary conditions, or from both (as discussed above). For solving the Navier-Stokes equations, a similar approach, also based on the FreeFEM code, is used here. Special care is required when the Dirac delta is located in $y = 0$ or the Heaviside step functions appear in the equations. The grid needs to be refined locally in these cases (cf. fig. A.1). As a normal distribution of variance $\Sigma^2 = 5 \times 10^{-7}$ have chosen to model the delta function:

$$\delta(y) \approx \frac{1}{\sqrt{2\pi\sigma^2}} e^{-y^2/2\sigma^2}, \tag{A.4}$$

and the step function as

$$H(-y) \approx 0.5[\tanh(\alpha y) - 1], \tag{A.5}$$

with $\alpha = 10^3$. All results reported here have been checked for grid-convergence; validation tests have also been carried out using the software COMSOL Multiphysics (2019). The results described in 2.2. obtained using the approximations (A.4) and (A.5), converge towards those presented in section 2.2.1. as the grid is refined and the parameters α and σ^2 are increased. Example of one Stokes like problem (2.13) written in freeFEM using weak formulation is given below:

```
// Geometry and Mesh
include "ffmatlib.idp"
real elle = 5;
real m0 = 3;
real m1 = 0.1;
real t0 = 0.3;
real a = (m1-m0-2*t0*(elle+0.5-m0))/(-2*t0+3*t0$^2$);
real b = elle+0.5-m0-a;
real c = m0;
border g1(t=0, 1){x=-0.4*t$^2$+0.9*t; y=-0.4*t$^2$+0.9*t-0.5;}
border g2(t=0, 1){x=0.4*t$^2$+0.1*t+0.5; y=-0.4*t$^2$-0.1*t;}
border g3(t=0, 1){x=1; y=a*t$^3$+b*t$^2$+c*t-0.5;}
border g4(t=0, 1){x=1-t; y=elle;}
border g5(t=0, 1){x=0; y=a*t$^3$+b*t$^2$+c*t-0.5;}
mesh Th=buildmesh(g1(100) + g2(100) + g3(250) + g4(24) + g5(-250)
   );
plot(Th, ps="grid.eps", wait=true);
```

```
// Fespace
fespace Uh(Th, [P2,P2,P1], periodic=[[3, y], [5, y]]);
Uh [u, v, p], [uu, vv, pp];
fespace Xh(Th,P2);
Xh uloc;
Xh vloc;
Xh ploc;
// Define the Dirac delta function
real sigma2 = 0.000001;
func dir = exp(-y*y/sigma2)/sqrt(pi*sigma2);
// Problem in weak form
solve stokes ([u, v, p], [uu, vv, pp])
= int2d(Th)
(
dx(u)*dx(uu)
+ dy(u)*dy(uu)
+ dx(v)*dx(vv)
+ dy(v)*dy(vv)
+ dx(p)*uu
+ dy(p)*vv
+ pp*(dx(u) + dy(v))
- 1e-10*p*pp
)
- int2d(Th)(dir*uu)
+ int1d(Th,g4)(uu*dx(v))
- int1d(Th,g4)(vv*p/2)
+ on(g1, u=0, v=0)
+ on(g2, u=0, v=0);
//output
plot(u, ps="$u_{plot}$.eps", value = true, wait=1, fill=true);
plot(v, ps="$v_{plot}$.eps", value = true, wait=1, fill=true);
plot(p, ps="$p_{plot}$.eps", value = true, wait=1, fill=true);
real intu=int2d(Th)(u);
real intv=int2d(Th)(v);
real intp=int2d(Th)(p);
uloc = u;
vloc = v;
ploc = p;
cout $<<$ "Max U = " $<<$ setw(12) $<<$ uloc[].max $<<$ " \t Max
   V = " $<<$ setw(12) $<<$ vloc[].max $<<$ " \t max P = " $<<$
   setw(12) $<<$ ploc[].max $<<$ endl;
cout $<<$ "Min U = " $<<$ setw(12) $<<$ uloc[].min $<<$ " \t Min
   V = " $<<$ setw(12) $<<$ vloc[].min $<<$ " \t min P = " $<<$
   setw(12) $<<$ ploc[].min $<<$ endl;
```

A better way to treat the delta and step functions would be to split the domain into two parts and enforce jump conditions across, as proposed by Sudhakar et al. (2019). How-

ever, it is not necessary to proceed this way, since a simpler and very accurate alternative is available (cf. section 2.2.1.). All closure Stokes like problems in the three-dimensional case presented in the section 2.2.3. are obtained via academic version of COMSOL Multiphysics (2019) using the weak formulation.

A.1.4. Grid Resolution and Grid Convergence Test

The mesh of the first (for both micro and macroscopic) problem is generated by both freeFEM and COMSOL for two and three-dimensional flow cases. It is observed that the model problem with the effective conditions (2.57-2.58) is computationally less expensive as compared to the full feature resolving case. Mesh independence test is taken place concerning the slip length for four different meshes using COMSOL and are presented in the tabular form given below:

Table A.1: Mesh convergence test for two-dimensional flow over a rough wall.

Mesh elements	λ
7728	7.7695×10^{-2}
13560	7.7760×10^{-2}
125720	7.7780×10^{-2}
508205	7.7780×10^{-2}

All two-dimensional microscopic problems with easier alternative approach (section 2.2.1.) are solved using mesh size 125720 (elements) in this case. Similarly, mesh convergence test for three dimensional case (conical rough wall) is also performed and obtained results are independent of the mesh.

A.1.5. Sample Solutions of Two-Dimensional Roughness Geometries

For a variety of wall shapes, the coefficient of effective slip conditions (2.37-2.38) to the second order is easily accessible by either of the approaches mentioned in this research. We have taken into account the indentations shown in Fig. A.2. In Table A.3, the relevant coefficients are listed. The pattern **B**, with the largest wetted surface at $y = 0$, shows the lowest coefficients of slip and transpiration. Since no-slip prevails at the roughness edge over half of the total streamwise distance, and this is expected. The converse argument is that the blade-like indentation **A** has greater coefficients (which can be further increased by decreasing the blade thickness). The shapes **D** and **E** have coefficient values very similar to each other and the slip is highest in the case of **D**, where a quasi-cusped tip is present. This also provides an indication of the geometries to be preferentially tested in cases where the microcavities are filled with an immiscible lubricant fluid such as air or vapor, when superhydrophobic coatings are taken into account; first order results (Alinovi and Bottaro (2018)) confirm this indication as well as feature-resolving direct numerical

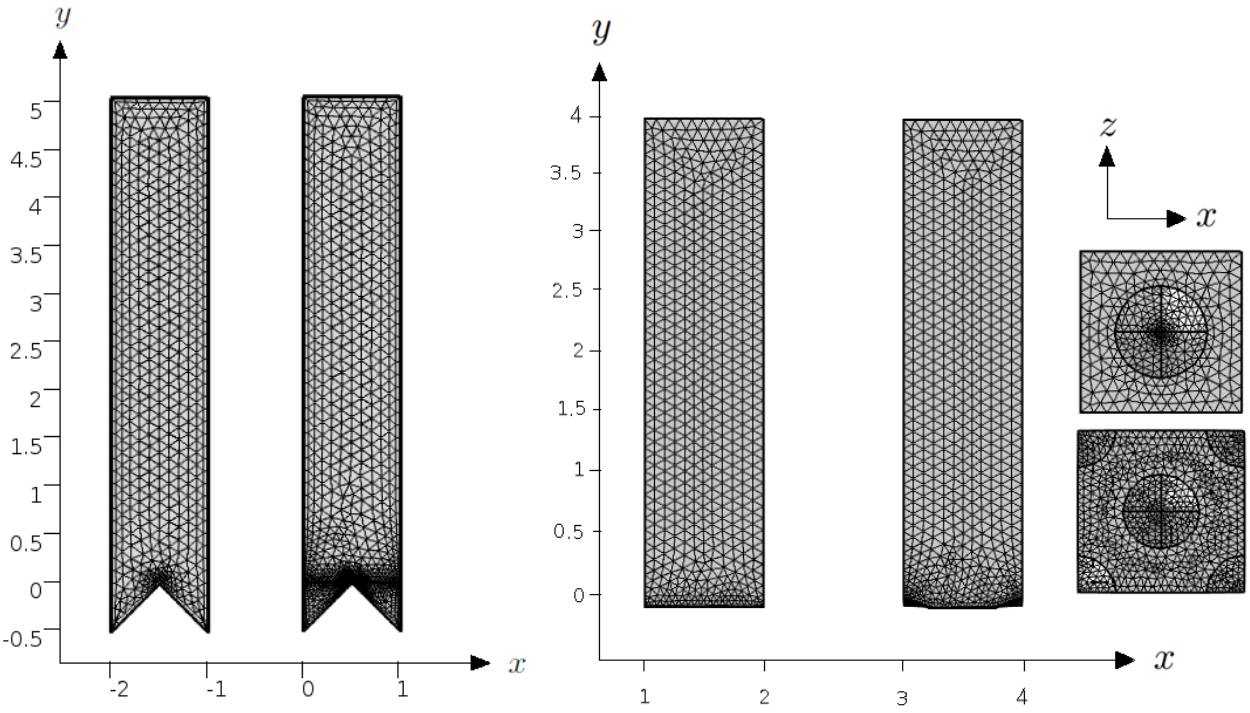

Figure A.1: Sample grids used in the absence (left) or presence of force singularities in the equations at $y = 0$. When a delta or a step function is present the grid is refined around the tip of the roughness in $y = 0$; conversely, when the fields are smooth the points are chosen to be uniformly distributed along each side of the domain. The grids displayed are composed by 1132 (left) and 1913 (right) triangles, whereas those used in the actual computations have, respectively, 125720 and 88419 triangles (left). Sample grids used in the three-dimensional cone configurations for inline (left frame) and staggered (middle) arrangement. On the right side, base of both arrangement is displayed. The grids displayed are composed by 12183 (left) and 25846 (right) tetrahedral, whereas those used in the actual computations have, respectively, 96808 and 117369 tetrahedral elements (right frame).

turbulence simulations in a channel bound to the lubricant-impregnated walls (Arenas et al. (2018)) further highlight the significance of wall-normal velocity fluctuations and their strong correlation to the total drag. In the case of lubricant-filled micro-cavities, the high-order approach mentioned here can easily be applied to better capture phenomena which to date, have only been modelled using the first-order Navier condition.

Table A.2: Variation of slip and transpiration parameters for different roughness geometries.

	A	**B**	**C**	**D**	**E**
λ^x	0.06293	0.01781	0.04087	0.08119	0.07991
$m_{12} = -m_{21}$	0.00325	0.00043	0.00182	0.00544	0.00551

The macroscopic problems, Hiemenz stagnation point flow over a rough wall in two- and three-dimensional configurations are numerically solved by COMSOL Multiphysics

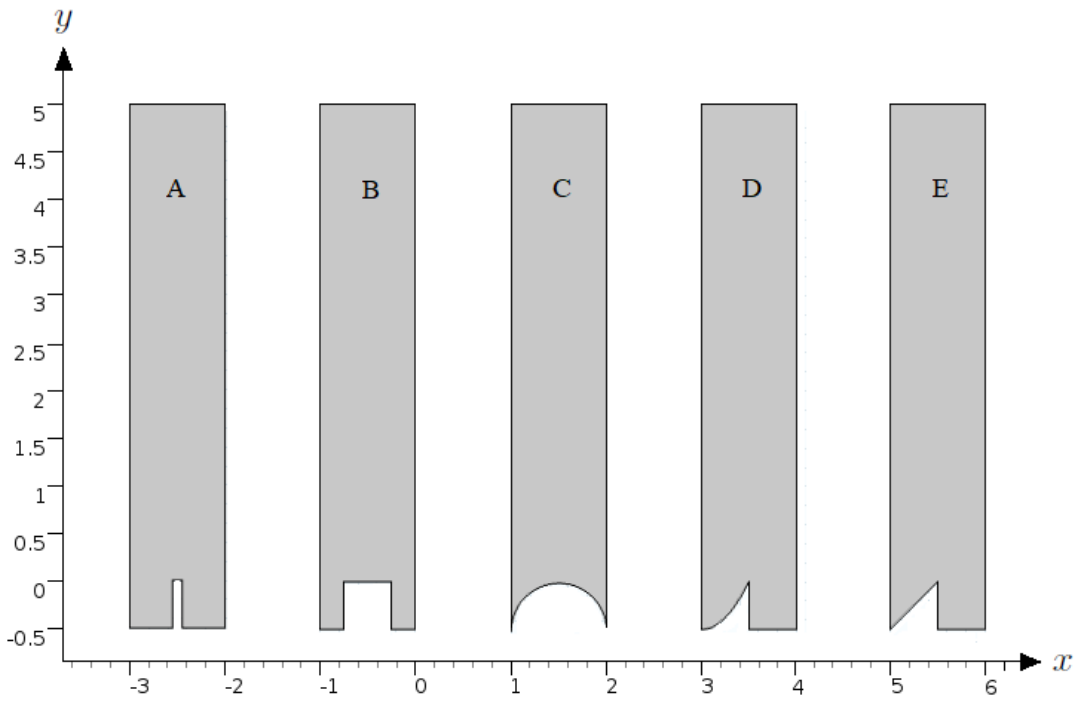

Figure A.2: Microscopic domains with some two-dimensional roughness shapes tested. Shape **A** is a blade of dimensionless thickness equal to 0.2. The thickness of the square roughness element **B** in 0.5. Roughness **C** is a semicircle. Roughness **D** is defined by a parabolic-linear contour, and roughness **E** is a 90 degrees triangle (right)

(2019). The steady state solutions are obtained for low and moderate Reynolds numbers. The PARDISO (parallel sparse direct solver) is used to solve the Navier Stokes equations. This solver is fast, robust, and multi-core capable (scales better than MUMPS on a single node with many cores).

A.1.6. Numerical Settings Using Weak Formulation: Flow over Porous Media

Following a similar approach opted in A.1.3., all auxiliary Stokes like problems reported in the section 2.3. are numerically solved using both freeFEM and COMSOL. The example of one solver written in freeFEM code for a Stokes problem (2.136) is given below:

```
1 //Geometry and Mesh
2 // include "ffmatlib.idp"
3 real elle = 5;
4 real[int] xx(21), yy(21);
5 border g1(t=0, 1){x=1; y=(elle+5)*t-5;label=1;}
6 border g2(t=0, 1){x=1-t; y=elle;label=2;}
7 border g3(t=0, 1){x=1-t; y=-5;label=3;}
```

```
8  border g4(t=0, 1){x=0; y=(elle+5)*t-5;label=4;}
9  border g5(t=0, 2*pi){x=0.5+0.4*cos(t); y=-0.5+0.4*sin(t); label
       =5;}
10 border g6(t=0, 2*pi){x=0.5+0.4*cos(t); y=-1.5+0.4*sin(t); label
       =6;}
11 border g7(t=0, 2*pi){x=0.5+0.4*cos(t); y=-2.5+0.4*sin(t); label
       =7;}
12 border g8(t=0, 2*pi){x=0.5+0.4*cos(t); y=-3.5+0.4*sin(t); label
       =8;}
13 border g9(t=0, 2*pi){x=0.5+0.4*cos(t); y=-4.5+0.4*sin(t); label
       =9;}
14 mesh Th = buildmesh(g1(300) + g2(100) + g3(-100) + g4(-300)+g5
       (-100)+g6(-100)+g7(-100)+g8(-100)+g9(-100));
15 plot(Th, ps="Thwithhole.eps", wait=true);
16
17 // Fespace
18 fespace Uh(Th, [P2,P2,P1], periodic=[[1, y], [4, y]]);
19 Uh [u, v, p], [uu, vv, pp];
20 fespace Xh(Th,P2);
21 Xh uloc;
22 Xh vloc;
23 Xh ploc;
24
25 // Problem in a weak form
26 solve stokes ([u, v, p], [uu, vv, pp])
27 = int2d(Th)
28 (
29 dx(u)*dx(uu)
30 + dy(u)*dy(uu)
31 + dx(v)*dx(vv)
32 + dy(v)*dy(vv)
33 + dx(p)*uu
34 + dy(p)*vv
35 + pp*(dx(u) + dy(v))
36 - 1e-10*p*pp
37 )
38 + int1d(Th,g2)(uu*dx(v))
39 - int1d(Th,g2)(uu)
40 - int1d(Th,g2)(vv*p/2)
41 - int1d(Th,g3)(uu*dx(v))
42 + int1d(Th,g3)(vv*p/2)
43 + on(g5, u=0, v=0)
44 + on(g6, u=0, v=0)
45 + on(g7, u=0, v=0)
46 + on(g8, u=0, v=0)
47 + on(g9, u=0, v=0);
48
```

```
49 //Output
50 plot(u, ps="$u_{plot}$.eps", value = true, wait=1, fill=true);
51 plot(v, ps="$v_{plot}$.eps", value = true, wait=1, fill=true);
52 plot(p, ps="$p_{plot}$.eps", value = true, wait=1, fill=true);
53 real intu=int2d(Th)(u);
54 real intv=int2d(Th)(v);
55 real intp=int2d(Th)(p);
56 uloc = u;
57 vloc = v;
58 ploc = p;
59 cout $<<$ "Max U = " $<<$ setw(12) $<<$ uloc[].max $<<$ " \t Max
      V = " $<<$ setw(12) $<<$ vloc[].max $<<$ " \t max P = " $<<$
      setw(12) $<<$ ploc[].max $<<$ endl;
60 cout $<<$ "Min U = " $<<$ setw(12) $<<$ uloc[].min $<<$ " \t Min
      V = " $<<$ setw(12) $<<$ vloc[].min $<<$ " \t min P = " $<<$
      setw(12) $<<$ ploc[].min $<<$ endl;
61
62 // Fespace of first order problem
63 fespace Vh1(Th, [P2,P2,P1], periodic=[[1, y], [4, y]]);
64 Vh1 [uh1, vh1, ph1], [uuh1, vvh1, pph1];
65
66 // Problem using weak form
67 solve stokesh1 ([uh1, vh1, ph1], [uuh1, vvh1, pph1])
68 = int2d(Th)
69 (
70 dx(uh1)*dx(uuh1)
71 + dy(uh1)*dy(uuh1)
72 + dx(vh1)*dx(vvh1)
73 + dy(vh1)*dy(vvh1)
74 + dx(ph1)*uuh1
75 + dy(ph1)*vvh1
76 + pph1*(dx(uh1) + dy(vh1))
77 - 1e-10*ph1*pph1
78 )
79 int2d(Th)(pph1*(u))
80 + int2d(Th)(uuh1*(p-2*dx(u)))
81 + int2d(Th)(vvh1*(-2*dx(v)))
82 - int1d(Th,g2)(vvh1*ph1/2)
83 - int1d(Th,g3)(uuh1*dx(vh1))
84 + int1d(Th,g3)(vvh1*ph1/2)
85 + on(g6, uh1=0, vh1=0)
86 + on(g7, uh1=0, vh1=0)
87 + on(g8, uh1=0, vh1=0)
88 + on(g9, uh1=0, vh1=0);
89 // Call once more so that mesh and fields are synchronised
90 // stokesh1;
91
```

```
92  //Output
93  plot(uh1, ps="$uh1_{plot}$.eps", value = true, wait=1, fill=true,
        grey = false);
94  plot(vh1, ps="$vh1_{plot}$.eps", value = true, wait=1, fill=true)
       ;
95  plot(ph1, ps="$ph1_{plot}$.eps", value = true, wait=1, fill=true)
       ;
96  real intuh1=int2d(Th)(uh1);
97  real intvh1=int2d(Th)(vh1);
98  real intph1=int2d(Th)(ph1);
99  uloc = uh1;
100 vloc = vh1;
101 ploc = ph1;
102 cout $<<$ "Max Uh1 = " $<<$ setw(12) $<<$ uloc[].max $<<$ " \t
       Max Vh1 = " $<<$ setw(12) $<<$ vloc[].max $<<$ " \t max Ph1 = "
        $<<$ setw(12) $<<$ ploc[].max $<<$ endl;
103 cout $<<$ "Min Uh1 = " $<<$ setw(12) $<<$ uloc[].min $<<$ " \t
       Min Vh1 = " $<<$ setw(12) $<<$ vloc[].min $<<$ " \t min Ph1 = "
        $<<$ setw(12) $<<$ ploc[].min $<<$ endl;
```

All microscopic solutions obtained from FreeFEM are compared with solutions of COMSOL and excellent agreement is found.

A.1.7. Grid Resolution and Grid Independence Test

The effective parameters involved in the interface conditions played a key role in the macroscopic solutions and needs to be accurately measure on high resolutions and it should be independent of the further grid refinement. In this problem, a grid independence study is conducted over three grid resolutions before performing the CFD simulations for microscopic problems. The information of the grid resolution and grid independence is provided in the graphical (figure A.3) and tabular (table A.3) form respectively. Particular effort is made to ensure that the effective parameters λ and $\mathcal{K}^{ift}$ which appear in the interface conditions for free-fluid and porous media obtained are sufficiently grid-independent. A similar effort is made for the rest of two-dimensional and three-dimensional cases.

Table A.3: Mesh independence test for two-dimensional porous media with $\theta = 0.4973$.

Mesh type	Finer	Fine	Normal
No. of elements	13101	4650	2596
λ	1.451×10^{-1}	1.451×10^{-1}	1.450×10^{-1}
$\mathcal{K}^{itf}$	1.173×10^{-2}	1.173×10^{-2}	1.172×10^{-2}

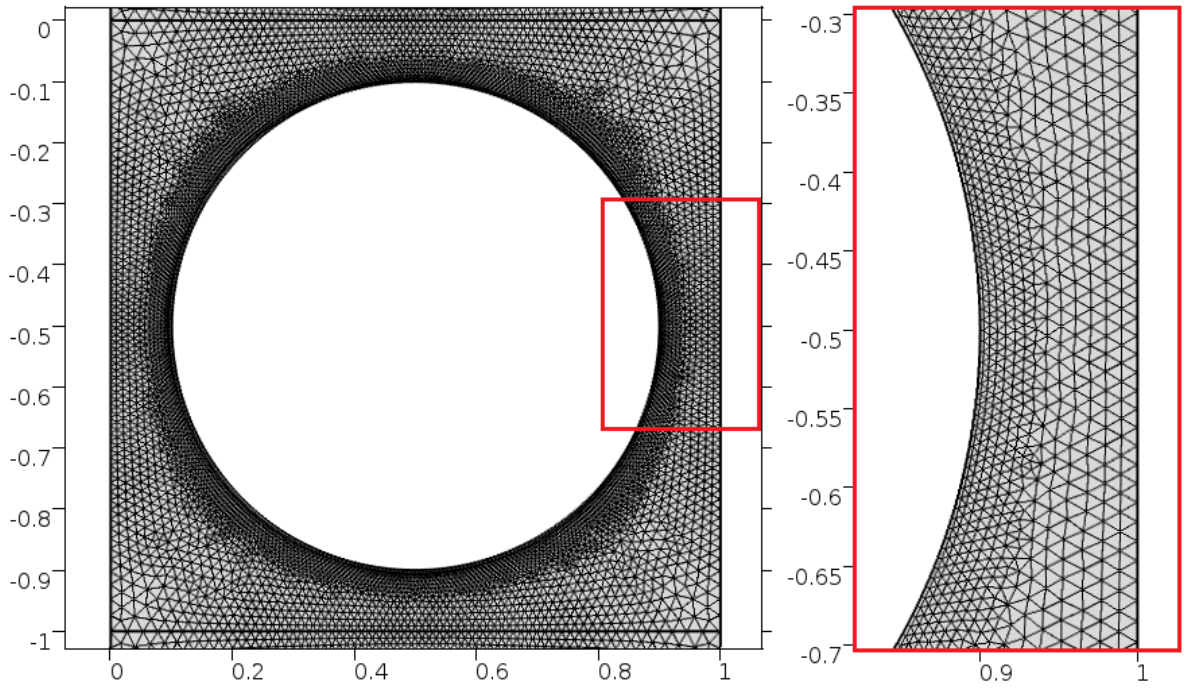

Figure A.3: Sample grid used in the microscopic domain of height $y_{-\infty}$ to y_{∞}, however in this figure only one unit-cell with circular inclusion is displayed for the clear vision of the mesh around the structures. The highlighted red box (right) is the close-up of the mesh around the crest of circular inclusion. The image is obtained for $\theta = 0.4973$. The total mesh used in the simulation for two-dimensional porous media case consists 13101 triangular elements. Where the number of triangular elements used in the FreeFEM are 19446.

A.2. Numerical Settings: Problem Formulation of the Flow Over Compliant Riblets

We have used the academic version of the software COMSOL Multiphysics (2019) (source: www.comsol.com) to obtain the numerical solution of the various closure problems. Convergence has been checked with respect to the computational grid and also with respect to the basis functions used in the finite elements discretization implemented in COMSOL (employing up to cubic polynomials for the Stokes problems in $\mathbb{F}$ and up to quintic polynomials for the solid problem in $\mathbb{S}$). The tetrahedral grid is used to discretize the whole domain and grid resolutions is shown in the figure A.4 for both fluid-solid domains separately. Same grid type is used in the blade type riblets but not displayed here.

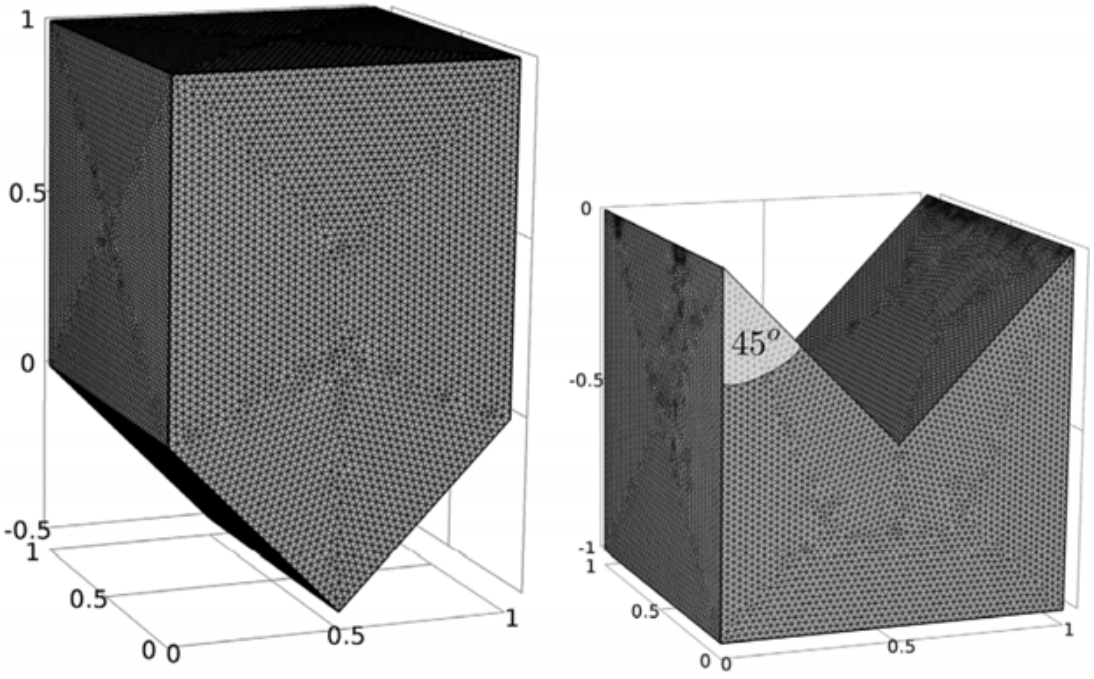

Figure A.4: Typical computational grid within the $\mathbb{F}$ (left) and $\mathbb{S}$ (right) domains for triangular riblets. In the present set-up, $\theta = 0.625$. When blade riblets are considered it is $\theta = 0.745$.

A.3. Finite Volume Method (FVM)

Finite volume method (FVM) is another widely used numerical technique (Chakraverty et al. (2019), Versteeg and Malalasekera (2007)). The fundamental conservation property of the FVM makes it the preferred method compared to various existing methods. In this approach, the volumes are evaluated at discrete places over a meshed geometry. This section explains a brief background of the FVM, and discretization techniques. The FVM depends on approximate solution of the integral form with respect to conservation equations. In the FVM, the given domain of differential equation is divided into a set of nonoverlapping finite volumes and then the respective integrals of the conservation equations are evaluated by using nodal (function) values at computational nodes.

A.3.1. Formal Procedure

Following The starting point is the discretization of the conservation equations such as conservation of mass, momentum and energy (energy equation is not included in our work but it is here just to clarify the starting point of FVM): the fluid domain is subdivided in a finite number of small, non overlapping, control volumes by a grid which defines the control volume boundaries. The computational nodes, where the unknown variables such

as velocity ($\mathbf{v}$) and pressure (p) are need to be computed, can be arranged mainly in two different ways: (i) staggered, (ii) collocated. The staggered arrangement, allocates the velocities at the control volume boundaries and the pressure in the cell center, while, in the collocated arrangement, all the unknowns are computed in the control volume center (in our case we are using collocated grid). The collocated arrangement is preferred thanks to its simplicity in Cartesian grid generation. The basic idea of the finite volume method is to require the satisfaction of the conservation equations at each control volume; thus, if the mass and momentum balance are satisfied at each control volume, they will be satisfied on the whole domain. The Navier-Stokes equations and continuity equation are integrated over each control volume assuming the following integral form:

$$\int_\Omega \frac{\partial u_i}{\partial t} d\Omega + \int_\Omega u_i \frac{\partial u_j}{\partial x_j} d\Omega = -\int_\Omega \frac{\partial p}{\partial x_j} d\Omega + \int_\Omega \frac{1}{Re} \frac{\partial}{\partial x_j} \frac{\partial u_i}{\partial x_j} d\Omega + \int_\Omega f_i d\Omega \tag{A.6}$$

$$\int_\Omega \frac{\partial u_i}{\partial x_i} d\Omega = 0 \tag{A.7}$$

The volume integrals involving the convective and the diffusion terms can be conveniently transformed into surface integrals over the control volume boundaries using Gauss divergence theorem and the incompressibility condition as follows:

$$\int_\Omega u_i \frac{\partial u_j}{\partial x_j} d\Omega = \int_S u_i \boldsymbol{u} \cdot \boldsymbol{n} dS \tag{A.8}$$

and

$$\int_\Omega \frac{1}{Re} \frac{\partial}{\partial x_j} \frac{\partial u_i}{\partial x_j} d\Omega = \int_S \frac{1}{Re} \nabla u_i \cdot \boldsymbol{n} dS \tag{A.9}$$

In figure A.5 a three-dimensional Cartesian control volume is presented together with the notations used. The control volume consist of six plane faces, denoted with lower case letters (e, w, n, s, t, b), corresponding to their orientation with respect to the central node (P).

An arbitrary flux F through the control volume boundaries can be calculated as the sum of all fluxes through the surface composing the control volume as:

$$\int_S F dS = \sum_{k=1}^{N} \int_{S_k} F dS \tag{A.10}$$

where N is the number of control volume faces and F can be either the convective or the diffusive flux. For collocated grids, the value of F at the face center is not known and an interpolation is needed in order to express F_k as a function of neighboring computational nodes. Referring to figure A.5, the value of F at the control volume face centers is obtained by linear interpolation between the two nearest nodes, as follows (e.g. for the "e" face):

$$F_e = W F_P + (1 - W) F_E \tag{A.11}$$

where W is a weight defined as:

$$W = \frac{x_e - x_E}{x_E - x_P} \tag{A.12}$$

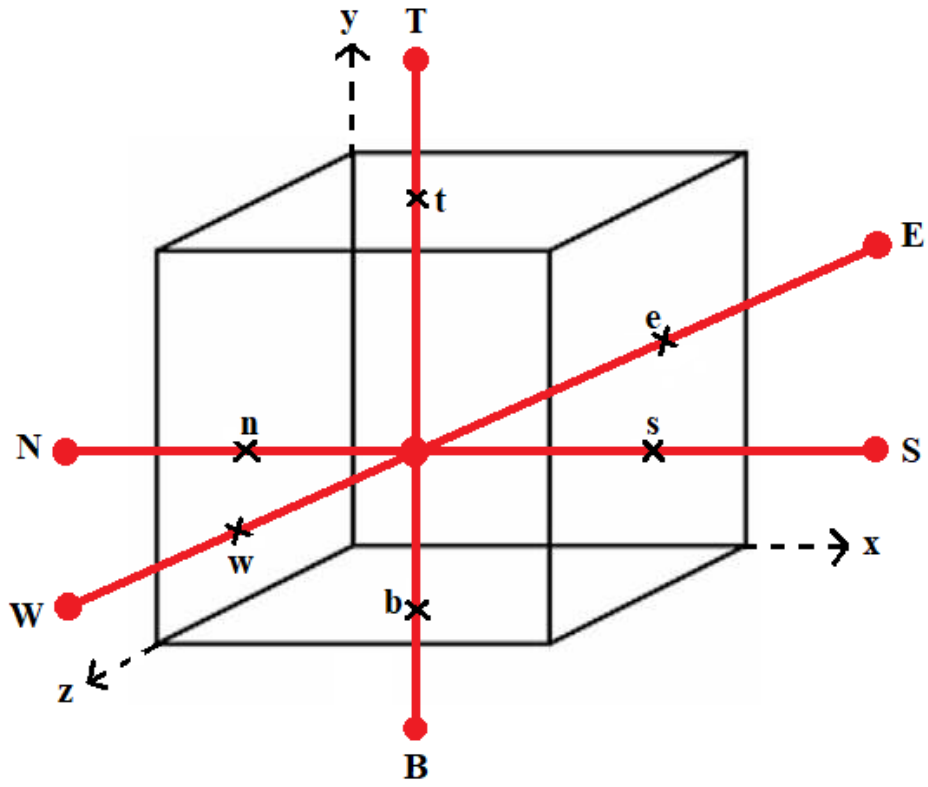

Figure A.5: A three-dimensional Cartesian control volume.

This scheme is called central difference scheme and it is of second order accuracy. For clarity, the discretization of the convective fluxes will be shown only for the e-face of the cartesian control volume shown in figure A.5 and only for the velocity component u along the x direction. The fluxes at the other surfaces can be treated in the same fashion applying the appropriate subscripts permutation. Applying the above approximation, the discrete convective and diffusive fluxes read

$$\int_{S_\varepsilon} u_i \boldsymbol{u} \cdot \boldsymbol{n}_e dS_e \approx m_e u_e = m_e \left[W u_P + (1 - W) u_E \right] \tag{A.13}$$

$$\int_{S_\varepsilon} u_i \boldsymbol{u} \cdot \boldsymbol{n}_e dS_e \approx m_e u_e = m_e \left[W u_P + (1 - W) u_E \right] \tag{A.14}$$

and

$$\int_{S_e} \frac{1}{Re} \nabla u_i \cdot \boldsymbol{n}_e dS_e \approx \frac{S_e}{\mathrm{Re}} \frac{u_E - u_P}{x_E - x_P} \tag{A.15}$$

where $m_e = u_e S_e$ is the mass flow rate through the surface e. The spatial discretization is completed by the approximation of the pressure gradient and the body forces, also called source terms. For an arbitrary source term f the following approximation is applied:

$$\int_{\Omega_P} f d\Omega \approx f_P \Delta\Omega_P \tag{A.16}$$

The integral is estimated by the product berween the central value of f in the control volume center and the cell volume $\Delta\Omega$. Adopting this rule, the finite volume approximation for the pressure term becomes (e.g along the x direction):

$$\int_{\Omega} \frac{\partial p}{\partial x_j} d\Omega \approx \frac{(p_e - p_w)}{\Delta x_p} \Delta\Omega \tag{A.17}$$

p_e and p_w are the interpolared values of p at the control volume faces e and w using the already defined central difference scheme. Analogously, the forcing term f is:

$$\int_{\Omega_P} f d\Omega \approx f_P \Delta\Omega_P \tag{A.18}$$

In the following subsections, we are presenting numerical setting of DNS turbulent flow in permeable channels.

A.3.2. Numerical Settings of Turbulent Channel Flow

FVM employed in our macroscopic calculations of DNS of turbulent channel flow over permeable walls using the STAR-CCM+ code by Siemens (2021) which is a finite volume-based commercial solver of CFD. When discretizing the domain, choosing the points at which the unknown variable will be computed is necessary. As the majority of commercial CFD code STAR-CCM+ stores all the variables at the same set of grid points and uses the same control volume for all variables. This kind of arrangement takes the name of collocated. This approach ensures simplicity to the program, especially for complicated domains, but it has some problems with pressure-velocity coupling at pressure oscillations. In the 1980s some special methods were developed (as Rhie-Chow interpolation) that permit overcoming this difficulty, and collocated arrangements grids began popular (Ferziger et al. (2002)).

A.3.3. Discretization Method

Since numerical approaches have the particularities to transform continuous differential equations into algebraic equations, much more handleable for a implementation and solving. With this aim, the equations that govern the motion are transformed into discrete equations. Regarding the two flow vectorial equations, the commercial code STAR-CCM+ solves them uncoupled, although they are clearly bonded to each other. The momentum and continuity equations are linked by a predictor-corrector method (SIMPLE). To solve the pressure-velocity incompatibility for collocated variable arrangement, the Rhie-Chow interpolation is used. For more information about discretization methods, (Versteeg and Malalasekera, 2007).

A.3.4. Transient Term

DNS of turbulent channel flow is a strongly unsteady problem and time derivative terms have to be discretized. STAR-CCM+ offers two different implicit temporal schemes: first order and second order. The former uses two different time levels, the current time level $(n + 1)$ and the previous one (n), while in the second-order scheme, one more time level appears $(n1)$. In this work second-order scheme has been chosen because of the numerical accuracy.

A.3.5. Convective Term

The convective term is discretized using a second order upwind scheme. The convection face value is calculated by summing at the upstream value, a term found by linear interpolation of the gradients. The Venkatakrishnan limiter is implemented in (Venkatakrishnan, 1995). The scheme is an improvement of the first-order upwind, but some numerical diffusion could still exist, especially for high gradients.

A.3.6. Diffusive Term

The diffusive term is discretized using a second-order scheme. Therefore, it is necessary to introduce a term that considers the non-orthogonality of the vector that connects two adjacent cell centers with the control-volume boundary. This is the so-called the cross-diffusion term and it is treated as a source term when the discretized equations are assembled.

A.3.7. Pressure-Velocity Coupling

As already referred, the continuity and the momentum equations are solved in an uncoupled manner. In order to ensure the correct linkage between pressure and velocity, SIMPLE is used. This algorithm, introduced in 1972 by (Patankar and Spalding, 1983), and is a predictor-corrector method for the calculation of pressure. In few words, the pressure field is guessed, and it permits the calculation of the velocity field to solve the momentum equations (predictor). However, these velocities do not respect the continuity equation. By solving the pressure correction equation (derived starting from the continuity equation), the velocities will be upgraded (corrector). These steps are solved until convergence is achieved.

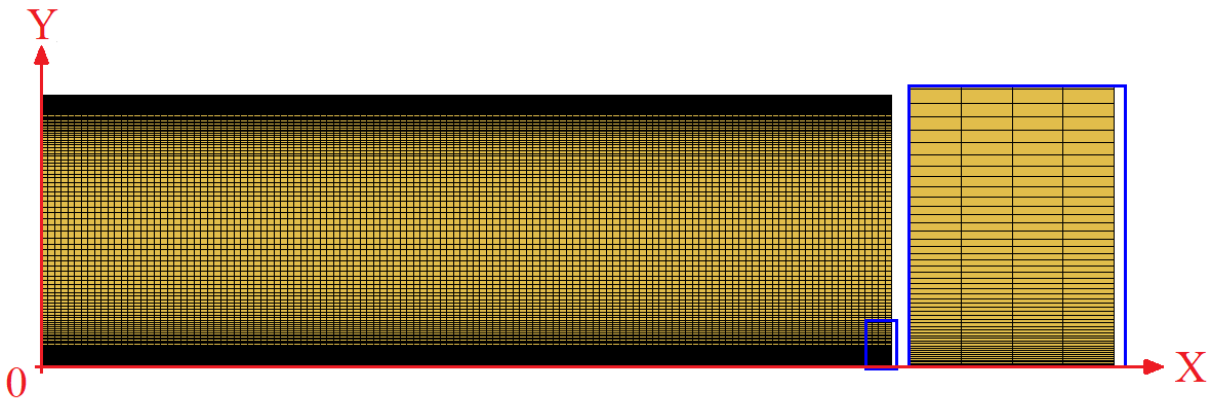

Figure A.6: Computational grid of the DNS of turbulent channel flow with a close-up near wall (blue box).

A.3.8. Solving the System of Equation

The discretized equations relative to the single control volume are coupled with the adjacent control volumes. So, in order to obtain the solution, a linear system of the equation has to be solved. Due to the large size of the involved matrices, the solution can not be found directly, and iterative methods are used. STAR-CCM+ uses the algebraic multigrid method that consists of the iteration on linear systems of different sizes (as we had different meshes): this improves a lot the convergence because low-wavelength errors (responsible for a low convergence rate) decrease rapidly on the small matrices, whereas short-wavelength errors reduce themselves in the full ones. To solve the systems of equation (one for each velocity component and one for pressure), the Gauss-Seidel Method relaxation scheme has been used. In addition, for the pressure system of the equation, the Conjugate-Gradient method as a preconditioner is used to improve the convergence rate. In contrast, no preconditioner is necessary for the velocities because, for its nature, it is usually characterized by a fast convergence rate.

The simulations were started using initial fields obtained by perturbing the solution, ensuring quick development of the turbulent flow. A hexahedral mesh (A.6) is used in all simulations, and some information of the grid resolution, geometric parameters of permeable and impermeable channel case from the current, and other resources are included in the following table.

Table A.4: Comparison and overview of current and publicly available database of DNS of wall bounded channel flow. The domain lengths are normalized with channel half-height H. The maximum grid sizes are listed in wall units. The averaging time T is normalized with H/u_τ^{top}. . FC represents a Fourier-Chebyshev method and FD a staggered finite difference method (fourth-orderin streamwise and spanwise, second-order in normal direction), S(/hp) is spectral (/H-type finite elements based discretization) methodFV represents a finite volume method. The superscipt * shows present simulation for smooth wall channel, ** shows a case of spanwise arranged cylinders with $\epsilon = 0.2$, *** shows a case of longitudinally arranged cylinders with $\epsilon = 0.2$, **** shows a case of longitudinally arranged cylinders with $\epsilon = 0.1$.

		Domain		Grid (max)					Centerline values			
Data base	Re_τ	L_x	L_z	Δx^+_{max}	Δy^+_{max}	Δz^+_{max}	T	Method	u^+	urms	vrms	wrms
Kim et al. (1987)	180	4π	2π	12	4.4	7	10	FC	18.209	0.7903	0.6044	0.6170
Moser et al. (1999)	178.1	4π	$\frac{4}{3}\pi$	17.7	4.4	5.9	-	FC	18.30	0.8140	0.6118	0.5893
Abe et al. (2001)	180	12.8	6.4	9.0	5.9	4.5	40	FD	18.64	0.8054	0.6368	0.6041
Kozuka et al. (2009)	180	6.5	3.2	0.56	0.97	1.1	3.1	FD	18.55	0.8084	0.6410	0.6280
Chu et al. (2021)	193	100	8π	6.3	0.43	4.9	15	S/hp	18.19	1.0004	0.5231	0.5200
Smooth channel*	193	2π	π	9.474	8.25	6.316	20	FV	18.75	0.8012	0.5911	0.5660
Porous bed channel**	193	2π	π	9.474	8.25	6.316	20	FV	16.146	0.942	0.642	0.680
Porous bed channel***	193	2π	π	9.474	8.25	6.316	20	FV	18.561	0.859	0.596	0.5935
Porous bed channel****	193	2π	π	9.474	8.25	6.316	20	FV	19.775	0.888	0.592	0.357

Table A.5: Flow characteristics of turbulent channel flow with lower impermeable and permeable walls.

θ	ν	$\approx Re$	$\approx Re_\tau^{top}$	$\approx Re_\tau^{bot}$	u_τ^{top}	u_τ^{bot}
0.5	5.181×10^{-3}	3100	193	193	1	1
0.5	5.181×10^{-3}	2718	170.430	194.943	0.883	1.101
0.5	5.181×10^{-3}	3354	192.241	193.399	0.996	1.002
0.5	5.181×10^{-3}	3122	186.100	199.228	0.964	1.032

Bibliography

Abderrahaman-Elena, N. and García-Mayoral, R. (2017). Analysis of anisotropically permeable surfaces for turbulent drag reduction. *Physical Review Fluids*, 2(11):114609.

Abe, H., Kawamura, H., and Matsuo, Y. (2001). Direct numerical simulation of a fully developed turbulent channel flow with respect to the reynolds number dependence. *Journal of Fluids Engineering*, 123(2):382–393.

Achdou, Y., Pironneau, O., and Valentin, F. (1998). Effective boundary conditions for laminar flows over periodic rough boundaries. *Journal of Computational Physics*, 147(1):187–218.

Agelinchaab, M., Tachie, M. F., and Ruth, D. W. (2006). Velocity measurement of flow through a model three-dimensional porous medium. *Physics of Fluids*, 18(1):017105.

Airiau, C. and Bottaro, A. (2020). Flow of shear-thinning fluids through porous media. *Advances in Water Resources*, 143:103658.

Aleyev, Y. G. (1977). Nekton and the body of water. In *Nekton*, pages 367–370. Springer.

Alinovi, E. and Bottaro, A. (2018). Apparent slip and drag reduction for the flow over superhydrophobic and lubricant-impregnated surfaces. *Physical Review Fluids*, 3(12):124002.

Angot, P., Bruneau, C.-H., and Fabrie, P. (1999). A penalization method to take into account obstacles in incompressible viscous flows. *Numerische Mathematik*, 81(4):497–520.

Ankhelyi, M. V., Wainwright, D. K., and Lauder, G. V. (2018). Diversity of dermal denticle structure in sharks: Skin surface roughness and three-dimensional morphology. *Journal of Morphology*, 279(8):1132–1154.

Arenas, I., García, E., Fu, M. K., Orlandi, P., Hultmark, M., and Leonardi, S. (2018). Comparison between super-hydrophobic, liquid infused and rough surfaces: a dns study. *arXiv preprint arXiv:1812.05674*.

Arthur, J. K., Ruth, D. W., and Tachie, M. F. (2009). Piv measurements of flow through a model porous medium with varying boundary conditions. *Journal of Fluid Mechanics*, 629:343.

Asai, M. and Floryan, J. M. (2006). Experiments on the linear instability of flow in a wavy channel. *European Journal of Mechanics-B/Fluids*, 25(6):971–986.

Auriault, J.-L., Boutin, C., and Geindreau, C. (2010). *Homogenization of coupled phenomena in heterogenous media*, volume 149. John Wiley & Sons.

Basson, A. and Gérard-Varet, D. (2008). Wall laws for fluid flows at a boundary with random roughness. *Communications on Pure and Applied Mathematics: A Journal Issued by the Courant Institute of Mathematical Sciences*, 61(7):941–987.

Batchelor, C. K. and Batchelor, G. K. (2000). *An introduction to fluid dynamics*. Cambridge University Press.

Battiato, I., Ferrero V, P. T., O'Malley, D., Miller, C. T., Takhar, P. S., Valdés-Parada, F. J., and Wood, B. D. (2019). Theory and applications of macroscale models in porous media. *Transport in Porous Media*, 130(1):5–76.

Battiato, I. and Tartakovsky, D. M. (2011). Applicability regimes for macroscopic models of reactive transport in porous media. *Journal of Contaminant Hydrology*, 120-121:18–26.

Beavers, G. S. and Joseph, D. D. (1967). Boundary conditions at a naturally permeable wall. *Journal of Fluid Mechanics*, 30(1):197–207.

Bechert, D., Bruse, M., Hage, W., Meyer, R., Bechert, D., Bruse, M., Hage, W., and Meyer, R. (1997a). Biological surfaces and their technological application-laboratory and flight experiments on drag reduction and separation control. In *28th Fluid Dynamics Conference, USA*, page 1960.

Bechert, D. and Reif, W. (1985). On the drag reduction of the shark skin. In *23rd Aerospace Sciences Meeting*, page 546.

Bechert, D. W. and Bartenwerfer, M. (1989). The viscous flow on surfaces with longitudinal ribs. *Journal of Fluid Mechanics*, 206:105–129.

Bechert, D. W., Bartenwerfer, M., Hoppe, G., and Reif, W.-E. (1986). Drag reduction mechanisms derived from shark skin. *IN: ICAS*, 2:1044–1068.

Bechert, D. W., Bruse, M., Hage, W., Hoeven, J. G. T. V. D., and Hoppe, G. (1997b). Experiments on drag-reducing surfaces and their optimization with an adjustable geometry. *Journal of Fluid Mechanics*, 338:59–87.

Bechert, D. W., Bruse, M., Hage, W., and Meyer, R. (2000). Fluid mechanics of biological surfaces and their technological application. *Naturwissenschaften*, 87(4):157–171.

Bensoussan, A., Lions, J.-L., and Papanicolaou, G. (2011). *Asymptotic analysis for periodic structures*, volume 374. AMS Chelsea Publishing, American Mathematical Society, Providence, Rhode Island.

Bhushan, B. (2009). Biomimetics: lessons from nature–an overview. *Philosophical Transactions of the Royal Society A: Mathematical, Physical and Engineering Sciences*, 367(1893):1445–1486.

Bird, R. B. (2002). Transport phenomena. *Applied Mechanics Reviews*, 55(1):R1–R4.

Biswas, G., Breuer, M., and Durst, F. (2004). Backward-facing step flows for various expansion ratios at low and moderate reynolds numbers. *Journal of Fluids Engineering*, 126(3):362–374.

Bixler, G. D. and Bhushan, B. (2012). Bioinspired rice leaf and butterfly wing surface structures combining shark skin and lotus effects. *Soft Matter*, 8(44):11271–11284.

Bolaños, S. J. and Vernescu, B. (2017). Derivation of the navier slip and slip length for viscous flows over a rough boundary. *Physics of Fluids*, 29(5):057103.

Bons, J. P. (2002). St and cf augmentation for real turbine roughness with elevated freestream turbulence. *Journal of Turbomachinery*, 124(4):632–644.

Boso, F. and Battiato, I. (2012). Homogenizability conditions in multicomponent reactive transport processes. In *AGU Fall Meeting Abstracts*, volume 2012, pages H42E–04.

Bottaro, A. (2019). Flow over natural or engineered surfaces: an adjoint homogenization perspective. *Journal of Fluid Mechanics*, 877.

Bottaro, A. and Naqvi, S. B. (2020). Effective boundary conditions at a rough wall: a high-order homogenization approach. *Meccanica*, 55(9):1781–1800.

Bruneau, C.-H., Lasseux, D., and Valdés-Parada, F. J. (2020). Comparison between direct numerical simulations and effective models for fluid-porous flows using penalization. *Meccanica*, pages 1–17.

Bruse, M., Bechert, D. W., Hoeven, J. G. T. V. D., Hage, W., and Hoppe, G. (1993). Experiments with conventional and with novel adjustable drag-reducing surfaces.

Carbou, G. (2008). Brinkmann model and double penalization method for the flow around a porous thin layer. *Journal of Mathematical Fluid Mechanics*, 10(1):126–158.

Carpenter, P. W., Davies, C., and Lucey, A. D. (2000). Hydrodynamics and compliant walls: Does the dolphin have a secret? *Current Science*, pages 758–765.

Carpenter, P. W. and Garrad, A. D. (1985). The hydrodynamic stability of flow over kramer-type compliant surfaces. part 1. tollmien-schlichting instabilities. *Journal of Fluid Mechanics*, 155:465–510.

Carpenter, P. W. and Garrad, A. D. (1986). The hydrodynamic stability of flow over kramer-type compliant surfaces. part 2. flow-induced surface instabilities. *Journal of Fluid Mechanics*, 170:199–232.

Carraro, T., Goll, C., Marciniak-Czochra, A., and Mikelić, A. (2013). Pressure jump interface law for the stokes–darcy coupling: confirmation by direct numerical simulations. *Journal of Fluid Mechanics*, 732:510–536.

Chakraverty, S., Mahato, N., Karunakar, P., and Rao, T. D. (2019). *Advanced numerical and semi-analytical methods for differential equations*. John Wiley & Sons.

Chandesris, M. and Jamet, D. (2006). Boundary conditions at a planar fluid–porous interface for a poiseuille flow. *International Journal of Heat and Mass Transfer*, 49(13-14):2137–2150.

Chavarin, A., Gómez-de Segura, G., García-Mayoral, R., and Luhar, M. (2021). Resolvent-based predictions for turbulent flow over anisotropic permeable substrates. *Journal of Fluid Mechanics*, 913.

Choi, H., Moin, P., and Kim, J. (1991). On the effect of riblets in fully developed laminar channel flows. *Physics of Fluids A: Fluid Dynamics*, 3(8):1892–1896.

Choi, K.-S. (1989). Near-wall structure of a turbulent boundary layer with riblets. *Journal of Fluid Mechanics*, 208:417–458.

Choi, K.-S., Yang, X., Clayton, B. R., Glover, E. J., Atlar, M., Semenov, B. N., and Kulik, V. M. (1997). Turbulent drag reduction using compliant surfaces. *Proceedings of the Royal Society of London. Series A: Mathematical, Physical and Engineering Sciences*, 453(1965):2229–2240.

Chu, D. C. and Karniadakis, G. E. (1993). A direct numerical simulation of laminar and turbulent flow over riblet-mounted surfaces. *Journal of Fluid Mechanics*, 250:1–42.

Chu, X., Wang, W., Yang, G., Terzis, A., Helmig, R., and Weigand, B. (2021). Transport of turbulence across permeable interface in a turbulent channel flow: interface-resolved direct numerical simulation. *Transport in Porous Media*, 136(1):165–189.

Chu, X., Weigand, B., and Vaikuntanathan, V. (2018). Flow turbulence topology in regular porous media: from macroscopic to microscopic scale with direct numerical simulation. *Physics of Fluids*, 30(6):065102.

Chu, X., Yang, G., Pandey, S., and Weigand, B. (2019). Direct numerical simulation of convective heat transfer in porous media. *International Journal of Heat and Mass Transfer*, 133:11–20.

Cowin, S. C. (2013). *Continuum mechanics of anisotropic materials*. Springer Science & Business Media.

Darcy, H. (1857). *Recherches expérimentales relatives au mouvement de l'eau dans les tuyaux*, volume 1. Mallet-Bachelier.

Debisschop, J. R. and Nieuwstadt, F. T. M. (1996). Turbulent boundary layer in an adverse pressure gradient-effectiveness of riblets. *AIAA Journal*, 34(5):932–937.

Devries, F., Dumontet, H., Duvaut, G., and Léné, F. (1989). Homogenization and damage for composite structures. *International Journal for Numerical Methods in Engineering*, 27(2):285–298.

Dixon, A. E., Lucey, A. D., and Carpenter, P. W. (1994). Optimization of viscoelastic compliant walls for transition delay. *AIAA journal*, 32(2):256–267.

Domel, A. G., Saadat, M., Weaver, J. C., Haj-Hariri, H., Bertoldi, K., and Lauder, G. V. (2018a). Shark skin-inspired designs that improve aerodynamic performance. *Journal of the Royal Society Interface*, 15(139):20170828.

Domel, A. G., Saadat, M., Weaver, J. C., Haj-Hariri, H., Bertoldi, K., and Lauder, G. V. (2018b). Shark skin-inspired designs that improve aerodynamic performance. *Journal of the Royal Society Interface*, 15(139):20170828.

Dupont, S., Gosselin, F., Py, C., Langre, E. D., Hemon, P., and Brunet, Y. (2010). Modelling waving crops using large-eddy simulation: comparison with experiments and a linear stability analysis. *Journal of Fluid Mechanics*, 652:5.

Dussan V., E. B. (1976). The moving contact line: The slip boundary condition.

Eggenweiler, E. and Rybak, I. (2020). Unsuitability of the beavers–joseph interface condition for filtration problems. *Journal of Fluid Mechanics*, 892.

Ern, A., G. J.-L. (2004). Theory and practice of finite elements.

Eshelby, J. D. (1957). The determination of the elastic field of an ellipsoidal inclusion, and related problems. *Proceedings of the Royal Society of London. Series A. Mathematical and Physical Sciences*, 241(1226):376–396.

Ferziger, J. H., Perić, M., and Street, R. L. (2002). *Computational methods for fluid dynamics*, volume 3. Springer.

Fish, J., Shek, K., Pandheeradi, M., and Shephard, M. S. (1997). Computational plasticity for composite structures based on mathematical homogenization: Theory and practice. *Computer Methods in Applied Mechanics and Engineering*, 148(1-2):53–73.

Fletcher, T., Altringham, J., Peakall, J., Wignall, P., and Dorrell, R. (2014). Hydrodynamics of fossil fishes. *Proceedings of the Royal Society B: Biological Sciences*, 281(1788):20140703.

Floryan, J. M. (2002). Centrifugal instability of couette flow over a wavy wall. *Physics of Fluids*, 14(1):312–322.

Floryan, J. M. (2003). Vortex instability in a diverging-converging channel. *Journal of Fluid Mechanics*, 482:17–50.

Floryan, J. M. (2005). Two-dimensional instability of flow in a rough channel. *Physics of Fluids*, 17(4):044101.

Floryan, J. M. (2007). Three-dimensional instabilities of laminar flow in a rough channel and the concept of hydraulically smooth wall. *European Journal of Mechanics-B/Fluids*, 26(3):305–329.

Floryan, J. M. and Floryan, C. (2009). Traveling wave instability in a diverging–converging channel. *Fluid Dynamics Research*, 42(2):025509.

Fu-quan, S., You-sheng, X., and Hua-mei, L. (2007). Blood flow in capillaries by using porous media model. *Journal of Central South University of Technology*, 14(1):46–49.

Gad-El-Hak, M., Blackwelder, R. F., and Riley, J. J. (1984). On the interaction of compliant coatings with boundary-layer flows. *Journal of Fluid Mechanics*, 140:257–280.

Gamrat, G., Favre-Marinet, M., Person, S. L., Baviere, R., and Ayela, F. (2008). An experimental study and modelling of roughness effects on laminar flow in microchannels. *Journal of Fluid Mechanics*, 594:399–423.

García-Mayoral, R. and Jiménez, J. (2011). Drag reduction by riblets. *Philosophical Transactions of the Royal Society A: Mathematical, Physical and Engineering Sciences*, 369(1940):1412–1427.

Garcia-Mayoral, R. and Jiménez, J. (2011). Drag reduction by riblets. *Philosophical Transactions of the Royal Society A: Mathematical, Physical and Engineering Sciences*, 369(1940):1412–1427.

Ghosh, S., Lee, K., and Moorthy, S. (1995). Multiple scale analysis of heterogeneous elastic structures using homogenization theory and voronoi cell finite element method. *International Journal of Solids and Structures*, 32(1):27–62.

Goldstein, D., Handler, R., and Sirovich, L. (1995). Direct numerical simulation of turbulent flow over a modeled riblet covered surface. *Journal of Fluid Mechanics*, 302:333–376.

Goldstein, D. B. (2006). Methods for reducing the viscous drag on a surface and drag reducing device. US Patent 7,044,073.

Goldstein, D. B. and Tuan, T.-C. (1998). Secondary flow induced by riblets. *Journal of Fluid Mechanics*, 363:115–151.

Gómez-de Segura, G., Fairhall, C. T., MacDonald, M., Chung, D., and García-Mayoral, R. (2018). Manipulation of near-wall turbulence by surface slip and permeability. In *Journal of Physics: Conference Series*, volume 1001, page 012011. IOP Publishing.

Guedes, J. M. and Kikuchi, N. (1990). Preprocessing and postprocessing for materials based on the homogenization method with adaptive finite element methods. *Computer Methods in Applied Mechanics and Engineering*, 83(2):143–198.

Guo, C., Li, Y., Nian, X., Xu, M., Liu, H., and Wang, Y. (2020). Experimental study on the slip velocity of turbulent flow over and within porous media. *Physics of Fluids*, 32(1):015111.

Guo, J., Veran-Tissoires, S., and Quintard, M. (2016). Effective surface and boundary conditions for heterogeneous surfaces with mixed boundary conditions. *Journal of Computational Physics*, 305:942–963.

Gupte, S. K. and Advani, S. G. (1997). Flow near the permeable boundary of a porous medium: An experimental investigation using lda. *Experiments in Fluids*, 22(5):408–422.

Hagen, G. H. L. (1854). *Über den einfluss der temperatur auf die bewegung des wassers in röhren–*. Königliche Akademie der Wissenschaften.

Han, X., Zhang, D., Li, X., and Li, Y. (2008). Bio-replicated forming of the biomimetic drag-reducing surfaces in large area based on shark skin. *Chinese Science Bulletin*, 53(10):1587–1592.

He, X., Apte, S., Schneider, K., and Kadoch, B. (2018). Angular multiscale statistics of turbulence in a porous bed. *Physical Review Fluids*, 3(8):084501.

Hecht, F. (2012). New development in freefem++. *Journal of Numerical Mathematics*, 20(3-4):251–266.

Herwig, H., Gloss, D., and Wenterodt, T. (2008). A new approach to understanding and modelling the influence of wall roughness on friction factors for pipe and channel flows. *Journal of Fluid Mechanics*, 613:35.

Hiemenz, K. (1911). Die grenzschicht an einem in den gleichformigen flussigkeitsstrom eingetauchten geraden kreiszylinder. *Dingler's Polytechnical Journal*, 326:321–324.

Hocking, L. M. (1976). A moving fluid interface on a rough surface. *Journal of Fluid Mechanics*, 76(4):801–817.

Holt, T. E. and Smith, D. M. (1989). Surface roughness effects on knudsen diffusion. *Chemical Engineering Science*, 44(3):779–781.

Hornung, U. (1996). *Homogenization and porous media*, volume 6. Springer Science & Business Media.

Hussain, A. K. M. F. and Reynolds, W. C. (1970). The mechanics of an organized wave in turbulent shear flow. *Journal of Fluid Mechanics*, 41(2):241–258.

Ibrahim, J. I., Gómez-de Segura, G., Chung, D., and García-Mayoral, R. (2021). The smooth-wall-like behaviour of turbulence over drag-altering surfaces: a unifying virtual-origin framework. *Journal of Fluid Mechanics*, 915.

Introïni, C., Quintard, M., and Duval, F. (2011). Effective surface modeling for momentum and heat transfer over rough surfaces: Application to a natural convection problem. *International Journal of Heat and Mass Transfer*, 54(15-16):3622–3641.

Itoh, M., Tamano, S., Iguchi, R., Yokota, K., Akino, N., Hino, R., and Kubo, S. (2006). Turbulent drag reduction by the seal fur surface. *Physics of Fluids*, 18(6):065102.

Jäger, W. and Mikelić, A. (2001). On the roughness-induced effective boundary conditions for an incompressible viscous flow. *Journal of Differential Equations*, 170(1):96–122.

Jamet, D. and Chandesris, M. (2009). On the intrinsic nature of jump coefficients at the interface between a porous medium and a free fluid region. *International Journal of Heat and Mass Transfer*, 52(1-2):289–300.

Jansons, K. M. (1988). Determination of the macroscopic (partial) slip boundary condition for a viscous flow over a randomly rough surface with a perfect slip microscopic boundary condition. *The Physics of Fluids*, 31(1):15–17.

Jiménez, J. (1994). On the structure and control of near wall turbulence. *Physics of Fluids*, 6(2):944–953.

Jiménez, J. (2004). Turbulent flows over rough walls. *Annual Review of Fluid Mechanics*, 36:173–196.

Jiménez, J., Uhlmann, M., Pinelli, A., and Kawahara, G. (2001). Turbulent shear flow over active and passive porous surfaces. *Journal of Fluid Mechanics*, 442:89.

Jones, I. P. (1973). Low reynolds number flow past a porous spherical shell. In *Mathematical Proceedings of the Cambridge Philosophical Society*, volume 73, pages 231–238.

Jung, Y. C. and Bhushan, B. (2009). Biomimetic structures for fluid drag reduction in laminar and turbulent flows. *Journal of Physics: Condensed Matter*, 22(3):035104.

Kamrin, K., Bazant, M. Z., and Stone, H. A. (2009). Effective slip boundary conditions for arbitrary periodic surfaces: the surface mobility tensor. *arXiv preprint arXiv:0911.1328*.

Khanafer, K., AlAmiri, A., Pop, I., and Bull, J. L. (2008). *Flow and Heat Transfer in Biological Tissues: Application of Porous Media Theory. In: Vadász P. (eds) Emerging Topics in Heat and Mass Transfer in Porous Media. Theory and Applications of Transport in Porous Media*. Springer.

Kim, J., Moin, P., and Moser, R. (1987). Turbulence statistics in fully developed channel flow at low reynolds number. *Journal of Fluid Mechanics*, 177:133–166.

Klausmann, K. and Ruck, B. (2017). Drag reduction of circular cylinders by porous coating on the leeward side. *Journal of Fluid Mechanics*, 813:382.

Kleinstreuer, C. and Koo, J. (2004). Computational analysis of wall roughness effects for liquid flow in micro-conduits. *Journal of Fluids Engineering*, 126(1):1–9.

Kouznetsova, V., Geers, M. G. D., and Brekelmans, W. A. M. (2002). Multi-scale constitutive modelling of heterogeneous materials with a gradient-enhanced computational homogenization scheme. *International Journal for Numerical Methods in Engineering*, 54(8):1235–1260.

Kozuka, M., Seki, Y., and Kawamura, H. (2009). Dns of turbulent heat transfer in a channel flow with a high spatial resolution. *International Journal of Heat and Fluid Flow*, 30(3):514–524.

Kramer, M. O. (1957). Boundary layer stabilization by distributed damping. *Journal of Aeronautical Sciences*, 24:459.

Kramer, M. O. (1961). The dolphins'secret. *Journal of the American Society for Naval Engineers*, 73(1):103–108.

Kuruneru, S. T. W., Vafai, K., Sauret, E., and Gu, Y. T. (2020). Application of porous metal foam heat exchangers and the implications of particulate fouling for energy-intensive industries. *Chemical Engineering Science*, page 115968.

Kuwata, Y. and Suga, K. (2016). Lattice boltzmann direct numerical simulation of interface turbulence over porous and rough walls. *International Journal of Heat and Fluid Flow*, 61:145–157.

Kuwata, Y. and Suga, K. (2017). Direct numerical simulation of turbulence over anisotropic porous media. *Journal of Fluid Mechanics*, 831:41–71.

Kuznetsov, A. V. (2008). New developments in bioconvection in porous media: bioconvection plumes, bio-thermal convection, and effects of vertical vibration. *Emerging Topics in Heat and Mass Transfer in Porous Media*, pages 181–217.

Lācis, U. and Bagheri, S. (2017). A framework for computing effective boundary conditions at the interface between free fluid and a porous medium. *Journal of Fluid Mechanics*, 812:866–889.

Lācis, U., Sudhakar, Y., Pasche, S., and Bagheri, S. (2020). Transfer of mass and momentum at rough and porous surfaces. *Journal of Fluid Mechanics*, 884.

Lang, A., Motta, P., Habegger, M. L., Hueter, R., and Afroz, F. (2011). Shark skin separation control mechanisms. *Marine Technology Society Journal*, 45(4):208–215.

Lang, A. W., Bradshaw, M. T., Smith, J. A., Wheelus, J. N., Motta, P. J., Habegger, M. L., and Hueter, R. E. (2014). Movable shark scales act as a passive dynamic micro-roughness to control flow separation. *Bioinspiration & Biomimetics*, 9(3):036017.

Lang, A. W., Motta, P., Hidalgo, P., and Westcott, M. (2008). Bristled shark skin: a microgeometry for boundary layer control? *Bioinspiration & Biomimetics*, 3(4):046005.

Larson, R. E. and Higdon, J. J. L. (1986). Microscopic flow near the surface of two-dimensional porous media. part 1. axial flow. *Journal of Fluid Mechanics*, 166:449–472.

Larson, R. E. and Higdon, J. J. L. (1987). Microscopic flow near the surface of two-dimensional porous media. part 2. transverse flow. *Journal of Fluid Mechanics*, 178:119–136.

Lasseux, D., Valdés-Parada, F. J., and Porter, M. L. (2016). An improved macroscale model for gas slip flow in porous media. *Journal of Fluid Mechanics*, 805:118–146.

Lee, C. K., Sun, C.-C., and Mei, C. C. (1996). Computation of permeability and dispersivities of solute or heat in periodic porous media. *International Journal of Heat and Mass Transfer*, 39(4):661–676.

Lee, S.-J. and Choi, Y.-S. (2008). Decrement of spanwise vortices by a drag-reducing riblet surface. *Journal of Turbulence*, (9):N23.

Lee, T., Fisher, M., and Schwarz, W. H. (1993). Investigation of the stable interaction of a passive compliant surface with a turbulent boundary layer. *Journal of Fluid Mechanics*, 257:373–401.

Lene, F. and Leguillon, D. (1982). Homogenized constitutive law for a partially cohesive composite material. *International Journal of Solids and Structures*, 18(5):443–458.

Li, L., Chen, Q., Jin, F., and Wu, C. (2015). How does a polymer chain pass through a cylindrical pore under an elongational flow field? *Polymer*, 67:A1–A13.

Liu, Q. and Prosperetti, A. (2011). Pressure-driven flow in a channel with porous walls. *Journal of Fluid Mechanics*, 679:77.

Luchini, P. (1992). Effects of riblets on the growth of laminar and turbulent boundary layers. In *7th European Drag Reduction Meeting*, pages 24–25.

Luchini, P. (1995). Asymptotic analysis of laminar boundary-layer flow over finely grooved surfaces. *European journal of mechanics. B, Fluids*, 14(2):169–195.

Luchini, P. (1996). Reducing the turbulent skin friction. In *Computational Methods in Applied Sciences' 96*, pages 465–470.

Luchini, P. (2013). Linearized no-slip boundary conditions at a rough surface. *Journal of Fluid Mechanics*, 737:349.

Luchini, P. (2018). Structure and interpolation of the turbulent velocity profile in parallel flow. *European Journal of Mechanics-B/Fluids*, 71:15–34.

Luchini, P., Manzo, F., and Pozzi, A. (1991). Resistance of a grooved surface to parallel flow and cross-flow. *Journal of Fluid Mechanics*, 228:87–109.

Luminari, N., Zampogna, G. A., Airiau, C., and Bottaro, A. (2019). A penalization method to treat the interface between a free-fluid region and a fibrous porous medium. *Journal of Porous Media*, 22(9).

Mei, C. C. and Vernescu, B. (2009). *Homogenization methods for multiscale mechanics*. World Scienctific.

Mei, C. C. and Vernescu, B. (2010). *Homogenization methods for multiscale mechanics*. World Scientific.

Meroney, R. N. (2007). Fires in porous media: Natural and urban canopies. In *Flow and Transport Processes with Complex Obstructions*, pages 271–310. Springer.

Miksis, M. J. and Davis, S. H. (1994). Slip over rough and coated surfaces. *Journal of Fluid Mechanics*, 273:125–139.

Millikan, C. B. (1939). A critical discussion of turbulent flow in channels and circular tubes. In *Proceedings of the 5th International Congress on Applied Mechanics*, pages 386–392. Wiley.

Mohammadi, A. and Floryan, J. M. (2012). Mechanism of drag generation by surface corrugation. *Physics of Fluids*, 24(1):013602.

Mohammadi, A. and Floryan, J. M. (2013a). Groove optimization for drag reduction. *Physics of Fluids*, 25(11):113601.

Mohammadi, A. and Floryan, J. M. (2013b). Pressure losses in grooved channels. *Journal of Fluid Mechanics*, 725:23–54.

Moody, L. F. and Princeton, N. J. (1944). Friction factors for pipe flow. *Transactions of the ASME*, 66:671–684.

Morad, M. R. and Khalili, A. (2009). Transition layer thickness in a fluid-porous medium of multi-sized spherical beads. *Experiments in Fluids*, 46(2):323.

Morkovin, M. V. (1990). On roughness—induced transition: facts, views, and speculations. In *Instability and Transition*, pages 281–295. Springer.

Moser, R. D., Kim, J., and Mansour, N. N. (1999). Direct numerical simulation of turbulent channel flow up to re τ= 590. *Physics of Fluids*, 11(4):943–945.

Multiphysics (2019). v.5.4.

Naqvi, S. B. and Bottaro, A. (2021). Interfacial conditions between a free-fluid region and a porous medium. *International Journal of Multiphase Flow*, page 103585.

Navier, C. L. M. H. (1823). Mémoire sur les lois du mouvement des fluides. *Mémoires de l'Académie Royale des Sciences de l'Institut de France*, 6(1823):389–440.

Nayfeh, A. H. (2008). *Perturbation methods*. John Wiley & Sons.

Nieuwstadt, F. T. M., Wolthers, W., Leijdens, H., Prasad, K. K., and Manen, A. S.-v. (1993). The reduction of skin friction by riblets under the influence of an adverse pressure gradient. *Experiments in Fluids*, 15(1):17–26.

Nikuradse, J. (1933). *Strömungsgesetze in rauhen Rohren*. VDI-Verlag.

Ochoa-Tapia, J. A., Valdés-Parada, F. J., Goyeau, B., and Lasseux, D. (2017). Fluid motion in the fluid/porous medium inter-region. *Revista Mexicana de Ingeniería Química*, 16(3):923–938.

Ochoa-Tapia, J. A. and Whitaker, S. (1995). Momentum transfer at the boundary between a porous medium and a homogeneous fluid-ii. comparison with experiment. *International Journal of Heat and Mass Transfer*, 38(14):2647–2656.

Orlandi, P. and Leonardi, S. (2006). Dns of turbulent channel flows with two-and three-dimensional roughness. *Journal of Turbulence*, (7):N73.

Papautsky, I., Brazzle, J., Ameel, T., and Frazier, A. B. (1999). Laminar fluid behavior in microchannels using micropolar fluid theory. *Sensors and Actuators A: Physical*, 73(1-2):101–108.

Patankar, S. V. and Spalding, D. B. (1983). A calculation procedure for heat, mass and momentum transfer in three-dimensional parabolic flows. In *Numerical prediction of flow, heat transfer, turbulence and combustion*, pages 54–73. Elsevier.

Prat, M., Plouraboué, F., and Letalleur, N. (2002). Averaged reynolds equation for flows between rough surfaces in sliding motion. *Transport in Porous Media*, 48(3):291–313.

Pu, X., Li, G., and Huang, H. (2016). Preparation, anti-biofouling and drag-reduction properties of a biomimetic shark skin surface. *Biology Open*, 5(4):389–396.

Rawlings, D. C. and Burg, A. G. (2016). Elastomeric riblets.

Reynolds, O. (1883). Iii. an experimental investigation of the circumstances which determine whether the motion of water shall be direct or sinuous, and of the law of resistance in parallel channels. *Proceedings of the Royal Society of London*, 35(224-226):84–99.

Richardson, S. (1971a). A model for the boundary condition of a porous material. part 2. *Journal of Fluid Mechanics*, 49(2):327–336.

Richardson, S. (1971b). A model for the boundary condition of a porous material. part 2. *Journal of Fluid Mechanics*, 49(2):327–336.

Saffman, P. G. (1971). On the boundary condition at the surface of a porous medium. *Studies in Applied Mathematics*, 50(2):93–101.

Sánchez-Palencia, E. (1980). *Non-homogeneous media and vibration theory: Lecture Notes in Physics*, volume 127. Springer-Verlag.

Saric, W. S., Carrillo, R. B., and Reibert, M. S. (1998). Nonlinear stability and transition in 3-d boundary layers. *Meccanica*, 33(5):469–487.

Sarkar, K. and Prosperetti, A. (1996). Effective boundary conditions for stokes flow over a rough surface. *Journal of Fluid Mechanics*, 316:223–240.

Schlichting, H. (1937). *Experimental investigation of the problem of surface roughness.* Number 823. National Advisory Commitee for Aeronautics Collection.

Schlichting, H. and Gersten, K. (1979). *Boundary-layer theory.* MacGraw Hill, New York.

Siemens (2021). Simcenter star-ccm+.

Sin, V. K. and Tong, T. Y. (2009). Stagnation-point pressure distribution and wall shear stress: numerical simulation and similarity solution. In *Proceedings of the World Congress on Engineering*, volume 2. Citeseer.

Sirovich, L. and Karlsson, S. (1997). Turbulent drag reduction by passive mechanisms. *Nature*, 388(6644):753–755.

Starzewski, M. O. (1998). Random field models of heterogeneous materials. *International Journal of Solids and Structures*, 35(19):2429–2455.

Sudhakar, Y., Lãcis, U., Pasche, S., and Bagheri, S. (2019). Higher order homogenized boundary conditions for flows over rough and porous surfaces. *arXiv preprint arXiv:1909.07125*.

Suquet, P., Sawczuk, A., and Bianchi, G. (1983). Local and global aspects in the mathematical theory of plasticity, plasticity today. (edited by a. sawczuk and g. bianchi). pages 279–310.

Szumbarski, J. and Floryan, J. M. (2006). Transient disturbance growth in a corrugated channel. *Journal of Fluid Mechanics*, 568:243.

Taylor, G. I. (1923). Viii. stability of a viscous liquid contained between two rotating cylinders. *Philosophical Transactions of the Royal Society of London. Series A, Containing Papers of a Mathematical or Physical Character*, 223(605-615):289–343.

Taylor, G. I. (1971). A model for the boundary condition of a porous material. part 1. *Journal of Fluid Mechanics*, 49(2):319–326.

Terzis, A., Zarikos, I., Weishaupt, K., Yang, G., Chu, X., Helmig, R., and Weigand, B. (2019). Microscopic velocity field measurements inside a regular porous medium adjacent to a low reynolds number channel flow. *Physics of Fluids*, 31(4):042001.

Tian, G., Fan, D., Feng, X., and Zhou, H. (2021). Thriving artificial underwater drag-reduction materials inspired from aquatic animals: progresses and challenges. *RSC Advances*, 11(6):3399–3428.

Tilton, N. and Cortelezzi, L. (2006). The destabilizing effects of wall permeability in channel flows: A linear stability analysis. *Physics of Fluids*, 18(5):051702.

Tilton, N. and Cortelezzi, L. (2008). Linear stability analysis of pressure-driven flows in channels with porous walls. *Journal of Fluid Mechanics*, 604:411.

Torquato, S. and Haslach Jr., H. W. (2002). *Random heterogeneous materials: microstructure and macroscopic properties*, volume 55.

Valdés-Parada, F. J., Aguilar-Madera, C. G., Ochoa-Tapia, J. A., and Goyeau, B. (2013). Velocity and stress jump conditions between a porous medium and a fluid. *Advances in Water Resources*, 62:327–339.

Valdés-Parada, F. J. and Lasseux, D. (2021). A novel one-domain approach for modeling flow in a fluid-porous system including inertia and slip effects. *Physics of Fluids*, 33(2):022106.

Van Rij, J. A., Belnap, B. J., and Ligrani, P. M. (2002). Analysis and experiments on three-dimensional, irregular surface roughness. *Journal of Fluids Engineering*, 124(3):671–677.

Venkatakrishnan, V. (1995). Convergence to steady state solutions of the euler equations on unstructured grids with limiters. *Journal of computational physics*, 118(1):120–130.

Versteeg, H. K. and Malalasekera, W. (2007). *An introduction to computational fluid dynamics: the finite volume method*. Pearson education.

Walsh, M. and Lindemann, A. (1984). Optimization and application of riblets for turbulent drag reduction. In *22nd Aerospace Sciences Meeting*, page 347.

Walsh, M. J. (1983). Riblets as a viscous drag reduction technique. *AIAA Journal*, 21(4):485–486.

Walsh, M. J. (1990). Riblets. *Viscous Drag Reduction in Boundary Layers*, pages 203–261.

Wang, W., Chu, X., Lozano-Durán, A., Helmig, R., and Weigand, B. (2021). Information transfer between turbulent boundary layers and porous media. *Journal of Fluid Mechanics*, 920.

Whitaker, S. (1986). Flow in porous media i: A theoretical derivation of darcy's law. *Transport in Porous Media*, 1(1):3–25.

Zampogna, G. A. and Bottaro, A. (2016). Fluid flow over and through a regular bundle of rigid fibres. *Journal of Fluid Mechanics*, 792:5–35.

Zampogna, G. A., Lācis, U., Bagheri, S., and Bottaro, A. (2019a). Modeling waves in fluids flowing over and through poroelastic media. *International Journal of Multiphase Flow*, 110:148–164.

Zampogna, G. A., Magnaudet, J., and Bottaro, A. (2019b). Generalized slip condition over rough surfaces. *Journal of Fluid Mechanics*, 858:407–436.

Zampogna, G. A., Magnaudet, J., and Bottaro, A. (2019c). Generalized slip condition over rough surfaces. *Journal of Fluid Mechanics*, 858:407–436.

Zampogna, G. A., Naqvi, S. B., Magnaudet, J., and Bottaro, A. (2019d). Compliant riblets: Problem formulation and effective macrostructural properties. *Journal of Fluids and Structures*, 91:102708.

Zhang, D., Luo, Y., Xiang, L., and Chen, H. (2011). Numerical simulation and experimental study of drag-reducing surface of a real shark skin. *Journal of Hydrodynamics, Ser. B*, 23(2):204–211.